Fundamentals and Applications of Super-Liquid-Repellent Surfaces

Dissertation
zur Erlangung des Grades
„Doktor der Naturwissenschaften“
im Promotionsfach Chemie

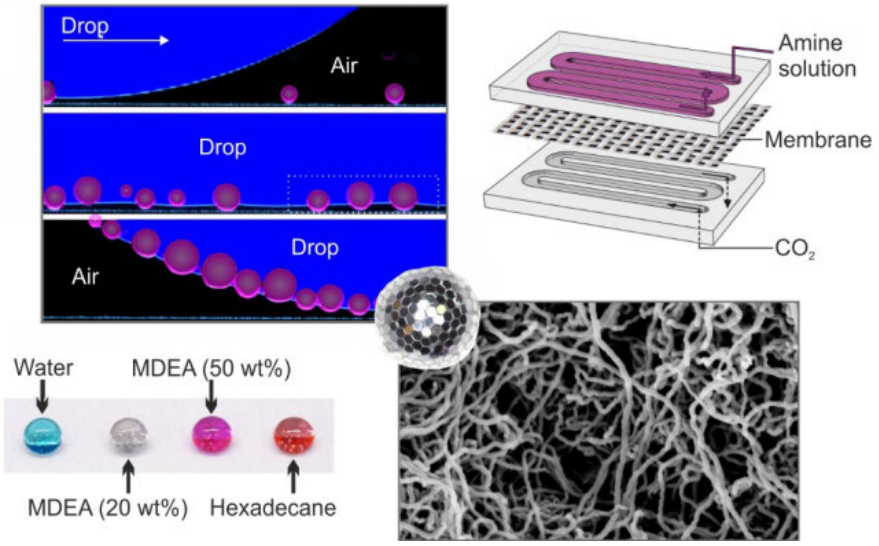

Fachbereich Chemie, Pharmazie und Geowissenschaften
der Johannes Gutenberg-Universität
in Mainz

Florian Geyer
geboren in Worms
Mainz, 2018

Die vorliegende Arbeit wurde am Max-Planck-Institut für Polymerforschung unter der Anleitung von [redacted] und [redacted] von Mai 2015 bis Dezember 2018 erstellt.

Tag der mündlichen Prüfung: 04.04.2019

Dekan: [redacted]
1. Berichterstatter: [redacted]
2. Berichterstatter: [redacted]
3. Berichterstatter: [redacted]

Dissertation an der Universität Mainz (D77)

TABLE OF CONTENTS

ABSTRACT 7

ZUSAMMENFASSUNG 9

1 INTRODUCTION 13

1.1 MOTIVATION AND OUTLINE 13
1.2 HOW TO DESCRIBE WETTABILITY — THE YOUNG EQUATION 15
1.3 WETTING OF ROUGH SURFACES — THE WENZEL EQUATION 16
1.4 WETTING OF HETEROGENEOUS SURFACES — THE CASSIE-BAXTER EQUATION 17
1.5 SUPERHYDROPHOBIC SURFACES 17
1.6 SURFACE TENSION AND ENERGY 19
1.7 CONTACT ANGLE MEASUREMENTS 21
1.8 CONTACT ANGLE HYSTERESIS 23
1.9 ROLL-OFF ANGLE MEASUREMENTS 26
1.10 SUPER-LIQUID-REPELLENT SURFACES 26
1.11 SILICONE NANOFILAMENTS 34
1.12 APPLICATIONS OF SUPERHYDROPHOBIC AND SUPER-LIQUID-REPELLENT SURFACES 38
1.13 PARTICLES AT INTERFACES — LIQUID MARBLES 43

2 HOW DROPS START SLIDING OVER SOLID SURFACES 48

2.1 INTRODUCTION 49
2.2 RESULTS AND DISCUSSION 50
2.3 EXPERIMENTAL SECTION 58
2.4 AUTHOR CONTRIBUTIONS 64
2.5 ACKNOWLEDGMENTS 65

3 WHEN AND HOW SELF-CLEANING OF SUPERHYDROPHOBIC SURFACES WORKS 66

3.1 INTRODUCTION 67
3.2 RESULTS AND DISCUSSION 68
3.3 EXPERIMENTAL SECTION 80
3.4 AUTHOR CONTRIBUTIONS 87
3.5 ACKNOWLEDGMENTS 87

4 ENHANCING CARBON DIOXIDE CAPTURE USING ROBUST SUPEROMNIPHOBIC MEMBRANES ... 88

4.1 INTRODUCTION 89
4.2 RESULTS AND DISCUSSION 91
4.3 CONCLUSION 98
4.4 EXPERIMENTAL SECTION 98
4.5 AUTHOR CONTRIBUTIONS 104
4.6 ACKNOWLEDGMENTS 105

5 HOW TO COAT THE INSIDE OF NARROW AND LONG TUBES WITH A SUPER-LIQUID-REPELLENT LAYER 106
5.1 INTRODUCTION 107
5.2 RESULTS AND DISCUSSION 108
5.3 CONCLUSION 117
5.4 EXPERIMENTAL SECTION 117
5.5 AUTHOR CONTRIBUTIONS 125
5.6 ACKNOWLEDGMENTS 126
6 POLYHEDRAL LIQUID MARBLES 127
6.1 INTRODUCTION 128
6.2 RESULTS AND DISCUSSION 128
6.3 CONCLUSION 138
6.4 EXPERIMENTAL SECTION 138
6.5 AUTHOR CONTRIBUTIONS 143
6.6 ACKNOWLEDGMENTS 143
7 IMPACT AND OUTLOOK 144
8 REFERENCES 146
9 ACKNOWLEDGMENTS 164
10 APPENDIX 165
10.1 SUPPORTING INFORMATION FOR CHAPTER 3 165
10.2 SUPPORTING INFORMATION FOR CHAPTER 6 169
11 CURRICULUM VITAE 173
12 LIST OF PUBLICATIONS AND CONTRIBUTIONS 175
12.1 PUBLICATIONS 175
12.2 PATENT APPLICATIONS 176
12.3 PRESENTATIONS (SELECTED) 176

ABSTRACT

Superhydrophobic, super-liquid-repellent, and superomniphobic surfaces have attracted much attention in industry and academia in the past two decades. Liquid drops on such surfaces take an almost spherical shape and easily roll off. Despite the substantial progress, there is a lack of understanding of how drops move on such surfaces. While there are various approaches for the fabrication of these surfaces on open and flat substrates, the coating of complex geometries such as long tubes remains difficult. Crucial to the success of super-liquid-repellent surfaces is to devise novel and promising applications. This involves understanding the advantages and challenges of these surfaces for industrial or large-scale applications. To approach this task, this work combines fundamental and applied aspects. On the one hand, the motion and lateral adhesion of drops on superhydrophobic surfaces are investigated, for example, to gain an in-depth understanding of how self-cleaning works and when it fails. On the other hand, novel and improved surfaces are designed. The questions are motivated by environmental and social demands. Can carbon dioxide (CO_2) be captured more efficiently using super-liquid-repellent membranes to reduce CO_2 emissions, e.g., in power plants? — To obtain a maximum packing of gas exchange membranes, flat sheet membranes need to be replaced by porous super-liquid-repellent tubes. A method to fabricate meter-long super-liquid-repellent tubes is developed. Long-term or biomedical gas exchange applications like blood oxygenation require anti-biofouling properties. Therefore, the antibacterial properties of the coated tubes are investigated. Finally, the design concepts are transferred to a different type of materials, the liquid marbles. Polyhedral liquid marbles are developed and characterized.

The *first part* of this thesis answers the question of how drops start moving on solid hydrophobic and superhydrophobic surfaces, in particular, which forces are involved during the onset and movement of the droplets. It is shown that the lateral adhesion force between a drop and a solid surface can be separated into a static and kinetic regime. This finding is unexpectedly similar to solid-solid friction. The force on the droplet increases until a specific threshold force is reached in the static regime. After overcoming the threshold force, the drop starts moving, and the friction force decreases to a constant value in the kinetic regime. This analogy is valid for various liquids of different surface tensions on smooth and rough surfaces.

The *second part* investigates one of the most relevant applications and properties of superhydrophobic surfaces, originally inspired by the lotus leaf: self-cleaning. Contaminations such as dust are easily cleaned away by water drops rolling across these surfaces. Despite the vast interest in the self-cleaning properties, only little is known about the influence of contaminant particle size, especially on the nanoscale and how the self-cleaning process proceeds on the micrometer scale. It is shown that the pore size of the super-

hydrophobic surface is crucial and needs to be smaller than the contaminant size to obtain contamination-resistant surfaces. The self-cleaning process is visualized on the micrometer scale using confocal microscopy, and the lateral adhesion forces while drops move over the contaminated surfaces are quantified, leading to a deeper understanding of the process. Outdoor environmental (>200 days) and industrial standardized contamination experiments show that the super-liquid-repellent surfaces used herein can resist contamination for prolonged periods.

The *third part* focuses on the development of a novel application for superomniphobic surfaces that is the use of such a surface as a gas exchange membrane. A chemically, mechanically, and thermally stable superomniphobic membrane for CO_2 capture is fabricated. This membrane can repel highly basic, concentrated amine solutions commonly used for CO_2 capture, e.g., in power plants. It provides a large liquid-gas interface and prevents wetting of the membrane, which usually reduces the gas exchange efficiency. This resulted in performance increasements of up to 40% relative to commercial membranes.

In the *fourth part*, a strategy to coat the inside of meter-long and narrow tubes (down to 1 mm inner diameter) with a super-repellent-layer is developed. An oxidative Fenton solution is pumped through the tubes for activation, and subsequently, a super-liquid-repellent nanofilament coating is applied to the tubes. This method can be used to coat tubes made of various materials ranging from polymers, organic/inorganic hybrids, and ceramics to metals. The super-liquid-repellent coating is applied to medical catheter tubes, and their antibacterial properties are investigated. It is found that the nanofilaments show pronounced antibacterial properties and retain these irrespective of the wetting state. This makes the coated tubes a promising material for antibacterial catheters, and the coating may be applied to porous tubes for gas exchange applications.

The *fifth part* utilizes mobile superhydrophobic layers to encapsulate droplets, forming liquid marbles. Here, a new type of liquid marble is introduced, a so-called polyhedral liquid marble. Hydrophobic hexagonal plates adsorb to the liquid-air interface, stabilizing the droplet. The plates are separated by tiny air gaps, resembling a superhydrophobic micropillar layer. The plates can self-assemble into highly ordered hexagonally-arranged domains. Liquid marbles composed of only 4 to 6 plates with tetrahedral, pentahedral, and cubic shapes can be realized. Highly asymmetric polyhedral liquid marbles and letters are obtained due to the strong interfacial jamming facilitated by the rigid hexagonal plates. The polyhedral liquid marbles show various stimuli-responsive properties when exposed to water, ammonia, or tetrahydrofuran vapors. The gases are exchanged through the tiny gaps between the plates.

ZUSAMMENFASSUNG

Superhydrophobe, superflüssigkeitsabweisende bzw. superomniphobe Oberflächen erzielten in den letzten zwei Jahrzehnten große Aufmerksamkeit in Industrie und Wissenschaft. Auf diesen Oberflächen nehmen Flüssigkeitstropfen eine fast sphärische Form an und rollen sehr leicht ab. Trotz des großen Fortschritts in diesem Forschungsfeld ist die Bewegung von Tropfen auf solchen Oberflächen nicht gut verstanden. Während es vielzählige Methoden zur Herstellung solcher Oberflächen auf offenen und flachen Substraten gibt, stellt sich die Beschichtung von komplexeren Geometrien, wie langen Schläuchen, als schwierig heraus. Für den Erfolg dieser Oberflächen ist es essenziell, neue und vielversprechende Applikationen zu entwickeln. Dazu ist es wichtig, die Vorteile und Herausforderungen dieser Oberflächen für industrielle und großskalige Anwendungen zu verstehen. Um sich dieser Aufgabe anzunähern, kombiniert diese Arbeit fundamentale und angewandte Aspekte. Auf der einen Seite werden die Bewegung und laterale Adhäsion von Tropfen auf superhydrophoben Oberflächen untersucht, um zum Beispiel ein tieferes Verständnis für die Frage, wie die Selbstreinigung dieser Oberflächen funktioniert und was deren Grenzen sind, zu erlangen. Auf der anderen Seite werden neuartige und verbesserte Oberflächen designt. Die Fragenstellungen sind hierbei u. a. durch umweltrelevante und soziale Erfordernisse motiviert. Wie zum Beispiel: Kann man CO_2 mit Hilfe von superflüssigkeitsabweisenden Membranen effektiver abscheiden, um die CO_2-Emissionen, beispielweise in Kraftwerken, zu senken? — Um eine maximale Packungsdichte an Gasaustauschmembranen zu erhalten, müssen Flachmembranen durch poröse superflüssigkeitsabweisende Schläuche oder Rohre ersetzt werden. Hierzu wird eine Methode zur Herstellung von meterlangen superflüssigkeitsabweisenden Schläuchen entwickelt. Langzeit- und biomedizinische Gasaustauschanwendungen wie beispielsweise Blutoxygenierung setzen Anti-Biofoulingeigenschaften voraus. Daher werden ebenfalls die antibakteriellen Eigenschaften der beschichteten Schläuche untersucht. Schließlich werden die Designkonzepte auf einen anderen Typ von Materialen übertragen, den Flüssigkeitsmurmeln. Hierbei werden sogenannte polyedrische Flüssigkeitsmurmeln entwickelt und charakterisiert.

Der *erste Teil* dieser Dissertation beantwortet die Frage, wie Tropfen sich auf hydrophoben und superhydrophoben Oberflächen bewegen. Im Speziellen, was die beteiligten Kräfte während des Anfangs sowie während der Bewegung der Tropfen sind. Es wird gezeigt, dass die laterale Adhäsionskraft zwischen einem Tropfen und einer festen Oberfläche in einen Haft- und Gleitbereich unterteilt werden kann. Diese Erkenntnis ist unerwarteterweise ähnlich zur Fest-Fest-Reibung. Im Haftbereich nimmt die Kraft auf den Tropfen bis zu einer gewissen kritischen Kraft zu. Nachdem diese kritische Kraft überwunden ist, fängt der Tropfen an, sich zu bewegen und die Reibungskraft nimmt im Gleit-

bereich auf ein konstantes Niveau ab. Diese Analogie ist gültig für verschiedene Flüssigkeiten mit unterschiedlichen Oberflächenspannungen auf glatten sowie auf rauen Oberflächen.

Der *zweite Teil* untersucht eine der relevantesten Applikationen und Eigenschaften von superhydrophoben Oberflächen, welche ursprünglich durch das Lotusblatt inspiriert wurde: die Selbstreinigung. Kontaminationen wie Staub werden problemlos von Wassertropfen, die über die Oberflächen rollen, mitgenommen. Trotz des großen Interesses an den selbstreinigenden Eigenschaften, gibt es nur wenige Erkenntnisse über den Einfluss der Kontaminationspartikelgröße, speziell auf der Nanoskala und wie der Selbstreinigungsprozess auf der Mikrometerskala abläuft. Es wird gezeigt, dass die Porengröße der superhydrophoben Oberfläche kleiner als die Kontaminantgröße sein muss, um eine verunreinigungsresistente Oberfläche herzustellen. Der Selbstreinigungsprozess wird auf der Mikrometerskala durch Verwendung von konfokaler Mikroskopie visualisiert und die lateralen Kräfte, während Tropfen sich über die kontaminierten Oberflächen bewegen, werden quantifiziert. Dies führt zu einem tieferen Verständnis des Selbstreinigungsprozesses. Außenbewitterungs- (>200 Tage) sowie industrielle, standardisierte Kontaminationstests zeigen, dass superflüssigkeitsabweisende Oberflächen mit Poren im Nanometerbereich Verunreinigungen im Allgemeinen widerstehen können.

Der *dritte Teil* fokussiert sich auf die Entwicklung einer neuartigen Anwendung für superomniphobe Oberflächen: die Verwendung als Gasaustauschmembranen. Eine chemisch, mechanisch und thermisch stabile superomniphobe Membran für die CO_2-Abscheidung wird hergestellt. Diese Membran kann stark basische und konzentrierte Aminlösungen abweisen, welche zur CO_2-Abscheidung, zum Beispiel in Kraftwerken, verwendet werden. Die Membran verfügt über eine große Flüssigkeit-Gas-Austauschfläche und die abweisenden Eigenschaften verhindern, dass die Membran benetzt wird, was üblicherweise zur Reduzierung der Gasaustauscheffizienz führt. Dies resultierte in Performanceverbesserungen von bis zu 40% im Vergleich zu kommerziellen Membranen.

Im *vierten Teil* wird eine Vorgehensweise zur Beschichtung des Inneren von meterlangen und schmalen Schläuchen (bis zu einem 1 mm Innendurchmesser) entwickelt. Eine oxidative Fentonlösung wird zur Aktivierung durch die Schläuche gepumpt und im Anschluss wird eine superflüssigkeitsabweisende Nanofilament-Beschichtung in den Schläuchen aufgebracht. Diese Methode kann zur Beschichtung von Schläuchen und Rohren aus unterschiedlichen Materialien, von Polymeren und organisch/anorganischen Hydriden bis hin zu Keramiken und Metallen, verwendet werden. Die superflüssigkeitsabweisende Beschichtung wird auf medizinischen Katheterschläuchen aufgebracht und deren antibakterielle Eigenschaften werden untersucht. Es zeigt sich, dass die Nanofilamente ausgeprägte antibakterielle Eigenschaften besitzen und diese unabhängig vom Be-

netzungszustand erhalten bleiben. Dies macht die beschichteten Schläuche zu einem vielversprechenden Material für antibakterielle Katheter und des Weiteren könnte die Beschichtung auch auf porösen Schläuchen für Gasaustauschanwendungen aufgebracht werden.

Der *fünfte Teil* benutzt mobile, superhydrophobe Schichten, um Tropfen einzuschließen, was zur Entstehung einer Flüssigkeitsmurmel führt. Hierbei wird ein neuer Typ von Flüssigkeitsmurmeln eingeführt, die sogenannten polyedrischen Flüssigkeitsmurmeln. Hydrophobe hexagonale Plättchen adsorbieren an der Flüssigkeit-Luft-Grenzfläche, um den Tropfen zu stabilisieren. Die Plättchen sind durch kleine Luftlücken voneinander getrennt, was einer superhydrophoben Mikrosäulenschicht ähnelt. Die Plättchen können sich zu hochgeordneten, hexagonalen Domänen selbstorganisieren. Es können Flüssigkeitsmurmeln bestehend aus lediglich vier bis sechs Plättchen mit tetraedrischen, pentaedrischen und kubischen Formen realisiert werden. Hochasymmetrische, polyedrische Flüssigkeitsmurmeln und -buchstaben werden aufgrund der starken Grenzflächenblockierung durch die steifen hexagonalen Plättchen erhalten. Die polyedrischen Flüssigkeitsmurmeln zeigen verschiedene stimuli-responsive Eigenschaften, sobald man diese Wasser-, Ammoniak- oder Tetrahydrofurandämpfen aussetzt. Die Gase werden durch kleine Luftlücken zwischen den Plättchen ausgetauscht.

1 INTRODUCTION

1.1 MOTIVATION AND OUTLINE

Superhydrophobic, super-liquid-repellent, and superomniphobic surfaces have attracted a lot of attention in industry and academia in the past decades. Since the 2000s, the interest in such surfaces has ever been increasing, currently peaking at almost 2000 papers published on superhydrophobic surfaces in 2018 (according to Web of Science, searching for "superhydrophobic"). These bio-inspired, self-cleaning surfaces are characterized by the fact that liquid drops show very low adhesion, take an almost spherical shape, and easily roll off the surface. Despite the large amount of research conducted, there are still many open questions and challenges to be addressed before these surfaces can be applied in real-world applications, which are vital for the success of these surfaces. The present thesis investigates both fundamental and applied aspects to contribute to the basic understanding as well as prospective applications of super-liquid-repellent surfaces.

Lateral adhesion force measurements are employed to reveal the onset of motion of drops on such surfaces (Chapter 2) and to characterize the forces needed to remove particle contamination on superhydrophobic surfaces. Self-cleaning is one of the most important properties and applications of superhydrophobic surfaces as the range of possible uses is large, e.g., for windows or as cover for solar cells. This work answers the question of what are the limits of self-cleaning and how to improve the surface design appropriately (Chapter 3). To fabricate super-liquid-repellent surfaces, this work generally employs a coating consisting of silicone nanofilaments. These nanofilaments have diameters between 10 and 100 nm and lengths of up to several micrometers to introduce a surface roughness with re-entrant morphology needed for super-liquid-repellency. Superomniphobic membranes based on nanofilament-coated fabrics are developed to answer the question if such membranes can be used to efficiently capture CO_2, a highly relevant issue in times of record CO_2 emissions and increasing global temperatures (Chapter 4). Here, it is particularly important that the membranes can super-repel highly concentrated amine solutions that are commonly used for gas scrubbing in industry. To obtain a maximal packing density of gas exchange membranes and thus a maximal exchange area per volume, coated hollow fiber membranes are needed. Even though there is a large variety of methods to coat open and flat surfaces, ways to coat tubes with super-liquid-repellent layers are limited. Here, a method to coat meter-long and narrow tubes (down to 1 mm in

diameter) is developed, and wide applicability to various materials is demonstrated (Chapter 5). Many long-term or biomedical applications like blood oxygenation demand anti-biofouling properties. Consequently, the anti-biofouling properties of the coated tubes are investigated for potential use in medical devices. This is important to answer another debated question in this field: Are superhydrophobic surfaces antibacterial?
During self-cleaning, particles accumulate at the air-water interface. This can result in the formation of so-called liquid marbles. Liquid marbles are droplets encapsulated in a mobile superhydrophobic layer and are commonly prepared by rolling droplets on a (super)hydrophobic powder. The powder usually consists of spherical particles or particle aggregates. This work investigates if well-defined non-spherical particles can be utilized to fabricate such armored droplets and how they assemble on the surface of the drop (Chapter 6). Potential applications of these liquid marbles, including their response to external stimuli like different gases and vapors, are explored.

This thesis[1] gives a brief introduction to the basics of wetting and characterization of surfaces in Chapters 1.2–1.9. Afterward, a brief overview of recent advances in the fabrication of super-liquid-repellent surfaces (Chapter 1.10), including the synthesis of silicone nanofilaments (Chapter 1.11), is presented. Prospective applications of super-liquid-repellent surfaces, including self-cleaning, oil/water separation, anti-biofouling, and gas exchange, are discussed in Chapter 1.12. Particles at interfaces are described in Chapter 1.13, which is relevant for self-cleaning and the formation of liquid marbles. Chapters 2–6 present original contributions to the fundamentals, fabrication, and application of super-liquid-repellent surfaces and liquid marbles as well as the basic understanding of droplet movement on such surfaces. Each chapter contains an Introduction, Results and Discussion, and an Experimental Section. The authors' contributions are summarized at the end of each chapter. Chapter 7 discusses the impact of the findings and gives a brief outlook.

[1]The present thesis is a cumulative publication-based thesis, and parts thereof are published or submitted for publication in peer-reviewed journals. A note is added to the corresponding chapters. The Supporting Information is available online for the published manuscripts. Important Supporting Figures can be found in the Appendix for the submitted manuscripts. The full Supporting Information is available from the Author. Supporting Figures are generally labeled with the letter "S."

1.2 HOW TO DESCRIBE WETTABILITY — THE YOUNG EQUATION[2]

Controlling the surface wettability[1-5] is essential in many areas of our daily life and industry. For instance, wettability determines the adhesion of drops[6-9] to window panes, paint to cars, and ice aggregation on airplanes.[10] Wettability is tuned in printing, microfluidics,[11] heat transfer applications,[12-16] and recently in the fabrication of metal-organic-frameworks.[17-21] Many natural surfaces, such as the wings of insects or birds, have unique nonwetting properties that are essential to their function.[22-23] The degree of wetting of a drop on a surface is determined by the interfacial tensions between the phases in contact, namely, the liquid, solid, and gas (air) phase. The fundamental equation correlating the contact angle of a drop with its interfacial tensions on an ideally flat, homogeneous, solid surface was developed by Thomas Young in 1805 (Eq. 1).[24]

$$\cos\theta\,\gamma_{\mathrm{LG}} + \gamma_{\mathrm{SL}} = \gamma_{\mathrm{SG}} \tag{1}$$

Here, γ_{LG}, γ_{SL}, and γ_{SG} are the liquid-gas, solid-liquid, and solid-gas γ_{LG}interfacial tensions, respectively. The angle θ is called Young's or intrinsic contact angle and is measured at the three-phase contact line where the liquid, the solid, and the gas phase meet. The Young equation describes the balance of forces at the three-phase contact line between the interfacial tensions acting parallel to the solid surface (**Figure 1**a). It should be noted that interfacial tensions are a force per unit length.

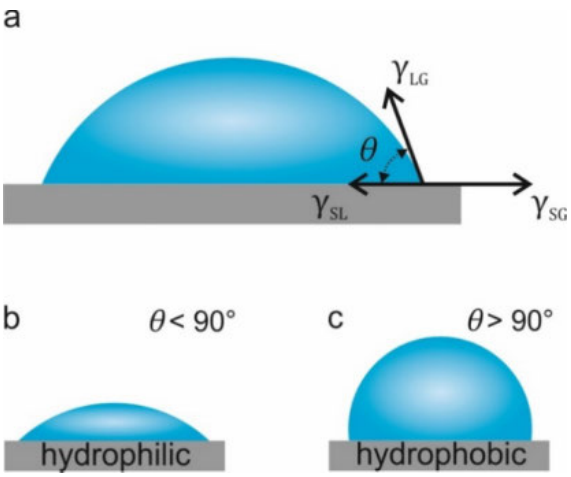

Figure 1. **a**) Schematic illustration of a sessile drop. The Young contact angle at the three-phase contact line depends on the liquid-gas (γ_{LG}), the solid-liquid (γ_{SL}), and the solid-gas (γ_{SG}) interfacial tensions. **b**,**c**) Sketch of a water drop on a hydrophilic surface (b) and on a hydrophobic surface (c).

A liquid assuming a contact angle below 90° on a substrate is considered to be (partially) wetting, and a liquid with a contact angle of 90° and greater is considered to be nonwetting

[2]Parts of the introduction are submitted and accepted for publication within a review article in *Adv. Mater.*

(**Figure 1**b,c). Similarly, surfaces showing a water contact angle below 90° are defined as hydrophilic, while surfaces that show a water contact angle of 90° and greater are defined as hydrophobic.[5, 25] Young's equation cannot be used to describe the contact angle of a sessile drop on rough or chemically inhomogeneous surfaces because the force balance at the three-phase contact line is affected by surface roughness or inhomogeneities. More complex approaches taking roughness and heterogeneities into account are needed.

1.3 WETTING OF ROUGH SURFACES — THE WENZEL EQUATION

The roughness factor r was introduced by Wenzel (**Figure 2**a) to account for surface roughness (Eq. 2):[26]

$$r = \frac{\text{Actual surface}}{\text{Apparent surface area}} \tag{2}$$

The roughness factor is the ratio of the actual surface area divided by the macroscopically apparent surface area and is thus larger than unity. The contact angle on a rough substrate is given by the Wenzel equation:

$$\cos\theta_W = r\cos\theta \tag{3}$$

Here, θ_W is the apparent contact angle a drop forms on a rough surface, i.e., on a length scale much larger than the surface roughness or protrusions, and θ is Young's contact angle of the material. In the Wenzel state, the liquid penetrates the pores of the rough surface. The introduction of surface roughness amplifies the intrinsic wetting properties of the material. On a hydrophobic material, roughness leads to a larger contact angle, whereas on a hydrophilic surface, roughness leads to a lower contact angle or complete wetting of the surface.[5, 26]

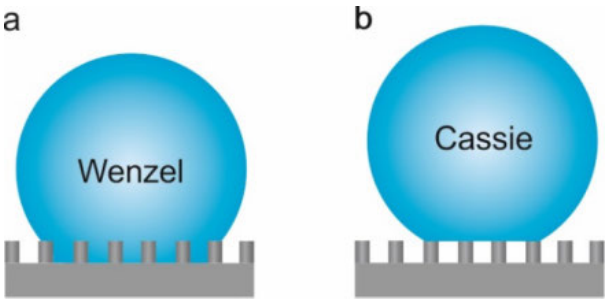

Figure 2. Different wetting states. **a**) Schematic illustration of a droplet in the Wenzel state.[26] **b**) Schematic illustration of a droplet in the Cassie state assuming a solid-liquid-air composite interface.[27]

1.4 WETTING OF HETEROGENEOUS SURFACES — THE CASSIE-BAXTER EQUATION

The wetting of composite surfaces consisting of different materials can be described using the so-called Cassie-Baxter equation (Eq. 4):[27]

$$\cos\theta_C = \sum_i \phi_i \cos\theta_i \tag{4}$$

Here, ϕ_i denotes the fraction of the surface in contact with the liquid that consists of material *i*, and θ_i is Young's contact angle of material *i*. The Cassie-Baxter equation thus describes the apparent contact angle θ_C based on the microscopic material composition.
The so-called Cassie state is a situation in which a liquid droplet rests on the asperities of a rough surface (**Figure 2**b), entrapping air underneath the droplet. This solid-liquid-gas composite interface can thermodynamically be more favorable than wetting the rough structure (Wenzel state). The Cassie state can be described using $i = 2$. Here, $\theta_1 = \theta$ describes the intrinsic contact angle of the solid material and $\theta_2 = \theta_{Air}$ is the contact angle of a drop solely in contact with air ($\theta_{Air} = 180°$). The Cassie-Baxter equation can then be simplified to Eq. 5:

$$\cos\theta_C = \phi_{SL}\cos\theta + \phi_{Air}\cos 180° = \phi_{SL}(1 + \cos\theta) - 1 \tag{5}$$

Here, $\phi_{SL} = 1 - \phi_{Air}$ describes the solid-liquid contact area. Such a composite interface usually results in contact angles far above 120°. Even though the Young, Wenzel, and Cassie-Baxter models and equations are important for the basic understanding of contact angle and wetting phenomena, it should be noted that these equations are derived assuming thermodynamic equilibrium between the three phases. Thus, none of the equations can account for pinning events or contact angle hysteresis (see Chapter 1.8 for a detailed discussion) as these considerably complicate the theoretical and mathematical description.[3, 28-29]

1.5 SUPERHYDROPHOBIC SURFACES

Extremely hydrophobic surfaces on which water drops adopt the Cassie state, show very high contact angles ($\theta_C > 150°$), and easily roll off when the surface is tilted by a few degrees (<10°) are so-called superhydrophobic surfaces (**Figure 3**).[28, 30-32] The first superhydrophobic surfaces were already described more than 50 years ago.[33] From the late 1970s

to the late 1990s, the biologist Barthlott and his co-workers shaped the term superhydrophobicity based on investigations of the microscopic structure and wetting properties of numerous plants.[34] These findings initiated a substantial increase in academic and industrial research on artificial superhydrophobic surfaces.[30] In nature, examples of superhydrophobic surfaces are lotus leaves (*Nelumbo nucifera*) or body parts of insects such as the legs of water striders, among others (**Figure 3**a).[34-35]

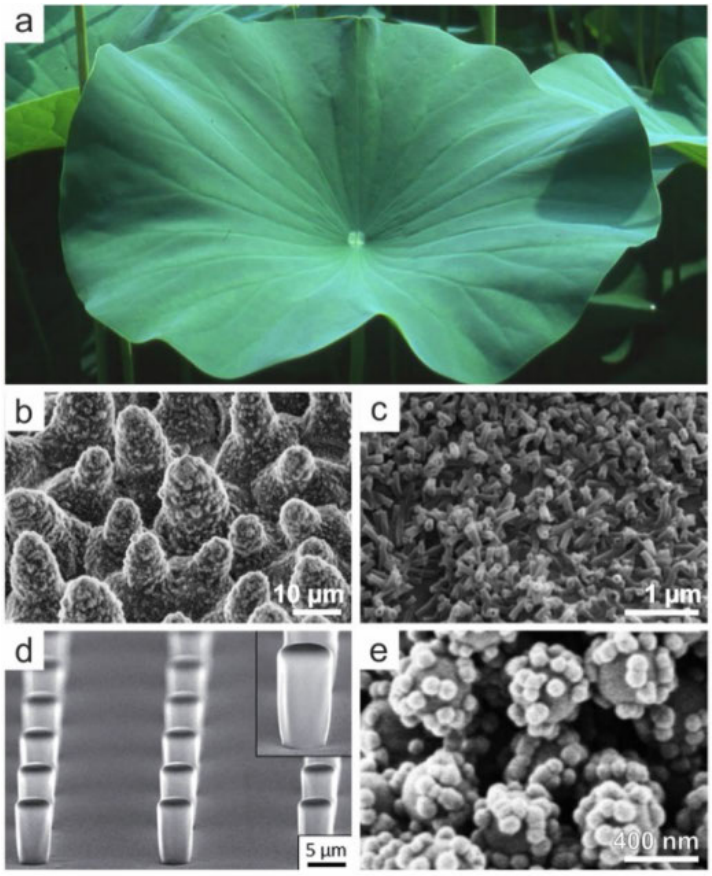

Figure 3. Natural and artificial superhydrophobic surfaces. **a**) Photograph of a lotus leaf. **b,c**) Micro- and nanostructure of the lotus leaf observed by scanning electron microscopy (SEM). Reproduced from ref.[36] Copyright 2011, Beilstein-Institut, licensed under CC BY 2.0. **d**) Model superhydrophobic surface consisting of SU-8 micropillar arrays. Reproduced from ref.[37] with permission from The Royal Society of Chemistry. **e**) Artificial lotus-like superhydrophobic surface consisting of raspberry-like nanoparticles. Reproduced from ref.[38] with permission from The Royal Society of Chemistry.

Therefore, superhydrophobicity is often referred to as the lotus effect.[39] Besides the super-repellency, these surfaces are known for their exceptional self-cleaning properties.[31] Common to these surfaces is that they combine two unique features; a high surface roughness on the nano- or micrometer scale and low surface energy, i.e., an intrinsically hydrophobic surface (intrinsic contact angle must close to or above 90°). The reason for the high water contact angles is that the solid-liquid contact area is very low[3], often even below 10% of the total composite interface. Due to the low solid-liquid contact area, water drops generally show low adhesion toward these surfaces and can easily roll off. Different

methods have been developed to prepare superhydrophobic surfaces, including the deposition of nanoparticulate coatings by spray[40] or dip coating,[38] candle soot deposition,[41] lithography,[42-43] chemical etching,[44] plasma etching,[45] and electrospinning.[46]

1.6 SURFACE TENSION AND ENERGY

The interfacial tension γ can be interpreted as the work dW required to generate a new surface area dA (Eq. 6):[5]

$$\gamma = \frac{\mathrm{d}W}{\mathrm{d}A} \tag{6}$$

It takes units of energy per area (J m^{-2}) or force per unit length (N m^{-1}). It should be noted that the term "surface energy" is preferred for solids, whereas "interfacial tension" or "surface tension" are commonly used for liquids. Different interactions like van-der-Waals forces, electrostatic interactions, or hydrogen bonds lead to strong attraction between molecules in the bulk. At the surface, parts of these interactions are absent, as the molecules at the surface are only partially surrounded by other molecules. Therefore, the transport of molecules from the bulk to the surface to increase the surface area requires energy to break intermolecular bonds. This energy is the surface energy or tension. Liquids' surface tensions generally range between 20 mN m^{-1} (= 20 × 10^{-3} N^{-1}) and 80 mN m^{-1}.[5] For instance, water has a surface tension of 72.5 mN m^{-1} at 20 °C. However, some fluorinated liquids have surface tensions as low as 12 mN m^{-1}.[47-48] Surface tensions of liquids can be easily measured using the sessile or pendant drop method or with tensiometers utilizing a Du Noüy-ring[49] or a Wilhelmy-plate.[5, 50] However, measuring the surface energy of a solid surface is less straightforward. The work required to deform a solid cannot easily be separated from the work that is required to create new surface area. Therefore, surface energies are mostly measured indirectly. There are several models for determining the surface energy. Most of these models rely on the measurement of contact angles for liquids with different surface tensions.

One of the first approaches is known as the Zisman plot (**Figure 4**).[51] Here, the cosines of the contact angles of various liquids are plotted against the respective surface tension of the liquid. It is important that the used liquids have largely different surface tensions to obtain a meaningful graph. The plot is extrapolated to $\cos\theta = 1$, which equals to an effective contact angle of 0°, symbolizing complete surface wetting. This point represents the so-termed critical surface tension γ_{crit} and may be considered as the surface energy. After

all, this is not entirely accurate since the Zisman model does not account for the different types of surface interactions. The Fowkes[52] and Owens-Wendt-Rabel-Kaelble (OWRK)[53-55] methods introduce a distinction between dispersive and non-dispersive interactions and are therefore more suitable for polar surfaces. However, all of these methods are only applicable to materials with flat surfaces. They also assume that the drop is in thermodynamic equilibrium.

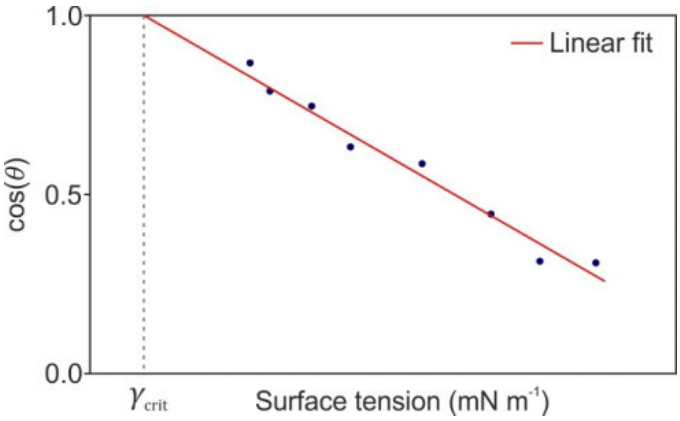

Figure 4. Sketch of a typical Zisman plot. The cosines of the contact angles of different liquids on a surface are plotted against the surface tension of these liquids. Extrapolation of a linear fit to $\cos\theta = 1$ yields the so-called critical surface tension γ_{crit}.

Solid surface energies can be as low as 6 mN m^{-1} and as high as several thousand micronewtons per meter.[56-58] Glass, metals, and metal oxides have high surface energies due to their strong (polar) intermolecular bonds and can form strong interactions with polar liquids, such as water. Conversely, low surface energy solids are nonpolar. Therefore, the intermolecular interactions of water are stronger than those between water molecules and nonpolar surfaces. Thus, water droplets assume high contact angles on such surfaces to minimize the contact area with the solid surface. Highly fluorinated surfaces have particularly low surface energies. An ideal surface fully covered with -CF_3 groups exhibits the lowest possible surface energy (6–7 mN m^{-1}).[58] Exchanging one fluorine atom for hydrogen (-CF_2H) already raises the surface energy to 15 mN m^{-1}. A further exchange of fluorine for hydrogen yields even higher surface energies (**Table 1**). It was also found that surfaces covered with terminal groups (-CF_3, -CH_3) have lower surface energies compared to their nonterminal counterparts (-CF_2-CF_2-, -CH_2-CH_2-).[56]

Table 1. Surface energies for various surface compositions and surfaces at 20°C.[56-58]

Surface composition/surface	Surface energy [10^{-3} N m^{-1}]
$-CF_3$	6–7
$-CF_2H$	15
$-CF_2-CF_2-$	18
$-CF_2-CH_2-$	25
$-CH_3$	20–24
$-CH_2-CH_2-$	31
-CH- (phenyl ring edge)	35
$-CCl_2-CH_2-$	40
MgO (100)	1200
Silicon (111)	1240

Thus, to obtain low surface energies and high hydrophobicity, a surface should have a high content of fluorocarbon compounds or at least large nonpolar hydrocarbon fragments.

1.7 CONTACT ANGLE MEASUREMENTS

Hydrophobic and superhydrophobic surfaces are typically characterized by conducting contact angle measurements with a goniometer. A liquid drop is deposited on the surface and observed using a camera from the side. The drop profiles of static or moving drops are then recorded.[59] The contact angle is extracted from a fit of the drop profile. The fitting method should be chosen with care because it can affect the extracted contact angle. **Figure 5** shows the fitting of a droplet using four common methods: ellipse, circle, tangent, and Young-Laplace fitting. These methods yield vastly different results for the same recording (ranging from roughly 150° to 180°).[60] The circle and Young-Laplace fits assume that the contact angles at the left and right sides of the drop are identical. This is rarely true for rough surfaces because the three-phase contact line is likely to be pinned at protrusions. The elliptical and tangent fits permit different angles at the left- and right-hand sides of the drop profile. The tangent fit tries to match the slope of the meniscus close to the three-phase contact line. Not only the fitting method but also the camera settings can influence the results. Particularly important parameters include the illumination, brightness, contrast, and gamma.[32]

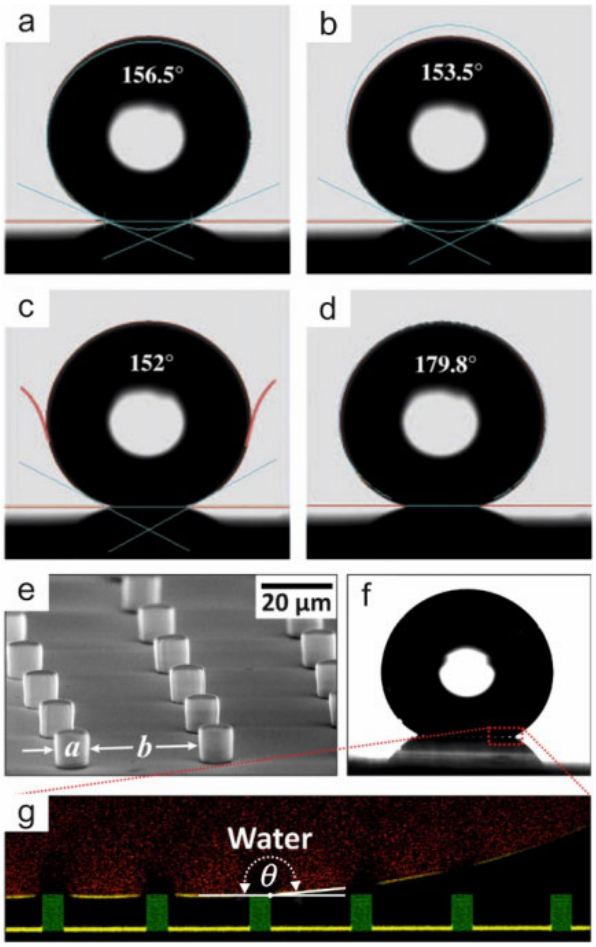

Figure 5. Side view of a sessile drop on a superhydrophobic surface. The lines show fits of the drop profile using different methods. **a**) Ellipse fitting. **b**) Circle fitting. **c**) Tangent fitting. **d**) Young-Laplace fitting. The baseline is shown in red. The turquoise lines show the fitting result. Reproduced from ref.[60] with permission from The Royal Society of Chemistry. **e**) SEM image of a superhydrophobic SU-8 micropillar array. **f**) Optical photograph of a water droplet on a superhydrophobic micropillar array. **g**) Laser scanning confocal microscopy image of a water droplet on the same superhydrophobic micropillar array. Reprinted figure with permission from ref.[61] Copyright 2016 by American Physical Society.

It is generally difficult to measure contact angles above 150° because the narrow gap between the liquid and the solid greatly reduces the amount of light passing through the gap and reaching the camera, making it difficult to identify the real contact line. Conventional optical methods also typically cannot resolve details underneath droplets, e.g., whether the droplet is in the Cassie or Wenzel state.[32, 60] It has recently been shown that other techniques like laser scanning confocal microscopy can be used to measure contact angles on superhydrophobic surfaces more accurately (**Figure 5**e–g).[61-62] In contrast to optical methods, the air cushion underneath a droplet on a superhydrophobic micropillar array and the position of the contact line can be fully resolved (compare **Figure 5**f to **Figure 5**g). A drawback of this method is that it requires a transparent substrate.

1.8 CONTACT ANGLE HYSTERESIS

On real surfaces with finite surface roughness and heterogeneity, one must discriminate between the so-called static, advancing, and receding contact angles.[63-64] The static contact angle can be measured directly after depositing the droplet on the surface. However, due to pinning of the three-phase contact line, deformation of the surface, evaporation, or slow spreading of the liquid, the static contact angle may change over time. Contact angles can also be influenced by the way the drop is deposited on the surface. The static contact angle is thus not a clearly defined state despite its importance for surface characterization. It lies between the advancing and receding contact angles, which can be measured using the following two methods.

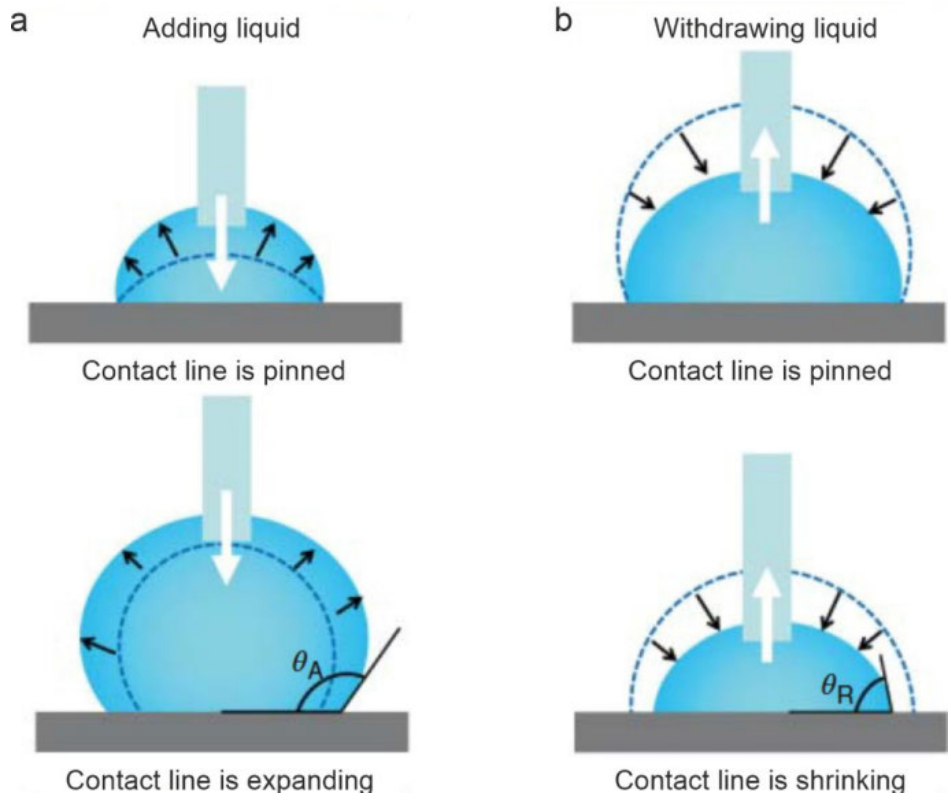

Figure 6. Advancing and receding contact angles can be measured by adding and withdrawing liquid from a droplet. **a**) During the addition of liquid, the droplet is expanding. After reaching the advancing contact angle, the contact line starts to Move. **b**) During the removal of liquid, the droplet is shrinking, and the contact line starts to recede just after reaching the receding contact angle. Reproduced with permission from ref.[65] Copyright 2017, John Wiley and Sons.

Firstly, by slowly adding and removing liquid from a deposited droplet with a rate of around 0.5 μL s^{-1} or less (**Figure 6**). During the addition of liquid and expansion of the droplet, the contact angle increases until the advancing contact angle θ_{Adv} is reached and the contact line starts advancing. Similarly, during the removal of liquid and contraction

of the droplet, the contact angle decreases until the receding contact angle θ_{Rec} is formed. The difference between the advancing and receding contact angles is called contact angle hysteresis (CAH):[59, 63, 65]

$$CAH = \theta_{Adv} - \theta_{Rec} \quad (7)$$

Another way to access the advancing and receding contact angles is to deposit a droplet on a surface and gradually increase the inclination of the surface (**Figure 7**). Just before the droplet starts to slide or roll down the inclined surface, the advancing and receding contact angles are formed at the lower and upper contact side of the droplet, respectively. However, the droplet's adhesion is often too high, preventing the drop from rolling off. In this case, the advancing and receding angles cannot be measured using this method.[32, 66]

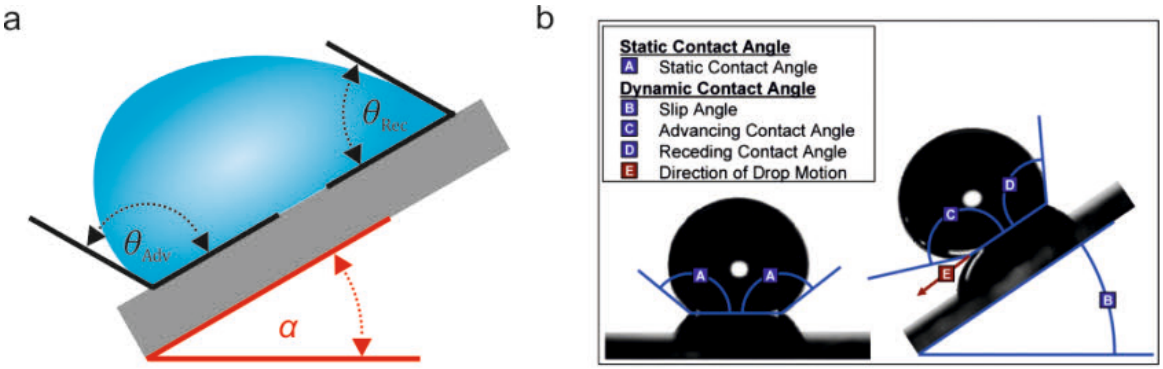

Figure 7. a) Schematic illustration of a drop on a substrate tilted by the inclination angle α. Just before the droplet starts rolling/sliding, the advancing and receding contact angles are formed on the droplet's lower and upper sides. **b**) Experimental comparison between the static contact angle and the advancing/receding contact angles formed on an inclined substrate. Reprinted with permission from ref.[66] Copyright 2009, American Chemical Society.

The contact angle hysteresis can be ≥100° on some surfaces; however, it can also be as small as a few degrees on specific substrates showing low drop adhesion, such as superhydrophobic[67] and liquid-like surfaces.[68] Nonetheless, also on superhydrophobic surfaces, the contact angle hysteresis can exceed 20° because the advancing contact angle should be close to 180°.[61] For these surfaces, the measurement of roll-off angles is more reliable because it does not require the measurement of the position of the three-phase contact line. Several factors and phenomena can cause contact angle hysteresis. One is surface roughness, whose effects can be explained by considering a simple case involving a droplet that is advancing over a surface with a microscopic protrusion or bump

(**Figure 8**; left to right from Position A). The droplet advances with an intrinsic contact angle of 90° until it reaches the protrusion. It then jumps to the middle of the bump, where it can assume the intrinsic contact angle of 90° again (**Figure 8**; Position B). To advance further, the droplet needs to overcome the bump. It microscopically retains its intrinsic contact angle of 90° and slowly moves over the bump causing macroscopic pinning and apparent contact angles exceeding 90°, which is the advancing contact angle (**Figure 8**; Position B to C). After overcoming the microscopic bump, it can spread further, restoring its intrinsic contact angle of 90°, as there are no further obstacles in this example. The same effect occurs for the receding contact line, but in the opposite direction, leading to contact angles below 90°.[5]

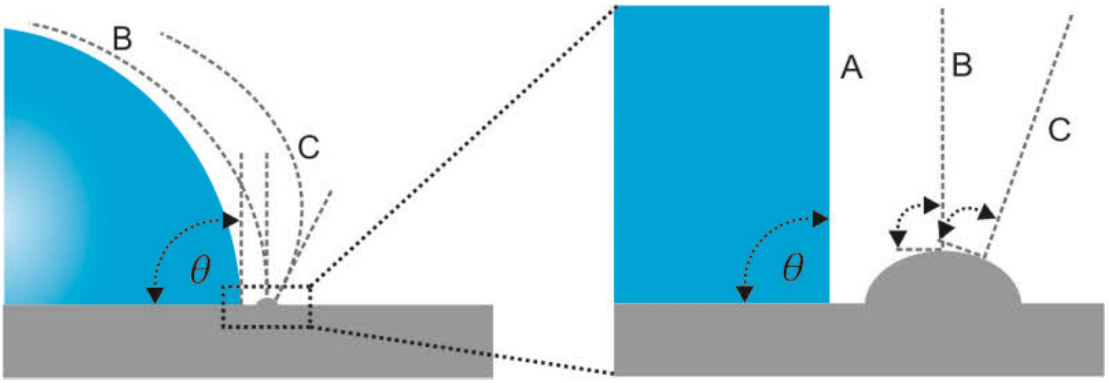

Figure 8. Schematic illustration of a droplet advancing over a surface with a small bump (left side) and a more detailed view of the movement over the bump (right side). Adapted with permission from ref.[5] Copyright 2003, John Wiley and Sons.

Real surfaces can be imagined as surfaces having lower or higher densities of these microscopic bumps, resulting in different contact angle hystereses. Another cause of contact angle hysteresis is surface inhomogeneity (either structural or chemical). Like surface roughness, these inhomogeneities can cause pinning of the contact line. The advancing contact line may be pinned in areas exhibiting a higher lyophobicity (liquid-repellency), whereas the receding contact line may be pinned in areas exhibiting a lower lyophobicity and thus a higher lyophilicity. Besides surface roughness and inhomogeneities, dissolved molecules can increase hysteresis as they often adsorb to the contact line and hinder the advancing and receding of the droplet. However, as mentioned before, high surface roughness must not necessarily cause a high contact angle hysteresis as the effect of roughness depends on the wetting state. For the superhydrophobic Cassie state, the roughness decreases the hysteresis, whereas, for rough surfaces in the Wenzel state, surface roughness highly increases contact angle hysteresis (the example in **Figure 8** resembles the Wenzel state).[5]

1.9 ROLL-OFF ANGLE MEASUREMENTS

In addition to contact angle measurements, roll-off angle experiments (sometimes called sliding angle measurements) are commonly conducted to determine the wettability of a substrate.[39, 69] A drop is deposited on the surface, and the surface is slowly tilted until the drop rolls off (**Figure 7**), which will occur if the drop's adhesion to the substrate is low enough to be overcome by the gravitational force acting on it. Therefore, the drop volume affects the tilting angle. Volumes of 5 to 10 µL are typically used. In particular, superhydrophobic surfaces,[67] slippery liquid-infused surfaces,[70-71] and liquid-like surfaces[68] show low roll-off angles. The roll-off angle is related to the contact angle hysteresis according to the following equation:[72-77]

$$F_{\mathrm{RA}} = mg \sin \alpha = kw\gamma(\cos \theta_{\mathrm{Rec}} - \cos \theta_{\mathrm{Adv}}) \tag{8}$$

Here, m is the mass of the drop, g is the gravimetric acceleration, and α is the inclination of the surface, i.e., the roll-off angle. The factor k depends on the shape of the three-phase contact line and is usually taken to be 1.[77] The contact width w of the drop is measured perpendicular to the movement of the drop. The contact angle hysteresis appears in the $(\cos \theta_{\mathrm{Rec}} - \cos \theta_{\mathrm{Adv}})$ term. Consequently, a low contact angle hysteresis is associated with a low roll-off angle. Roll-off angle measurements have the advantage of being fast and more reproducible than contact angle measurements because they do not depend on the illumination, the choice of the baseline, and do not require fitting.

1.10 SUPER-LIQUID-REPELLENT SURFACES

Superhydrophobic surfaces can only repel water and other aqueous solutions with high surface tensions (≈70 mN m^{-1}). Polar liquids with lower surface tensions, such as surfactant solutions, and especially non-polar liquids like oils and hydrocarbons wet these surfaces. The intrinsic contact angle of low surface tension liquids like oils is usually below 90° on flat surfaces, even on perfluorinated ones.[51] Therefore, the oil penetrates the pores of a superhydrophobic surface and assumes the Wenzel state. Usually, this leads to superspreading as a high surface roughness combined with intrinsic contact angles much below 90° yield negligible apparent contact angles (≈0°). Capillary forces pull the liquid into the pores of the nano or microrough surface and cause a high spreading velocity.[78] There-

fore, these surfaces are usually called superhydrophobic and superoleophilic. This specific wetting scenario can be utilized for oil/water separation[78-80] applications. The first approaches toward oil-repellent surfaces have been made as early as 1997 by Tsujii *et al.*[81] Ten years later, in 2007, Tuteja *et al.*[82] experimentally showed and explained the mechanism of super oil-repellent surfaces, i.e., superoleophobic surfaces. The wetting of rough structures by oils can be prevented by the introduction of overhanging morphologies or "re-entrant" structures. These overhanging morphologies act as an energy barrier such that the liquid cannot easily penetrate the pores of the rough structure. Examples of such overhanging morphologies are microfibers and model hoodoo-shaped micropillars (**Figure 9**a–d). The liquid is trapped at the lower side of the microfibers or at the lower side of the top face of the hoodoo-shaped micropillars, respectively. Here, the liquid can assume its Young's contact angle θ without further penetrating toward the bottom of the substrate. The drop rests on the re-entrant structures entrapping air underneath and thus assuming the Cassie state. The oil drop forms a large contact angle and can easily roll off the surface.[82] The criterion for superoleophobicity is commonly defined as showing high contact angles (>150°) and low roll-off angles (<10°) toward oils having surface tensions around 20–30 mN m^{-1}. A surface that shows high contact angles and low roll-off angles toward aqueous and non-aqueous liquids is usually called a superamphiphobic or superomniphobic surface. Therefore, in most cases, superoleophobic surfaces are also superamphiphobic (amphiphobic expresses the combination of hydrophobic and oleophobic) or superomniphobic (expressing that "all" or most common liquids are repelled). It should be noted that the criterion for superoleophobicity, superamphiphobicity, and superomniphobicity is not as clearly defined and agreed on as the one for superhydrophobic surfaces. For instance, these terms do not clearly define which liquids are being repelled. Kota *et al.* suggested that superomniphobic surfaces should be able to super-repel hexadecane in order to justify the terminology.[83] Herein, surfaces that repel water and aqueous solutions with surface tensions around 70 mN m^{-1} are termed superhydrophobic. Surfaces that repel liquids with lower surface tensions, such as diiodomethane (50.8 mN m^{-1}),[48] blood (or blood plasma; ≈50 mN m^{-1}),[84-85] or iodobenzene (39.7 mN m^{-1})[48] and below, are called super-liquid-repellent. Finally, surfaces able to repel hexadecane and liquids with even lower surface tensions are called superamphiphobic or superomniphobic.

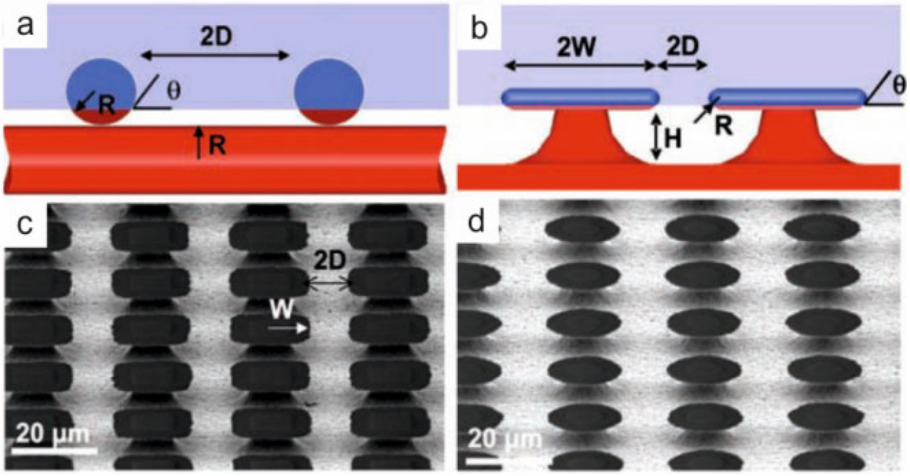

Figure 9. Design of superamphiphobic surfaces. **a**) Scheme of the solid-liquid-air interface on a surface consisting of microfibers. **b**) Scheme of the solid-liquid-air interface on a surface consisting of hoodoo-shaped micropillars (or micro-hoodoos). **c**,**d**) SEM images of a superamphiphobic surface consisting of hoodoo-shaped micropillars with squared (c) and round top faces (d). Reprinted from ref.[82] with permission from AAAS.

The robustness of the Cassie state on surfaces like electrospun microfibers depends on the morphology of the structures (e.g., the diameter of the fibers) and the spacing between the re-entrant structures (e.g., the average spacing between the fibers). Tuteja *et al.* introduced two design parameters for superamphiphobic or superomniphobic surfaces.[82, 86] Firstly, the spacing ratio D^*, which is given by Eq. 9 for microfibers:

$$D^* = \frac{D + R}{R} \tag{9}$$

Here, $2D$ is the average edge-to-edge spacing of the fibers, and R is the radius of the fibers. The spacing ratio D^* directly governs the solid fraction ϕ_{SL} of the composite interface and thus the apparent contact angle θ_C. The second design parameter is the robustness factor H^*, which is given by Eq. 10 for microfibers.

$$H^* = \frac{2(1 - \cos\theta)Rl_C}{D^2} \tag{10}$$

Here, θ is the intrinsic contact angle, and $l_C = \sqrt{\gamma_{LG}/\rho g}$ is the capillary length. The robustness factor H^* is a measure for the stability of the Cassie state against applied pressure. It depends on the geometry like the spacing and the radius of the microfibers, the intrinsic contact angle of the material, and the liquid properties. Both R and D directly affect the spacing ratio and robustness factor. It should be noted that increasing D leads to a higher D^* and thus θ_C, but highly decreases the robustness factor H^*. Therefore, a metastable

Cassie state may not be achievable for all surfaces having re-entrant features. Generally, H^* and D^* should be $\gg 1$, and the surface should have sparsely distributed highly overhanging structures. Tuteja *et al.* found $D^* = 9$ and $H^* = 46$ for octane on their electrospun microfibers.[82]

Butt *et al.* suggested design principles based on force balance considerations for pillars consisting of sintered spherical particles (**Figure 10**).[87] It was shown that the depinning impalement pressure P, i.e., depinning from the lower side of the top particles, is given by Eq. 11:

$$P = \frac{2\pi\gamma_{LG}R}{A_0}\sin^2\left(\frac{\theta_{Adv}^{Micro}}{2}\right) \tag{11}$$

Here, R is the radius of the spherical particles, θ_{Adv}^{Micro} is the microscopic advancing contact angle on the particles, A_0 is the total area per pillar, which is equal to a^2 for the unit cell of a square lattice with a being the lattice constant (distance between adjacent pillars in a row). Thus, the impalement pressure critically depends on the ratio of R/a^2, which is similar to the robustness factor H^* by Tuteja *et al.*[82]

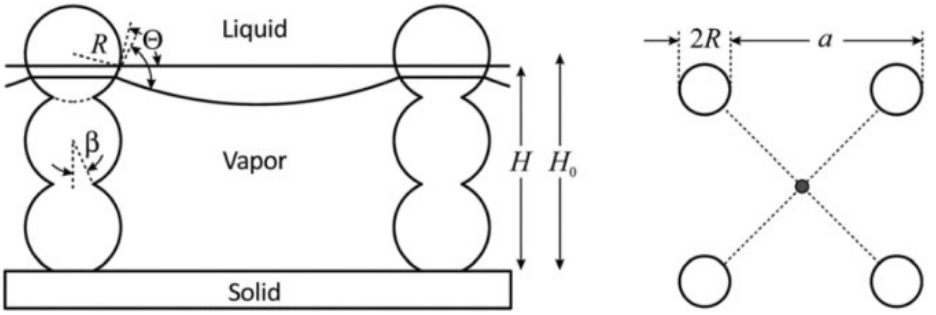

Figure 10. Design parameters for superamphiphobic surfaces consisting of pillars of sintered particles with radius *R* and a pillar-to-pillar spacing of *a*. In the Cassie state, the contact line is pinned at the lower half of the particles at the height *H*. Without external pressure, the liquid-air interface is planar. Upon applying a force, the liquid-air interface bends downward. Reproduced from ref.[87] with permission from The Royal Society of Chemistry.

The apparent receding contact angle θ_{Rec} at the rim of a drop moving perpendicular to a row of pillars can be related to the pillar structure using Eq. 12:

$$\theta_{Rec} = \pi\left(1 - \frac{2R}{a}\cos^2\left(\theta_{Rec}^{Micro}/2\right)\right) \tag{12}$$

Here, θ_{Rec}^{Micro} denotes the microscopic receding contact angle on the particles. To obtain a high receding contact angle θ_{Rec}, the ratio R/a should be as low as possible for a fixed value of θ_{Rec}^{Micro}. This again conflicts the impalement pressure P. Thus, the ratio between

the radius of the particles and distance of the pillars must be tuned carefully to obtain high receding contact angles and a high impalement pressure.[87]

Compared to superhydrophobic surfaces, there is a limited number of methods to synthesize or fabricate superamphiphobic and superomniphobic surfaces. For instance, searching for "superamphiphobic surface" in Web of Science yields ≈340 results as of Dec 2018, whereas searching for "superhydrophobic surface" yields ≈11200 results. Nonetheless, different methods[83, 88] have been developed to fabricate such surfaces, including various etching methods such as wet chemical etching,[89] electrochemical etching,[81, 90-91] plasma etching,[92] and reactive ion etching;[93] other methods include candle soot deposition as a template,[41] (flame) spray coating,[94-96] dip coating,[97-98] spin coating,[99] electrospinning,[82, 86, 100] and electropolymerization.[101] In the following, a few prominent examples are presented.

One of the early reports showing exceptional superamphiphobicity is based on a candle soot template. Candle soot was collected from a paraffin candle by holding a glass slide above the flame (**Figure 11**a). The black deposit consisted of fractal-like chains of carbon nanoparticles with diameters of ≈40 nm (**Figure 11**b,c). The loose structure was superhydrophobic and quite fragile. Water droplets easily rolled off the candle soot-coated surface but took soot particles along. To strengthen the network, a 20 nm thick silica shell (**Figure 11**d,e) was deposited on the brittle soot by chemical vapor deposition (CVD). Therefore, a candle soot-coated glass slide was placed in a desiccator containing vials with tetraethylorthosilicate (TEOS) and ammonia for 24 h. To yield a transparent coating, the silica-coated glass slide was calcinated at 600 °C in air. During heating, the carbon was burned out, but the silica network mostly kept its integrity and turned transparent (**Figure 11**f). The hydrophilic coating was now fluorinated by CVD of 1*H*,1*H*,2*H*,2*H*-perfluorooctyltrichlorosilane. After the fluorination, the coating was superamphiphobic, showing high contact and low roll-off angles for water and various oils like hexadecane and tetradecane (≈5° roll-off angle for 6 µL tetradecane droplets; **Figure 11**g,h). This super-liquid-repellency can be explained by the fractal-like overhanging structure of the candle soot template, preventing the liquids from penetrating the rough structure (**Figure 11**i). Hexadecane droplets (5 µL) impacting at a velocity of $v = 1$ m s^{-1} could easily bounce off the coating (**Figure 11**j) without transitioning into the Wenzel state. After the initial impact, the drop bounced twice, followed by some oscillations until the drop came to rest.[41]

Pan *et al.* coated stainless steel wire meshes (**Figure 12**a) by electrospinning a mixture of polydimethylsiloxane (PDMS) and fluorodecyl polyhedral oligomeric silsesquioxane (F-POSS), followed by a curing step to crosslink the PDMS.

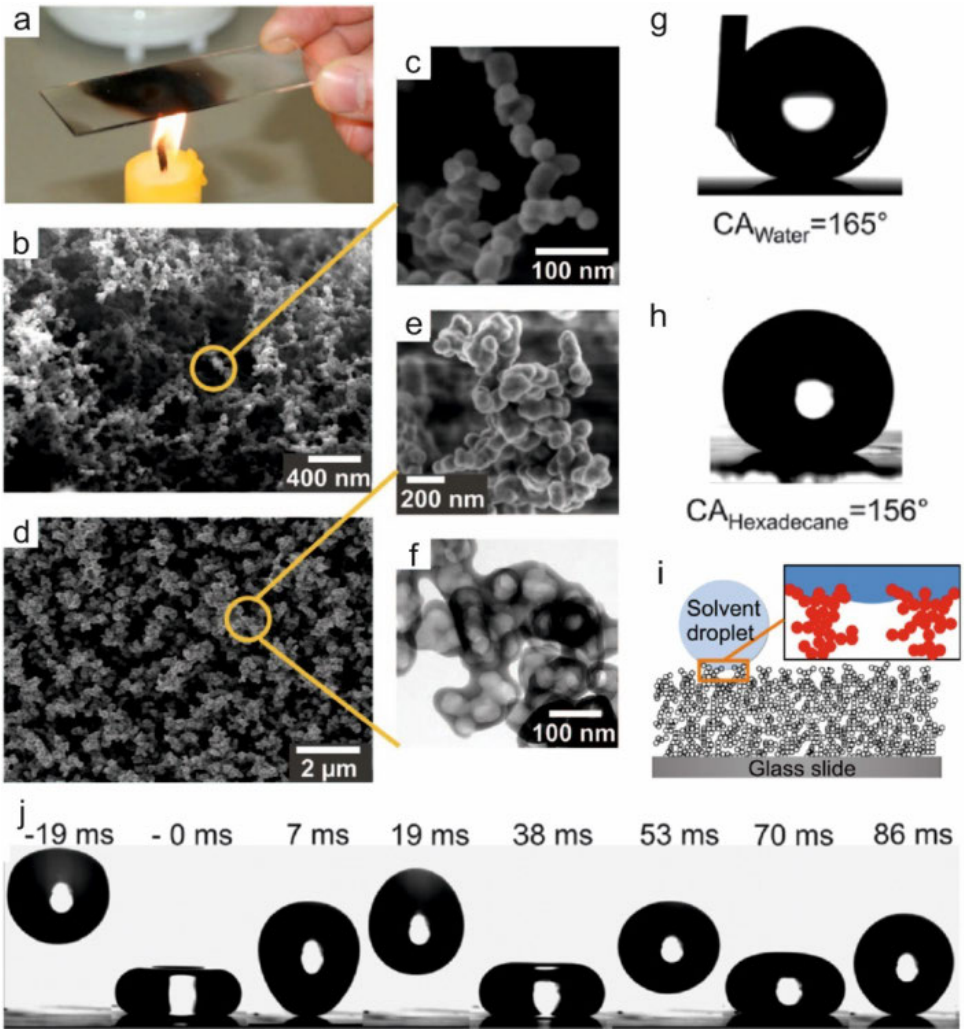

Figure 11. Candle soot-based superamphiphobic Coating. **a**) Candle soot is deposited on a glass slide using a paraffin candle. **b**,**c**) SEM images of the candle soot deposited on a glass slide. The coating consists of carbon nanoparticle (≈40 nm diameter) chains. **d**,**e**) SEM images of the candle soot after application of a silica shell. **f**) TEM image of the hollow silica shells after calcination at 600 °C. **g**,**h**) A 2 µL water (g) and 5 µL hexadecane (h) drop on a candle soot-based superamphiphobic glass slide showing contact angles of 165° ± 1° and 156° ± 1°, respectively. **i**) Schematic illustration of a drop on a candle soot-based superamphiphobic surface. The particle chain-like morphology acts as a re-entrant structure. **j**) Hexadecane droplet bouncing on a candle soot-based superamphiphobic surface. Reprinted from ref.[41] with permission from AAAS.

The crosslinked PDMS and F-POSS mixture had a solid surface energy of $\gamma_{SG} \approx 12$ mN m^{-1}. It is argued that the F-POSS molecules preferentially migrate to the surface, lowing its surface energy (**Figure 12**b). The coated mesh had overhanging structures at different length scales. The wires of the mesh itself act as a re-entrant structure and are combined

with the microstructure of the electrospun coating (**Figure 12**c). The superomniphobic meshes showed extreme repellency against liquids down to 19.8 mN m^{-1} with roll-off angles below 3° for all liquids (**Figure 12**d). Various liquids having a low surface tension, including dimethylformamide (DMF), toluene, acetic acid, hexadecane, hexylamine, and PDMS, showed high contact angles (**Figure 12**e), and jets of these liquids could easily bounce off the surface (**Figure 12**f). The coating could also shield the underlying mesh from corrosive liquids, such as concentrated bases and acids, e.g., hydrochloric acid and sodium hydroxide solutions.[100]

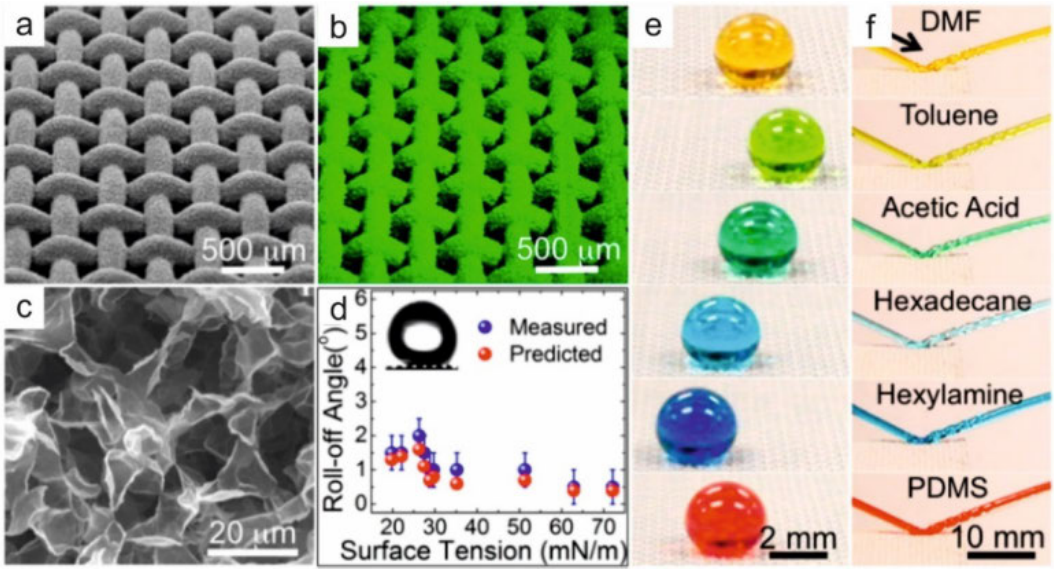

Figure 12. Superomniphobic stainless steel mesh by electrospinning a mixture of polydimethylsiloxane (PDMS) and fluorodecyl polyhedral oligomeric silsesquioxane (F-POSS). **a**) SEM image of the coated hierarchically structured superomniphobic steel wire mesh 70. **b**) Elemental mapping of fluorine on the superomniphobic mesh. **c**) Higher magnification SEM image of the overhanging electrospun microstructure on the mesh. **d**) Predicted and measured roll-off angles of various liquids (5 µL) on the superomniphobic mesh. The photograph depicts an ethanol drop rolling on the mesh at an inclination of 2°. **e**) Photographs of various liquid droplets, including dimethylformamide (DMF), toluene, acetic acid, hexadecane, hexylamine, and PDMS, on the coated mesh. The liquids were dyed. **f**) Photographs of jets of the same liquids rebounding off the superomniphobic mesh. Reprinted with permission from ref.[100] Copyright 2013, American Chemical Society.

Very recently, a simple spray method was developed by Pan *et al.* to fabricate superomniphobic surfaces on various substrates. Here, 1*H*,1*H*,2*H*,2*H*-perfluorohexyltrichlorosilane (PFHTS) and *n*-butyl cyanoacrylate (*n*-BCA) were mixed in dichloropentafluoropropane. This mixture could be sprayed on various substrates, such as polymers, metals, glass, wood, and fabrics. As an example, the coating was sprayed on PDMS disks. The spray coating yielded a hierarchal structure with re-entrant morphologies

(**Figure 13**a,b). The surface energy of the coating was $\gamma_{SG} \approx 12$ mN m^{-1} due to the perfluorinated groups of PFHTS (**Figure 13**c). The superomniphobic coating was able to superrepel various liquids (**Figure 13**d) such as tetrahydrofuran (THF), DMF, a hydrofluoric acid (HF) solution, and even *n*-hexane ($\gamma_{LG} \approx 17.9$ mN m^{-1}).

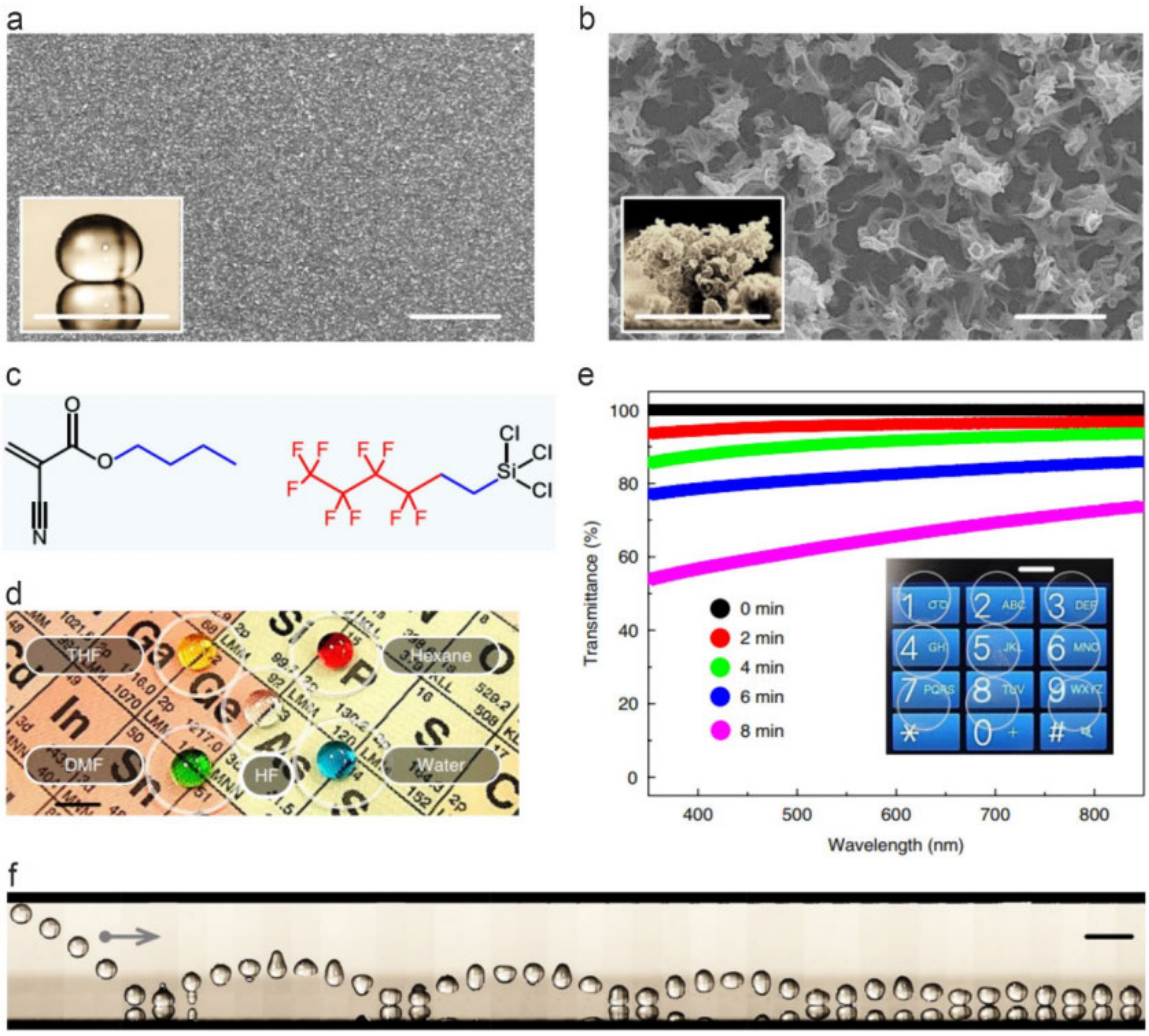

Figure 13. Superomniphobic coating based on spray coating of a mixture of 1*H*,1*H*,2*H*,2*H*-perfluorohexyltrichlorosilane (PFHTS) and *n*-butyl cyanoacrylate (*n*-BCA). **a**) SEM image of a superomniphobic spray-coated PDMS disk. The inset shows an *n*-hexane droplet resting on the superomniphobic surface. Scale bars: 50 µm, 5 mm (inset). **b**) Higher magnification SEM images of the coating. The inset shows a cross-section of the hierarchical overhanging structure of the coating. Scale bars 5 µm. **c**) Chemical structure of PFHTS (left) and *n*-BCA (right). **d**) Photographs of drops of various liquids, including water, tetrahydrofuran (THF), DMF, hydrofluoric acid (HF) solution, and *n*-hexane, on the superomniphobic coating. **e**) Ultraviolet-visible (UV-Vis) spectra showing the transparency of the superomniphobic coating depending on the coating time. The inset shows nine spray-coated PDMS disks on a mobile phone screen. The disks were coated for 1–9 min as indicated by the numbers on the screen. Scale bar: 1 cm (inset). **f**) An *n*-hexane drop bouncing on the superomniphobic coating. The time between the frames is 6 ms. Scale bar: 5 mm. Reprinted from ref.[96] by permission from Springer Nature: Nature, Copyright 2018.

Additionally, the coating showed high transparency depending on the spraying time (**Figure 13**e). A transparency of 95% of the visible light was achieved using a spray time of 4 min and 20% PFHTS. Nonetheless, the coating was still super-repellent to *n*-hexane. The superomniphobic coating could not only repel resting but also impacting *n*-hexane drops. The impacting drops showed low adhesion on the surface and could bounce five times before coming to rest (**Figure 13**f).[96] While there are various methods to coat flat and open substrates, coating the inside of tubes with a super-liquid-repellent layer remains difficult, especially for polymeric tubes. Wet chemical or electrochemical treatments can fabricate superhydrophobic metal pipes.[102-104] However, these methods are limited to the respective metal. A "near"-superhydrophobic tube was fabricated by coating a thick PVC tube (14 mm inner diameter) using a commercial liquid-repellent coating (Neverwet).[105] To circumvent the problems associated with coating procedures, in some works, tubes were rolled from a flat superhydrophobic substrate.[106-108] Other works employed a rough solid template pipe, and a polymer was crosslinked or cured around this template.[109-110] These methods require to etch away the inner template pipe or require a radial tube expansion to yield a superhydrophobic tube, which considerably reduces the choice of polymers. Another approach inserted a mesh into glass tubes followed by applying a commercial superhydrophobic coating.[111] In Chapter 5, a coating method based on silicone nanofilaments (Chapter 1.11) is introduced to overcome such limitations. Using this method, meter-long and narrow tubes of various materials can be coated with a super-liquid-repellent layer.

1.11 SILICONE NANOFILAMENTS

A versatile approach to transform various substrates into superhydrophobic, superhydrophilic, or superamphiphobic surfaces is the silicone nanofilaments (SNF) coating.[67, 112] To coat a surface with these nanofilaments, the substrate is exposed to trichloromethylsilane (TCMS) in the gas phase[112-113] or dissolved in a solvent.[114-116] The gas phase or solvent must contain a certain water content to hydrolyze the TCMS slowly. For the solvent phase reaction, various non-polar solvents like toluene or *n*-hexane can be used.[115-118] A necessity for the nanofilament growth is a hydrophilic substrate, preferentially containing hydroxy groups.[112, 115, 119] Therefore, surfaces are usually activated using cleaning and oxidizing agents like piranha, basic surfactant solutions, or oxygen plasma treatments. The hydrolyzed or partially hydrolyzed TCMS molecules react with hydroxy groups on the surface

inducing a polysiloxane (silicone) polymerization (**Figure 14**a). Due to steric reasons, a maximum of two silanol groups can attach to the surface. During the polymerization, the polysiloxane chains start crosslinking, leading to the growth of the nanofilaments. Hydrochloric acid (HCl) gas is formed as a byproduct during the hydrolysis.[119-120] Diverse substrates can be coated, including glass, silicon wafers, cotton and PET fabrics, polyolefins, metals, and ceramics.[80, 112-113, 118, 121-122] Besides TCMS, also other organosilanes, such as vinyltrichlorosilane,[119-120] or a mixture of tetraethoxysilane/tetrachlorosilane with an organosilane (e.g., long-chain alkylsilanes or perfluoroalkylsilanes) can be used.[123-124] The nanofilaments possess high chemical and environmental stability.[125-126] The length and thickness of the nanofilaments can vary and depend on many parameters like the TCMS concentration, water concentration, temperature, solvent, activation, and the substrate (**Figure 14**b).[114-115, 127-129]

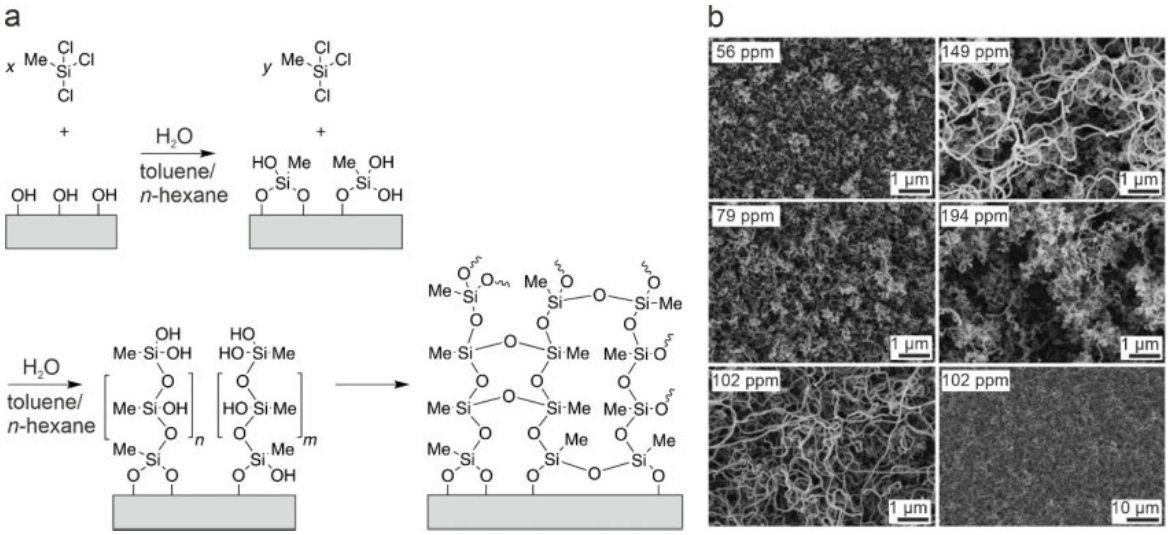

Figure 14. Silicone nanofilaments. **a**) Reaction scheme for the formation of silicone nanofilaments. Trichloromethylsilane (TCMS) hydrolyzes due to trace amounts of water and reacts with hydroxy groups on the surface. A polysiloxane polymerizes on the surface and eventually starts crosslinking.[116, 118-120] Reproduced with permission from ref.[118] Copyright 2018, John Wiley and Sons. **b**) Nanofilaments on glass slides coated at different water concentrations using TCMS in toluene. Reproduced with permission from ref.[115] Copyright 2011, John Wiley and Sons.

The mechanism of the nanofilament growth is not fully understood due to the inherent complexity of the self-assembly. There are several suggested mechanisms proposing quite different approaches.[119-120, 130-131]

An early approach by Rollings *et al.* proposed a diffusion-controlled mechanism for the gas-phase reaction. The hydrolyzed silanes react with hydroxy groups on the surface, acting as seeds for further nanofilament growth. The high density of hydroxy groups on a glass surface, for example, should limit the mobility of the silanes on the surface, leading

to small islands growing on the seeds. These small islands start extending into the gas phase where they are more exposed compared to the valleys in between. The diffusion of the silanes to the tips of these islands is more efficient, leading to preferential one-dimensional growth at the tip. Consequently, nanofilaments are eventually formed on the surface.[119-120]

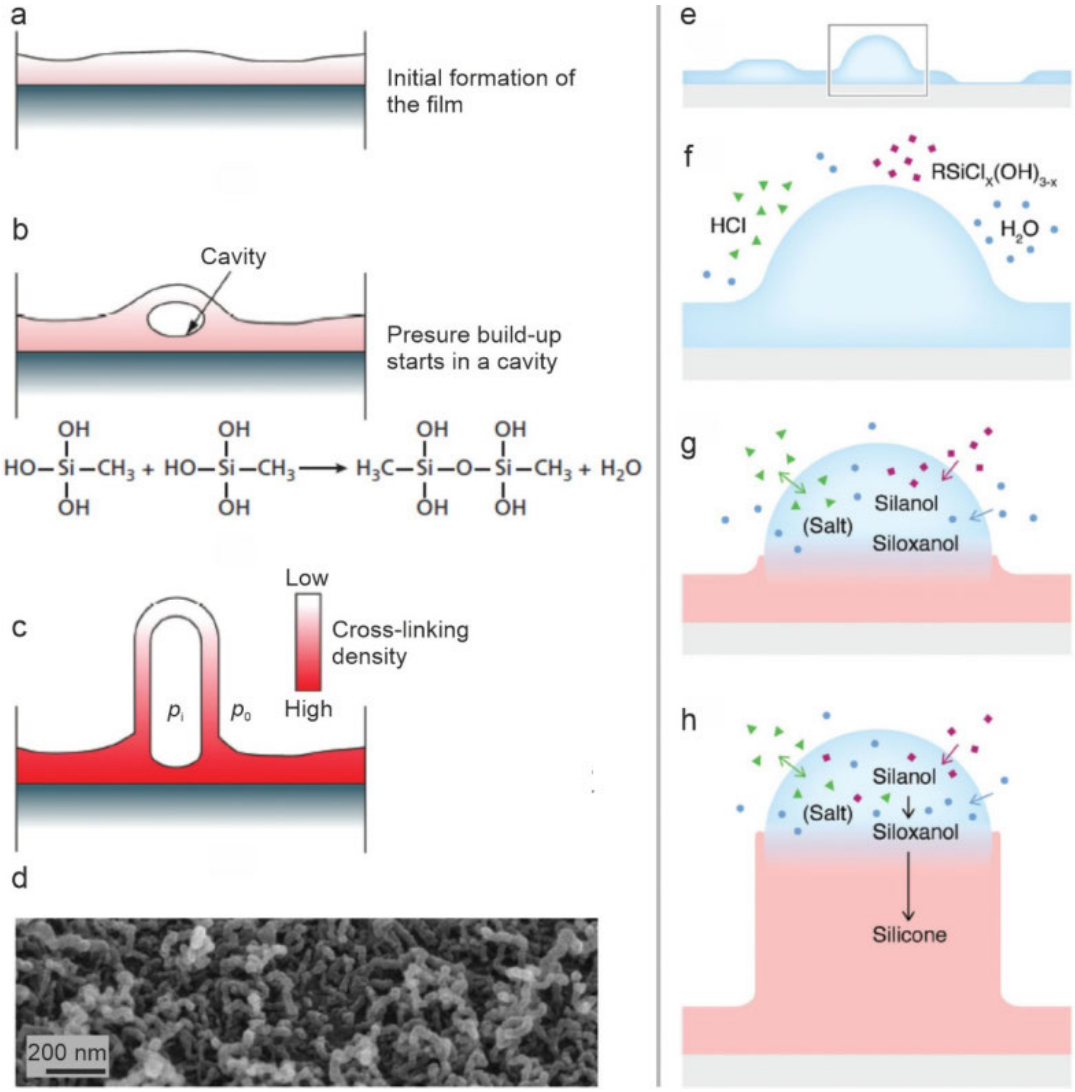

Figure 15. Proposed growth mechanisms for the silicone nanofilaments. **a**–**c**) Uniaxial elongation of a partly crosslinked polysiloxane film. **d**) SEM of hollow silicone nanofilaments. Reproduced with permission from ref.[131] Copyright 2014, ICE Publishing. **e**–**h**) Droplet assisted growth and shaping (DAGS) mechanism. Reproduced with permission from ref.[128] Copyright 2017, John Wiley and Sons.

Korhonen *et al.* assume that first a flat polysiloxane film is formed on the surface of the substrate (**Figure 15**a–d). The gaseous byproducts of the hydrolysis and condensation reaction (HCl and H_2O) preferentially migrate into defects inside of the film and form bub-

bles inside of it. The bubbles expand and elongate in one direction as the lowest cross-linking density is at the upper side of the cavity inside of the film. Thus, the formation of nanofilaments is caused by a "pressure-induced uniaxial elongation of a partially cross-linked polysiloxane film." This mechanism eventually yields hollow silicone nanofilaments (h-SNF).[131]

Recently, Artus *et al.* proposed a so-called droplet assisted growth and shaping (DAGS) mechanism (**Figure 15**e–h). Nano- or micrometer-sized droplets are formed on the surface due to humidity in the gas phase or water dispersed in the solvent and chemical or topographic inhomogeneities on the substrate. It is argued that these droplets are stable since their activity is lowered by the absorption of various chemical species such as HCl, silanols, and siloxanes, which are formed during the hydrolysis of TCMS. These microscopic drops act as a spatial confinement for the polysiloxane polymerization. The polycondensation at the liquid-solid interface inside of the droplet leads to one-dimensional growth and, finally, to the peculiar nanofilament structure.[128-129]

The methyl groups of the polysiloxane polymer orient to the outside, i.e., the surface of the nanofilaments, to minimize the surface energy. The high surface roughness of the coating and the intrinsically hydrophobic properties of the nanofilaments result in the superhydrophobic properties.[112-113] To obtain superoleophobic properties, the surface energy of the nanofilaments must be further reduced. Therefore, the nanofilaments are first activated in an oxygen plasma to oxidize their surface, forming hydroxy and other functional groups. In this oxidized state, the coating is superhydrophilic (and superoleophilic) due to the high surface roughness and hydrophilized nanofilaments. This leads to the spreading of liquid droplets (contact angle $\approx 0°$), in agreement with the Wenzel equation. After activation, the nanofilaments are modified with a perfluoro silane (usually 1*H*,1*H*,2*H*,2*H*-perfluorooctyltrichlorosilane [PFDTS] or 1*H*,1*H*,2*H*,2*H*-perfluoro-decyltrichlorosilane [PFOTS]).[115, 132-133] After modification, the surface energy of the nanofilaments is highly reduced, minimizing dispersive and non-dispersive interactions. The fluorinated nanofilaments usually exhibit super-liquid-repellent or superamphiphobic (superomniphobic) properties. Depending on the specific structure of the nanofilaments, i.e., the thickness and spacing between the nanofilaments, the repellency toward low surface tension liquids, such as oils, may vary.[115, 133] Nonetheless, superhydrophobic properties are (almost) always achieved. The super-liquid-repellency can be explained by the cylindrical geometry of the nanofilaments acting as re-entrant structures (as described in Chapter 1.10) similar to the electrospun fibers by Tuteja *et al.*[82]

1.12 APPLICATIONS OF SUPERHYDROPHOBIC AND SUPER-LIQUID-REPELLENT SURFACES

Since a large variety of methods to fabricate superhydrophobic and super-liquid-repellent surfaces has been established, it is important to utilize their unique properties and abilities in our daily life or the industry. So far, prospective applications of super-liquid-repellent surfaces include particle synthesis,[134-138] water-proof textiles,[79, 139] oil/water separation,[20, 78-80, 140-142] anti-icing,[143-144] self-cleaning,[145-146] drag-reduction,[102, 147] anti-biofouling,[118, 148] gas exchange,[84, 116] membrane distillation,[149-150] and chemical shielding.[96, 100] In the following, a brief overview containing selected examples is given.

Exposition of surfaces to outdoor environments inevitably results in contamination by particulate matter. There are different types of particulate matter from natural (e.g., microorganisms, pollen) and anthropogenic sources (soot from combustion or other industries). The size distribution of particulate matter is broad. It can range between tens of nanometers to hundreds of micrometers.[151] Superhydrophobic and super-liquid-repellent surfaces are known for their self-cleaning behavior (**Figure 16**). Water drops can easily clean contaminated superhydrophobic surfaces. In contrast, contamination particles on common hydrophobic surfaces usually stick to the surface and cannot be simply cleaned by rinsing with water droplets. On superhydrophobic surfaces, macroscopic contamination particles rest on top of the rough structure. Therefore, macroscopic contamination can be easily removed by rinsing with water drops.[31, 34, 145, 152] Even though self-cleaning is one of the reasons for the huge interest in superhydrophobicity, only a few articles are dedicated to self-cleaning performances.

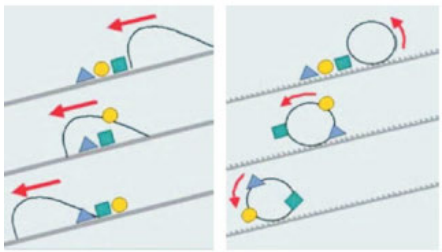

Figure 16. A drop on a hydrophobic surface moves across the contamination particles being unable to pick them up (left). On a superhydrophobic self-cleaning surface, the drop easily picks up the contamination and takes it away. (right). Reproduced from ref.[152] with permission from The Royal Society of Chemistry.

For instance, previous research investigated the contamination of superhydrophobic surfaces with millimeter- to micrometer-sized contaminants such as hydrophobic powder,[145] micrometer-sized particulates,[153-155] and aggregated bioparticles.[156] As an example, Fürstner *et al.* studied the wetting and self-cleaning properties of artificial superhydrophobic surfaces, including silicon wafers with regular micropillars, microrough metals,

and replicas of superhydrophobic plants.[145] The surfaces were contaminated by blowing a hydrophobic powder (a mixture of a luminescent material and a fluorinated agent) onto the surface using a fan.[3] Subsequently, the surfaces were cleaned using artificial fog (8–20 µm droplets, 1500 mL m^{-2}) and artificial rain (water drops larger than 2 mm). The fog was less efficient for cleaning the surfaces compared to artificial rain. Especially on samples with pronounced structures above 5 µm, the fog treatment yielded a liquid film on the surface having no cleaning effect. The other samples with smaller structures were efficiently cleaned by the fog. The artificial rain led to almost "perfect" cleaning. Here, higher impact pressures showed more efficient cleaning performances. In contrast, a smooth surface could not be entirely cleaned by impacting droplets. However, it is still unclear how surfaces are affected if they are contaminated with particles of smaller sizes, especially in the nanometer regime, how the self-cleaning process works in detail, and which forces are involved. Chapter 3 will give an answer to that.

Super-liquid-repellent surfaces can be utilized for the fabrication of various types of microparticles.[134-135, 137-138, 157] This may contribute to a greener synthesis of such particles as no toxic solvent is needed. A monomer drop, e.g., consisting of methacrylates and containing a photoinitiator, is deposited on a super-liquid-repellent surface (**Figure 17**).

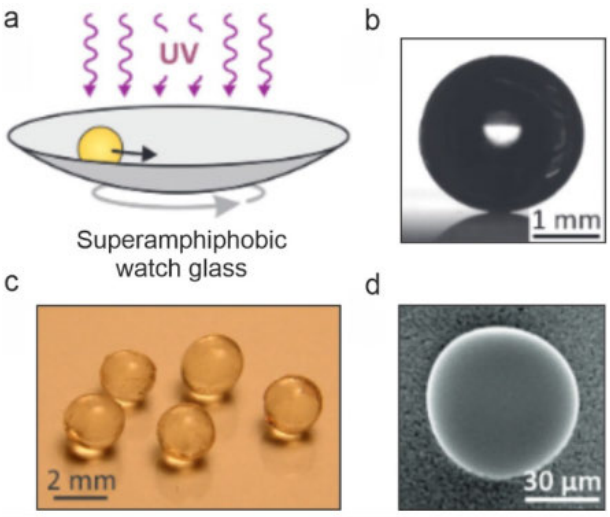

Figure 17. Solvent-free particle synthesis on a superamphiphobic substrate. **a**) A monomer drop (here: a mixture of bisphenol A glycerolate dimethacrylate (bis-GMA), triethylene glycol dimethacrylate (TEGDMA), and the photoinitiator phenylbis(2,4,6-trimethylbenzoyl)phosphine oxide) is deposited on the surface and exposed to UV irradiation. **b**,**c**) Photographs of resultant polymerized microparticles prepared with a mixture of bis-GMA (15 wt%), TEGDMA (84 wt%), and a photoinitiator (1 wt%). **d**) SEM image of a microsphere prepared with a mixture of TEGDMA (99 wt%) and a photoinitiator (1 wt%). The monomer droplet was deposited using an inkjet printer. Reproduced with permission from ref.[134] Copyright 2013, John Wiley and Sons.

Due to the super-liquid-repellency, the drop shows an almost spherical shape having a high contact angle >150° and a low roll-off angle. Consequently, the drop can easily roll

[3]Powders are highly aggregated. Thus, it is likely that the average aggregate size was above 10 µm. The authors mention that no fragments or particles below 1 µm were found.

on the super-liquid-repellent substrate. The drop is exposed to UV light to initiate cross-linking. During the UV exposure, the drop should be kept in motion to avoid deformation due to adhesion at the contact line or due to gravity. This can be realized by employing a curved super-liquid-repellent watch glass on a 2D orbital shaker (**Figure 17**a). After polymerization, spherical and solid microspheres are obtained (**Figure 17**b–d). Alternatively, polymer powders are melted on a super-liquid-repellent surface. After the transition from the solid to the liquid state, the melted polymer assumes a spherical shape and can be cooled down, obtaining a polymeric microsphere.[134]

Another approach utilizes aqueous solutions of titania nanoparticles or other metal oxides to fabricate inorganic mesoporous supraparticles on a super-liquid-repellent substrate. The particles are formed by slowly evaporating the aqueous solution. During evaporation, the drop keeps its spherical shape until the water is completely evaporated, and a mesoporous inorganic particle is left.[157]

Oil spills on the oceans by offshore oil production and transportation, for example, are frequent problems and can cause severe damage to humans, nature, and animals.[80] One of the most highly covered applications is oil/water separation using superhydrophobic membranes and sponges.[20, 78-80, 140-142, 158] This is achieved by the fact that most superhydrophobic surfaces are superoleophilic, i.e., the surface repels water, but oils easily spread on it.

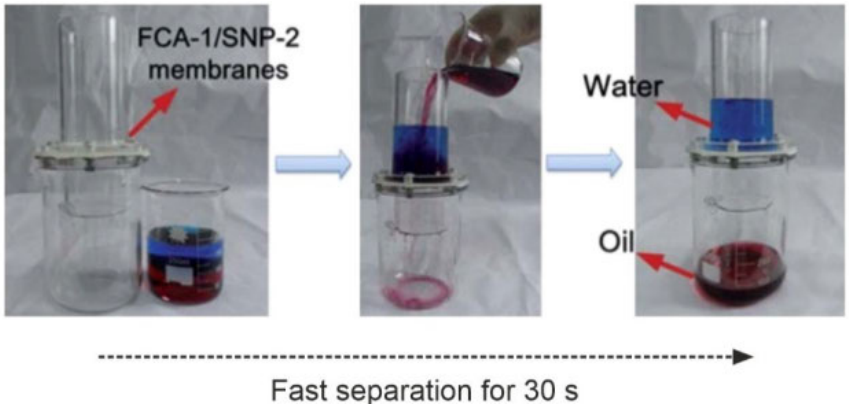

Figure 18. Oil/water separation using a superhydrophobic/superoleophilic electrospun membrane. An oil/water mixture is poured on top of the membrane. The oil (red) passes through the membrane, but the water (blue) is repelled and stays on top of the membrane. Within 30 s, the oil/water mixture is separated. Reproduced from ref.[140] with permission from The Royal Society of Chemistry.

The principle is simple; a porous superhydrophobic/superoleophilic membrane is placed between two columns (**Figure 18**). An oil/water mixture is poured on top of the membrane. The oil spreads on the superoleophilic membrane, and gravity pushes the oil through the

membrane. Nonetheless, the water phase stays on top of the membrane as it is water-repellent. Thus, oil can be efficiently separated from the water.[140] One of the drawbacks is that a small amount of oil usually remains in the water. Superhydrophobic/superoleophilic sponges were used to pick up oil spills from water surfaces. Due to the superhydrophobic properties, the sponge can float on water without taking up water. However, as soon as the sponge contacts oil, the oil spreads on the sponge's surface and gets sucked inside. This proved to be an efficient way to remove oil spills from a water surface.[158]
Another promising feature of superhydrophobic surfaces is that they may have antibacterial properties.[118, 148, 159-164] Formation of biofilms,[165-166] i.e., the irreversible attachment and colonization of bacteria on surfaces like medical devices, can lead to infections and eventually cause the death of patients. Also, due to the increasing resistance of bacteria against common antibiotics,[167] it is crucial to control and reduce the bacterial adhesion on such devices. Bacterial solutions on superhydrophobic surfaces show high contact angles and easily roll off because of the low solid-liquid contact area in the Cassie state. Due to the few contact points with the superhydrophobic surface, bacteria can only attach to a few sites on the surface. This can lead to highly reduced bacterial adhesion and prevention of biofilm formation on superhydrophobic surfaces. However, there is a variety of conflicting results found in the literature concerning the antibacterial properties of superhydrophobic surfaces. Some groups find highly reduced bacterial adhesion,[148, 159-162] whereas other groups report enhanced adhesion.[163] Bacterial adhesion is a very complex topic and, therefore, cannot be discussed in detail herein. Many different parameters generally influence the adhesion and biofilm formation, such as surface wettability, surface charge, and surface topography. Different bacteria show varied interactions with the surface due to differences in the composition of their cell wall and are influenced by environmental factors.[161] The differing findings for superhydrophobic surfaces may be caused by the limited stability of the Cassie state.[163] After a Cassie-to-Wenzel transition, the surface is fully wetted. Bacteria may be able to attach to the surface and form a biofilm since it has been shown that roughness can also enhance bacterial adhesion.[161, 168] Chapter 5 sheds light on the controversial question if superhydrophobic surfaces are antibacterial and the effect of roughness.

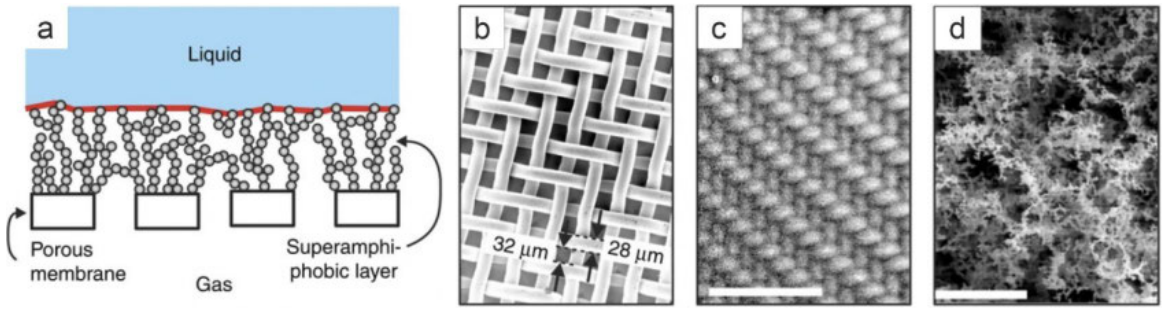

Figure 19. Super-liquid-repellent gas exchange membrane. **a**) Schematic illustration of gas transfer through a superamphiphobic membrane. The liquid rests on top of the superamphiphobic layer. The liquid-gas interface is marked in red. **b**) SEM image of a bare stainless steel mesh. **c**,**d**) SEM images of the ≈35 µm thick superamphiphobic coating on the steel mesh from b). The coating is based on the candle soot template. Reproduced from ref.[84] Copyright 2013, Springer Nature: Nature, licensed under CC BY-NC-SA 3.0.

Few reports investigate the potential of porous super-liquid-repellent surfaces or membranes for gas exchange applications.[84, 169] In such a gas contactor membrane system, a liquid flows across one side of the membrane, whereas a gas streams over the other side. The membrane physically separates the liquid and gas streams.[170] The gas must be able to efficiently diffuse through the membrane. However, it is essential that the liquid does not penetrate through the membrane. The liquid is usually a solution or chemical agent that can bind one or more gases present in the gas stream. For instance, hydrogen sulfide and carbon dioxide can be bound with amine solutions[171-174], or olefins can be separated from paraffin gases using a silver nitrate solution.[175] One of the major drawbacks of such membrane systems is that the gas capture solutions or agents wet the membranes.[176] Wetting significantly decreases the performance of gas contactor membranes. It leads to a stationary liquid film inside of the membrane pores, and the gas must diffuse through this stationary film, which considerably slows down the gas exchange. Therefore, super-liquid-repellent membranes may be beneficial to prevent wetting. The capture medium stays on top of the hydrophobic protrusions leading to a high liquid-gas interface (**Figure 19**a). Paven *et al.* prepared a super-liquid-repellent membrane for oxygenation of blood.[84] A stainless steel mesh with rectangular pores of ≈30 × 30 µm^2 was coated with a ≈35 µm thick super-liquid-repellent layer based on the candle soot template[41] to obtain a super-liquid-repellent membrane (**Figure 19**b–d). Blood on such a membrane showed basically no adhesion or wetting. Even after 48 h of incubation, a blood puddle was easily rinsed off and left no traces behind. Blood showed a contact angle of $\theta = 162°$ and a roll-off angle of $\alpha = 5°$ and could be oxygenated without clogging. Besides, CO_2 gas exchange

using an aqueous sodium hydroxide solution was demonstrated. Despite some initial reports, the potential of super-liquid-repellent and superomniphobic membranes remains mostly unexplored. In Chapter 4, a superomniphobic membrane is introduced that prevents wetting of highly basic and concentrated amine solutions that are industrially used for CO_2 capture[177-178]. This led to performance increasements of up to 40%.

1.13 PARTICLES AT INTERFACES — LIQUID MARBLES

There are several different scenarios for particles to adsorb at a fluid-fluid interface (**Figure 20**).[179] Oil-in-water emulsions are typically not stable and start demixing through the coalescence of the dispersed oil drops to reduce the overall energy of the system. Therefore, emulsions are commonly stabilized using surfactants or tensides. These amphiphilic molecules adsorb and stabilize the liquid-liquid interface, preventing coalescence of the oil drops. Another way to stabilize oil-in-water emulsions is through the addition of hydrophilic particles. The particles adsorb at the interface of the oil drops and form a particle coating around the oil drops. These particle-stabilized emulsions are called Pickering emulsions.[180] The inverse case, a water-in-oil emulsion, can be stabilized using hydrophobic particles. In addition to liquid-liquid interfaces, also liquid-air interfaces can be stabilized using particles resulting in air-in-water foams, dry water, and liquid marbles.[181-183]

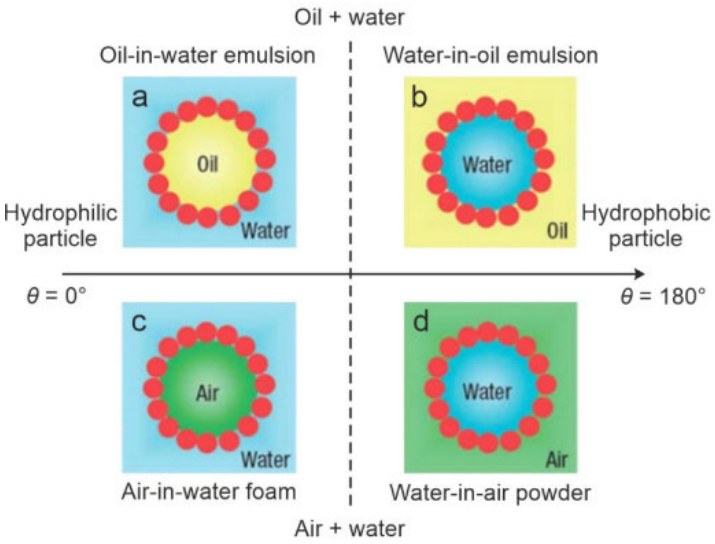

Figure 20. Particles at interfaces. **a**) Oil-in-water emulsion separated by hydrophilic particles, a so-called Pickering emulsion. **b**) Water-in-oil emulsion separated by hydrophobic particles, an inverse Pickering emulsion. **c**) Air bubbles in water stabilized by particles at the interface, an air-in-water foam. **d**) Microscopic water droplets in air coated with particles, often referred to as dry water. Reprinted from ref.[179] by permission from Springer Nature: Nature, Copyright 2006.

The reason why particles attach and adsorb to liquid-air interfaces is to reduce the total interfacial energy (**Figure 21**a). The liquid-air interface forms a well-defined contact an-

gle θ with respect to the particle's surface. The contact angle depends on the hydrophobicity of the particle and determines how much the particle sticks out of the liquid-air interface. The distance H_p the particle protrudes out of the interface is given by $H_\mathrm{p} = R(1 - \cos\theta)$. Here, R is the radius of the particle, and θ is the intrinsic contact angle of the solid particle material. The adsorption energy ΔG is obtained by subtracting the solid-liquid interfacial energy $E_\mathrm{Interface}$ of a spherical cap (of a particle) attached to a drop from the interfacial energy E_Air, which is the interfacial energy of the same spherical cap in air and a cap-shaped portion of the liquid-air interfacial energy of the drop (Eq. 13):[184]

$$\Delta G = E_\mathrm{Air} - E_\mathrm{Interface} = A_\mathrm{SA}(\gamma_\mathrm{SL} - \gamma_\mathrm{SA}) - A_\mathrm{LA}\gamma_\mathrm{LA} \tag{13}$$

Here, $A_\mathrm{SA} = A_\mathrm{SL}$ is the solid-air and solid-liquid interfacial area of the spherical cap, A_{LA} is the liquid-air interfacial area and γ_SL, γ_SA, and γ_LA are the respective interfacial energies. Eq. 14 follows using Young's equation:

$$\Delta G = A_\mathrm{SA}\gamma_\mathrm{LA}\left(\cos\theta + \frac{A_\mathrm{LA}}{A_\mathrm{SA}}\right) \tag{14}$$

The ratio of the liquid-air interfacial area compared to the solid-air interfacial area is given by $A_\mathrm{LA}/A_\mathrm{SA} = (1 - \cos\theta)/2$. Only for $\theta = 180°$ and $\theta = 0°$ the ratio is zero. In these cases, the particle either has no contact to the droplet ($\theta = 180°$) or enters the drop ($\theta = 0°$). For all other cases, the ratio is positive, and the attachment is energetically favored.[184] A liquid marble consists of a drop covered with a layer of particles (**Figure 21**b). To fabricate a liquid marble, a water drop is placed on a powder bed consisting of hydrophobic particles, grains, or often particle aggregates. The drop is now rolled on the powder bed. During rolling, the hydrophobic particles, grains, or aggregates attach to the drop, encapsulating the liquid inside (**Figure 21**c,d). The formed liquid marble is soft, elastic, non-wetting, and can be transferred to other substrates, including hydrophilic ones. Due to the particle armor, the liquid marble does not contact and wet the underlying substrate.[184-188] Certain insect species, like the aphids, use these unique properties for their survival. Aphids excrete large amounts of honeydew as these insects consume nitrogen-deficient sugary liquids from the phloem of plants as a nutrient. The excreted honeydew poses a threat to their lives as entrapment results in drowning, and the dried honeydew is a perfect matrix for the growth of pathogens like fungi. Therefore, aphids living in plant galls produce wax tufts to coat the inside of their gall.

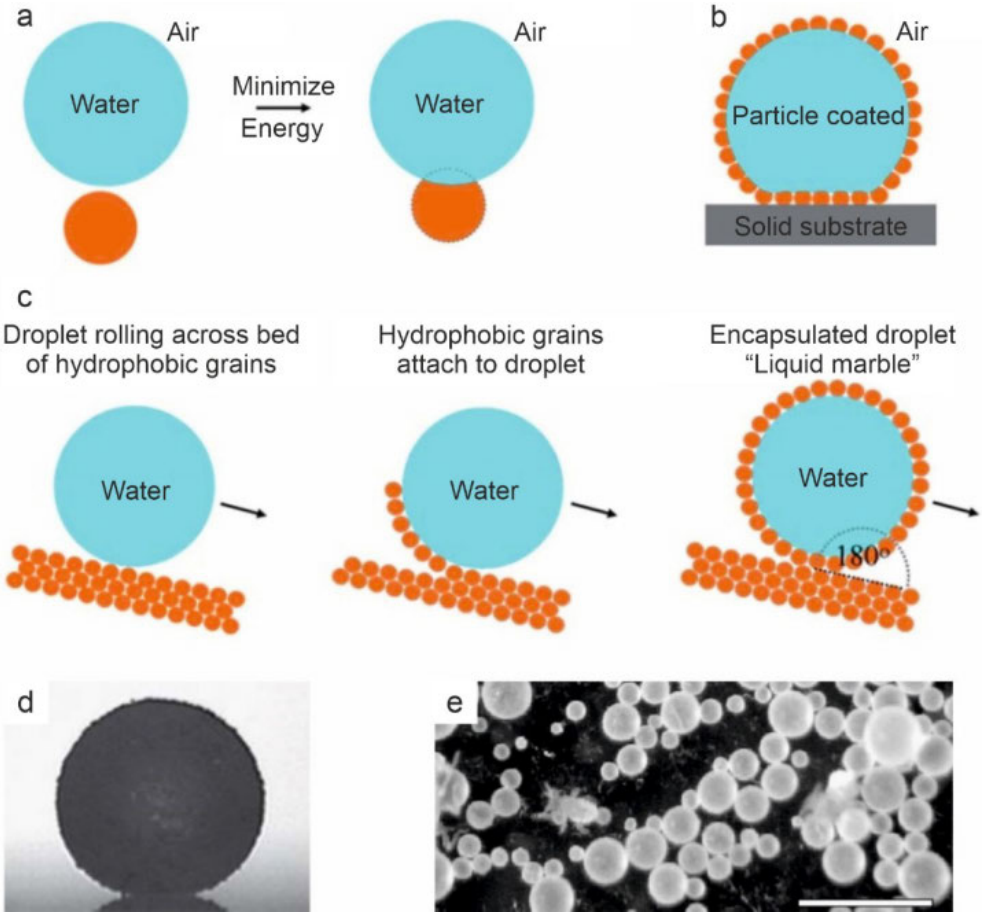

Figure 21. Liquid Marbles. **a**) Particles adsorb at the air-water interface to minimize interfacial energy. **b**) Droplet coated with particles on a solid substrate, a liquid marble. The particle layer separates the water drop from the underlying substrate. **c**) Formation of a liquid marble by rolling a water drop over a hydrophobic powder consisting of hydrophobic grains. During rolling, the hydrophobic grains attach to the drop. **d**) Photograph of a liquid marble. Reproduced from ref.[184] with permission from The Royal Society of Chemistry. **e**) Liquid marbles in nature. The armored droplets consist of honeydew encapsulated by wax powder, which was produced by aphids. Scale bar: 1 mm. Reproduced with permission from ref.[189] Copyright 2002, The Royal Society.

The wax consists of long-chained alcohols, aldehydes, esters, and fatty acids and is highly hydrophobic. The excreted honeydew is now encapsulated by the wax powders leading to the formation of liquid marbles (**Figure 21**e). These honeydew liquid marbles are non-wetting and can be moved by the aphids. Soldier aphids do not only defend the gall but are also responsible for cleaning, i.e., rolling the honeydew liquid marbles out of the gall through a small opening, ensuring the survival of the aphids.[189] Liquid marbles have been prepared using various kinds of stabilizers, including organic,[190-192] inorganic,[193-195] and composite[196] particles and powders. They can encapsulate different liquids, including functional liquids like blood.[197-198] Xue *et al.* prepared F-POSS powders and F-POSS/Fe_3O_4 nanoparticle composite powders to encapsulate various kinds of polar and non-polar liquids, including water, dimethyl sulfoxide, toluene, ethanol, and octane (**Figure 22**a).

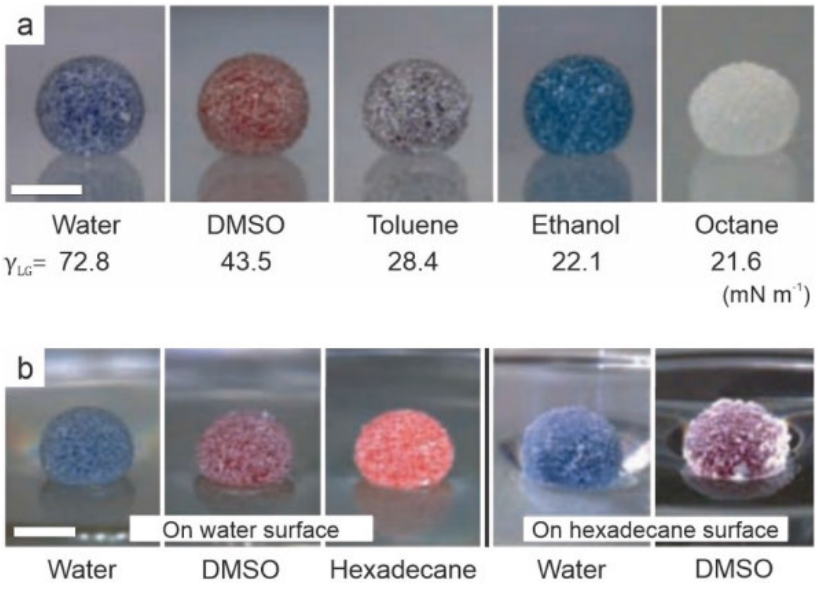

Figure 22. Liquid marbles prepared with F-POSS powder. **a**) Various liquids (3 µL), including water, dimethyl sulfoxide (DMSO), toluene, ethanol, and octane, can be encapsulated using the hydrophobic fluorinated powder. Dyes were added to the liquids for better visibility. **b**) Liquid marbles prepared with F-POSS powder and various liquids (3 µL) floating on water and hexadecane. Dyes were added for visibility. Reproduced with permission from ref.[199] Copyright 2010, John Wiley and Sons.

These liquids have largely different surface tensions, even down to $\gamma_{LG} = 21.6$ mN m^{-1} for octane. The liquid marbles could be transferred and float on a water surface and even on a hexadecane surface (**Figure 22**b). Liquid marbles prepared with the F-POSS/Fe_3O_4 nanoparticle composite powder could be opened and moved using magnetic fields and be utilized as a reactor. Besides that, liquid marbles were used in diverse applications, including transport of liquids,[200] miniature reactors,[194, 199] micro bioreactors, and drug screening,[198, 201-202] microcapsules,[192] sensors,[190] accelerometers,[203] and pressure-sensitive adhesives.[193] For instance, Fujii *et al.* embedded pressure-sensitive adhesive (PSA) polymer solutions in liquid marbles (**Figure 23**). As a liquid marble stabilizer, $CaCO_3$ nanoparticles were hydrophobized using octadecanoic acid. Poly(*n*-butyl acrylate) (PBA) latex particles were synthesized as PSA base polymer. An aqueous dispersion (180 µL) of the PBA latex particles (≈50 wt% solid content) was deposited on the hydrophobized $CaCO_3$ powder, which immediately encapsulated the PBA particle dispersion. Afterward, the formed liquid marbles were dried for several hours to evaporate the water content. The dried PSA marbles remained non-sticky and were flowing freely like a powder. After the application of shear stress, the pressure-sensitive adhesive could be released unfolding its adhesive behavior. These PSA marbles may be useful to transport glues into confined, hard-to-reach spaces.[193]

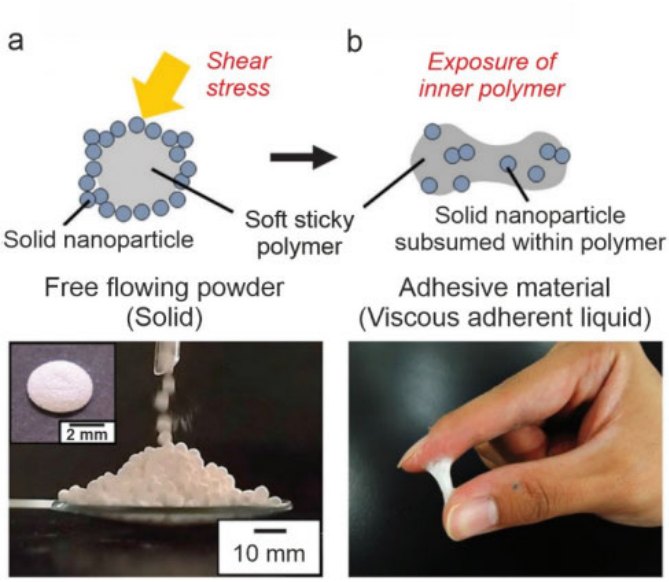

Figure 23. Pressure-sensitive adhesive (PSA) Marbles. **a**) A PSA is armored with hydrophobic $CaCO_3$ nanoparticle powder. After encapsulation, the PSA marbles are non-sticky and act as a free-flowing powder. **b**) Only upon applying pressure, the PSA marbles break and release the sticky PSA polymer. Reproduced from ref.[193] with permission from The Royal Society of Chemistry.

It should be noted that there is a distinct similarity between liquid marbles and superhydrophobic or superamphiphobic surfaces (**Figure 24**). A water droplet on a superhydrophobic surface takes an almost spherical shape due to the rough and hydrophobic layer on the substrate. On the other hand, a liquid marble is a droplet coated with a rough, hydrophobic layer. Thus, a liquid marble can be regarded as a droplet covered by a superhydrophobic layer that was previously detached from the substrate.[187]

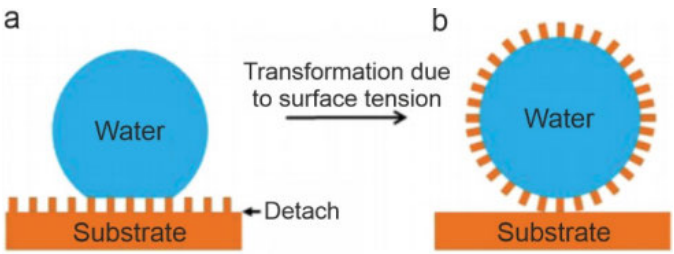

Figure 24. Similarities between superhydrophobic surfaces and liquid Marbles. **a**) Superhydrophobic layer attached to a substrate. **b**) Superhydrophobic layer on a liquid marble. Reproduced from ref.[187] with permission from The Royal Society of Chemistry.

The in-situ formation of a liquid marble is observed during the self-cleaning of a superhydrophobic surface in Chapter 3, and these principles are used in Chapter 6 to prepare unique liquid marbles.

2 HOW DROPS START SLIDING OVER SOLID SURFACES

Nan Gao,[1,2] Florian Geyer,[1] Dominik W. Pilat,[1] Sanghyuk Wooh,[1] Doris Vollmer,[1] Hans-Jürgen Butt,[1] and Rüdiger Berger[1]

[1]Max Planck Institute for Polymer Research, Ackermannweg 10, 55128 Mainz, Germany
[2]Fudan University, 220 Handan Road, Shanghai 200433, People's Republic of China

Abstract: It has been known for more than 200 years that the maximum static friction force between two solid surfaces is usually greater than the kinetic friction force — the force that is required to maintain the relative motion of the surfaces once the static force has been overcome. But the forces that impede the lateral motion of a drop of liquid on a solid surface are not as well characterized, and there is a lack of understanding about liquid-solid friction in general. Here, we report that the lateral adhesion force between a liquid drop and a solid can also be divided into a static and a kinetic regime. This striking analogy with solid-solid friction is a generic phenomenon that holds for liquids of different polarities and surface tensions on smooth, rough, and structured surfaces.

Keywords: Applied physics, fluids

This chapter is reprinted with permission from N. Gao, F. Geyer *et al.*, *Nat. Phys.* **2018**, *14*, 191.

The Supporting Information is available from nature.com:
https://www.nature.com/articles/nphys4305#supplementary-information

2.1 INTRODUCTION

When two solid objects are brought into contact, a threshold force F_{THRD} must be overcome in order for one of the objects to slide.[204-206] This phenomenon can be visualized in a typical classroom experiment where a solid block attached to a spring is pulled over a solid surface (**Figure 25**a). The static force F_{S} is applied to the stationary block and then increased until it exceeds F_{THRD}, upon which the block begins to slide. After that, a lower kinetic force F_{KIN} is required to maintain the block's motion.[206] However, it is not clear whether these forces develop in a comparable manner when a drop of liquid resting on a solid surface starts to slide. This gap in our understanding is astonishing, given the fact that liquid drops are omnipresent in our lives, and their motion is relevant for numerous applications, including microfluidics,[11] printing,[207] condensation,[14-15] and water collection.[12-13] Hence insight on the behavior of drops that start sliding over solid surfaces is needed.

A sessile drop of liquid is usually in molecular contact with the supporting solid surface. In contrast, two solid bodies are in direct contact only at asperities owing to surface roughness.[208-209] Thus, the real contact area of a solid-solid contact is much smaller than the apparent contact area. Consequently, the sliding of drops might be fundamentally different. However, by simply observing a drop of water on a pivot window pane, we know that also sessile drops start sliding when a critical tilt angle is reached, i.e., when the gravitational force acting on the drop overcomes the lateral adhesion force.[210] The question may, therefore, be raised whether a static and a kinetic regime are also present for sessile drops. The general question is: How do drops start sliding over solid surfaces, and how do the forces develop while the drops slide?

Owing to higher gravitational forces, larger drops start sliding at lower tilt angles. Sliding is opposed by capillary forces. They are associated with a contact angle difference between the rear and the front of the drop. Indeed, the interactions between solid surfaces and liquids are described by the liquid-air surface tension γ and the apparent rear and front contact angles of the drop, θ_{Rear} and θ_{Front}, respectively. Thus, the surface tension, the contact angles and the drop contact width L determine the lateral adhesion force F_{LA} by[211-215]

$$\Delta F_{\mathrm{LA}} = kL\gamma(\cos\theta_{\mathrm{Rear}} - \cos\theta_{\mathrm{Front}}). \tag{15}$$

The dimensionless factor k accounts for the precise shape of the solid-liquid-air three-phase contact line of the drop. Values for k were calculated to be between 1/2 and $\pi/2$.[211, 216-218]

Despite the omnipresence of drops, the onset of motion has never been correlated with the development of lateral adhesion forces. The lateral adhesion force has been related to external forces that cause a drop to slide, such as gravitational,[219-220] centrifugal,[9] magnetic,[221] or capillary forces.[6-8] The contact angles have also been experimentally and numerically investigated for the pinned state, i.e., just before and during steady motions.[222-223] However, once a drop has started to slide, the lateral adhesion force cannot be tracked using simple techniques. Astonishingly, it is unclear how the force develops and how it depends on sliding velocity. We will demonstrate that, for the lateral liquid-solid adhesion, we can distinguish a static and a kinetic regime, analogous to solid-solid friction.

2.2 RESULTS AND DISCUSSION

To measure the lateral adhesion force between a drop of liquid and a solid substrate, a capillary is positioned in the center of the drop. The substrate with the drop is moved sideways against the capillary at a constant velocity. When the capillary reaches the edge of the drop, it sticks to the drop. Consequently, the motion of the substrate is accompanied by a deformation of the drop as well as a deflection of the capillary. Initially, the drop remains pinned to the substrate (**Figure 25**b).

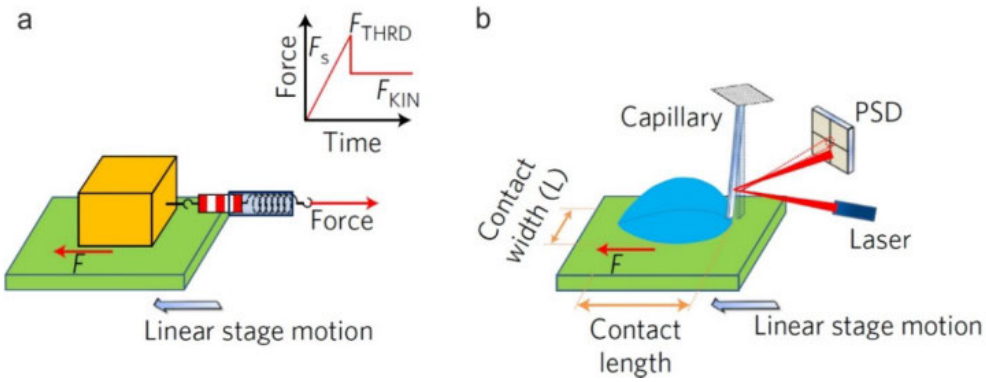

Figure 25. Schematics of friction force measurements. **a**) Textbook configuration for demonstrating solid-solid friction. **b**) Homemade setup for measuring liquid-solid friction. A drop of liquid is placed on a solid substrate mounted on a linear stage driven by a step motor. A laser beam incident on the capillary is reflected to a position-sensitive detector (PSD). The contact width between the drop of liquid and the solid surface (orthogonal to the direction of motion) and contact length (parallel to the direction of motion) are simultaneously monitored by cameras (not shown).

Once the capillary exerts a certain critical force, the drop overcomes the lateral adhesion and is set into translational motion relative to the substrate, i.e., the front and rear side of the drop start moving. The deflection D of the capillary is measured by recording the position of a reflected laser beam with a position-sensitive detector.[7] Then, the lateral adhesion force acting on the drop can be calculated by $F_{LA} = \kappa D$, where κ is the spring constant of the capillary. Simultaneously, the drop's shape is monitored by two cameras, which are synchronized with the force measurement. In this way, the lateral adhesion force can be correlated with the contact angles. Velocities ranged from 1 μm s^{-1} to 50 mm s^{-1} (see Experimental Section 2.3).

As a representative example, we start with a drop of an ionic liquid placed on a fluorinated Si wafer. It forms a contact angle of ≈70°. Moving the wafer laterally increased the force (blue circles in **Figure 26**a) until a maximum force of 50 μN was reached (after 11 s). This maximum force corresponded to the threshold force for the drop, upon which it started to slide. Then the force subsequently decreased to a constant level of ≈33 μN, which was only 66% of the maximal force (after 17 s). Accordingly, we distinguish a static, a transition, and a kinetic regime shown in different shades of green in **Figure 26**a. The presence of a higher threshold force compared to the force required for continuous motion explains the manner a drop slides downhill in a tilted-plate experiment. It is analogous to solid-solid friction, where a solid object placed on a tilted plane keeps sliding once the static friction threshold force has been overcome.[224] Initially, the contact line of the drop was pinned, and the contact width and length remained constant at about 2.3 mm (**Figure 26**b, first 5 s). Meanwhile, the front and rear contact angles increased and decreased, respectively, as the drop deformed (**Figure 26**c). After 5–8 s, the contact line started reforming, resulting in a longer and narrower drop shape. After about 10 s, the contact angles reached a maximum value of ≈86° at the front and a minimum of ≈43° at the rear. At this point of maximum contact angle difference of ≈40°, the static adhesion force reached its maximum, which constituted the threshold force of the translational motion. In the transition regime, the contact length decreased continuously. The rear contact angle increased by more than 10°, whereas the front contact angle decreased by ≈5° over time. Finally, a kinetic regime was reached (after ≈18 s), which was characterized by constant lateral adhesion forces, constant contact angles, constant contact widths, and contact lengths.

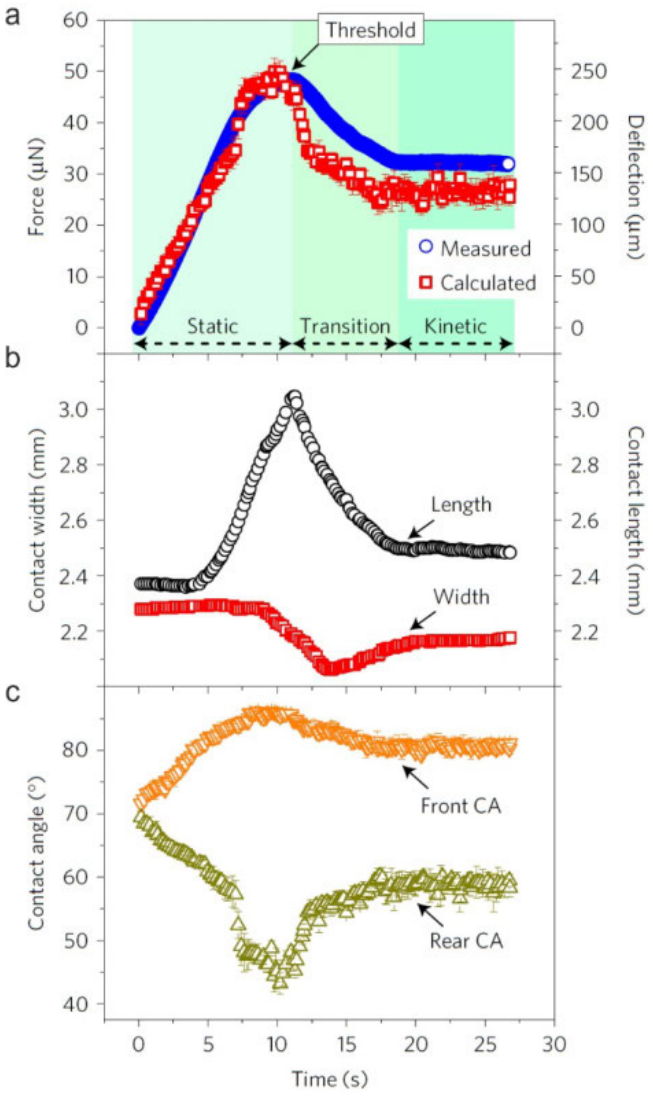

Figure 26. Lateral adhesion force experiment of a drop of ionic liquid (volume ≈1.5 μL) on a fluorinated silicon wafer. The measurement was performed at a constant linear stage velocity of 200 μm s^{-1}. The surface tension of the ionic liquid 1-butyl-2,3-dimethylimidazolium bis(trifluoromethanesulfonyl)imide is 34.6 mN m^{-1}. **a**) The measured lateral adhesion force is plotted with blue circles. The error in force measurement is ±1 μN and smaller than the symbol size. The calculated force is plotted with red Squares. **b**) Simultaneously determined contact width and length of the drop during the force measurement shown in a). **c**) Front and rear contact angles during the force measurement. Movie S1 shows the motion of the ionic liquid drop on the fluorinated Si wafer during the lateral adhesion force measurement.

We then took the measured contact widths (**Figure 26**b) and contact angles (**Figure 26**c) to calculate the lateral adhesion force using Eq. 1. Thereby we simplified Eq. 1 by assuming a constant value of $k = 1$ thus disregarding shape changes of the drop contour and variations of the contact angle along the contour[216] (see Supplementary Information for a discussion of the k factor and its temporal development). This calculation almost quantitatively agreed with the measured lateral adhesion force (red squares in **Figure 26**a). In particular, the calculated lateral adhesion force reproduced the transition between the static and kinetic regimes. Once the threshold adhesion force F_{THRD} has been overcome, the drop transitions from a static regime to a steady kinetic regime. Consequently, the liquid-solid adhesion forces in the static and kinetic regimes are substantially different, owing to different contact angles and contact widths in these two regimes:

$$F_{\mathrm{S}} = \gamma L_{\mathrm{S}}\left(\cos\theta_{\mathrm{S}}^{\mathrm{Rear}} - \cos\theta_{\mathrm{S}}^{\mathrm{Front}}\right) \tag{16}$$

$$F_{\mathrm{KIN}} = \gamma L_{\mathrm{KIN}}\left(\cos\theta_{\mathrm{KIN}}^{\mathrm{Rear}} - \cos\theta_{\mathrm{KIN}}^{\mathrm{Front}}\right) \tag{17}$$

Here, F_{S}, L_{S}, $\theta_{\mathrm{S}}^{\mathrm{Front}}$ and $\theta_{\mathrm{S}}^{\mathrm{Rear}}$ are the lateral adhesion force, contact width, and front and rear contact angles in the static (S) regime. F_{KIN}, L_{KIN}, $\theta_{\mathrm{KIN}}^{\mathrm{Front}}$ and $\theta_{\mathrm{KIN}}^{\mathrm{Rear}}$ are the lateral adhesion force, contact width, and front and rear contact angles in the kinetic (KIN) regime. To verify whether the discrimination between static and kinetic lateral adhesion forces is a generic feature, we analyzed a number of different liquid-solid combinations (**Figure 27**). We used water and hexadecane in addition to a non-volatile ionic liquid (1-butyl-2,3-dimethylimidazolium bis(trifluoromethanesulfonyl)imide). The solid surfaces include superhydrophobic fluorinated silicone nanofilaments (SNFs), fluorinated silicon wafers (Si), fluorinated SU-8 micropillar arrays, fluorinated multilayers of titanium dioxide nanoparticles (TiO_2) and cross-linked polydimethylsiloxane (PDMS) substrates (Figure S1). All samples were homogeneous at the scale of the drop radius and did not have distinct pinning centers. For all liquid-solid combinations, we observed a static, a transition, and a kinetic regime (**Figure 27**a, Figure S5–S10). It should be noted that the lateral adhesion force in the kinetic regime never exceeded the threshold force (**Figure 27**a):

$$F_{\mathrm{THRD}} \geq F_{\mathrm{KIN}} \tag{18}$$

Notably, $F_{\mathrm{THRD}} = F_{\mathrm{KIN}}$ is possible, too.[7] Surfaces coated with brushes of liquid-like PDMS showed no difference between F_{THRD} and F_{KIN}. The reason is that these surfaces show almost identical contact angle hysteresis for water at the threshold and in the kinetic regimes (Figure S11).

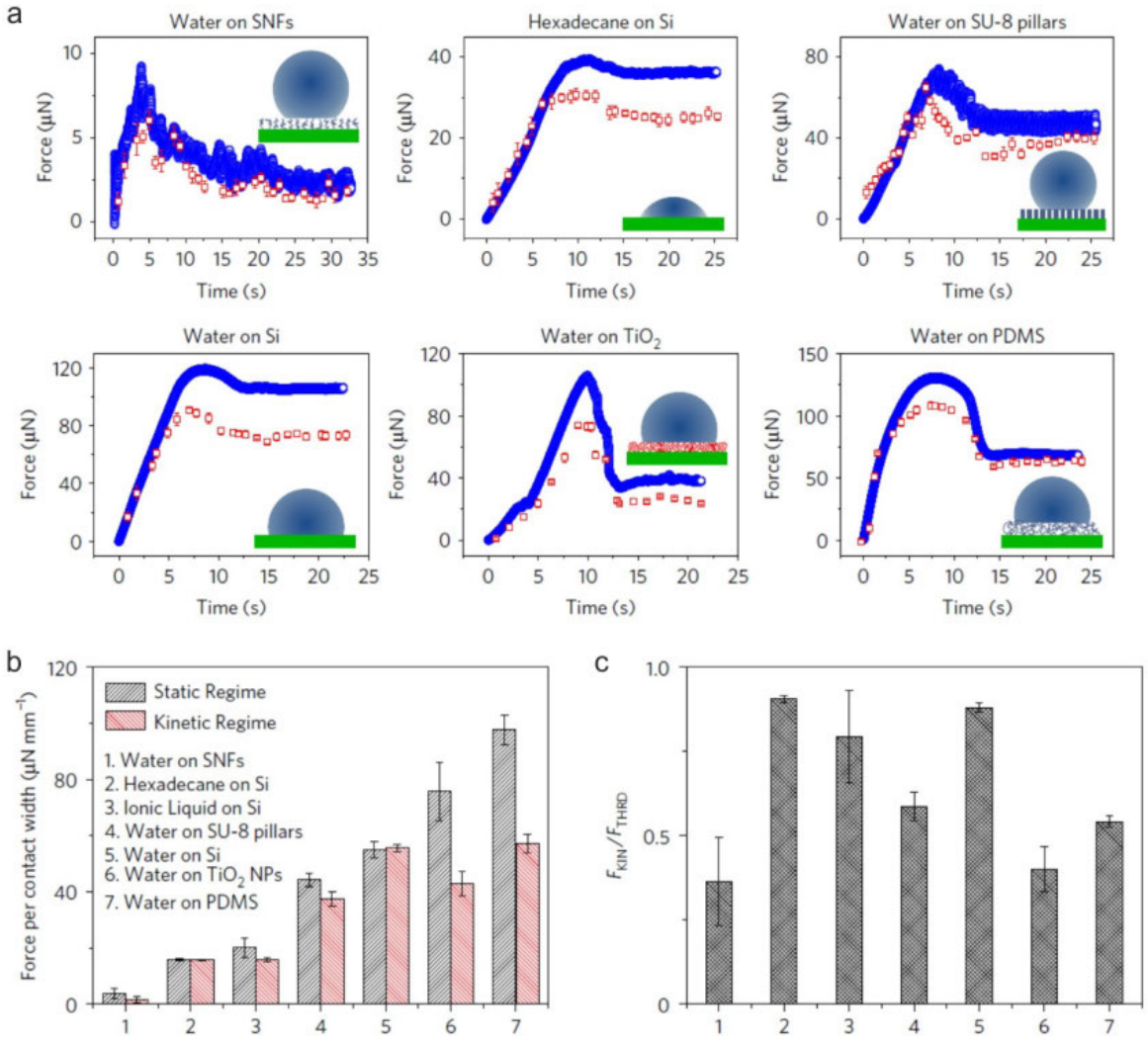

Figure 27. Lateral adhesion forces for drops of different liquids on solid surfaces. **a**) Measured (blue circles) and calculated lateral adhesion forces using k = 1 (red squares). The surfaces include silicone nanofilaments (SNFs), silicon wafers (Si), SU-8 square pillar arrays (height: 25 μm, width: 50 μm, center-center distance: 100 μm), multilayers of 20-nm titanium dioxide nanoparticles (TiO_2 NPs), and crosslinked polydimethylsiloxane (PDMS). All surfaces except for those of PDMS were fluorinated before use. All fabrication details are provided in the Experimental Section 2.3. The adopted surface tensions of water and hexadecane are 72.5 mN m^{-1} and 27.5 mN m^{-1}, respectively. The front and rear contact angles in the kinetic regimes were 171° ± 1° and 164 ± 1° for water on fluorinated silicone nanofilaments, 83° ± 1° and 59° ± 1° for hexadecane on fluorinated silicon wafers, 169° ± 2° and 122° ± 2° for water on fluorinated SU-8 pillars, 128° ± 1° and 95° ± 1° for water on fluorinated silicon wafers, 164° ± 1° and 128° ± 2° for water on titanium dioxide nanoparticles, and 121° ± 1° and 81° ± 1° for water on crosslinked PDMS, respectively (Figure S5–S10). Movies S2–S7 show the motions of drops on the different surfaces during the lateral adhesion force measurements. **b**) Lateral adhesion force per contact width. Drop volumes between 1.5 and 8.0 μL were chosen to avoid the rupturing of drops during motion. **c**) Ratios of the kinetic friction force F_{KIN} and its threshold force F_{THRD} of all liquid-solid combinations that are studied. Here we used F_{KIN} and F_{THRD} prior normalization with the respective contact widths in order to point out $F_{KIN}/F_{THRD} \leq 1$. Error bars in b and c indicate variability between different experiments.

Furthermore, good agreement between calculated and measured lateral adhesion forces was observed for various wetting scenarios, including hexadecane and ionic liquid on

fluorinated silicon wafers, and water on superhydrophobic silicone nanofilaments and fluorinated SU-8 pillars, where drops partially rested on air cushions. The differences in adhesion between the drops and the substrates resulted in different apparent contact angles and contact widths among the liquid-solid combinations (Figure S5–S10). We attribute the small discrepancies between calculated and measured lateral adhesion forces to microscopic distortions of the three-phase contact lines.[210] The latter can be accounted for by the *k* factor (Figure S5–S10 and Table S1). Indeed, the *k* factor of our measurements lies between 0.25 and 4. It is worth emphasizing that the *k* factor changed continuously while the drop passed from the static to the kinetic regime. These observations indicate that a constant *k* factor is not sufficient to describe how drops slide over a solid surface. For large scale heterogeneous surfaces that exhibit distinct pinning centers, F_{KIN} occasionally exceeded F_{THRD} (Figure S12 and Griffiths and colleagues[225]). Thus, the lateral adhesion force provides quantitative information on the homogeneity or cleanliness of a surface.

To compare the different liquid-solid combinations independently from drop size, we calculated the static and lateral adhesion force per contact width (**Figure 27**b). This analysis yielded values ranging from 2 μN mm^{-1} to 110 μN mm^{-1}. The increasing lateral adhesion force per contact width depends on the interplay between surface tension and contact angle hysteresis. In addition, we calculated the ratios of the kinetic force divided by the static threshold force. For all different liquid-solid combinations, we obtained a ratio of $F_{KIN}/F_{THRD} \leq 1$ (**Figure 27**c).

In general, contact angles depend on the sliding velocity.[226] Therefore we measured F_{KIN} and F_{THRD} in a velocity range from 10^{-3} to 34 mm s^{-1} for hexadecane on a fluorinated silicon wafer surface (filled symbols in **Figure 28**a,b). We found that F_{KIN} and F_{THRD} are relatively constant up to a capillary number Ca of 10^{-5}. Then they increase with velocity. Furthermore, the dependence and magnitude of the measured forces are in agreement with the forces calculated by the front and rear contact angles (inset of **Figure 28**b) using Eq. 15 (open symbols in **Figure 28**a,b). Similarly, an increase in lateral adhesion forces was observed for ionic liquid and water on fluorinated silicon wafers, respectively (**Figure 28**c,d). Perrin *et al.* measured the dynamic macroscopic contact angle of a silicon wafer withdrawn from a silicone oil bath.[227] These experiments revealed a strong change in the cosines of the contact angles between $10^{-5} < Ca < 10^{-3}$. This region marked the transition from energy dissipation dominated by defects to viscous dissipation.

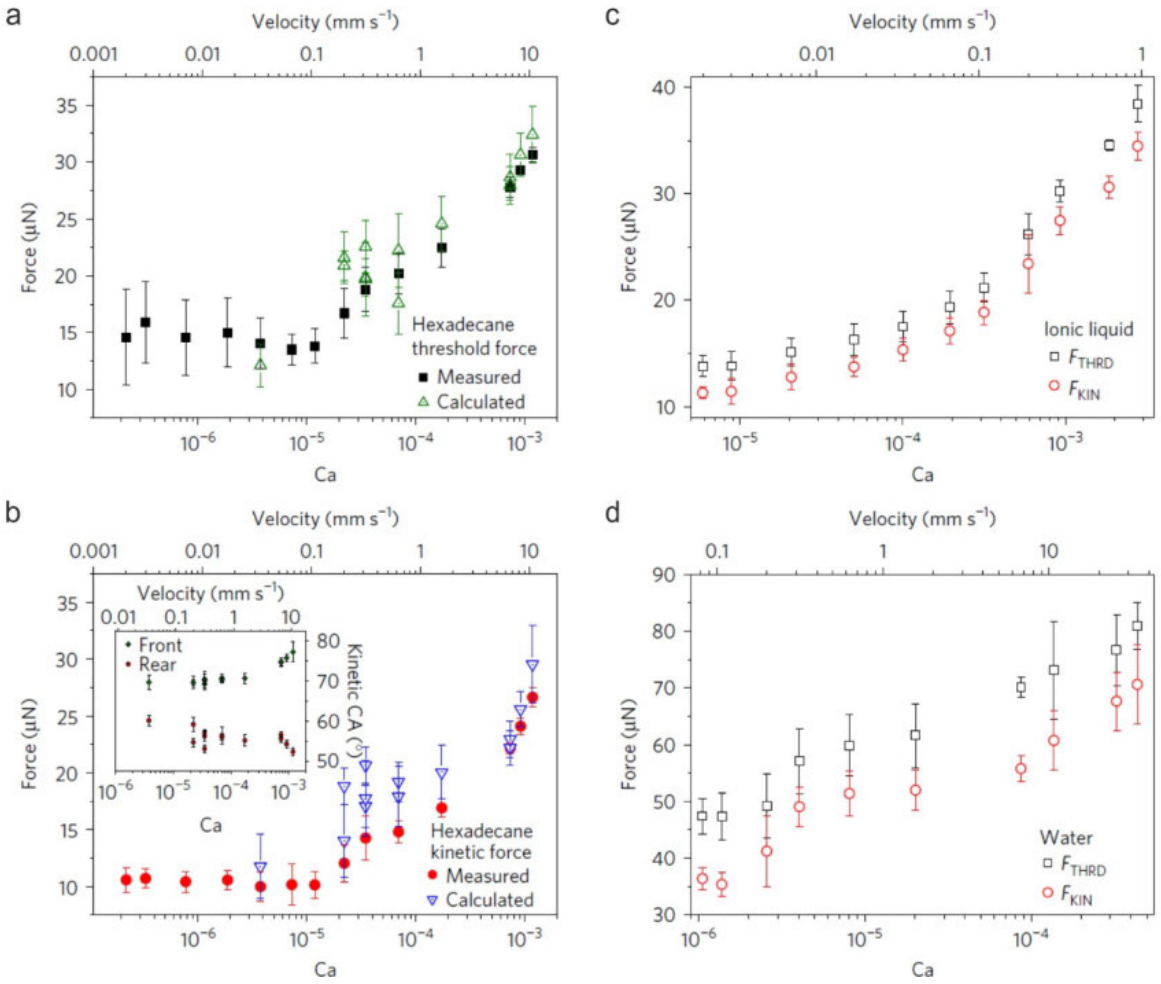

Figure 28. a,b) Velocity dependence of lateral adhesion forces. Development of the lateral adhesion force of hexadecane drops (≈3 μL) on a fluorinated Si wafer surface (a) at the threshold and (b) in the kinetic regime. The inset shows the front and rear contact angles measured in the kinetic regime. **c,d**) Velocity dependence of lateral adhesion forces of an ionic liquid (1-butyl-2,3-dimethylimidazolium bis(trifluoromethanesulfonyl)imide) drop (≈2 μL) on a fluorinated Si wafer substrate (c) and water drops (≈7.5 μL) on a fluorinated Si wafer substrate (d). Here velocities below 0.08 mm s^{-1} were not studied owing to evaporation of water. The error bars correspond to the standard deviation calculated from 5–7 independent measurements. The highest velocity that can be probed is given by the threshold force where the liquid drop detaches from the glass capillary (≈81 μN for water, ≈36 μN for ionic liquid, and ≈31 μN for hexadecane).

The increase in F_{KIN} falls in this regime, and therefore we attribute the increase of F_{KIN} at $Ca > 10^{-5}$ to viscous dissipation in addition to thermally activated processes at the contact line. The latter was discussed as a result of a rugged energy landscape of the sample surface, leading to a thermally activated process of the contact line dynamics.[227] In our measurements, we could not resolve a logarithmic dependence of F_{KIN} and F_{THRD} at $Ca < 10^{-5}$, which would have given insight into such a thermally activated process of the moving liquid. In particular, we found that the ratio of $F_{KIN}/F_{THRD} \leq 1$ holds within the probed velocity range (Figure S13 and S14).

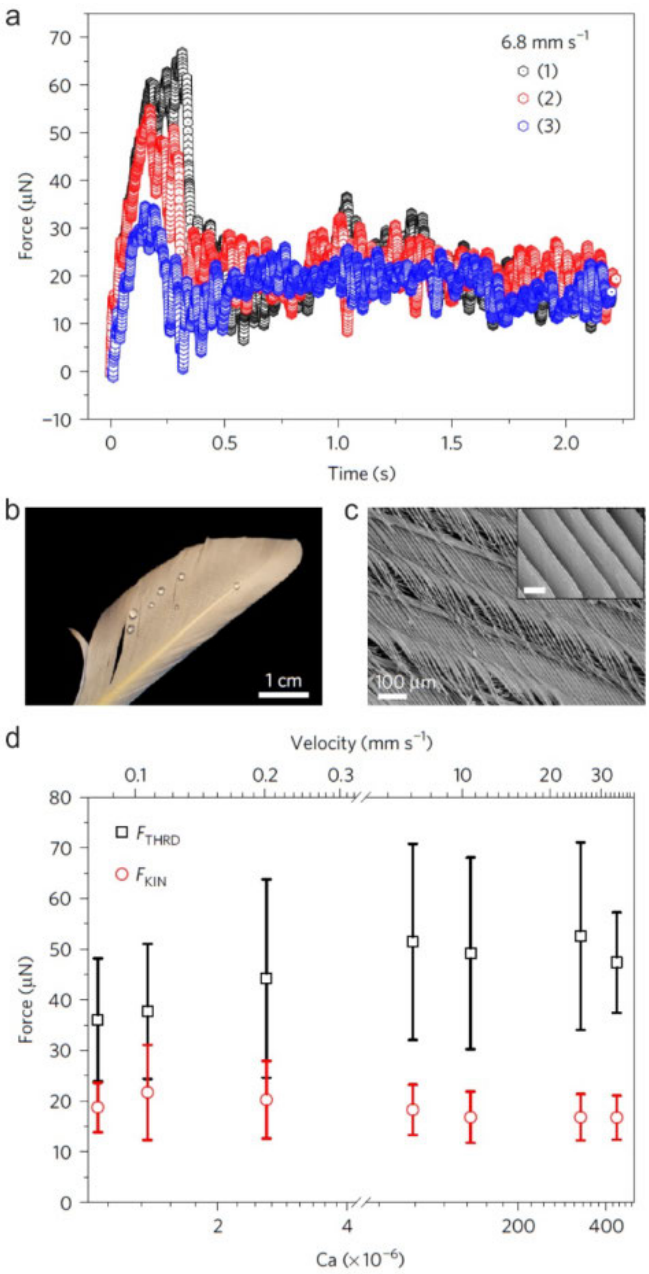

Figure 29. Lateral adhesion force measurement of a water drop on a goose feather. **a**) Three different lateral adhesion force measurements of a water drop on a goose feather at different areas at a velocity of 6.8 mm s^{-1} (drop volume of 8.0 µL). The threshold lateral adhesion force varied between 35 ± 1 µN and 67 ± 2 µN. Continuing the kinetic motion of the water drop required a force up to 35 µN. **b**) An optical image of the feather with resting water drops. **c**) Scanning electron microscopy images reveal the detailed structure of the feather. The inset is an enlarged area showing the microscopic structure. The scale bar in the inset is 10 µm. **d**) No velocity dependence of the lateral adhesion force at threshold (black squares) and in the kinetic regime (red circles) could be measured. The error bars correspond to the standard deviations calculated from 5–7 measurements each.

In order to study whether drop-solid friction scales with the contact line or with the contact area, we varied the drop volume resulting in a variation of the contact area by a factor of >4 (Figure S13). The linear extrapolation of the kinetic force suggests a linear dependence with an intercept slightly below zero force. Therefore we conclude that the liquid drop friction is dominated by contact line friction, and interfacial friction only plays a minor role. This conclusion is supported by an estimation of the friction force contribution of a solid-liquid interface based on a Green-Kubo relation of Huang and Szlufarska[228]

and by monitoring the motion of drops over the surfaces, showing that the motion is dominated by rolling (Figure S15, Movies S8–S11). In contrast, contact line friction does not play a role for liquid-liquid interfaces, such as drops on lubricated surfaces.[229]

As an example of a natural, structured surface, we measured the lateral adhesion of a water drop on a goose feather (**Figure 29**a). Again, we observed a static regime and a kinetic regime. The static threshold force was up to 3 times larger than the average kinetic force required for the continuous motion of the water drop. In addition, the lateral adhesion force varied in the kinetic regime. Likely, these variations are related to the flexibility and the microscopic structures of the feather (**Figure 29**b,c), which lead to a stick-slip motion of the drop. Energy is dissipated mainly by depinning from a few surface protrusions, which shows no velocity dependence of the lateral adhesion force at the threshold and in the kinetic regime (**Figure 29**d and Figure S16).[230] The latter is in contrast to the stick-slip motion of two solids.[231-232] Consequently, for such rough and elastic surfaces, the contribution of viscous dissipation to the overall energy dissipation of the sliding drop is low. It is not clear what role such a stick-slip motion and the associated velocity independence play for the life of a goose in water. The constant and low kinetic force could potentially reduce energy losses at the three-phase contact line of the feather with water and air.

2.3 EXPERIMENTAL SECTION

2.3.1 MATERIALS

The following chemicals were used to fabricate the solid substrates: trichloromethylsilane (TCMS, 99%, Sigma-Aldrich), 1*H*,1*H*,2*H*,2*H*-perfluorodecyltrichlorosilane (PFDTS, 96%, Alfa Aesar), 1*H*,1*H*,2*H*,2*H*-perfluorooctyltrichlorosilane (PFOTS, 97%, Sigma-Aldrich), trimethylsiloxy-terminated polydimethylsiloxane (PDMS, 200 cSt, ABCR), sulfuric acid (95%, VWR), Sylgard 184 (PDMS precursor, Dow Corning), Sylgard 184 curing agent (Dow Corning), ammonia solution (28%, VWR), hydrogen peroxide solution (Sigma-Aldrich, 34.5–36.5%), *n*-hexane (99.99%, Fisher Chemical), toluene (99.99%, Fisher Chemical), isopropanol (99.5%, Fisher Chemical), acetone (99.98%, Fisher Chemical), ethanol (absolute, 99.96%, VWR Chemicals), tetrahydrofuran (99.9%, Sigma-Aldrich), SU-8 3025 photoresist (MicroChem), mr-Dev 600 developer (micro resist technology), 18NR-T (Dyesol) and sodium hydroxide (98%, Sigma-Aldrich). Reagents were used as received. Polished silicon wafers were obtained from Si-Mat. Thin glass slides of

24 × 60 mm^2 and 170 ± 5 µm thickness were obtained from Carl-Roth. All syntheses were carried out at room temperature. The liquids drops used for force measurements included those of hexadecane, 1-butyl-2,3-dimethylimidazolium bis(trifluoromethanesulfonyl)-imide and water. Hexadecane (99%, Sigma-Aldrich) and 1-butyl-2,3-dimethylimidazolium bis(trifluoromethanesulfonyl)imide (99%, IoLiTec) were used as received. Water with a typical resistivity of 18.2 MΩ·cm was obtained from a Sartorius Arium 661 VF Water Purification System.

2.3.2 SILICONE NANOFILAMENTS

Silicone nanofilaments on glass slides were synthesized by modifying previously reported methods.[112, 115] The fabrication contained the following steps:[116, 118, 233] First, 120 µL of TCMS was added into a reaction chamber containing 50 mL of water-saturated *n*-hexane. The resulting solution was stirred for 60 s. Then, cover glass slides were immersed in the solution before sealing the reaction chamber. After 3 days, the TCMS-coated glass slides were removed from the reaction chamber, rinsed with *n*-hexane, and dried under a nitrogen stream. The TCMS-coated glass slides were activated in an oxygen plasma chamber (75 W, 2 min, 7 $cm^3 min^{-1}$ oxygen flow rate, Diener Electronic Femto) before modification with the fluorinated silane PFDTS. Therefore, the activated substrates were immersed in a solution containing 25 µL of PFDTS dispersed in 50 mL of *n*-hexane for 20 min. Subsequently, the substrates were rinsed with *n*-hexane and dried under a nitrogen stream. Representative scanning electron microscopic images of the resulting silicone nanofilaments are shown in Figure S1a,b.

2.3.3 SILICON WAFERS

Pristine silicon wafers were cleaned by ultra-sonication in toluene, acetone, and ethanol for 15 min, respectively. Subsequently, the pre-cleaned wafers were plasma-cleaned and activated in an oxygen plasma chamber (300 W, 10 min, 6 $cm^3 min^{-1}$ oxygen flow rate). To fluorinate the surfaces, 25 µL of PFDTS was mixed with 50 mL of *n*-hexane. The activated silicon wafers were immersed in the solution for 5 to 15 min. Afterward, the silicon wafers were rinsed with *n*-hexane, followed by ultrasonication in isopropanol for 5 min. The cleaned silicon wafers were dried under a nitrogen stream. It should be noted that the immersion time influences the lateral adhesion force of the fluorinated silicon wafers. To access higher sliding velocities, we improved the preparation of the Si wafers. We found that ultrasonication in isopropanol helps to remove residues from the fluorination. Generally, shorter fluorination times (5 min) yielded a lower adhesion. Therefore the lateral

adhesion forces measured for fluorinated silicon wafers in **Figure 28** are lower compared to **Figure 26**. Lower lateral adhesion forces allowed us to investigate higher velocities. The scanning electron microscopy analysis revealed featureless, smooth surfaces, as shown in Figure S1c,d.

2.3.4 SU-8 PILLARS

SU-8 micropillar arrays were prepared on thin glass slides by photolithography.[62] The square pillars were designed 25 μm high, with 50 × 50 μm^2 top areas. The pillar–pillar distance between centers of two adjacent pillars in a row was 100 μm. The fabrication process consisted of the following steps. First, glass slides (Carl-Roth) were cleaned by ultra-sonication in tetrahydrofuran, acetone, and ethanol for 15 min, respectively. Then, SU-8 photoresist was spin-coated (500 rpm for 5 s followed by 3000 rpm for 30 s, SÜSS MicroTec) on the glass slides. The coated glass slides were heated at 65 °C for 3 min, 95 °C for 10 min, and then 65 °C for 30 min, respectively. Subsequently, the samples were slowly cooled down within 2 h and exposed to UV light (mercury lamp, 350 W) under a photolithography mask for 15 s (masker aligner SÜSS MicroTec MJB3 UV400). To crosslink the photoresist, the samples were heated up again at 65 °C for 3 min, 95° C for 10 min, and 65 °C for 30 min, and then cooled down slowly. Next, the samples were immersed in the SU-8 developer solution for 5 min, washed with isopropanol, and then dried in air, resulting in surfaces coated with SU-8 pillars. The dried samples were immersed in a 0.1 M NaOH solution overnight to hydrolyze the surfaces of the SU-8 pillars. After rinsing the hydrolyzed surfaces with water and ethanol, the samples were immersed in a solution containing 25 μL of PFDTS dispersed in 50 mL of *n*-hexane for 20 min. Finally, the fluorinated SU-8 micropillar surfaces were rinsed with *n*-hexane and dried under a nitrogen stream. Representative scanning electron microscopic images of an obtained SU-8 micropillar array are shown in Figure S1e,f.

2.3.5 PDMS

Crosslinked PDMS surfaces: Sylgard 184 PDMS precursor was mixed with Sylgard 184 curing agent in a ratio of 10:1 by weight and then degassed three times in a vacuum chamber for 5 min, respectively. Afterward, the viscous mixture was deposited on glass slides and cured at 60 °C overnight. The scanning electron microscopy analysis revealed featureless, smooth surfaces, as shown in Figure S1g,h.

Liquid-like PDMS surfaces: So termed "liquid-like" PDMS samples were prepared following the method reported by Krumpfer and McCarthy.[234] Pre-cleaned cover slides were placed in a 2:1 mixture of sulfuric acid and hydrogen peroxide solution, placed in a water bath and held at 70 °C for 2 h. Then the samples were rinsed with pure water and ethanol. After being dried, the cover slides were put into 500 mL ultraclean borosilicate glass vials (Duran Pure vials GL45 with a dust cover, Duran Group, SCHOTT) and sufficiently wetted with PDMS. The vials were resealed and placed in an oven at 100 °C for 24 h. Then the samples were properly rinsed with *n*-hexane, acetone, and water and dried.
The flexibility of the O-Si-O bonds confers high mobility to PDMS chains. As only one end of the PDMS is covalently grafted on the substrate, the remaining part of the PDMS keeps its high mobility with rotational and/or bending motion. Thus, these grafted layers are rotationally dynamic and behave "liquid-like." Water drops slide off these "liquid-like" surfaces when tilting the surface by 4° (drop volume: 20 mL).[234]

2.3.6 TITANIUM DIOXIDE NANOPARTICLES

TiO_2 surfaces consisting of ≈20 nm TiO_2 nanoparticles (NPs) were fabricated from TiO_2 nanoparticle paste (18NR-T, Dyesol).[235] First, TiO_2 nanoparticle paste was coated on a silicon wafer by doctor blade coating with 50 µm spacers. Then, the coated wafer was sintered at 500 °C for 30 min, resulting in nano-roughened TiO_2 structures. After cooling down, the TiO_2 structures were modified with PFOTS by chemical vapor deposition (CVD) in a desiccator for 2 h in vacuo. Scanning electron microscopic images of a resulting TiO_2 surface are shown in Figure S1i,j.

2.3.7 FORCE MEASUREMENTS: SENSITIVITY OF THE LASER DEFLECTION SYSTEM

For the measurement of the lateral adhesion force by means of our laser deflection system illustrated in **Figure 25**b, a hollow rectangle capillary was used to move a liquid drop against a substrate underneath.[7, 236] A laser beam was incident on the capillary, which reflected the beam to the center of a position-sensitive detector (PSD). The capillary was manufactured in borosilicate glass (VitroCom's Vitrotubes, CM Scientific). It was 35 mm long. The dimensions of the capillary were 0.04 × 0.40 mm^2, with a wall thickness of 0.028 mm. In order to increase the reflectivity of the capillary, its wide side was sputter-coated with a 5-nm-thick layer of chromium and a 50-nm-thick layer of gold. The chromium was used as an adhesion layer for the gold. When the laser hit the PSD, four photocurrents were generated by the PSD at two opposite sides along the horizontal axis and two opposite sides along the vertical axis. These four photocurrents were collected and

converted into four voltages (U_{x1}, U_{x2}, U_{y1}, and U_{y2}) using an amplifier with a current-to-voltage converter. These four voltages were read out in two values by the amplifier corresponding to the horizontal (x) and vertical (y) coordinates of the laser spot on the PSD:

$$U_x = 5\text{V} \cdot \frac{U_{x1} - U_{x2}}{U_{x1} + U_{x2}} \tag{19}$$

$$U_y = 5\text{V} \cdot \frac{U_{y1} - U_{y2}}{U_{y1} + U_{y2}} \tag{20}$$

The divisions were performed by an analog divider (Burr-Brown DIV100). $U_y = U_{\text{PSD}}$ and corresponded to the deflection of the capillary in the measurement of the lateral adhesion force. These voltage values were digitalized in an AD converter (National Instruments (NI)). Furthermore, the data acquisition software-generated triggers for the cameras to ensure synchronization between the cameras and the PSD signals.

The relationship between the deflection of the capillary, D, and the generated U_{PSD} represents the sensitivity S of the laser deflection system:

$$S = \frac{U_{\text{PSD}}}{D} \tag{21}$$

For calibration, a defined deflection of the capillary was applied close to its free end by a micromanipulator. A linear correlation was found between U_{PSD} and D for deflections up to 800 µm. The corresponding sensitivities were in the range of -4 to -5 × 10^{-3} V µm^{-1}. We performed a calibration for each new capillary and after each readjustment of the setup. Figure S2 shows a representative plot, with S = -4.16 × 10^{-3} V µm^{-1} and Pearson $r = 0.9999$. The sign of the voltage corresponds to the direction of the laser displacement on the PSD along the *y*-axis.

2.3.8 SPRING CONSTANT OF THE CAPILLARY

The spring constant κ of the glass capillary was calibrated by measuring the force acting on the capillary with respect to the lateral deflection. First, the capillary was fixed at one end into a copper holder as a fixture (Figure S3). Then the entire fixture was mounted to a micromanipulator (MMO-203, Narishige), which allowed us to move the fixture precisely (with 1 µm precision). A pin with supporting pedestals at the bottom and a pointy tip facing up were placed on a microgram balance (Figure S3). Using the micromanipulator, the free end of the capillary was located right above the tip of the pin. Afterward, the capillary was lowered down slowly by means of the micromanipulator to engage with the

tip until a slight deflection of the capillary was generated. The place where the free end of the capillary was contacted by the pin was within 1 ± 0.2 mm from the edge of the free end.

The microgram balance read out the weight that reflected the force, *F,* between the pin and the deflected capillary, as $F = mg$, where $g = 9.81$ m s^{-2}. Figure S4 is a representative plot of the calibration of the spring constant of the glass capillary. The relation between the force, F, and the deflection, D, followed Hooke's law[237]

$$F = \kappa \cdot D \tag{22}$$

with $\kappa = 0.202 \pm 0.002$ N m^{-1}.

2.3.9 FORCE CONVERSION

In order to obtain the lateral adhesion force, the voltage values directly collected from the PSD need to be converted into forces. Combining Eq. 21 and Eq. 22 yielded the relationship between the lateral adhesion forces, F_{LA}, and the generated voltage:

$$F_{\mathrm{LA}} \equiv F = \kappa \cdot D = \kappa \cdot \frac{U_{\mathrm{PSD}}}{S} F_{\mathrm{LA}} \equiv F = \kappa \cdot D = \kappa \cdot \frac{U_{\mathrm{PSD}}}{S} \tag{23}$$

2.3.10 SUBSTRATE MOVEMENT SYSTEM

Drops were deposited on solid substrates using a pipette (Thermo Scientific, Finnpipette F2). In order to probe a velocity regime that spans 5 orders of magnitudes, we implemented 3 different motorized stages to drive the relative motion between the drop and the substrate. The low-velocity regime of 2 μm s^{-1} to 200 μm s^{-1} was realized by a slow linear stage consisting of a custom-made step motor whose single steps are approximately 34.2 nm. The medium-velocity regime of 0.2 μm s^{-1} to 1.6 mm s^{-1} was achieved by using a circular disk driven by a linear motor (Faulhaber 2232 A 012 SR with transmission gear 22 EK 23014:1). The circular disk rotated at a constant angular velocity in the regime of 0.02 rpm to 0.15 rpm. The liquid drops were placed at a radius of 100 mm to the rotation center. The high-velocity regime of 6.8 mm s^{-1} to 33.9 mm s^{-1} was realized again by a linear stage consisting of a custom-made step motor, which single steps were approximately 5 μm.

2.3.11 Drop imaging

A high-speed camera (FASTCAM Mini UX100 type 800K-M-8G, Photron) equipped with a manual zoom lens was placed orthogonal to the drop motion. Its lens was focused on the drop with the narrow side of the capillary facing this orthogonal camera to monitor the change in front and rear contact angles as well as contact length. A second camera (Marlin F131B, Allied Vision) equipped with a manual zoom lens was placed parallel to the drop motion. Its lens was focused on the drop with the wide side of the capillary facing the parallel camera to monitor the change in contact width. Using the cameras, contact angles above approximately 160° are hardly accessible due to the narrow gap between the liquid and the solid. Therefore, the values do not reflect the real contact angles but should be considered as a lower boundary. On superhydrophobic surfaces, the advancing contact angle should always be close to 180°.[61] Before the sample was moved, the glass capillary was placed in the center of the drop. Both cameras were synchronized in time with the data acquisition system. Throughout an experiment, the synchronization between force and optical measurements via the cameras was <60 ms. The drop was illuminated with two cold-light sources (KL 2500 LCD, Zeiss; L2, Leica), each of them located opposite to a camera, respectively. The contact angles, as well as the contact widths and lengths, were measured by means of ImageJ. The contact widths and lengths were calculated using the known dimensions of the capillary as scale. Figure S5–S10 show representative lateral adhesion forces with measured contact widths, contact lengths, and contact angles corresponding to the cases presented in **Figure 27**a. Movies S1–S7 show the motions of drops on different surfaces during the lateral adhesion force measurements corresponding to the cases presented in **Figure 26** and **Figure 27**.

2.4 Author Contributions

N. Gao carried out the experiments and wrote the manuscript. D. W. Pilat, N. Gao, R. Berger, and H.-J. Butt designed and constructed the homebuilt setup. F. Geyer and S. Wooh prepared the solid surfaces. R. Berger, D. Vollmer, N. Gao, and H.-J. Butt contributed to experimental planning, data analysis, and manuscript preparation. All authors reviewed and approved the manuscript.

2.5 ACKNOWLEDGMENTS

We thank [redacted] for stimulating discussions, and [redacted] for technical support. This work was supported by the Collaborative Research Center 1194 (H.-J.B.), ERC advanced grant 340391 SUPRO (H.-J.B.), SPP 8173 (D.V.) and the EU Marie Sklodowska-Curie grant 722497 (D.V.). N. Gao thanks the National Postdoctoral Science Foundation of China for the International Postdoctoral Fellowship, and S. Wooh thanks the Alexander von Humboldt Foundation for a postdoctoral fellowship. D.W. Pilat is grateful for funding from the German National Academic Foundation.

3 WHEN AND HOW SELF-CLEANING OF SUPERHYDROPHOBIC SURFACES WORKS

Florian Geyer,[1] Maria D'Acunzi,[1] Azadeh Sharifi-Aghili,[1] Alexander Saal,[1] Nan Gao,[1,2] Anke Kaltbeitzel,[1] Tim-Frederik Sloot,[3] Rüdiger Berger,[1] Hans-Jürgen Butt,[1] and Doris Vollmer[1]

[1]Max Planck Institute for Polymer Research, Ackermannweg 10, 55128 Mainz, Germany.
[2]Future Industries Institute, The University of South Australia, Mawson Lake Campus, 5095 South Australia, Australia.
[3]Evonik Resource Efficiency GmbH, Goldschmidtstraße 100, 45127 Essen, Germany

Abstract: Macroscopic contamination, such as dust, is easily cleaned away by water drops rolling across a superhydrophobic surface. Despite the enormous interest in superhydrophobicity, it is still unclear when microscopic and, in particular, nanoscopic contamination (e.g., soot, aerosols) influences superhydrophobicity and how self-cleaning works in detail. Here, we show that the pore size of the superhydrophobic surface is crucial and needs to be smaller than the contaminant size. This design principle is established using hydrophilic and hydrophobic particles varying four orders of magnitude in size (diameters from 80 nm to 50 μm). We gain an in-depth understanding of self-cleaning by monitoring it on the micrometer scale using confocal microscopy and quantify the forces of drops rolling over contaminated surfaces. Outdoor environmental (>200 days) and industrial standardized contamination experiments demonstrate that nanoscale superhydrophobic surfaces can resist severe contamination.

Keywords: self-cleaning, superhydrophobic, contamination, nanoparticles

This chapter is submitted for publication, **2019**.

Important Supporting Figures can be found in Appendix 10.1.

3.1 INTRODUCTION

Surfaces exposed to the ambient atmosphere are contaminated by particulate matter over time. Particulate matter originates from nature (e.g., microorganisms and pollen) or is man-made, such as soot from combustion.[151] This makes easy cleaning or, rather, self-cleaning desirable. Self-cleaning is one of the most prominent features of superhydrophobic surfaces. Although almost 2000 articles were published on superhydrophobicity in 2018 alone, it is still unclear how self-cleaning works in detail and which forces are involved in the process. To obtain a comprehensive understanding, it is important to visualize how the self-cleaning process evolves on the micrometer scale. The resistance of superhydrophobic surfaces to particulate matter and nano-sized contamination is inevitable for the employment of these surfaces for a variety of real-world applications. Apart from self-cleaning,[34] for instance, this is essential for the development of water-proof textiles,[79, 139] anti-biofouling surfaces,[148, 238] drag reduction,[31, 102] anti-icing,[143, 239] membranes for gas exchange,[84, 116] oil/water separation,[78-79] membrane distillation,[149-150] or fog harvesting.[240-241] Thus, the need for clear design principles on how to construct surfaces to resist particle contamination should be addressed (**Figure 30**).

On superhydrophobic surfaces, water drops assume an almost spherical shape (contact angle, $\theta > 150°$) and easily roll off when the surface is tilted by a few degrees (<10°).[28] To achieve superhydrophobicity, the surface has to be coated by hydrophobic nano- or micrometer-sized protrusions. The protrusions need to be such that air is entrapped underneath, leading to the so-called Cassie state.[27] This results in low adhesion of drops to the surface. Macroscopic contamination can easily be removed by rinsing with water drops, e.g., during rain or artificial showers.[145]

Previous contamination studies focused on the influence of millimeter- to micrometer-sized contaminants on the performance of superhydrophobic surfaces, such as hydrophobic powder,[145] micrometer-sized particulates,[153-155] and aggregated bioparticles.[156]

Here, we observe the self-cleaning process on the micrometer scale using laser scanning confocal microscopy (LSCM) and quantify the forces involved. We investigate the influence of particles of various sizes (four orders of magnitude) and polarities. To design superhydrophobic surfaces that are resistant to hydrophilic as well as hydrophobic particle contamination, we found that the pore size of the superhydrophobic surface needs to be smaller than the contamination particle size. Even smaller nanoscopic contaminants do

not necessarily degrade superhydrophobicity. Finally, we demonstrate that superhydrophobic surfaces having a nanoscale pore size are capable of resisting long-term real-world exposure and industrial contamination tests.

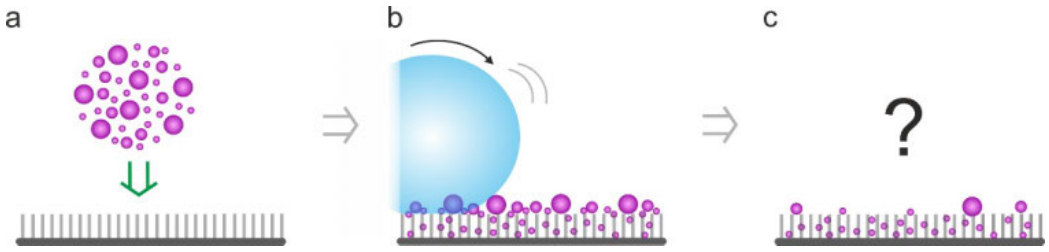

Figure 30. Illustration of contamination and self-cleaning of superhydrophobic surfaces. **a**) The surfaces are contaminated with particles of different sizes (80 nm to 50 µm) and polarities (hydrophobic/hydrophilic). **b**) Water drops roll over the contaminated Surface. **c**) Can the water drops remove the contamination and how is superhydrophobicity affected? How does the self-cleaning evolve on the micrometer scale and which forces are involved in the self-cleaning process?

3.2 RESULTS AND DISCUSSION

As an example of a superhydrophobic nanoporous surface, glass slides were coated with silicone nanofilaments.[112, 115, 118, 132] Briefly, the glass slides were immersed in a mixture of toluene with a certain water content and trichloromethylsilane (TCMS). After a reaction time of 6 h, the glass slides were covered by a 1–2 µm thick layer of nanofilaments with diameters between 20 and 50 nm and spacings between 50 nm and 500 nm. To reduce the surface energy, the coated slides were fluorinated using a perfluoro silane. These surfaces show a high static water contact angle of 161° ± 4° and low roll-off angles of ≈1° for 6 µL water drops.

Spherical, fluorescently labeled, hydrophilic and hydrophobic particles were used to mimic different types of atmospheric particle contaminants. Our particles covered a size range from 80 nm to 50 µm and were made of silica nanoparticles of avg. diameters $2R = 84 \pm 9$ nm (denoted as 80 nm particles), 210 ± 30 nm (200 nm particles), and 580 ± 120 nm (600 nm particles), silica-coated polystyrene particles of $2R = 1.45 \pm 0.14$ µm (1.5 µm particles), and silica-coated glass beads of 32 ± 7 µm (10–50 µm particles). Scanning electron microscopy (SEM) images of these particles are provided in the Supporting Information (Figure S1). Without further treatment, the particles were hydrophilic and dispersed in ethanol. To vary inherent wetting properties, a portion of the previously mentioned particles were hydrophobized using an octyl silane.

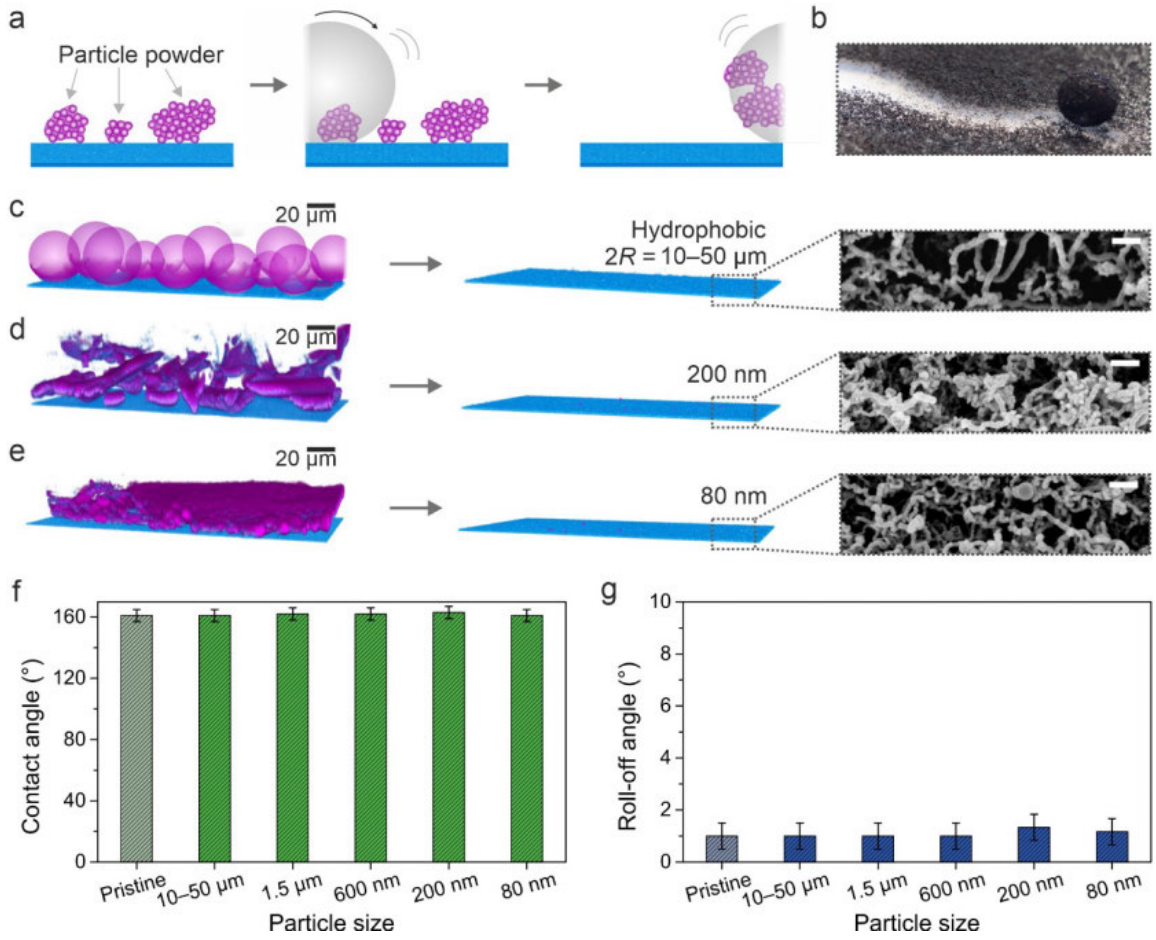

Figure 31. Effect of differently sized hydrophobic particle powder contamination on nanoporous superhydrophobic surfaces. **a**) Schematic illustration of the self-cleaning process of hydrophobic particle powders (purple) by a water drop (gray) on a superhydrophobic surface (blue). Colors and texture were chosen to match the laser scanning confocal microscopy (LSCM) images. **b**) Photograph of a 10 µL water drop cleaning a nanoporous superhydrophobic surface contaminated with Oil Red dye particles (appear black). **c–e**) LSCM images after contaminating the nanoporous superhydrophobic surfaces (left) with powders of hydrophobic particles with diameters of 10–50 µm, 200 nm, and 80 nm (see Experimental Section 3.3.11 and Figure 36 for details of image processing). Efficient cleaning of all hydrophobic powders was verified by LSCM (center) and scanning electron microscopy (SEM, right). Scale bars: 200 nm (SEM). **f,g**) Contact and roll-off angles using 6 µL water drops after self-cleaning of a nanoporous surface consecutively contaminated with hydrophobic particle powders.

In order to mimic common hydrophobic contamination sources, such as soot or dust, we applied hydrophobic particle powder to the nanoporous superhydrophobic surfaces (**Figure 31**a,b). After contaminating the surfaces with the particle powder, the surfaces were cleaned by rinsing with 20–50 water drops of 16 ± 1 µL. These drops rolled off the inclined surfaces and took away the particles. We found that hydrophobic powder contaminants (purple) could be effectively removed from the superhydrophobic surfaces (blue) as verified by LSCM (**Figure 31**c–e, Figure S2 in Appendix 10.1). SEM analysis con-

firmed the results. Hardly any contamination could be found within or on top of the coating for all particle sizes (**Figure 31**c–e, Figure S3 for more details of the sample contaminated with 80 nm particles). The excellent self-cleaning is corroborated by low roll-off (<2°) and high contact angles (>150°; **Figure 31**f,g).

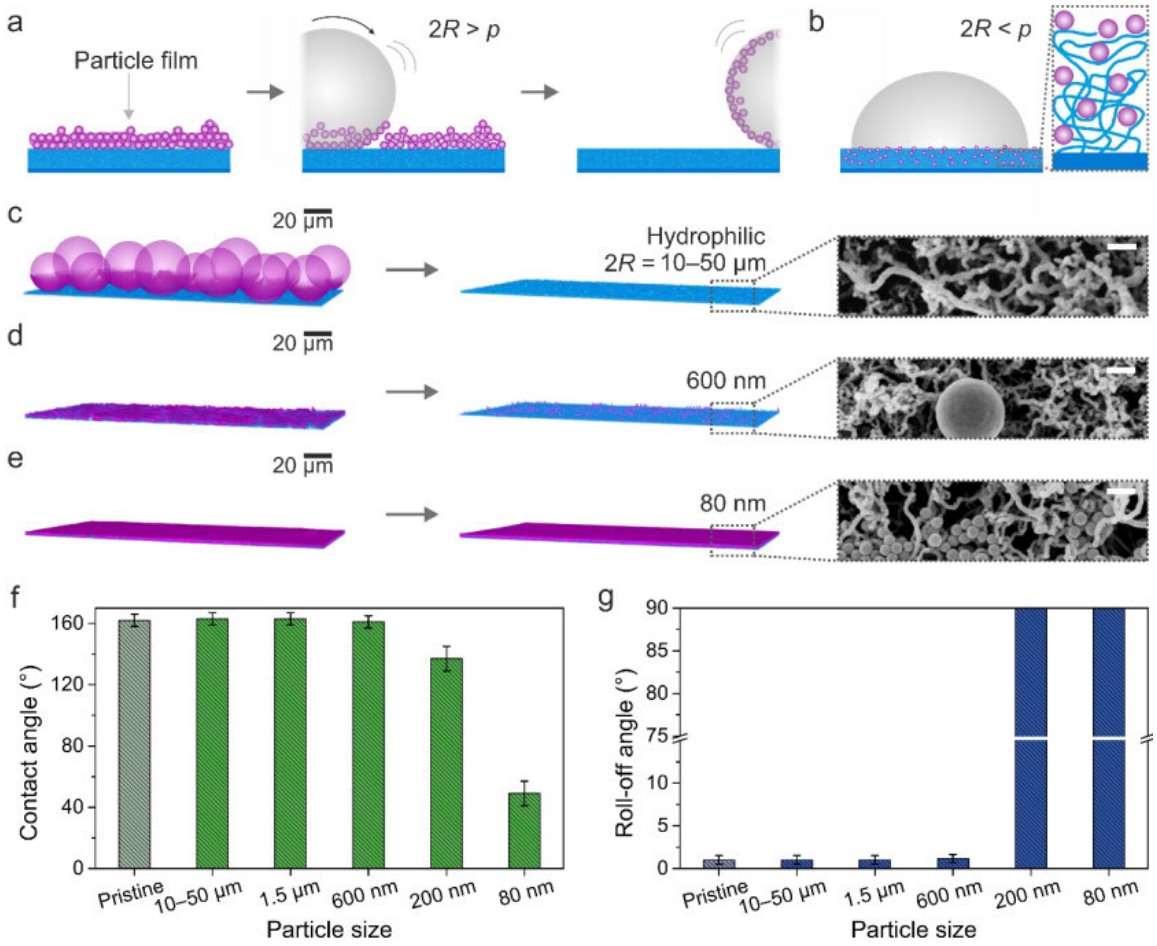

Figure 32. Effect of hydrophilic particle contamination having various particle sizes deposited from ethanol dispersion on nanoporous superhydrophobic surfaces. **a**) Schematic illustration of the self-cleaning process of hydrophilic particles (purple; $2R > p$) deposited from ethanol dispersion by a water drop (gray). **b**) Particles of smaller diameter than the pore diameter ($2R < p$) can penetrate the coating (blue), affecting wetting properties. **c–e**) LSCM images (left) after contamination of the superhydrophobic surfaces with hydrophilic particles with diameters of 10–50 µm, 600 nm, and 80 nm (see Experimental Section 3.3.11 and Figure 36 for details of image processing). LSCM (center) and SEM images (right) show the surfaces after rinsing. Scale bars: 200 nm (SEM). **f,g**) Contact and roll-off angles using 6 µL water drops after self-cleaning of nanoporous surfaces contaminated with various hydrophilic particles (dried from ethanol dispersion).

Even after five consecutive contamination steps by particles of all different sizes followed by subsequent self-cleaning, the roll-off angles remained at 1° ± 1° and the static contact angle at 161° ± 4°. Thus, even nanoscopic hydrophobic particle powders did not affect the superhydrophobicity of the nanofilament-coated surfaces.

Particulates such as water-soluble organic carbon (WSOC) are hydrophilic, can disperse in water, and can thus stick much better to surfaces.[151, 242-243] To investigate the most severe case of contamination, we applied hydrophilic particles dispersed in ethanol to the nanoporous surfaces (**Figure 32**). Fifty microliters of the particle dispersions with a concentration of ≈10 g L^{-1} were cast onto the surfaces by a pipette. The dispersion wetted the surface and finally completely dried out on the surface. Here, three cases of particle sizes can be distinguished:

i) The particle diameter $2R$ is larger than the pore diameter p (with $p < 2R$), and the particles cannot enter the coating (**Figure 32**a). The 10–50 µm and 1.5 µm particles (**Figure 32**c, Figure S4 in Appendix 10.1) fall in this category. In this case, the first water drop was able to remove most of the contamination. After the contaminants were removed, the contact angles stayed above 150°, and the roll-off angles remained below 2° (**Figure 32**f,g).

ii) The particle diameter is similar in size to the largest pores ($p \approx 2R$). The 600 nm particles were slightly above the largest pore diameter of the nanoporous coating but in a similar size range. Even in this case, for thin contamination layers (1–2 loose particles layers), most particles could be removed. We only found some rarely distributed particles and particle aggregates using LSCM and SEM (**Figure 32**d, Figure S5 in Appendix 10.1). These remaining particles did not change the wetting properties (**Figure 32**f,g). Only in the case of a thick aggregated contamination layer, the self-cleaning of the surface failed. In particular, areas of up to 10 µm thick contamination were found on the edge of the contamination spot because of the coffee stain effect during drying.[244] On the coffee stain ring of the dried sample, the droplets stuck to the surface, and the roll-off angle increased to 90°.

iii) The particle diameter is smaller than the pore size ($p > 2R$), and the particles can enter the coating (**Figure 32**b). Here, the 80 and 200 nm particles could enter and dry out within the pores (**Figure 32**e, Figure S7 in Appendix 10.1 for details). Even after rinsing, strong fluorescence of the nanoparticles could be observed within the coating (**Figure 32**e, Figure S4 in Appendix 10.1). Indeed, hydrophilic 80 and 200 nm particles led to the failure of superhydrophobicity. The contact angles decreased to ≈140° and ≈40° for the 200 and 80 nm particles, respectively, and the roll-off angles increased above 90° for both (**Figure 32**f,g).

In contrast to the 80 and 200 nm hydrophobic particle powders, which were littered over the surface, the hydrophilic counterpart particles were applied from a dispersion. To examine whether the way how we applied the particles to the surfaces caused the superior

performance of the hydrophobic particles, we performed an additional experiment. We applied the 80 and 200 nm hydrophobic particles from dispersion in *n*-hexane. Now, the roll-off angles of 6 µL water drops slightly increased to 8° ± 6° and 20° ± 15° for the 200 and 80 nm particles, respectively. The large scatter of the roll-off angles indicates large local differences in particle contaminations.

Our experiments reveal that nanoporous superhydrophobic surfaces can withstand most scenarios of particle contamination. Only hydrophilic and, to a certain extent, hydrophobic particles smaller than the pore size that are dispersed in a liquid capable of wetting the surface could lead to a failure of self-cleaning. Therefore, to design superhydrophobic surfaces that are resistant to hydrophilic and hydrophobic particle contamination, the pore size needs to be below the lowest expected particle size ($p < 2R$).

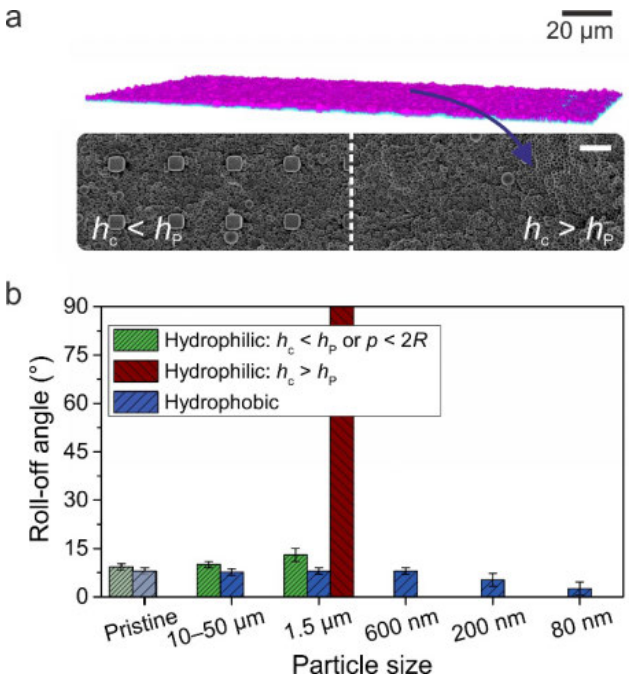

Figure 33. Contamination and self-cleaning of superhydrophobic microstructured SU-8 pillars (rectangular, 10 µm height with 5 × 5 µm² top areas; center-center distance of pillars: 20 µm). **a**) LSCM (top) and SEM (bottom) images showing a surface contaminated with 1.5 µm particles. On the left side of the SEM image, the micropillar array is only partially filled with particles ($h_c < h_P$), whereas on the right, the particles completely covered the microstructure ($h_c > h_P$). Scale bar: 10 µm (SEM). **b**) Roll-off angles of 6 µL water drops after contamination of the micropillar array with hydrophilic and hydrophobic particles of various sizes and subsequent self-cleaning.

Many superhydrophobic surfaces rely on microstructures.[37] As a model, we investigated microstructured superhydrophobic surfaces that were made from SU-8 micropillars (rectangular, 10 µm height with 5 × 5 µm² top areas; center-center distance of pillars: 20 µm) on glass slides using photolithography. The SU-8 micropillar surfaces were fluorinated

and showed a static contact angle of 154° ± 4° and roll-off angles of 9–10° for 6 µL water drops. The superhydrophobic microstructured surfaces were exposed to hydrophilic 10–50 µm and 1.5 µm particles dispersed in ethanol (**Figure 33** and Figure S10a–c). We found that water drops could easily remove the 10–50 µm particles. The 1.5 µm particles were stuck between the micropillars since $p > 2R$ (**Figure 33**a). However, whether this causes degradation of the surface depends on the filling height of the contaminants h_c compared to the pillar's height h_P. If the particles only partially fill up the space between the pillars ($h_c < h_P$), the superhydrophobicity will remain intact (**Figure 33**b) because the drop only rests on the top faces of the pillars (Figure S10d,e). If the coating is filled up or covered with particles ($h_c \geq h_P$), superhydrophobicity will break down. This emphasizes the need for a small pore size to prevent small particles from penetrating the coating. Interestingly, exposing a surface to hydrophobic particle powders led to decreasing roll-off angles with each contamination step (**Figure 33**b). The reason is that residual particles of the powders remained on the surface, especially on the pillars' top faces (Figure S11 in Appendix 10.1). These particles add a second scale of roughness to the surface and thus yield a hierarchical nano/microstructured surface. Therefore, nanoscopic hydrophobic contamination can even reduce the roll-off angles of the coating.

However, while the ability to withstand various kinds of contamination is essential, the ease of self-cleaning is equally crucial. How are individual particles removed from the surfaces by single drops, and how large are the involved forces? To image the pickup process of particles, we modified a confocal microscope with a stage holding a needle. This setup allowed us to move drops over the surfaces during imaging. We investigated the self-cleaning process of hydrophilic 10–50 µm particles deposited on a nanoporous superhydrophobic surface using 10 µL drops (**Figure 34**a and Movie S1; particle fluorescence: purple; drop fluorescence: navy blue; reflections: light blue). Confocal microscopy enabled us to measure the local contact angle on the surface of the micrometer-sized particles (**Figure 34**b,c). When the drop was moved over the contaminated surface, individual particles were picked up at the advancing contact line (**Figure 34**a, top). Upon further movement of the drop, these particles accumulated at the lower air-water interface of the drop (**Figure 34**a, center). The drop rested on these hydrophilic particles. The air-water-particle contact lines were pinned at the lower side of the hydrophilic particles and showed contact angles of $\theta \approx 40°–50°$ (**Figure 34**b). At the receding side, the drop lifted the particles from the surface, yielding a layer of particles on the droplet, and a so-called liquid

marble formed (**Figure 34**a, bottom).[185, 197] The same behavior was observed for hydrophobic 10–50 µm particles (**Figure 34**c and Movie S2). However, the hydrophobic particles exhibited contact angles of $\theta \approx 90°–100°$, and the water drop rested on the top half of the particles. The experiments with both hydrophilic and hydrophobic particles clearly showed an air gap underneath the drop. The gap distance H can be calculated using $H = R(1 - cos\theta)$. For a sufficient number of large particles of $R \approx 20$ µm and a contact angle of 100°, we calculated $H \approx 24$ µm. This value is in good agreement with the confocal image (**Figure 34**c). Smaller-sized particles were picked up similarly; however, the gap cannot be resolved by LSCM (Movie S3).

To remove particles from a superhydrophobic surface, the capillary force F_C acting on the particle at the rear side of the drop needs to overcome the adhesion force between the particle and the surface, F_{Adh}. When the drop recedes and starts pulling on a particle that is adhering to the substrate at the bottom and to the air-water interface at the top side, the interface is deforming and a meniscus forms (**Figure 34**d). The meniscus acts as a spring with spring constant k[230, 245-246]

$$k \approx \frac{2\pi\gamma}{0.81 - \ln(R/l_C)} \tag{24}$$

and pulls on the particle with a capillary force $F_C = k\delta$. Here, δ is the deformation of the surface of the drop in normal direction, γ is the surface tension of water, R is the radius of the particle, and $l_C = \sqrt{\gamma/g\rho} = 2.7$ mm is the capillary length of water. The capillary force pulls on the particle until the adhesion force between the substrate and the particle is overcome, that is for $F_C \geq F_{Adh}$. The adhesion force between a flat surface and a spherical particle can be estimated by the Johnson-Kendall-Roberts (JKR) theory:[247]

$$F_{Adh} \approx \frac{3}{2}\pi R\varphi\Delta\gamma \tag{25}$$

Here, $\Delta\gamma$ is the work of adhesion between the hydrophobic substrate and the particle surface (see Experimental Section 3.3.15). We estimate it to be in the order of $\Delta\gamma = 0.11$ N m^{-1}. To take into account that superhydrophobic surfaces are rough, and roughness greatly reduces the effective contact area between the particle and the surface, we added φ, which is the surface fraction in contact with the particle surface as compared with the apparent contact area. From SEM images, we estimate it to be $\varphi \approx 0.2$. The work to pick up a single particle W_s is given by the deformation δ of the air-water meniscus before the adhesion force is overcome (**Figure 34**d):

$$W_s = \frac{1}{2}k\delta^2 = \frac{1}{2}k\frac{F_{Adh}^2}{k^2} = \frac{F_{Adh}^2}{2k} \tag{26}$$

When the drops move a distance Δx horizontally on the superhydrophobic surface, the work required is $\Delta W = wnW_s\Delta x$, accordingly. Here, n is the number of particles per unit area, and w is the width of the apparent contact area of the drop. Now we can estimate the amount of the lateral adhesion force from:

$$F_L = \frac{\Delta W}{\Delta x} = wnW_s = \frac{wnF_{Adh}^2}{2k} \tag{27}$$

We estimate the particle density to be approximately 0.1 R^{-2}. Thus we can estimate the lateral force caused by the removal of particles from a surface:

$$F_L \approx w\frac{1}{10R^2}\frac{1}{2k}\left[\frac{3}{2}\pi R\varphi\Delta\gamma\right]^2 = 1.1\frac{w\varphi^2\Delta\gamma^2}{k} \tag{28}$$

Here, we further neglected lateral interactions between particles and assumed that each particle is detached independently from its neighbor. With $w \approx 0.5$ mm and $k = 0.082$ N m^{-1} for $R = 25$ µm, the lateral adhesion force is $F_L \approx 3$ µN (see Experimental Section 3.3.15 for a more detailed discussion). This force can be compared to the force measured by our custom-built droplet adhesion force instrument (DAFI).[77] Here, a capillary drags a liquid drop over a surface (**Figure 34**e), and the lateral adhesion force is measured using a force sensor (see Chapter 2 and Experimental Section 3.3 for details). The force required to pick up a thin contamination layer (<50 µm) of hydrophilic particles using a 10 µL water drop ranged from 2 µN to 5 µN (**Figure 34**f). Thus, the estimated values agree well with the experimental results. This agreement indicates that the model captures the essential process. Note that the lateral friction force only slightly exceeded the friction force on the pristine substrate (≈1 µN). The static lateral adhesion force is overcome when a drop starts rolling off a surface: $F_L = F_g = mg\,sin\alpha$. Here, $m = 10$ mg is the mass of the water drop and α is the roll-off angle. The friction force on slightly contaminated surfaces remained below 5 µN, corresponding to a roll-off angle ≤ 3°. These low roll-off angles demonstrate that the surfaces can be easily cleaned. The drops roll off the contaminated surface and simultaneously clean it.

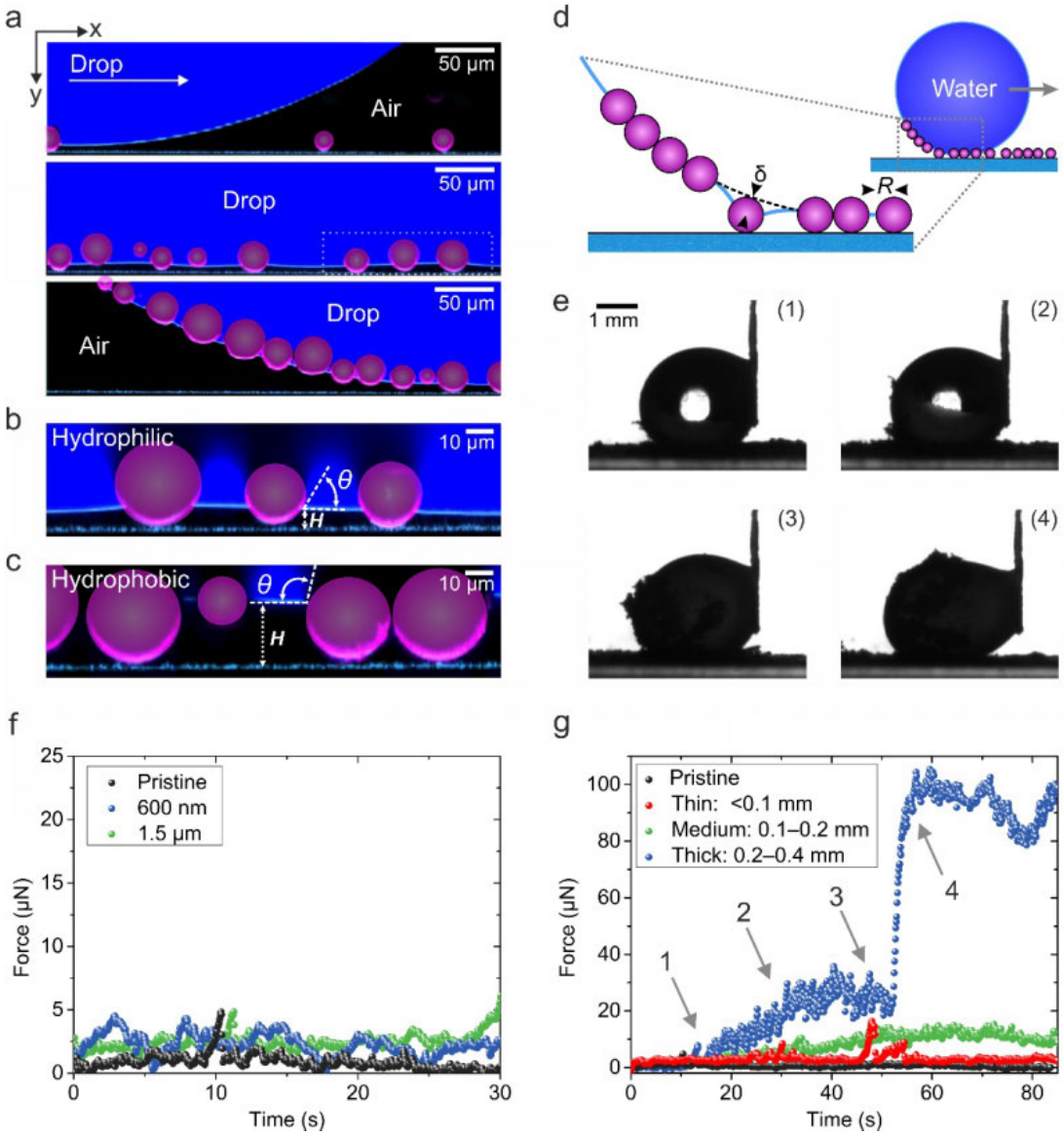

Figure 34. Illustration of the self-cleaning of a contaminated superhydrophobic surface using confocal microscopy and friction force measurements. **a**) A 10 µL water drop (dyed with ATTO 488, navy blue) is dragged over a nanoporous superhydrophobic surface contaminated with 10–50 µm hydrophilic particles (purple). The interface between the drop and the surface is monitored by LSCM. Particle contamination is completely taken along by the water drop (see Experimental Section 3.3.11 and Figure 36 for details of image processing). **b**,**c**) High magnification LSCM images showing the contact angle θ of the hydrophilic and hydrophobic particles in contact with water. Smaller particles lost contact with the solid surface. **d**) Sketch of the pickup process of particles. The deformed meniscus pulls on the particle. **e**) Macroscopic observation of a 10 µL drop being dragged over a surface heavily contaminated with hydrophilic 10–50 µm particles. **f**) Force required to clean a surface contaminated with hydrophilic 1.5 µm and 600 nm particles. The drop is moved at a velocity of v = 250 µm s^{-1}. **g**) Effect of the thickness of the contamination layer (<0.1 mm, 0.1–0.2 mm, and 0.2–0.4 mm) for hydrophilic 10–50 µm particles on the force required to clean the surface. For strongly contaminated surfaces (0.2–0.4 mm contamination layer), a continuous increase in the force during the self-cleaning can be observed (1 and 2). Upon complete coverage of the drop's surface with particles (between 3 and 4), a sudden increase in force can be observed. Drop velocity: v = 250 µm s^{-1}.

Whereas a thin layer of hydrophilic 10–50 µm particles (1–2 layers of particles, **Figure 34**g, thin) can easily be removed from the surface, the force increased with an increasing contamination layer thickness (≈3–6 layers of particles, **Figure 34**g, medium). For a thick contamination layer (≈8–12 layers), the force increased sharply to 100 µN at $t = 50$ s (**Figure 34**g, thick).

This increase corresponds to a travel distance of $s = v\,t = 1.3$ cm, for a drop velocity of $v = 250$ µm s^{-1}. Within this distance, the drop performed approximately 1.5 revolutions, as $2\pi R_{\mathrm{Drop}} \approx 0.8$ cm. After this distance, the drop is surrounded by a layer of particles and particle aggregates, as verified by video microscopy (**Figure 34**e). The particles rapidly leave the contact area, trying to provide a homogeneous coverage of the surface. This proceeds until no more particles can be taken up and leads to interfacial jamming. As soon as the drop is covered by a layer of particles, a liquid marble is formed. After that, the particle-loaded drop rolls over particles. This is associated with a force of 100 µN, which is 10 to 20 times higher than the lateral adhesion force for a drop only partially coated with particles (roll-off angle > 90°). Thus, thick contamination layers may not be cleaned with a single drop. Consequently, the drop size needs to be increased, or several drops are required to clean the surface.

To compare the results based on model contamination to real-world outdoor exposure, we fixed several coated fabrics on a car. These so-termed superomniphobic fabrics repelled water and organic liquids and were chosen because of their robustness.[113, 116] They were obtained by coating polyester fabrics with the same nanostructured coating consisting of silicone nanofilaments. Fluorination renders the superhydrophobic fabrics superomniphobic (**Figure 35**a,b). Various liquids like water, coffee, wine, and hexadecane showed high receding contact angles and typically rolled off below 10°. The fabrics on the car were exposed to the atmosphere of the Rhineland-Palatine area in Germany for 257 days within a period of 426 days, covering all seasons and exposure to high UV radiation, rain, frost, and icing (temperatures ranged between -10 °C and 32 °C, and humidities ranged between 40% and 100%; Table S1 summarizes the temperatures, humidities, and rainfall during the exposure periods). This also included daily driving at velocities of 60 km h^{-1} and maximal velocities on the highway of up to 140 km h^{-1}. During this period, the owner drove more than 5000 km. The car was parked outside, i.e., not in a garage. The experiment started beginning of October 2016. The fabrics were fixed at the front window (A-pillar), side mirror, rear side window, and back window of the car (**Figure 35**c and Figure S12 in Appendix 10.1).

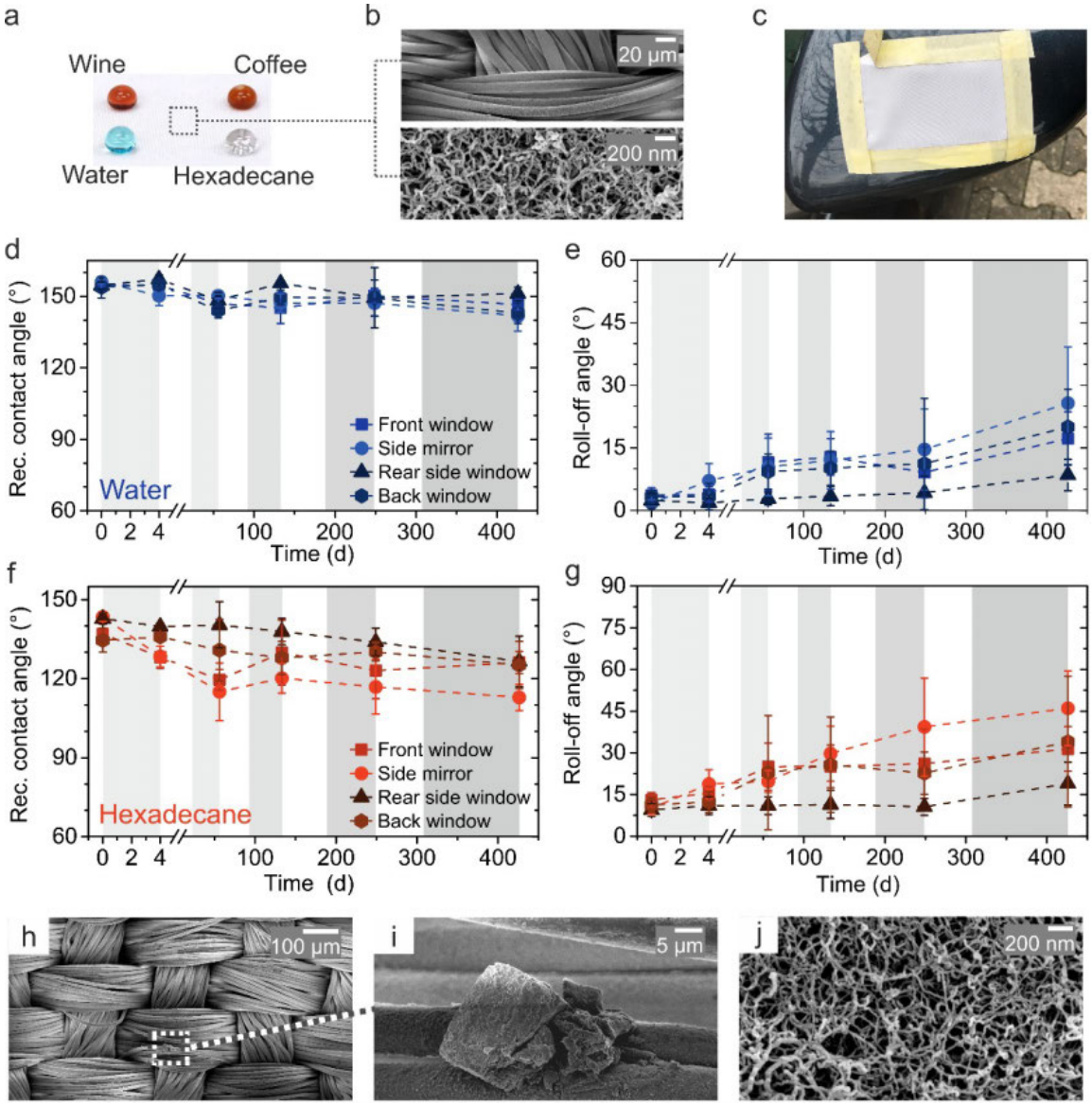

Figure 35. Real-world contamination test through outdoor exposure of superomniphobic fabrics fixed on a car for 257 days. **a**) Photograph of 20 µL drops of water (stained with methylene blue), coffee, wine, and hexadecane on a superomniphobic fabric. **b**) SEM images of a coated superomniphobic polyester fabric at different magnifications. **c**) Superomniphobic fabric fixed on the side mirror of the car. The fabric remained white even after 257 days of outdoor exposure. **d**,**e**) Receding contact angles and roll-off angles of 5 µL water drops in the course of the outdoor exposure of 257 days within a period of 426 days. Periods of outdoor exposure are marked in gray. **f**,**g**) Receding contact angles and roll-off angles of 5 µL hexadecane drops in the course of the outdoor exposure. Periods of outdoor exposure are marked in gray. **h**) SEM image of a superomniphobic fabric after 257 days of outdoor exposure. **i**) Higher magnification SEM image of a dirt particle on a superomniphobic fabric. **j**) High magnification SEM image of the nanofilaments on a superomniphobic fabric after 257 days of outdoor exposure.

Superomniphobic fabrics with slightly different wetting properties were used to account for variances in the fabrication of the surfaces. Therefore, we observed roll-off angles for water and hexadecane ranging between 2° and 4° and between 9° and 13° for 5 µL water

and hexadecane drops, respectively (**Figure 35**d–g). Roll-off and receding contact angles were measured after 4, 38, 79, 139, and 257 days of outdoor exposure. In between these days, the superomniphobic fabrics were removed, and the measurements were conducted. Even after 257 days of exposure, the roll-off angles stayed below 25° and 50° for water and hexadecane, respectively. The superomniphobic fabric fixed at the front of the side mirror experienced the most wear and contamination under the impact of insects and dirt. SEM analysis of the fabrics taken after 426 days without any further rinsing or cleaning showed only sparse particle contamination (in the 10 μm range) (**Figure 35**h,i). No nanocontamination between the nanofilaments could be detected (**Figure 35**j). Likely, contamination was removed by morning dew or rain. For example, particles can dissolve in the water or stick to the air-water interface and roll off as soon as the dew drop can overcome the lateral adhesion force. Furthermore, the release of surface energy after coalescence of neighboring dew drops can cause merged drops to jump off the surface,[248] taking particles along. Additionally, rain periods contribute to the self-cleaning of the surfaces. Likely, the major part of the reduction in repellency properties was due to mechanical damages (Figure S13).

The results of the tests mentioned above were further supplemented by an industrial dirt pickup simulation test for paints and coatings from Evonik Resource Efficiency GmbH (Figure S14 in Appendix 10.1). Here, superomniphobic fabrics and benchmarks were exposed to a dirt treatment inside an industrial dishwasher. The dirt simulation process and dirt mixture are adapted from a method described in European patent application EP1302765. Afterward, the surfaces were cleaned in a washing step by spraying distilled water. The whole procedure lasted 3 h, which effectively corresponds to 18 months of outdoor exposure. Finally, the change in whiteness ΔL was measured. The superomniphobic fabrics retained their whiteness, showing only a minor change of $\Delta L = 8 \pm 1$ (Figure S14c in Appendix 10.1). In comparison, an untreated fabric showed $\Delta L = 59$, and benchmark surfaces ranged between 30 and 40.

Due to the small pore size of the nanofilament coating, the superomniphobic fabrics could withstand severe environmental and industrial contamination tests and remain mostly intact after prolonged periods of exposure. This demonstrates that well-designed superhydrophobic and superomniphobic surfaces can resist real contamination scenarios.

3.3 EXPERIMENTAL SECTION

3.3.1 MATERIALS

Experiments were carried out at room temperature. The following chemicals were used: trichloromethylsilane (TCMS, 99%, Sigma-Aldrich), 1*H*,1*H*,2*H*,2*H*-perfluorodecyltrichlorosilane (PFDTS, 96%, Alfa Aesar), tetraethoxysilane (TEOS, 98%, Sigma-Aldrich), octyltrichlorosilane (97%, Sigma-Aldrich), (3-amino-propyl)triethoxysilane (98%, Sigma-Aldrich), iron(II) sulfate heptahydrate (>99%, Sigma-Aldrich), styrene (99%, Acros Organics, stabilized), acrylic acid (99.5%, Acros Organics), ammonium persulfate (98%, Acros Organics), sodium chloride (99.8%, Riedel-de Haën), sodium hydroxide (98%, Sigma-Aldrich), ammonia (25%, VWR Chemicals), hydrogen peroxide (35 wt%, VWR Chemicals), SU-8 3010 photoresist (MicroChem), mr-Dev 600 developer (micro resist technology), *n*-hexane (99.99%, Fisher Chemical), toluene (99.99%, Fisher Chemical), m-xylene (98%, Sigma-Aldrich), isopropanol (99.5%, Fisher Chemical), ethanol (absolute, 99.96%, VWR Chemicals), hexadecane (99%, Sigma-Aldrich), methylene blue (>82%, Sigma-Aldrich), rhodamine B isothiocyanate (mixed isomers, Sigma-Aldrich), Nile red (Sigma-Aldrich), and ATTO488 (ATTO-TEC). Reagents were used as received. Wine and coffee were purchased from the local supermarket. Polyester fabrics (76 g m^{-2}, weave "Crêpe de chine") were obtained from Karstadt. Glass beads (10–50μm) were obtained from Duke Scientific Corp. Glass slides of 24 × 60 mm^2 and a thickness of 150 ± 5 μm were obtained from Menzel-Gläser. Purified Milli-Q water from Sartorius Arium Pro VF was used for all experiments.

3.3.2 PREPARATION OF THE SUPERHYDROPHOBIC NANOPOROUS GLASS SLIDES

The nanoporous superhydrophobic glass slides were prepared as previously reported.[116, 118, 233] Typically, glass slides were plasma-cleaned and activated in an oxygen plasma chamber (Diener Electronic Femto, 120 W, 5 min, 6 cm^3 min^{-1} oxygen flow rate). TCMS was mixed with toluene having a water content of 180 ± 10 ppm (400 μL TCMS per 100 mL toluene). The water content was evaluated using a Karl Fischer coulometer (Mettler Toledo C20 Compact KF coulometer). The solution was stirred for 60 s. Afterward, the activated glass slides were immersed in the solution, and the reaction chamber was sealed. After 6 h, the TCMS-coated glass slides were rinsed with *n*-hexane and dried under a nitrogen stream. To modify the TCMS-coated glass slides with PFDTS, they were activated in an oxygen plasma chamber (Diener Electronic Femto, 120 W, 2 min,

7 cm^3 min^{-1} oxygen flow rate). Subsequently, 50 µL of PFDTS was mixed with 100 mL of *n*-hexane. The activated substrates were immersed in the solution for 20 min, rinsed with *n*-hexane, and dried under a nitrogen stream. Details on the synthesis of silicone nanofilaments can be found elsewhere.[112, 115, 120, 127]

3.3.3 PREPARATION OF THE SUPEROMNIPHOBIC FABRICS

The superomniphobic fabrics were prepared as previously reported (see also Chapter 4).[116] Polyester fabrics were cleaned by ultrasonication in ethanol. The dried polyester fabrics were coated with nanofilaments by adding 1400 µL of TCMS to a reaction chamber containing 350 mL of toluene with a water content of 150–160 ppm. The water content was evaluated using a Karl Fischer coulometer (Mettler Toledo C20 Compact KF coulometer). The solution was stirred for 60 s. Afterward, fabrics were immersed in the solution, and the reaction chamber was sealed. After 3 h, the TCMS-coated fabrics were rinsed with *n*-hexane and dried under a nitrogen stream. To modify the TCMS-coated fabrics with PFDTS, they were activated in an oxygen plasma chamber (Diener Electronic Femto, 120 W, 2 min, 7 cm^3 min^{-1} oxygen flow rate). Subsequently, 180 µL of PFDTS was mixed with 350 mL of *n*-hexane. The activated substrates were immersed in the solution for 20 min, rinsed with *n*-hexane, and dried under a nitrogen stream.

3.3.4 PREPARATION OF THE SUPERHYDROPHOBIC SU-8 MICROPILLARS

SU-8 micropillar arrays were prepared on glass slides by photolithography as previously reported.[62, 77] The rectangular pillars were designed 10 µm high with 5 × 5 $µm^2$ top areas. The pillar–pillar distance between the centers of two adjacent pillars in a row was 20 µm. Details are described in Experimental Section 2.3.4. The SU-8 micropillars were activated in an oxygen plasma chamber (Diener Electronic Femto, 30 W, 2 min, 6 cm^3 min^{-1} oxygen flow rate). Subsequently, PFDTS was mixed with *n*-hexane (50 µL PFDTS per 100 mL *n*-hexane). The activated SU-8 micropillar-coated glass slides were immersed in the solution, and the reaction chamber was sealed. After 20 min, the fluorinated pillars were rinsed with *n*-hexane and dried under a nitrogen stream.

3.3.5 SYNTHESIS OF A FLUORESCENT SILICA SHELL ON 10–50 µM GLASS PARTICLES

M. D'Acunzi coated the particles according to the procedure described in her dissertation,[249] which is based on the procedure reported by Verhaegh *et al.*[250] Glass beads (2 g; 10–50 µm) were washed and activated using the Fenton reagents.[118, 251-252] The beads were dispersed in a solution prepared by slowly dissolving (*caution!*) iron sulfate heptahydrate

(2 g) in 35 wt% hydrogen peroxide solution (20 mL). After 1 h, the particles were washed 3 times with water and 3 times with ethanol. Finally, they were dispersed in ethanol (80 mL), and reagents were added in this order: ammonia (6.4 mL), APS-RITC (0.17 mL; rhodamine B isothiocyanate coupled to (3-aminopropyl)triethoxysilane, see ref.[249-250])), and TEOS (0.480 mL). The mixture was kept under stirring for 24 h and then washed 3 times with ethanol. The particle size was analyzed by scanning electron microscopy (SEM).

3.3.6 SYNTHESIS OF FLUORESCENT SILICA PARTICLES

Fluorescent silica particles with diameters of 80 nm and 200 nm were synthesized by the same experimental procedure (Experimental Section 3.3.5). The size was tuned by varying the amount of ammonia in the reaction mixture. Ethanol (160 mL) and ammonia (9.6 mL for 80 nm particles and 12.8 mL for 200 nm particles) were homogeneously mixed, and APS-RITC (0.34 mL) was added. After 1 min under stirring, TEOS (0.96 mL) was supplied. The mixture was kept under stirring for 24 h at 500 rpm. The particle suspension was washed 4 times with ethanol. The particle size was analyzed by SEM.

3.3.7 SYNTHESIS OF 1.5 µM POLYSTYRENE-SILICA CORE-SHELL PARTICLES WITH POLYSTYRENE CORE DYED WITH NILE RED

M. D'Acunzi prepared the polystyrene particles according to the procedure described in her dissertation,[249] which is based on the procedure reported by Zhang *et al.*[253]: "Polystyrene cores (PS) were synthesized by soap-free emulsion polymerization. Before starting the synthesis, the inhibitor was removed from the styrene by washing with 3 aliquots of 2 M sodium hydroxide solution and 3 aliquots of water. The washed styrene was distilled under reduced pressure before use. A 2000 mL three-necked flask was equipped with a condenser, a PTFE stirrer, and a gas inlet. Water (1000 mL) was put in the reactor, and nitrogen was bubbled for 20 min. Ammonium persulfate (0.37 g) and sodium chloride (0.66 g) were dissolved in 10 mL water and put into the flask. After that, styrene (50 mL) and acrylic acid (0.66 mL) were added. The system was closed, and the mixture was heated to 75 °C under stirring at 350 rpm. After 1 day, the heating was turned off, and the mixture was cooled down to room temperature; particles were cleaned by at least 6 centrifugation steps with water and ethanol.

The polystyrene particles were dyed using the method described by Schaertl *et al.*[254] It is based on the preparation of a double-phase system formed by particles dispersed in water

and Nile Red dissolved in xylene. Dye and xylene molecules diffuse through the water medium into the polystyrene particles. A solution of Nile Red (0.6 mg) in m-xylene (0.6 mL) was added to a dispersion of PS particles (1 g) in water (22 mL) and left under stirring for 1 day. After that time, the particles were swollen with xylene and dye. Xylene was removed by applying vacuum for 2 days. The particles were washed several times with water and ethanol and finally dispersed in ethanol (50 mL). A silica shell was grown on the particles by adding ammonia (4.2 mL) and TEOS (1 mL) and leaving the system under stirring for 1 day." The particle size was analyzed by SEM.

3.3.8 HYDROPHOBIZATION OF THE PARTICLES

The hydrophilic particles were dried and then suspended in 50 mL *n*-hexane. Afterward, 50 µL of octyltrichlorosilane was added, the mixture was sonicated for 60 s, and stirred at 250 rpm for 45 min. Then, the hydrophobized particles were washed with *n*-hexane for 3 times and dispersed in *n*-hexane.

3.3.9 CONTAMINATION EXPERIMENTS

To contaminate the superhydrophobic surfaces with hydrophobic particle powders, ≈10 mg of the dried particle powder was distributed on an area of ≈1 cm^2. To contaminate the superhydrophobic surfaces with hydrophilic particles, 50–100 µL of 10 g L^{-1} dispersions of the particles in ethanol was slowly pipetted onto the surface. The dispersion was dried under ambient atmosphere at room temperature. Afterward, the contamination was cleaned by placing 20–50 water drops (16 ± 1 µL) on the inclined surface. The first few drops (<10) removed the most visible contamination. However, to ensure that all contamination that can be cleaned by water drops was removed, an excess number of drops was used.

3.3.10 LASER SCANNING CONFOCAL MICROSCOPY

Laser scanning confocal microscopy (LSCM) images were taken using an inverted confocal microscope (Leica TCS SP8 SMD, HCX PL APO 40x/0.85 CORR CS dry objective) using the Leica LAS X software. The surfaces were contaminated, as described in Experimental Section 3.3.9. LSCM images were taken before and after cleaning. For the visualization of the self-cleaning process, 10 µL water drops (dyed with ATTO 488, 1 mg L^{-1}) were placed onto sparsely contaminated superhydrophobic nanoporous glass slides. The drops were slowly dragged over the surface using a metal needle (0.26 mm outer diameter, 31G) attached on a stage similar to the droplet adhesion force measurements. The self-cleaning

process was recorded using the LSCM. The fluorescence of ATTO488 in water and the fluorescence of the dyed particles is shown in navy blue and pink, respectively. The reflection of light is shown in light blue. Reflection and fluorescence signals were recorded simultaneously.

3.3.11 PROCESSING OF LSCM IMAGES

The laser scanning confocal images in **Figure 34** were processed according to the procedure illustrated in **Figure 36**. For the creation of the three-dimensional (3D) LSCM images, Leica LAS X (3D viewer) software was used. Intensities of the reflection and fluorescence channels were adjusted for best clarity. In **Figure 31**c and **Figure 32**c, particle illustrations were added as described in **Figure 36**a,b.

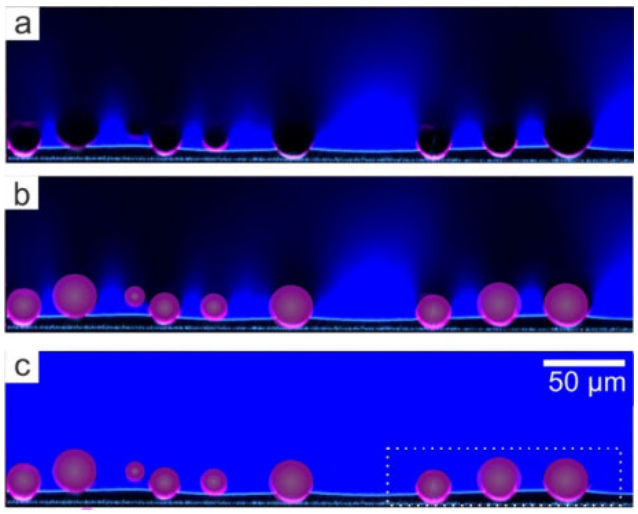

Figure 36. Processing of the LSCM images. **a**) Original image. Due to strong absorption and scattering of light, the upper part of the particle, as well as the fluorescence of the aqueous solution above, is not visible (black holes). **b**) Particle illustrations are added based on the positions of the reflection and fluorescence at the lower side of the particles. **c**) The missing fluorescence intensity above the particles, scale bars, and highlights are added to complement the image.

3.3.12 DROPLET ADHESION FORCE INSTRUMENT EXPERIMENTS

Droplet adhesion force experiments were conducted with a custom-built setup similar to that in Chapter 2.[77] A glass capillary was coupled to a force sensor (FTS-1000, FemtoTools; instead of the laser and PSD in Chapter 2). The sensor had a resolution in the range of a single micronewton and a time resolution of 1 kHz. To measure the lateral adhesion force, a drop was deposited on a substrate, and the drop was approached using the glass capillary. The substrate movement was realized using a linear stage with a customized stepper motor and gear set. The measurements were conducted at a speed of 250 µm s^{-1}.

3.3.13 SCANNING ELECTRON MICROSCOPY

Scanning electron microscopy (SEM) images were taken with a Zeiss LEO 1530 Gemini SEM at gun voltages of 3 kV using the in-lens detector. To avoid charging, samples were sputtered with Pt before measurement using a BalTec MED 020 modular high vacuum coating system (with an argon pressure of 2×10^{-5} bar and a current of 30 mA, 7 nm Pt).

3.3.14 CONTACT ANGLE MEASUREMENTS

Static contact angles were measured using a DataPhysics OCA35 contact angle goniometer. Six microliter drops were deposited onto the substrate. The measurement was repeated in three different spots per substrate. The error of the static contact angle measurements was estimated to be between ±4° and ±8° depending on the substrate.

For advancing and receding contact angles, 6 µL drops were deposited on the surface. Afterward, 20 µL of the liquid was added to and removed from the drop. The measurement was consecutively repeated three times at the same spot and at three different spots per substrate. The error of the advancing and receding contact angle measurements was estimated to be ±4°.

Roll-off angles were measured using the DataPhysics OCA35 contact angle goniometer. Therefore, 6 µL drops (6 µL for nanofilament-coated glass slides and 5 µL for nanofilament-coated fabrics) were deposited on the substrates, and the measuring plate was tilted until the drops rolled off. The roll-off angle was determined in at least 6 different spots per substrate, and mean roll-off angles and corresponding standard deviations were calculated.

3.3.15 ESTIMATION OF LATERAL ADHESION FORCE OF A PARTICLE-COVERED SUBSTRATE

This section describes the estimation of the force required to roll a drop over a layer of spherical particles of radius R on a superhydrophobic surface. The apparent contact area between the drop and the surface is supposed to have a width w. The density of particles on the substrate n (in number per unit area) is supposed to be lower than a full monolayer but large enough to support the drop and keep it from touching the substrate. We neglect forces between neighboring particles. When the drop moves a distance x in lateral direction particles attached to the air-water interface are lifted because the apparent contact angles are high (**Figure 34**).

The work required to move the drop a distance x is:

$$W = w \cdot x \cdot n \cdot W_s \tag{29}$$

Here, W_s is the work required to detach a single particle from the substrate. The lateral force required to move the drop is:

$$F_L = \frac{dW}{dx} = w \cdot n \cdot W_s \tag{30}$$

To obtain W_s, we consider an individual particle in contact with the substrate and being attached to the air-water interface. When the drop moves, the particle at some point will find itself at the receding side. From the perspective of the particle, the air-water interface mainly moves upwards. It starts pulling on the particle. When pulling on a particle sticking at a liquid-air interface in the normal direction, the air-water interface deforms. The force increases linearly with the distance the particle is moved out of equilibrium.[255-258] The air-water interface acts as a spring with spring constant k:[230, 245-246]

$$k = \frac{2\pi\gamma}{0.8091 - \ln(R/l_C)} \tag{31}$$

Here, $l_C = \sqrt{\gamma/g\rho}$ is the capillary length. For water, it is 2.7 mm. Since the radius of curvature of the drop is much larger than the particle size, the interface can be described by a spring with spring constant k. With $R = 25$ µm we get $k = 0.0082$ N m^{-1}.

The capillary force pulls on the particle until the adhesion force between substrate and particle is overcome. The adhesion force F_{Adh} between a flat surface and a spherical particle is given, e.g., by the JKR theory:[247]

$$F_{Adh} = \frac{3}{2}\pi R\varphi(\gamma_S + \gamma_P - \gamma_{SP}) \tag{32}$$

Here, γ_S is the surface energy of the substrate, γ_P is the surface energy of the particle, and γ_{SP} is the interfacial energy between the two solids. Neglecting γ_{SP} and taking the surface energy of the fluorinated surface to be 10 mN m^{-1} and that of the hydrophilic oxide to be 100 mN m^{-1} we estimate $(\gamma_S + \gamma_P - \gamma_{SP}) = 110$ mN m^{-1}. Since the actual contact area is reduced on a superhydrophobic surface, we insert a factor φ. φ is the ratio of the actual to the apparent contact area of the particle. For the nanofilaments used in the experiment shown in **Figure 34**, we estimate $\varphi = 0.2$ from SEM images. With $R = 25$ µm, we get 2.6 µN. Capillary forces can usually overcome the adhesion forces. The capillary force can reach

$F_{c,max} = 2\pi R\gamma \cos^2 \frac{\theta}{2}$, where θ is the contact angle the particle forms with the air-water interface. If the actually applied force exceeds this value, the liquid will fully dewet the particle, and the capillary forces vanish. The air-water interface pulls on the particle until the particle detaches from the substrate. The deformation of the air-water interface at this point is $\delta = F_{Adh}/k$. The work required to reach that point is:

$$W_s = \frac{1}{2}k\delta^2 = \frac{kF_{Adh}^2}{2k^2} = \frac{F_{Adh}^2}{2k} \tag{33}$$

To estimate n in our experiments, we assume that the large particles dominate. Their packing will not exceed the close random packing density of $0.82/(\pi R^2)$.[259] In our case, we estimate that the particle density is roughly a factor 2 lower. Thus, we take $n = 1/(10R^2)$. Putting everything together for an estimate and taking a typical width of $w \approx 0.5$ mm for 10 µL-sized water drops, we obtain:

$$F_L = wnW_s = \frac{wF_{Adh}^2}{20kR^2} = \frac{0.0005\ \text{m} \cdot (2.6 \times 10^{-6}\text{N})^2\ \text{m}}{20 \cdot 0.082\ \text{N} \cdot 6.25 \times 10^{-10}\ \text{m}^2} \approx 3\ \mu\text{N} \tag{34}$$

3.4 AUTHOR CONTRIBUTIONS

F. Geyer fabricated the surfaces, carried out the experiments and characterization, unless stated otherwise below, and wrote the manuscript. M. D'Acunzi prepared the nano- and microparticles. A. Saal, F. Geyer, and N. Gao carried out the lateral adhesion force experiments. A. Sharifi-Aghili fabricated and characterized the superomniphobic fabrics for the outdoor exposure experiments. A. Kaltbeitzel assisted the laser scanning confocal measurements. T.-F. Sloot was responsible for the dirt dishwasher experiments. H.-J. Butt and D. Vollmer devised the theoretical calculation of the lateral adhesion force. F. Geyer, D. Vollmer, R. Berger, and H.-J. Butt contributed to experimental planning, data analysis, and manuscript preparation. All authors reviewed and approved the manuscript.

3.5 ACKNOWLEDGMENTS

D. Vollmer kindly provided her car for the outdoor experiments. We thank [redacted] for carefully reading the manuscript. We thank [redacted] for technical support. This work was supported by the ERC Advanced Grant No. 340391 "SUPRO" (H.-J.B., D.V., F.G.), the German Research Foundation (DFG) with the Collaborative Research Center 1194 (H.-J.B., F.G.), the European Union's Horizon 2020 research and innovation program LubISS No. 722497 (D.V.).

4 ENHANCING CARBON DIOXIDE CAPTURE USING ROBUST SUPEROMNIPHOBIC MEMBRANES

Florian Geyer,[1] Clarissa Schönecker,[1] Hans-Jürgen Butt,[1] and Doris Vollmer[1]

[1]Max Planck Institute for Polymer Research, Ackermannweg 10, 55128 Mainz, Germany

Abstract: Superomniphobic membranes for post-combustion CO_2 capture are introduced. Concentrated aqueous amine solutions stay on the topmost part of the membranes, providing a large liquid-CO_2 interface. Wetting of the membrane, which reduces the capture efficiency, is prevented. The CO_2 capture rates using the chemically, mechanically, and thermally stable superomniphobic membranes are enhanced by up to 40% relative to commercial membranes.

Keywords: wetting, superhydrophobic, superoleophobic, CO_2 capture, membrane

This chapter is reprinted with permission from F. Geyer *et al., Adv. Mater.* **2017**, *29*, 1603524.

The Supporting Information is available from Wiley Online Library:
https://doi.org/10.1002/adma.201603524

4.1 INTRODUCTION

The atmospheric concentration of CO_2 has increased substantially in recent decades.[178, 260] This increase results from both natural and anthropogenic emissions. Major anthropogenic sources of CO_2 include cement production, the iron and steel industry, gas flaring, and combustion of fossil fuels. Slowing global warming requires a substantial reduction of CO_2 emission. However, according to the recent report "Global Carbon Budget," the world pumped 39.8 billion tons of CO_2 into the air in 2014.[261] Despite urgent warnings about the necessity to curb greenhouse gases, this is a 2.3% *increase* in CO_2 release compared to 2013. The search for alternative or improved methods to reduce CO_2 emission and to capture and store released CO_2 has stimulated intense research in academia and industry.[170, 262-264]

Today so-called absorbers are used in power plants for post-combustion capture of CO_2. In an absorber, an aqueous alkanolamine solution flows downward while flue gas streams upward.[177-178] The tertiary alkanolamine *N*-methyl diethanolamine (MDEA), often promoted by piperazine,[265] shows one of the best combinations of high loading capacity, low volatility, and good thermal stability. For further processing or storage, CO_2 is released by heating the alkanolamine solution to above 100 °C.[266] To keep the thermal energy required for releasing the captured CO_2 low, the alkanolamine concentration should be as high as possible. This increases the overall CO_2 capacity of the capture medium. However, the loading ratio α_{Load}, which is the amount of bound CO_2 molecules per amine molecule, decreases at concentrations above 20 wt%. Beyond ≈50 wt%, the loading ratio becomes so low that the overall capacity decreases by adding more MDEA.[267] Therefore, alkanolamine concentrations between 20 and 50 wt% are most commonly used depending on the specific requirements.

As an alternative to absorbers, we focus on CO_2 capture using gas contactor membranes.[171, 173] Here, a porous membrane spatially separates the gas and liquid streams. The flue gas is pumped across one side of the membrane and the capturing solution across the other. Advantages are its modular, easily-scalable nature[173-174] and compactness facilitating process intensification.[268-271] In addition, liquid and gas flow rates can be independently tuned and controlled. Even at high flow rates, dragging of drops from the capturing media into the CO_2 stream is reduced as the liquid and gas phase are separated by the membrane.[173-174] However, three challenges need to be addressed before this technology can be implemented on an industrial scale:[173, 176] *i) Wetting of membrane pores.* Wetting of the membrane pores greatly lowers the membrane performance as gas diffusion

is greatly reduced in the almost stagnant liquid. *ii) Long-term stability*. Most membrane materials show an insufficient chemical resistance to the alkaline capturing solution, typically accompanied by poor mechanical and thermal stability resulting in a breakdown of the membrane and thus a complete failure. *iii) Clogging*. Often, particles or other components present in the flue gas cause clogging of the pores. Thus, mass transfer is reduced accordingly.

To reduce wetting of the pores, the membrane material needs to be hydrophobic.[13] The most common materials are polypropylene (PP), polyvinylidene fluoride (PVDF), and polytetrafluoroethylene (PTFE).[173-174] Progress has been reported using superhydrophobic membranes, such as polypropylene,[272] fluorinated PDMS/PVDF,[273], or fluorinated ceramic membranes.[274] However, alkanolamine solutions have a low surface tension and wet superhydrophobic surfaces. To circumvent wetting, the gas flow can be increased,[274] causing gas bubbles to form in the capturing medium. However, this leads to foaming, transfer of particulate matter and gaseous impurities into the amine solution.[173] Therefore, the main challenge is to find membranes that repel concentrated amine solutions. These membranes must also show good chemical stability as amine solutions are strongly basic and thus highly corrosive.

Highly liquid-repellent membranes — so-called superomniphobic membranes — may be the key to overcoming the limitations of conventional gas contactor membranes. Superomniphobicity requires that the surface is coated by overhanging hydrophobic nano- or micrometer-sized protrusions.[41, 82, 275] When placing an aqueous or non-aqueous drop on such a surface, the drop takes an almost spherical shape and rolls off when the surface is tilted by less than 10 degrees.[41, 82] On superomniphobic surfaces, the liquid does not wet the surface but stays on top of the overhangs, entrapping gas underneath. This results in a liquid-gas contact area close to 100%.[84, 87-88] The large liquid-gas contact area potentially translates into a high CO_2 capture rate. Here we show the potential of superomniphobic membranes for CO_2 capture. We present the first superomniphobic membranes that prevent wetting of membrane pores by highly concentrated alkanolamine solutions, despite being highly alkaline. Due to their superomniphobic nature, the membranes provide a large liquid-gas interface for efficient gas exchange.

4.2 RESULTS AND DISCUSSION

We fabricated chemically and mechanically robust superomniphobic flat-sheet membranes based on a polyester fabric (**Figure 37** and Figure S1 and S2, in the following, denoted as superomniphobic membrane or SOM). The 160 µm thick fabrics comprise interwoven networks of fibers with diameters between 8 and 15 µm (**Figure 37**a–c). To render the hydrophilic polyester fabrics superomniphobic, we first immersed the fabrics in toluene containing trichloromethylsilane and trace amounts of water (≈150 ppm). Trichloromethylsilane hydrolyzes and reacts with the hydroxy groups on the polyester surface, forming silicone nanofilaments (**Figure 37**d–f, Figure S3 summarizes the involved chemical reactions).[67, 112, 115, 120, 133] After a reaction time of 3 h, the fibers were surrounded by a 1–2 µm thick layer of silicone nanofilaments with a diameter of 20–80 nm (**Figure 37**f).

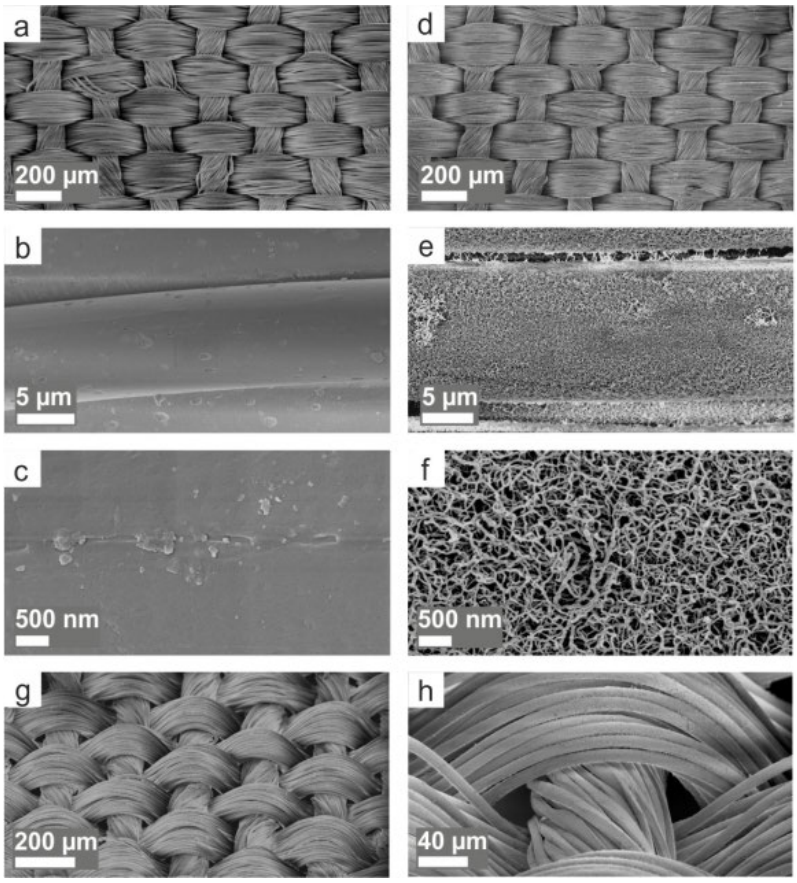

Figure 37. a–f) Morphology of the superomniphobic membrane. Scanning electron microscopy (SEM) images of bare (a–c) and coated (d–f) polyester fabrics at different magnifications. **f**) Higher magnification SEM image of the coated polyester shows the nanofilaments on a polyester fiber. **g,h**) SEM images, taken under an angle of 45°, reveal the micrometer-sized pores of the superomniphobic membrane. The pore size ranges from less than 1 µm between single fibers up to 80 µm between bundles of fibers.

To achieve superomniphobicity, the fabrics were activated in an oxygen plasma and modified with 1*H*,1*H*,2*H*,2*H*-perfluorodecyltrichlorosilane to reduce the surface energy. The nanofilament coating introduces a surface roughness with overhang geometry on the polyester microfibers (**Figure 37**e,f). Nitrogen adsorption-desorption isotherms showed the appearance of meso- (2–50 nm) and macropores (>50 nm) after application of the coating

to the polyester fabric (Figure S4). The BET (Brunauer-Emmett-Teller) surface area increased from ≈0.2 m^2 g^{-1} for the bare fabric to 3.9 m^2 g^{-1} for the superomniphobic membrane. In addition to the pores introduced by the nanofilament coating, the superomniphobic membrane had micrometer-sized pores ranging from less than 1 µm between single polyester microfibers up to 80 µm between bundles of microfibers (**Figure** 37g,h and Figure S1). Mercury intrusion porosimetry measurements confirmed the presence of micrometer-sized pores (Figure S5, average pore diameter 70 µm; pores below 0.5 µm were not considered in the calculation). The coating did not change the overall morphology of the fabrics (compare **Figure 37**a,b to **Figure 37**d,e).

To investigate the difference between superhydrophobic and superomniphobic membranes for CO_2 capture, we also coated a commercial polypropylene membrane (avg. pore size 200 nm, porosity 75%, obtained from 3M) with nanofilaments (denoted as SHPP-200). As we did not fluorinate the nanofilaments, the membranes were solely superhydrophobic but not superomniphobic. Figure S6 shows SEM images of the superhydrophobic membrane. The wetting behavior of the membranes was tested using liquids of greatly different surface tension and polarity, including water, hexadecane, and concentrated MDEA solutions (**Figure 38** and Table S2). To quantify the wetting behavior of the membranes, we measured receding contact angles and roll-off angles, as the static contact angle depends on how a drop is deposited on a surface (see Experimental Section 4.4.5 for details, contact angles and contact angle hystereses are summarized in Table S2). The receding contact angle θ_{Rec} scales with the adhesion of the liquid to the substrate. The adhesion is high if the solution wets the membrane.[87] On the polyester fabrics coated with fluorinated silicone nanofilaments all liquids showed high receding contact angles (>150°) and low roll-off angles (<10°), demonstrating their superomniphobicity for liquids with surface tensions greater or equal to 27.5 mN m^{-1} (**Figure 38**d,e and Movie S1 and S2). Laser scanning confocal microscopy revealed that the nanofilament coating is not wetted by MDEA solutions (**Figure 38**c). This is proven by the extremely high contact angle (176°) and the *air*-cushion between the glass substrate and the MDEA (50 wt%) droplet (see Experimental Section 4.4.8 for further details). On the polypropylene membranes coated with nanofilaments (SHPP-200), water showed high receding contact angles (>150°), and water drops easily rolled off (<10°), demonstrating their superhydrophobicity. However, the super-liquid-repellency broke down for MDEA solutions (roll-off angle > 40°).

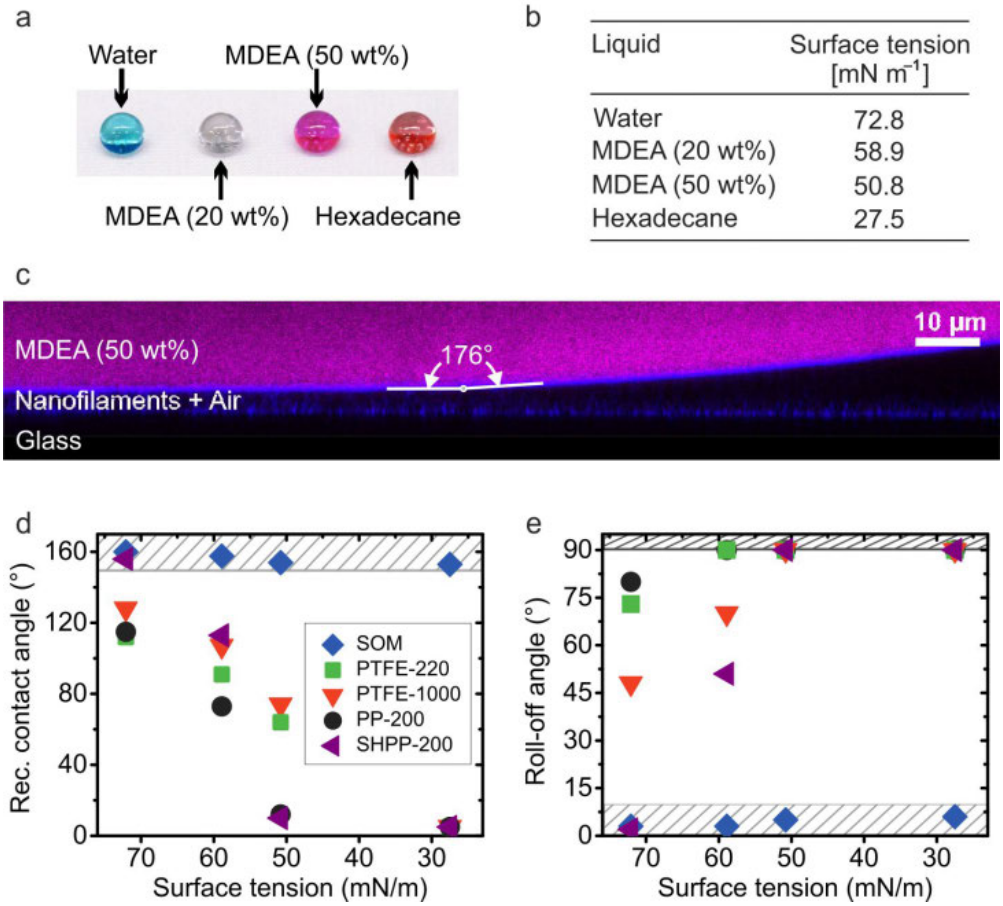

Figure 38. Wetting properties of the superomniphobic, superhydrophobic, and commercial membranes. **a**) Photograph of 15 µL drops of water (stained with methylene blue), aqueous MDEA solutions (20 wt%, colorless and 50 wt%, phenolphthalein) and hexadecane (oil red) on a superomniphobic membrane. **b**) Surface tensions of the investigated liquids. **c**) Laser scanning confocal microscope image of an MDEA solution (50 wt% with ATTO488 dye) drop on a nanofilament-coated superomniphobic glass slide. Reflections are shown in blue and fluorescence in pink. **d**) Receding contact angles for water, MDEA solutions (20 and 50 wt%), and hexadecane on the superomniphobic (blue), superhydrophobic (violet), and the commercial membranes (green, red, black). **e**) Roll-off angles for 6 µL water, MDEA solution (20 and 50 wt%), and hexadecane drops on the superomniphobic, superhydrophobic, and the commercial membranes. The color code is identical to d). For error bars, see Table S1 and Table S2.

In contrast, state-of-the-art commercial polypropylene membranes (avg. pore size 200 nm, porosity 75%, denoted as PP-200, obtained from 3M) and polytetrafluoroethylene membranes (avg. pore size 220 nm denoted as PTFE-220; avg. pore size 1 µm denoted as PTFE-1000, both 85% porosity, obtained from Merck Millipore) were wetted by the liquids (**Figure 38**d,e and Movie S3). This is reflected in the low receding contact angles (<110°) and high roll-off angles (>70°) for all liquids except water. Hexadecane immediately spread on the superhydrophobic and on all the commercial membranes (Movie S4). Figures S7–S9 show SEM images of the commercial membranes.

Uptake of CO_2 was quantified using a custom-made attenuated total reflection Fourier transform infrared (ATR-FTIR) spectrometer (**Figure 39**a). The ATR-FTIR spectrometer

had a built-in flow cell to monitor the CO_2 uptake in solution directly. To measure the CO_2 exchange performance, a membrane was inserted between the upper and lower parts of the exchange chamber and fixed in a holder (**Figure 39**b). The gas diffuses through the superomniphobic membrane, whereas the liquid flows over the topmost part of the fluorinated nanofilaments (**Figure 39**c). For capturing CO_2, a 20 wt% MDEA solution was used. A small part of the flow was split off and ran parallel to the main stream through the IR spectrometer (see Experimental Section 4.4.7 for details). We used a 20 wt% MDEA solution as it shows a high loading ratio and a 5× lower viscosity than a 50 wt% solution. The lower viscosity reduces the flow resistance.[276]

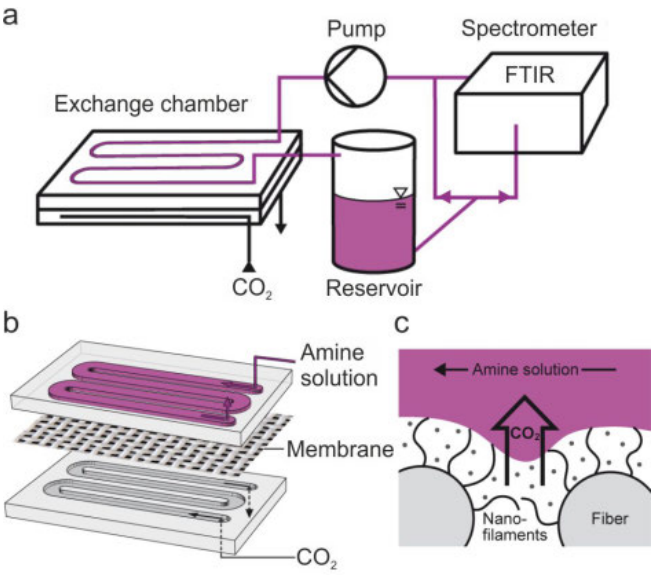

Figure 39. Setup for quantifying CO_2 uptake. **a**) Sketch illustrating the CO_2 exchange setup, including the ATR-FTIR spectrometer. **b**) Layout of the two halves of the exchange chamber showing inlets and outlets as well as flow channels for CO_2 and liquid flow. The superomniphobic membrane is placed in between. Flow velocity of MDEA solution: 2.7 cm s^{-1}. **c**) Schematic of polyester fibers coated with nanofilaments. CO_2 diffuses through the superomniphobic membrane into the MDEA solution.

CO_2 is captured in the form of bicarbonate by MDEA, according to $CO_2 + (CH_3)(CH_2CH_2OH)_2N + H_2O \rightarrow (CH_3)(CH_2CH_2OH)_2NH^+ + HCO_3^-$. Formation of bicarbonate bands was observed in the IR spectra, e.g., at 1302 cm^{-1} (HCO_3^- scissoring) (**Figure 40**a). The peaks at 1026 cm^{-1}, 1076 cm^{-1}, 1360 cm^{-1}, and 1643 cm^{-1} correspond to MDEA, $MDEAH^+$, HCO_3^- and OH stretching, respectively.[277] The height of the bicarbonate band (α) scales with the concentration of CO_2 in solution. Initially, the CO_2 absorption increases almost linearly with time (**Figure 40**b). After 180 min, the increase in CO_2 absorption slows down, indicating saturation of the solution with CO_2. Please note that the time to reach saturation depends on the interplay between the volume of the capture solution and the gas exchange area through the membrane. Here, it was chosen to enable a good time-resolution of the capturing process.

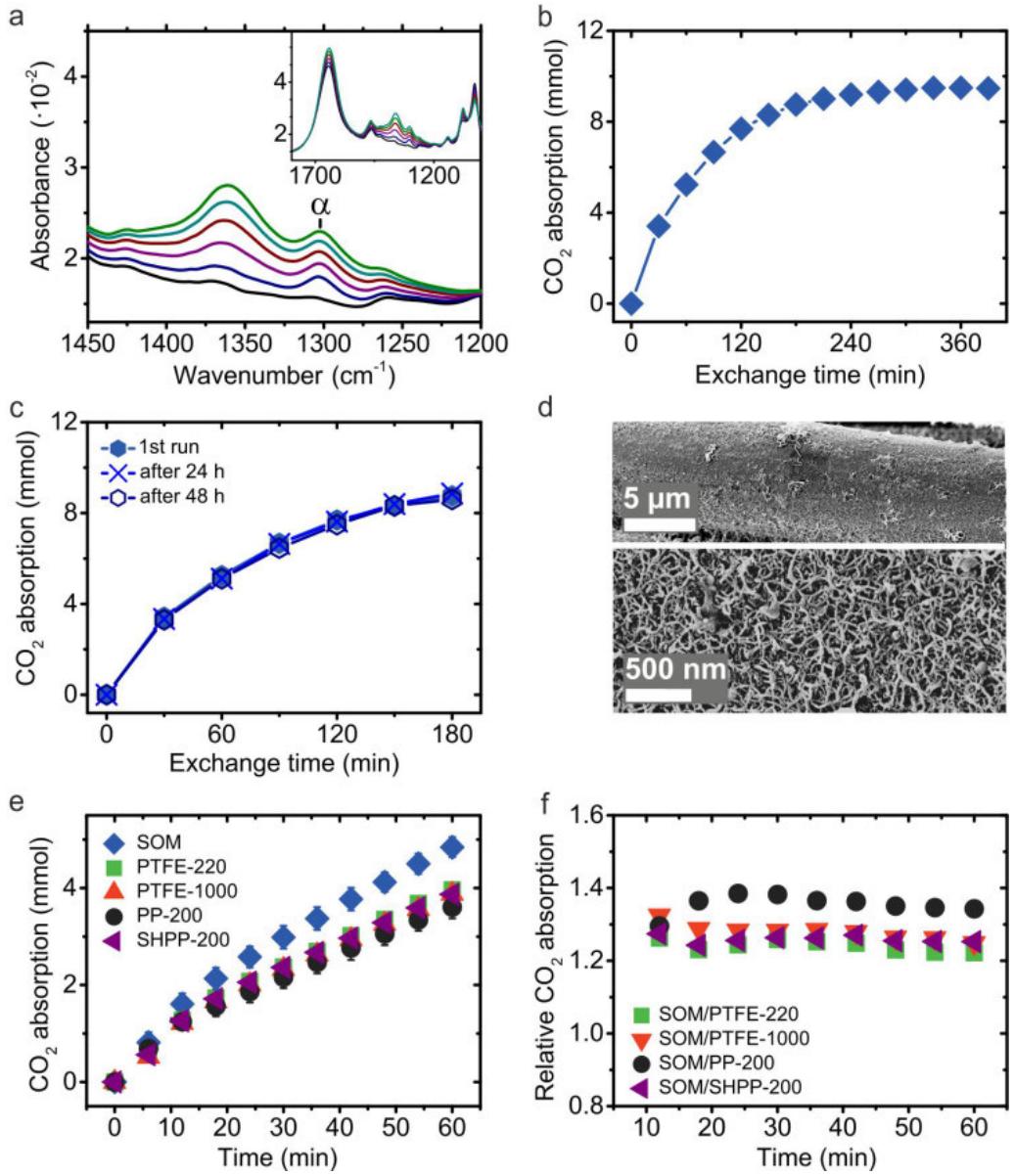

Figure 40. CO_2 absorption and exchange performance. **a**) Time-evolution of FTIR spectrum of MDEA solution (20 wt%) over 60 min gas exchange through a superomniphobic membrane. Colored graphs show the temporal changes of the spectrum in 12 min intervals (bottom to top). α denotes the bicarbonate band at 1302 cm^{-1}. **b**) CO_2 absorption over 390 min of gas exchange using a superomniphobic membrane. **c**) Long-term performance of the superomniphobic membrane. MDEA solution (20 wt%) was exchanged during operation after each 24 h. **d**) SEM images of the superomniphobic membrane after 50 h of gas exchange revealing hardly any damage. **e**) CO_2 absorption using the superomniphobic (blue), superhydrophobic (violet), and state-of-the-art commercial membranes (green, red, black) over 60 min of gas exchange. Data are each based on three independent measurements. **f**) Comparison of the CO_2 absorption performance of the superomniphobic membrane to the superhydrophobic and commercial membranes. See Figure S10 for error bars.

To investigate the long-term performance of the superomniphobic membranes, we replaced the MDEA solution during operation by fresh solutions after 24 h and again after 48 h. The CO_2 absorption rate was identical for all three runs (**Figure 40**c), thus even after 50 h of continuous operation, the membrane remained intact, and wetting of pores can

be excluded (**Figure 40**d). The CO_2 uptake via the superomniphobic membranes exceeded those of all tested state-of-the-art commercial as well as superhydrophobic membranes by up to 40% under identical conditions (**Figure 40**e,f). The average CO_2 gas flux during the first 30 min was ≈2.5 mmol m^{-2} s^{-1} (see Experimental Section 4.4.12 for details of the calculation). Notably, the large gas transfer rate is achieved solely via diffusion of CO_2 through the superomniphobic membrane. Even after 50 h of operation, we did not observe any gas bubbles in the capturing solution, i.e., foaming is not a problem (Movie S5). By applying a superhydrophobic coating, the performance of the PP-200 membrane increased. However, in comparison to the superomniphobic membranes, the superhydrophobic SHPP-200 membranes cannot avoid wetting by the MDEA solution. Thus the CO_2 uptake via the SOM was more than 20% higher.

To verify the chemical stability of the superomniphobic membranes, we exposed them to 50 wt% MDEA solutions for up to two weeks (**Figure 41**a and Figure S11). Even after 14 days, the membranes were not wetted. A plastron layer was still visible. With prolonged exposure time, the receding contact angles slightly decreased. Both hexadecane and MDEA (20 wt%) solution showed roll-off angles below 30°. Such low roll-off angles document the membranes' good chemical resistance toward amine solutions and the presence of air cushions. Exposure to the amine solution caused neither swelling nor deformation of the membranes. The slight reduction of the receding contact angles was caused by the amine solution attacking parts of the topmost area of the coating, leading to partial detachment of nanofilaments from polyester microfibers (Figure S12). On a nanofilament-coated glass slide, no detachment of nanofilaments was observed after 14 days of exposure to an MDEA (50 wt%) solution (Figure S13). Thus, the polyester or the bond of the filaments to the polyester fabric was possibly hydrolyzed (Figure S14 summarizes the possible degradation mechanisms). The superomniphobic membranes kept their super-liquid-repellency after being heated to temperatures up to 200 °C for 24 h, demonstrating their high thermal stability (**Figure 41**b and Figure S15). Thus, hot flue gas streams need not be cooled to room temperature. At higher temperatures, the polyester fabric starts melting. Superomniphobic membranes have another advantage compared to hydrophobic ones. The self-cleaning nature of superomniphobicity also reduces the problem of clogging of the membrane by particles (Movie S6). Moreover, the superomniphobic membrane showed a superior ultimate tensile strength, even though it had the lowest thickness (160 µm, see Experimental Section 4.4.11). All tensile specimens had a width of 4 mm.

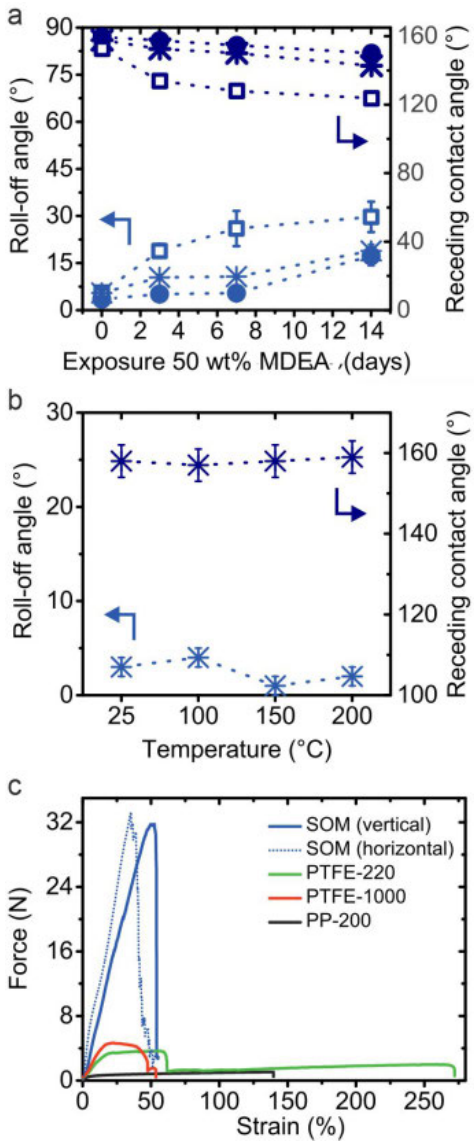

Figure 41. Chemical, mechanical, and thermal stability of the superomniphobic membrane. **a**) Receding contact angles and roll-off angles for 6 µL water (solid circles), MDEA (20 wt%) solution (stars), and hexadecane drops (open squares) on superomniphobic membranes that were exposed to MDEA (50 wt%) solutions for up to 14 days. **b**) Receding contact angles and roll-off angles for 6 µL drops of an MDEA (20 wt%) solution on superomniphobic membranes that were heated at the given temperatures for 24 h. **c**) Force-versus-strain curves. The force maxima denote the maximal strains the membranes can resist. The superomniphobic membrane was stressed in horizontal and vertical directions, showing the isotropy of the mechanical strength.

The rupture force was 6× higher than the supported PTFE membranes and 30× higher than the polypropylene membranes (**Figure 41**c). The stability of the PTFE membranes without the supporting mesh is even lower. The excellent mechanical stability of the superomniphobic membranes enables easy handling during operation. Even after we applied a load of 25 N on a tensile specimen, the contact angles remained unaltered. Also, the stability of the nanofilaments against high liquid flow velocities was investigated by exposing the superomniphobic membrane to a stream of tap water for 60 min at an inclination of ≈15° relative to the stream (Movie S7). The water jet had a flow velocity of ≈220 cm s^{-1}, which is 80× higher than the employed flow velocity for the gas exchange experiments. Nonetheless, after 60 min the SOM was still dry, and the receding contact angles and roll-off angles for an MDEA (20 wt%) solution remained identical ($\theta_{Rec} = 158° \pm 4°$,

roll-off angle = 4° ± 1°). SEM images confirmed that the nanofilaments did not detach (Figure S16).

4.3 CONCLUSION

In conclusion, preventing wetting of membrane pores by the capturing media is the key challenge for gas contactor membranes to achieve higher capture efficiency. Inspired by the super-liquid-repellent and self-cleaning properties of superomniphobic surfaces, one can devise superomniphobic membranes as novel gas contactor membrane material, as these can prevent wetting of the pores by the capturing solution. Simultaneously the large liquid-gas interface of the superomniphobic membranes ensures a high gas absorption flux. The fabricated superomniphobic membranes also keep their super-liquid-repellency for more than two weeks being exposed to 50 wt% MDEA solution and show excellent tensile strength. As aqueous alkanolamine solutions are strongly basic, the textured membrane has to be coated with a dense and chemically stable layer of fluorinated molecules to prevent decomposition of the underlying substrate. Keeping this in mind, cheap, flexible, and mechanical robust materials such as polyester fabrics can be transformed into robust superomniphobic gas contactor membranes. Furthermore, the self-cleaning properties of superomniphobic membranes reduce fouling of the membrane by particulate matter. Superomniphobic gas contractor membranes are not limited to CO_2 capture but may also be applied to scrubbing of other gases, for example, H_2S. The modular setup and compactness of gas contactor membranes render a downscaling of absorber chambers possible. This might also encourage capture of hazardous gases at processes releasing only smaller gas quantities.

4.4 EXPERIMENTAL SECTION

4.4.1 MATERIALS

If not stated otherwise, experiments were carried out at room temperature. The following chemicals were used: trichloromethylsilane (TCMS, 99%, Sigma-Aldrich), 1*H*,1*H*,2*H*,2*H*-perfluorodecyltrichlorosilane (PFDTS, 96%, Alfa Aesar), *n*-hexane (99,99%, Fisher Chemical), toluene (99,99%, Fisher Chemical), ethanol (99.8%, Sigma-Aldrich), *N*-methyl diethanolamine (99%, Sigma-Aldrich), ethylene glycol (99%, Sigma-Aldrich), hexadecane (99%, Sigma-Aldrich), methylene blue (>82%, Sigma-Aldrich), oil red (>75%,

Sigma-Aldrich), phenolphthalein (Sigma-Aldrich), ATTO488 (ATTO-TEC), carbon black (99.9%, Alfa Aesar). Reagents were used as received. Polyester fabrics (polyethylene terephthalate (PET), 76 g m^{-2}, weave "Crêpe de chine") were obtained from Karstadt. Polypropylene (PP) membranes (ACCUREL PP 2E HF, denoted as PP-200) with an average pore size of 200 nm were obtained from 3M. Polytetrafluoroethylene (PTFE) membranes (Fluoropore FGLP and FALP) with an average pore size of 220 nm (denoted as PTFE-220) and 1 µm (denoted as PTFE-1000) were obtained from Merck Millipore. Glass slides of 24 × 60 mm^2 and a thickness of 170 ± 5 µm were obtained von Menzel-Gläser. CO_2-gas bottle (99.99%) was obtained from Westfalen AG. Purified Milli-Q water from Sartorius Arium Pro VF was used for all experiments.

4.4.2 PREPARATION OF THE SUPEROMNIPHOBIC MEMBRANES

Polyester fabrics were cleaned by ultrasonication in ethanol. The dried polyester fabrics were coated with nanofilaments by adding 1400 µL of TCMS to a reaction chamber containing 350 mL of toluene with a water content of 150 ppm. The water content was evaluated using a Karl Fischer coulometer (Mettler Toledo C20 Compact KF coulometer). The solution was stirred for 60 s. Afterward, fabrics were immersed in the solution, and the reaction chamber was sealed. After 3 h, the TCMS-coated fabrics were rinsed with *n*-hexane and dried under a nitrogen stream. To modify the TCMS-coated fabrics with PFDTS, they were activated in an oxygen plasma chamber (Diener Electronic Femto, 120 W, 2 min, 7 cm^3 min^{-1} oxygen flow rate). Subsequently, 180 µL of PFDTS was mixed with 350 mL of *n*-hexane. The activated substrates were immersed in the solution for 20 min, rinsed with *n*-hexane, and dried under a nitrogen stream. Details on the synthesis of silicone nanofilaments can be found elsewhere.[112, 115, 127]

4.4.3 PREPARATION OF THE SUPERHYDROPHOBIC MEMBRANES

Polypropylene membranes (PP-200) were activated in an oxygen plasma chamber (Diener Electronic Femto, 30 W, 1 min, 7 cm^3 min^{-1} oxygen flow rate). The activated polypropylene membranes were coated with nanofilaments by adding 1400 µL of TCMS to a reaction chamber containing 350 mL of toluene with a water content of 180 ppm. The water content was evaluated using a Karl Fischer coulometer (Mettler Toledo C20 Compact KF coulometer). The solution was stirred for 60 s. Afterward, the membranes were immersed in the solution, and the reaction chamber was sealed. After 3 h, the TCMS-coated membranes were rinsed with *n*-hexane and dried under a nitrogen stream.

4.4.4 PREPARATION OF THE SUPEROMNIPHOBIC GLASS SLIDES

Silicone nanofilaments on glass slides were synthesized by modifying previously reported methods.[112, 115] The fabrication contained the following steps:[116, 118, 233] Glass slides were plasma-cleaned and activated in an oxygen plasma chamber (Diener Electronic Femto, 120 W, 5 min, 7 cm^3 min^{-1} oxygen flow rate). The activated glass slides were coated with nanofilaments by adding 250 µL of TCMS to a reaction chamber containing 350 mL of toluene with a water content of 125 ppm. The water content was evaluated using a Karl Fischer coulometer (Mettler Toledo C20 Compact KF coulometer). The solution was stirred for 60 s. Afterward, the glass slides were immersed in the solution, the reaction chamber was sealed, and stirring was continued (250 rpm). After 6 h, the TCMS-coated glass slides were rinsed with *n*-hexane and dried under a nitrogen stream. To coat glass slides with a thin nanofilament film (1–2 µm thickness) for the chemical stability test, the reaction time was reduced to 3 h without stirring, and a water concentration of 180 ppm was used. To modify the TCMS-coated glass slides with PFDTS, they were activated in an oxygen plasma chamber (Diener Electronic Femto, 120 W, 2 min, 7 cm^3 min^{-1} oxygen flow rate). Subsequently, 180 µL of PFDTS was mixed with 350 mL of *n*-hexane. The activated substrates were immersed in the solution for 20 min, rinsed with *n*-hexane, and dried under a nitrogen stream.

4.4.5 ADVANCING, RECEDING AND ROLL-OFF ANGLE MEASUREMENTS

Receding contact angles (θ_{Rec}) and roll-off angles were measured for different liquids in order to characterize the gas contactor membranes. The receding contact angle denotes the lowest contact angle during the receding of a drop. On a rough surface, the receding contact angle is defined as the apparent, macroscopic contact angle of the liquid observed during receding on a length scale much larger than the scale of the microstructures. In many cases, the static contact angle depends on how a drop is deposited on a surface and can adopt every value between the receding and advancing contact angle.[29, 61, 278-283] Furthermore, even a wetted surface can show a high static contact angle.[29, 284] The receding contact angle enables an accurate comparison between different membranes, as it depends on the adhesion of the liquid to the substrate.[7, 87] If the liquid penetrates in the pores, the adhesion is high, resulting in a pinned contact line and low θ_{Rec}. On superhydrophobic and superomniphobic surfaces, the advancing contact angle is close to 180°, as the advancing front needs to bend down to touch the next protrusion.[61, 283] Nonetheless,

advancing contact angles using a goniometer with a video camera were measured and summarized in Table S2. For transparent substrates, contact angles can be measured with much higher accuracy by laser scanning confocal microscopy (see **Figure 38**c).

Advancing and receding contact angles were measured using a DataPhysics OCA35 contact angle goniometer (Table S2). Initially, 6 µL drops were deposited on the membranes. Afterward, 20 µL of the liquid was added to and removed from the drop. The measurement was consecutively repeated three times at the same spot and at three different spots per membrane. The error of the advancing and receding contact angle measurements was estimated to be ±4° (or greater) depending on the liquid and the membrane.

For the superhydrophobic and commercial PTFE and PP membranes, the three-phase contact line of 20 wt% and 50 wt% aqueous MDEA solutions was strongly pinned. The contact line did not recede when removing 20 µL liquid. Especially the 50 wt% MDEA solution wetted these membranes. To determine the receding contact angle for the superhydrophobic, PP and PTFE membranes 20 µL MDEA solution was added to the initial 6 µL droplet, and then 24 µL was removed. The contact line started to recede during the removal of the last few microliter (Movie S3). For the superhydrophobic and PP-200 membranes and 50 wt% MDEA solution, 20 µL MDEA (50 wt%) solution was added to the initial 6 µL droplet, and then 25.5 µL was removed. The contact line only started moving when almost the whole liquid was removed, again resulting in a low receding contact angle for MDEA (50 wt%) solution. Hexadecane instantly spread on superhydrophobic and all commercial membranes and diffused through the membranes (Movie S4). Therefore, the receding contact angle could not be determined and was estimated to be below 5°.

Roll-off angles were measured using the same DataPhysics OCA35 contact angle goniometer (Table S2). Therefore, 6 µL drops were deposited on the membranes, and the measuring plate was tilted until the drops rolled off. The roll-off angle was determined at least at 6 different spots per membrane, and mean roll-off angles and deviations were calculated.

4.4.6 SURFACE TENSION MEASUREMENTS

Surface tensions of the aqueous MDEA solutions were determined with a DataPhysics DCAT11EC tensiometer using a cylindrical Wilhelmy plate (PT10, DataPhysics). Each sample was measured three times. Average surface tension and standard deviations were calculated.

4.4.7 CARBON DIOXIDE EXCHANGE EXPERIMENTS

The home-built setup (**Figure 39**a) consisted of an ATR-FTIR spectrometer (Bruker Vertex 70 with external chamber XSA), a glass reservoir for the amine solution, a pump (Ismatec REGLO Digital) and the home-built exchange chamber (**Figure 39**b). The individual parts were connected using flexible Tygon tubes (Ismatec Tygon MHSL 2001) with an inner diameter of 1.5 mm. The spectrometer had a home-made flow cell with a height of 100 µm (Hellma Analytics). A germanium ATR-IR crystal was used (Korth-Kristalle). The measuring chamber was continuously purged with nitrogen to minimize the water and carbon dioxide content in the chamber. To measure the CO_2 exchange, a membrane was put between the upper and lower part of the exchange chamber and fixed in a holder. The flow channels of the exchange chamber had a width of 2 mm and a height of 1 mm (**Figure 39**b). The reservoir was filled with 6 mL aqueous MDEA (20 wt%) solution, and the pump was started (flow rate: 3.2 mL min^{-1}, flow velocity: 2.7 cm s^{-1}). The flow was split up before passing the spectrometer as the built-in flow cell had a height of 100 µm. Due to the large flow resistance, a 50 wt% MDEA solution could not be pumped through the flow cell, viscosity at 20 °C: 11.7 mPa · s.[276] After the membrane was covered with the MDEA solution, the CO_2 stream (1.5 mL min^{-1}, 99.99%, Westfalen AG) valve was opened, and the FTIR measurement was started. FTIR-spectra were accumulated over a period of 30 s and averaged (≈120 spectra at a mirror frequency of 40 kHz) every 1.5 min until the measurement was stopped. The obtained spectra were analyzed using the Bruker OPUS 7.5 software. Therefore, the baseline of all spectra was corrected to take into account the drift of the baseline. The peak height/absorbance at 1302 cm^{-1} (bicarbonate band) was determined. The peak height was converted into the number of moles CO_2 absorbed, as described in Experimental Section *4.4.12 Estimation of CO_2 absorption and CO_2 absorption flux*.

4.4.8 SCANNING ELECTRON MICROSCOPY

Scanning electron microscopy (SEM) images were taken with a Zeiss LEO 1530 Gemini SEM at gun voltages of 1.5–3 kV using the in-lens detector. To avoid charging, samples were sputtered with 5 nm Pt before measurement using a BalTec MED 020 modular high vacuum coating system (with an argon pressure of 2×10^{-5} bar and a current of 60 mA).

4.4.9 PORE CHARACTERIZATION

The samples were dried at 70 °C in vacuo for 20 h. Nitrogen adsorption-desorption isotherms at 77 K were measured using a Quantachrome Autosorb-1. BJH (Barrett-Joyner-

Halenda) analysis was used to determine the pore size distribution.[285] BET (Brunauer–Emmett–Teller) analysis was used to determine the BET surface area.[286]
For the mercury intrusion porosimetry, the samples were dried at 70 °C for 19 h. Mercury intrusion porosimetry was measured using a Quantachrome Poremaster 60 GT. The Washburn equation was used to determine the pore size corresponding to the applied pressure. Gas pycnometry (in accordance with DIN 66137) using helium was measured using a Quantachrome Ultrapycnometer.

4.4.10 LASER SCANNING CONFOCAL MICROSCOPY

Laser scanning confocal microscopy (LSCM) images were taken using Leica LAS X software and an inverted confocal microscope (Leica TCS SP8 SMD, HCX PL APO 40x/0.85 CORR CS dry objective) with a resolution of about 0.3 and 1.0 μm in the horizontal and vertical direction, respectively. A superomniphobic glass slide was placed in the sample holder of the microscope, and an MDEA (50 wt%) droplet stained with ATTO488 dye was placed on the glass slide. The surface tension of the MDEA (50 wt%) drop did not change due to the addition of the dye (concentration: 1 mg L^{-1}). The fluorescence of ATTO488 in the MDEA solution is shown in pink, and the reflection of light from the air-MDEA solution interface is shown in blue. Reflection and emission signals were recorded simultaneously.

4.4.11 TENSILE STRENGTH MEASUREMENTS

Tensile specimens (4 mm width) were punched out of the superomniphobic and the commercial membranes. The thicknesses of the superomniphobic, the PTFE (220 nm and 1 µm avg. pore size) and the PP membranes were 160 µm, 220 µm, 200 µm, and 170 µm, respectively. The PTFE membranes had a high-density polyethylene supporting mesh at the backside. The tensile specimens were fixed in the holder of Zwick/Roell Z005 universal testing machine. A preload of 0.05 N was applied, and the samples were extended at 10 mm min^{-1} until rupture. Force-strain curves were recorded.

4.4.12 ESTIMATION OF CO_2 ABSORPTION AND CO_2 ABSORPTION FLUX

First, the CO_2 loading of a CO_2-saturated aqueous 20 wt% MDEA solution at 20 °C and standard pressure (1 atm) was determined by bubbling CO_2 in 3.385 g MDEA solution for 2.5 h. The mass increase caused by the uptake of CO_2 was Δm_{CO2} = +0.157 g. Since a small amount of the solution evaporates, the same experiment was repeated using N_2 instead of

CO_2; Δm_{N2} = -0.074 g. The decrease in mass caused by evaporation was added to the increase in mass due to CO_2 uptake, Δm_{total} = 0.231 g. Using the molecular weight of CO_2 (44.01 g mol^{-1}), we found that 5.25 mmol of CO_2 was absorbed by the MDEA solution. As a result, the loading of a CO_2-saturated MDEA (20 wt%) solution was $\alpha_{Load} \approx 0.93$ mol CO_2 per mol MDEA. This result is in good agreement with previously published data (α_{Load} = 0.786 for 20.5 wt% MDEA solution at 50 °C and 106 kPa CO_2 partial pressure,[267] α_{Load} = 0.866 for 23.4 wt% MDEA solution at 40 °C and 101 kPa CO_2 partial pressure,[33] higher temperatures decrease the loading capacity).[267, 287]

The average CO_2 absorption flux during the first 30 min of gas exchange (using a superomniphobic membrane) was estimated by measuring the peak height of the carbonate band at 1302 cm^{-1} after 30 min (average peak height based on three individual measurements). During the first 30 min, the peak height increased almost linearly. The saturation ratio was calculated by dividing the peak height after 30 min by the peak height at saturation: $S_r = 0.0051/0.0162 = 0.31$ (= 31%). Knowing the volume of the MDEA solution and the concentration (6 mL, density ρ = 1.0169 g cm^{-3} at 20 °C),[23] the number of moles of MDEA in the solution was calculated to be 10.2 mmol. Using the loading ratio ($\alpha_{Load} \approx$ 0.93 mol CO_2 per mol MDEA) of a saturated MDEA solution and S_r = 0.31, we found that 2.9 mmol of CO_2 were transferred through the membrane and absorbed by the solution during the first 30 min. Thus, over an exchange area of A = 6.36 cm^2 of our exchange chamber, the CO_2 absorption flux was calculated to be J = 2.5 mmol m^{-2} s^{-1} for the superomniphobic membrane.

4.5 AUTHOR CONTRIBUTIONS

F. Geyer fabricated the superomniphobic membranes, carried out the experiments, and wrote the manuscript. C. Schönecker and F. Geyer developed the setup for CO_2 quantification. F. Geyer, C. Schönecker, D. Vollmer, and H.-J. Butt contributed to experimental planning, data analysis, and manuscript preparation. All authors reviewed and approved the manuscript.

4.6 ACKNOWLEDGMENTS

We thank [redacted] for stimulating discussions, [redacted] for technical support and [redacted] for carefully reading the manuscript. We thank [redacted] for the graphical realization of Figure 39. We thank [redacted] for nitrogen isotherm measurements. This work was supported by the ERC advanced grant 340391-SUPRO and COST MP1106.

5 HOW TO COAT THE INSIDE OF NARROW AND LONG TUBES WITH A SUPER-LIQUID-REPELLENT LAYER — A Promising Candidate for Antibacterial Catheters

Florian Geyer,[1] Maria D'Acunzi,[1] Ching-Yu Yang,[1] Michael Müller,[1] Philipp Baumli,[1] Anke Kaltbeitzel,[1] Volker Mailänder,[1] Noemí Encinas,[1] Doris Vollmer,[1] and Hans-Jürgen Butt[1]

[1]Max Planck Institute for Polymer Research, Ackermannweg 10, 55128 Mainz, Germany

Abstract: Fouling of thin tubes is a major problem, leading to various infections and associated morbidities while cleaning is difficult or even impossible. Here, a generic method is introduced to activate and coat the inside of meter-long and, at the same time, thin (down to 1 mm) tubes with a super-liquid-repellent layer of nanofilaments, exhibiting even antibacterial properties. Activation is facilitated by pumping an oxidative Fenton solution through the tubes. Subsequent pumping of a silane solution renders the surface of the tubes super-liquid-repellent. The wide applicability of the method is demonstrated by coating stiff and flexible tubes made of polymers, inorganic/organic hybrids, metals, and ceramics. Coated medical catheters show excellent antibacterial properties. Notably, the nanofilaments retain their antibacterial properties even in the superhydrophilic state. These findings open new avenues toward the design of biocide-free, antibacterial tubings and catheters.

Keywords: wetting, superhydrophobic, superoleophobic, medical, anti-biofouling

This chapter is reprinted with permission from F. Geyer *et al., Adv. Mater.* **2019**, *31*, 1801324.

The Supporting Information is available from Wiley Online Library:
https://doi.org/10.1002/adma.201801324

5.1 INTRODUCTION

Pipes, tubes, capillaries, and hoses (in the following summarized as tubes) of different shapes and materials are essential for our daily life and numerous industrial processes. For example, thin tubes are used for food processing, water filtration[288], gas separation,[173] microfluidics[289], or as an insulating material. In medicine, the use of polymeric tubes is inevitable, for example, for infusions or catheters.[290] An ideal coating permits to tune the flow,[31, 289] the wetting properties,[1, 3-4, 291] and to suppress biofilm formation.[165-166, 292] As cleaning of thin tubes is challenging or even impossible, the development of improved coatings is a prominent issue. Some super-liquid-repellent layers can effectively reduce or delay biofilm formation, which is the irreversible attachment and proliferation of bacteria,[159-160, 162] thereby diminishing the risk of infection-related problems (failure and replacement of implants or devices, and even sepsis). Thus, a promising strategy might be to coat the inside of tubes with a super-liquid-repellent layer. Applying such a coating may suppress biofilm formation and thus save the lives of thousands of patients in hospitals and retirement homes through the reduction of pathogenic infections. Although several methods exist to coat an open surface with a super-liquid-repellent layer,[30, 82, 84, 293-294] to the best of our knowledge, no technique is described that allows coating the inside of meter-long and narrow medically relevant tubes (diameter down to 1 mm). Here, we introduce a generic method to overcome this challenge.

Characteristic for super-liquid-repellent coatings are their outstanding self-cleaning properties.[31, 145, 153] When placing drops of water or complex liquids like blood on such a surface, the drop takes an almost spherical shape and rolls off when the surface is tilted by less than 10°.[41, 82, 95] To render a surface super-liquid-repellent, it needs to be coated with nano- or micrometer-sized protrusions with overhanging morphology and low surface energy.[87, 295-297] Such topology generates an energy barrier for the liquid so that water drops rest on the protrusions entrapping air underneath. As a result of this so-called Cassie state,[27] the liquid is more in contact with air rather than with a solid, leading to high apparent contact angles.[28, 298] Current methods to generate superhydrophobic and super-liquid-repellent coatings on non-tubular substrates such as electrospinning,[82] lithography,[42] dip coating,[38] spin coating,[144] or spray coating[40, 299] are unsuitable for tubes having an inner diameter of only a few millimeters. Chemical etching methods of metal pipes, for example, copper,[102] can produce microroughness. Nonetheless, etching is limited to the respective metal, and metal tubes are rigid and prone to corrosion. Other techniques

require activation of the surface, a challenge for long and narrow polymeric tubes. Piranha cleaning solutions (a mixture of sulfuric acid, water, and hydrogen peroxide) are suitable for glass surfaces but cannot effectively activate polymeric surfaces. Usual plasma treatments are only applicable to activate short tubes as the plasma cannot be inducted inside of high aspect ratio tubes. Being able to coat the inside of high aspect ratio tubes will extend the range of applications of super-liquid-repellent surfaces.[102, 147]

Here, we develop a universal route to activate and subsequently coat the inside of meter-long and, at the same time, thin tubes (down to 1 mm) with a super-liquid-repellent layer of nanofilaments. Activation of long tubes is enabled by making use of the Fenton reaction, which can be pumped through the tubes. The wide applicability of the coating method is demonstrated for tubes consisting of various materials, including polymers, hybrid materials, metals, and ceramics. Excellent anti-biofouling properties are demonstrated using nanofilament-coated polyurethane catheters used in hospitals.

5.2 RESULTS AND DISCUSSION

To coat the inside of the tubes with a super-liquid-repellent layer of nanofilaments, the surface needs to be hydrophilic, having polar functional groups, preferentially hydroxy groups. Thus hydrophobic, unfunctionalized polymer surfaces need to be activated. Short polymer tubes can be activated via oxygen plasma because the ionizing plasma can sufficiently penetrate from the ends of the tube. Plasma activation leads to the formation of various functional groups like hydroxy, carboxyl, carbonyl, and peroxide.[300] After activation, the standard procedure (**Figure 42**a) to coat tubes with a layer of silicone nanofilaments is to immerse the hydrophilic tubes in a solution of trichloromethylsilane (TCMS), in toluene or *n*-hexane for example, in the presence of trace amounts of water (85–225 ppm). After a reaction time of at least 1 h, the surface is covered with a layer of nanofilaments having a thickness of a few micrometers. During the reaction, the TCMS hydrolyzes due to water traces in the solvent. The hydrolyzed TCMS molecules react with hydroxy groups on the surface and induce a polysiloxane (i.e., silicone) polymerization on the surface of the tube (Figure S1 summarizes the involved chemical reactions). The coating is superhydrophobic as the methyl groups of the polysiloxane orient to the outside to lower the surface energy.[67, 112, 115-116]

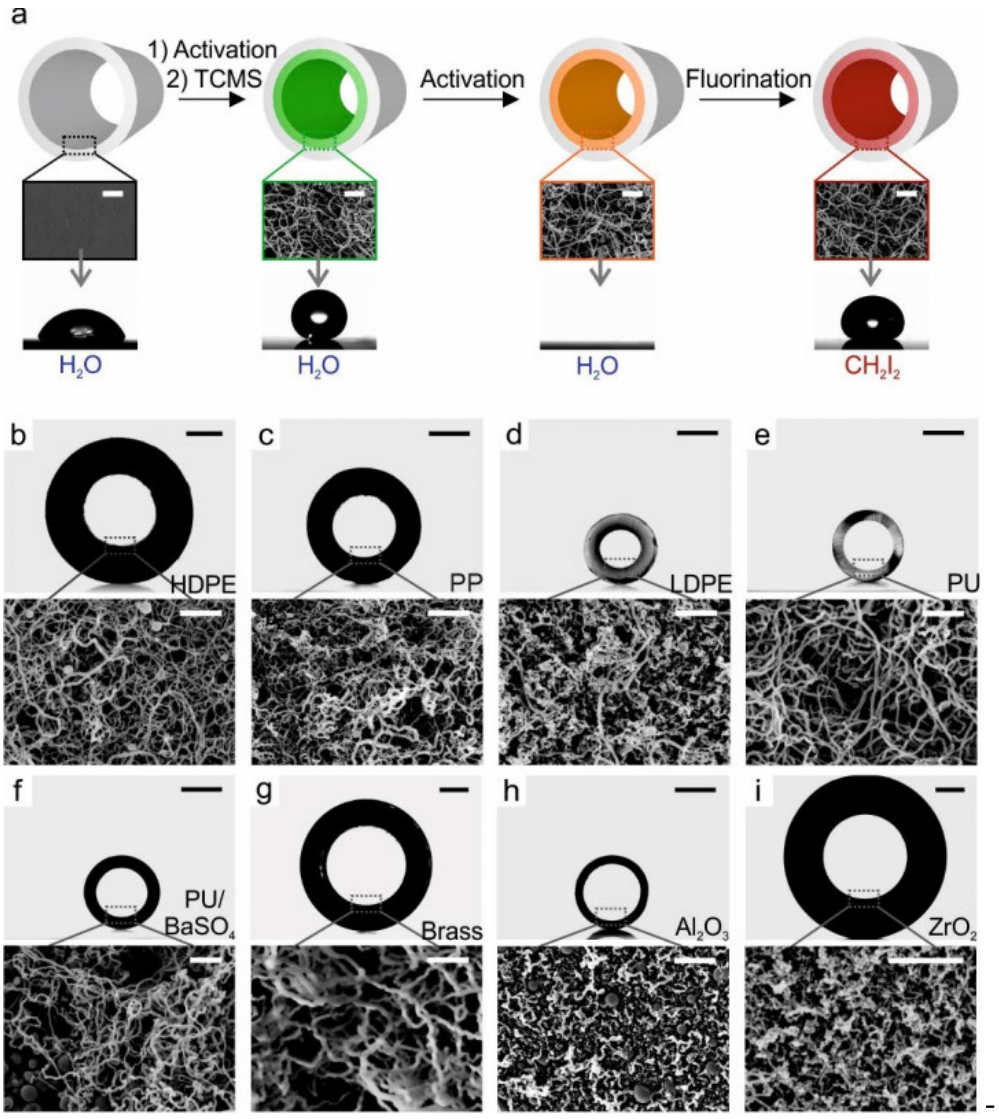

Figure 42. Illustration of the coating procedure, cross-sectional optical images, and scanning electron microscopic (SEM) images of the inner surface of the nanofilament-coated tubes. **a**) After activation, the nanofilament coating can be applied by immersing in or flushing the tubes with a trichloromethylsilane solution for a certain reaction time. SEM images demonstrate the formation of nanofilaments. Subsequent activation and fluorination yield a super-liquid-repellent coating. The different colors mark the change of the surface chemistry or topography of the interior surface. The photographs of the drops illustrate the changes in the wetting properties after each individual step on a flat surface. **b**) High-density polyethylene (HDPE) tube. **c**) Polypropylene (PP) tube. **d**) Low-density polyethylene (LDPE) tube. **e**) Polyurethane (PU) tube. **f**) Polyurethane/barium sulfate (PU/$BaSO_4$) tube. **g**) Brass tube. **h**) Alumina (Al_2O_3) ceramic tube. **i**) Zirconia (ZrO_2) ceramic tube. All SEM images show the formation of nanofilaments having diameters between 10–100 nm on the inner surface of the tubes. Scale bars: a) 500 nm; b–i) 500 nm for SEM images; 1 mm for optical images.

To render the coating super-liquid-repellent toward surfactant solutions or blood, the nanofilament-coated tubes are activated and modified with a perfluoro silane (1*H*,1*H*,2*H*,2*H*-perfluorodecyltrichlorosilane; see Figure S2 for XPS spectra of as-synthesized, plasma-activated and fluorinated nanofilaments in a tube).

Notably, fluorinated nanofilaments can also be achieved in a one-step reaction[123] as verified by coating high-density polyethylene with filaments (Figure S3). Here, a mixture of tetraethoxysilane (TEOS) and 1*H*,1*H*,2*H*,2*H*-perfluorodecyltrichlorosilane (PFDTS) in toluene was used, containing trace amounts of water (100 ± 5 ppm). TEOS and PFDTS hydrolyze due to the water traces in solution, inducing a polymerization on the surface of the tube, co-assembling into nanofilamentous structures.

The wide applicability of the method is demonstrated by coating tubes of varied materials having diameters between 1 mm and 3 mm. We applied the coating on commonly used and medically relevant polymer tubes, ranging from high-density polyethylene (HDPE), polypropylene (PP), low-density polyethylene (LDPE), and polyurethane (PU) to organic/inorganic hybrid polyurethane/BaSO4 (**Figure 42**b–f). The PU and PU/$BaSO_4$ tubes are used in hospitals as catheter tubes, with $BaSO_4$ as an X-ray contrast medium. In addition, the coating was applied to rigid brass, alumina (Al_2O_3), zirconia (ZrO_2), and copper (Cu) tubes (**Figure 42**g–i; Figure S10 for Cu.

The HDPE, PP, LDPE, and ceramic tubes were coated using TCMS (34 mmol L^{-1}) dissolved in toluene with 135 ± 10 ppm water content for 3 and 20 h, respectively. The brass and copper tubes were coated using a water content of 225 ± 5 ppm for 3 h. The polyurethane tubes (PU and PU/$BaSO_4$) were coated in a water-saturated (85 ± 5 ppm water content) TCMS (17 mmol L^{-1}) solution in *n*-hexane for 20 h, showing that nanofilaments grow in both, toluene and *n*-hexane. Scanning electron microscopic (SEM) images demonstrate the formation of nanofilaments on all tubes. On the HDPE, PP, and LDPE tubes, a coating consisting of mainly thinner nanofilaments (10–30 nm diameter) and some lone thicker nanofilaments (40–70 nm diameter) was obtained (**Figure 42**b–d). On the polyurethane tubes, the diameter of the nanofilaments varied between 20 and 70 nm in diameter. In addition, silicone nanoparticles between 150 and 500 nm diameter were found inside the coating (**Figure 42**e,f). On brass, the coating consisted of nanofilaments with ≈50 nm diameter (**Figure 42**g). Ceramic tubes showed rather short and thin nanofilaments between 15 and 40 nm in diameter (**Figure 42**h,i). More detailed SEM images of the bare and coated tubes are shown in Figure S4–S12.

The necessity of activation is demonstrated for LDPE tubes as a model system (**Figure 43**). Without activation, only a few randomly distributed nanofilaments formed on LDPE (**Figure 43**a). After plasma activation, a short tube was coated with a homogeneous layer of nanofilaments (**Figure 43**b). However, plasma activation is only applicable inside of

short tubes because of limitations of the flux to penetrate longer tubes. Thus, a more versatile method to activate the inner surface of tubes of arbitrary length is required. Here, we introduce the Fenton reaction[251] for activating the surfaces. The Fenton reaction is industrially widely used to oxidize contaminants or to treat wastewater.[252] Fenton's reagent is an aqueous solution of hydrogen peroxide and ferrous iron. The ferrous iron acts as a catalyst to produce hydroxyl radicals and hydroxide ions as a byproduct:

$$Fe^{2+} + H_2O_2 \rightarrow Fe^{3+} + HO^{\cdot} + OH^{-}$$

These hydroxyl radicals have the second-highest oxidation potential (redox potential 2.80 V) of all common oxidation agents, only surpassed by fluorine (redox potential 3.03 V). Similar to the oxygen plasma, the hydroxyl radicals oxidize the polymeric surface inside the tubes introducing functional groups containing oxygen, like hydroxy, peroxide, and carboxyl (**Figure 43**c). X-Ray photoelectron spectroscopy (XPS) spectra of a bare and Fenton-activated LDPE tube revealed an increase of oxygen-containing functional groups (**Figure 43**d). This is manifested in the increase of the ratio between the oxygen (O1s) peak to the carbon (C1s) peak. The structure of the nanofilament coating depends on the activation time with Fenton's reagent and thus on the density of oxygen-containing functional groups on the polymer surface. Already after 30 min of exposure to a Fenton solution (22 mmol L^{-1} $FeSO_4$, 0.50 mol L^{-1} H_2O_2, pH = 2.8, cooled in an ice bath) under a flow rate of 8 mL min^{-1}, a coating featuring mostly thick nanofilaments resembling particles chains (>100 nm) could be obtained on an LDPE tube (**Figure 43**e and Figure S13). After 60 min exposure, the coating was composed of filaments with an average diameter below 100 nm. After 90 min, the average nanofilament diameter decreased to ≈50 nm. After 120 and 180 min exposure to Fenton's solution, the nanofilaments were thicker than 50 nm. In addition, more nanoparticles started to form, which were mostly assembled into particle chains.

To coat a 2 m long and 1 mm thick LDPE tube, the inner surface was activated by pumping Fenton's reagent (22 mmol L^{-1} $FeSO_4$, 0.50 mol L^{-1} H_2O_2, pH = 2.8, 90 min, cooled in an ice bath) through the tube at a flow rate of 8 mL min^{-1} (see Experimental Section 5.4.7 for further details). After Fenton-activation, a TCMS-solution (34 mmol L^{-1} in toluene, 150 ± 5 ppm water content) was slowly pumped (0.1 mL min^{-1}) through the tube to ensure a homogeneous coating and to prevent the depletion of silane within the tube.

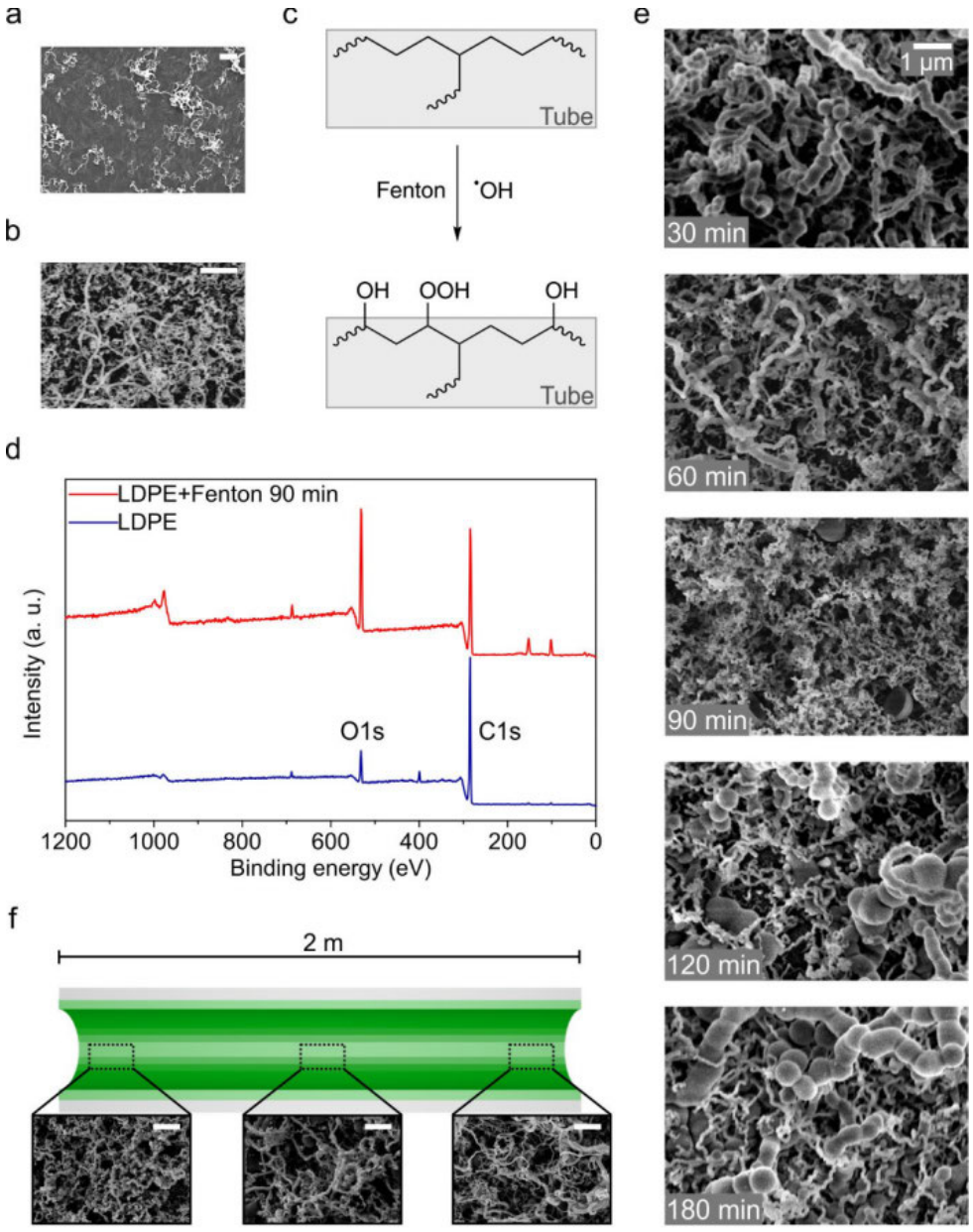

Figure 43. Activation and coating of a two-meter long tube. **a**) SEM image of low-density polyethylene (LDPE) tube coated without prior activation. **b**) SEM image of a short tube activated using oxygen plasma before the coating was applied. **c**) Scheme of the activation of polymer surfaces using the Fenton reagent. **d**) X-ray photoelectron spectroscopy (XPS) spectra of a bare and Fenton-activated LDPE tube. **e**) SEM images of coated Fenton-activated LDPE tubes after different Fenton reagent exposure times using a flow rate of 8 mL min^{-1}. **f**) SEM images of a coated LDPE tube with a total length of 2 m and an inner diameter of 1 mm at both endings and the middle of the tube. The formation of nanofilaments could be observed at all positions. Scale bars: a, b) 500 nm; f) 1 µm.

Indeed, SEM images, taken at both endings of the tube and in the middle of the tube, document the formation of nanofilaments along the inside of the tube having an aspect ratio of 2000:1 (**Figure 43**f and Figure S14). Due to the ability to pump the Fenton solution and the coating solution through the tube, the whole coating procedure can be applied to

tubes of greatly varying materials and aspect ratios. The Fenton reaction can also be utilized to activate the nanofilaments and thus replace the plasma activation before fluorination of the nanofilaments (Figure S15a,b). A nanofilament-coated tube was hydrophilized by pumping the Fenton solution through the tube for 50 min at a flow rate of 8 mL min^{-1}. Afterward, water drops easily spread inside the tube (Figure S15c,d).

The wetting properties of a bare PU/$BaSO_4$ tube, fluorinated nanofilaments on polyurethane tubes, and fluorinated nanofilaments on the 2 m-long LDPE tube were investigated using different liquids, including liquids relevant for biomedical applications (**Figure 44**; Figure S16 and S17). Due to the small inner diameters (1.3 and 0.95 mm) and the high curvature of the tubes, contact angles cannot be determined in a standard way, i.e., using the goniometer technique. However, super-liquid-repellency is typically accompanied by only a few pinning sites and low adhesion of drops to the surface. We quantified the wettability indirectly by monitoring the adhesion of drops to the coating. Therefore, the PU tubes were horizontally cut in the middle prior to coating in order to avoid pinning sites at the cut surface. Drops between 1 and 3 µL volume were placed onto the inside of the tubes. Next, the syringe was slowly moved up and down (see also Movie S1–S4). On bare PU/$BaSO_4$ tubes, the high adhesion between the phosphate-buffered saline (PBS, surface tension, $\gamma = 72.8$ mN m^{-1}) and PU/$BaSO_4$ caused that the drop detached and stuck at the surface (**Figure 44**a). Contrary, on the PU/$BaSO_4$ tubes coated with fluorinated nanofilaments, drops of PBS, urine, and blood plasma hardly showed any adhesion (**Figure 44**b–d). The drops could be easily removed by retracting the syringe. Drops of diiodomethane (CH_2I_2, $\gamma = 50.8$ mN m^{-1}) detached from the syringe upon retraction due to the high density of CH_2I_2 (3.3 g mL^{-1}) and rolled out of the tube (**Figure 44**e). Also, common food liquids like water, Cola, apple juice spritzer, and the non-polar aromatic liquid iodobenzene ($\gamma =$ 39.7 mN m^{-1}) showed low adhesion and could be easily removed from a coated PU tube (Figure S16). The low adhesion of CH_2I_2 and iodobenzene drops showed the super liquid-repellency of the coating also to non-polar liquids. The super liquid-repellency of the coated 2 m-long LDPE tube was confirmed at both endings and in the middle (Figure S17). Video microscopy showed that all aqueous drops exhibited a lower adhesion than 3 µL water drops on a superhydrophobic micropillar array (rectangular, 10 µm height with 5×5 μm^2 top areas; pillar–pillar distance (center to center): 20 µm; $9° \pm 1°$ roll-off angle for 6 µL water drops). On the micropillar array, the drop either stuck to the surface or its detachment from the surface caused visible vibrations of the drop (Movie S5). As a reference, we also measured the receding contact angles and roll-off angles on nanofilament-

coated glass slides and on flat polyurethane/$BaSO_4$. The tube material was flattened by heating. Phosphate buffered saline on flat PU/$BaSO_4$ showed a receding contact angle of 43° ± 4° and did not roll off. However, PBS on a nanofilament-coated glass slide showed a receding contact angle (RCA) of 158° ± 4° and a roll-off angle of 2° ± 1° for 6 µL drops. After plasma or Fenton activation of the nanofilaments, the receding contact angle of PBS was ≈0°, due to spreading. On a glass slide coated with fluorinated nanofilaments, PBS and CH_2I_2 as an example showed a receding contact angle of 160° ± 4° and 149° ± 4°, respectively, and roll-off angles of 1° ± 1° and 1° ± 1° for 6 µL drops, respectively. The extremely low adhesion of the drops to the coated inner surfaces of the tubes is in agreement with the high receding contact angles and low roll-off angles measured on nanofilament-coated glass slides.

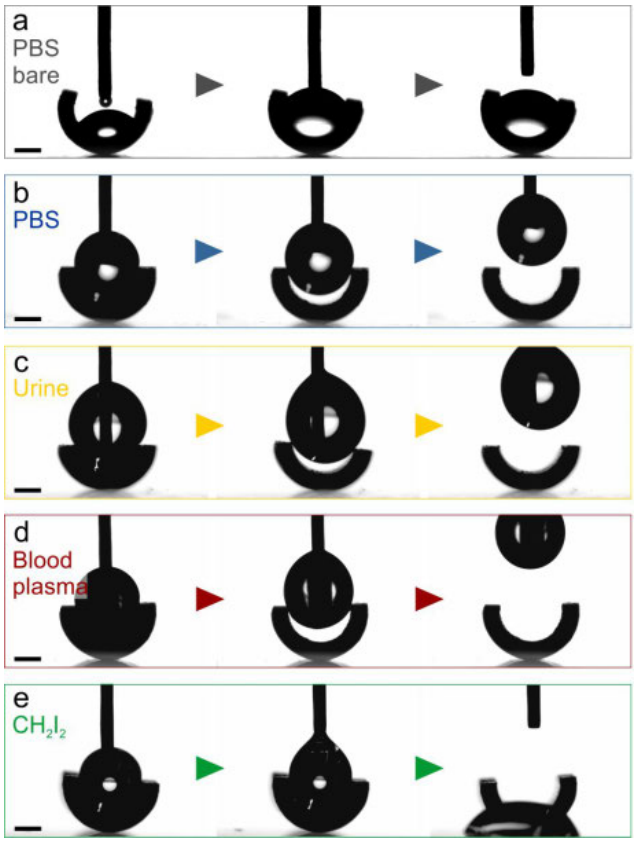

Figure 44. Wetting properties of a coated and fluorinated PU/$BaSO_4$ catheter tube in comparison to a bare PU/$BasO_4$ tube. **a**) A 2 µL PBS (phosphate-buffered saline) drop sticking on a bare tube. **b**,**c**) A 2 µL PBS and a 3 µL urine droplet on a coated tube; both showed very low adhesion and could be easily removed by retracting the syringe. **d**) Even a 2 µL blood plasma drop showed very low adhesion to a coated tube and was easily removed from it. **e**) A 2 µL diiodomethane drop on a coated tube; during retraction of the syringe, the droplet detached from the syringe due to the high density of diiodomethane and rolled out of the tube. Scale bars: 0.5 mm.

Many super-liquid-repellent coatings suffer from poor mechanical stability or easy delamination.[301] To test the long-term stability of the coating against flow-induced shear, water was pumped through a nanofilament-coated LDPE tube (0.95 mm inner diameter) for up to 10 months. The flow was adjusted to the maximum accessible pumping speed of the peristaltic pump (11 mL min^{-1}), which corresponds to an average flow velocity of

≈30 cm s^{-1} and a shear rate at the tubes' inner surface of $|\dot{\gamma}| \approx 2 \times 10^3$ s^{-1} and a shear force per unit area of $\dot{\gamma}\eta = 2$ N m^{-2} (here, $\eta = 0.001$ Pa·s is the viscosity of water; see Experimental Section 5.4.15 and **Figure 46** for further details). The morphology of the coating was checked after 5, 10, 30 d, and 2, 3, and 10 months (Figure S18). Surprisingly, even after 10 months, SEM images show that the morphology remained unaltered, which demonstrates the excellent adhesion of the nanofilaments to the substrate and the high stability of the coating. Additionally, we exposed fluorinated nanofilaments coated on a glass slide to an even higher flow velocity of >220 cm s^{-1} by impacting a water jet at an angle of ≈35° for 1 h (Figure S19a,b). SEM analysis revealed that the coating was not abraded, delaminated, or destroyed but remained unaltered (Figure S19c,d). The roll-off angle of 6 µL water drops stayed at 1° ± 1°, confirming the high stability of nanofilaments against liquid streams. Furthermore, tubes are typically subjected to bending, and thus the coating needs to be flexible. Therefore, we tested the flexibility and resistance of the coating toward bending. The coating did not alter, delaminate, or break even after 1000× bending cycles (Figure S20). The methyl groups confer flexibility to the siloxane polymer. It has been shown that superhydrophobic and liquid-repellent coatings may effectively delay biofilm formation.[159-160, 162] Superhydrophobicity leads to very high contact angles of the bacterial suspension on the surfaces as well as a low solid-liquid contact area. This translates into few adhesion sites (Cassie state) that can be accessed by the bacteria, resulting in low bacterial adhesion. Inspired by these results, we evaluated the potential of coated PU tubes regarding their anti-biofouling properties for medical devices.[4] Therefore, we coated and incubated PU tubes (1 cm) in concentrated *E. coli* bacteria solutions (10^8 cells mL^{-1}) for 168 h at 37 °C. The samples included bare PU catheters as a reference, as-prepared nanofilament-coated PU tubes (Me-NF), superhydrophilic nanofilament-coated PU tubes (OH-NF) and fluorinated nanofilament-coated PU tubes (F-NF) (**Figure 45**). After incubation, the inside of the bare PU tubes was homogeneously covered with *E. coli* throughout the whole tube (**Figure 45**a). On the nanofilament-coated tubes, the coverage with *E. coli* was greatly reduced. Hardly any *E. coli* could be found (**Figure 45**b–d). The squares mark positions where a single bacterium was located. The *E. coli* bacteria had a few micrometers in length and adhered to the top faces of a few nanofilaments (**Figure 45**b, right). On the as-prepared and fluorinated nanofilaments, the

[4]During the publication of this work, also another research group investigated the antibacterial properties of superhydrophobic nanofilaments (coated on glass slides).[164]

number of adhered bacteria was reduced by more than 20 times. Notably, on the superhydrophilic nanofilaments, the number of bacteria per cm^2 was reduced by up to almost two orders of magnitude, 85 times (**Figure 45**e, see Note S1 in the Supporting Information for an in-depth discussion on the role of superhydrophobicity, Cassie state, and cell motility on bacterial adhesion).

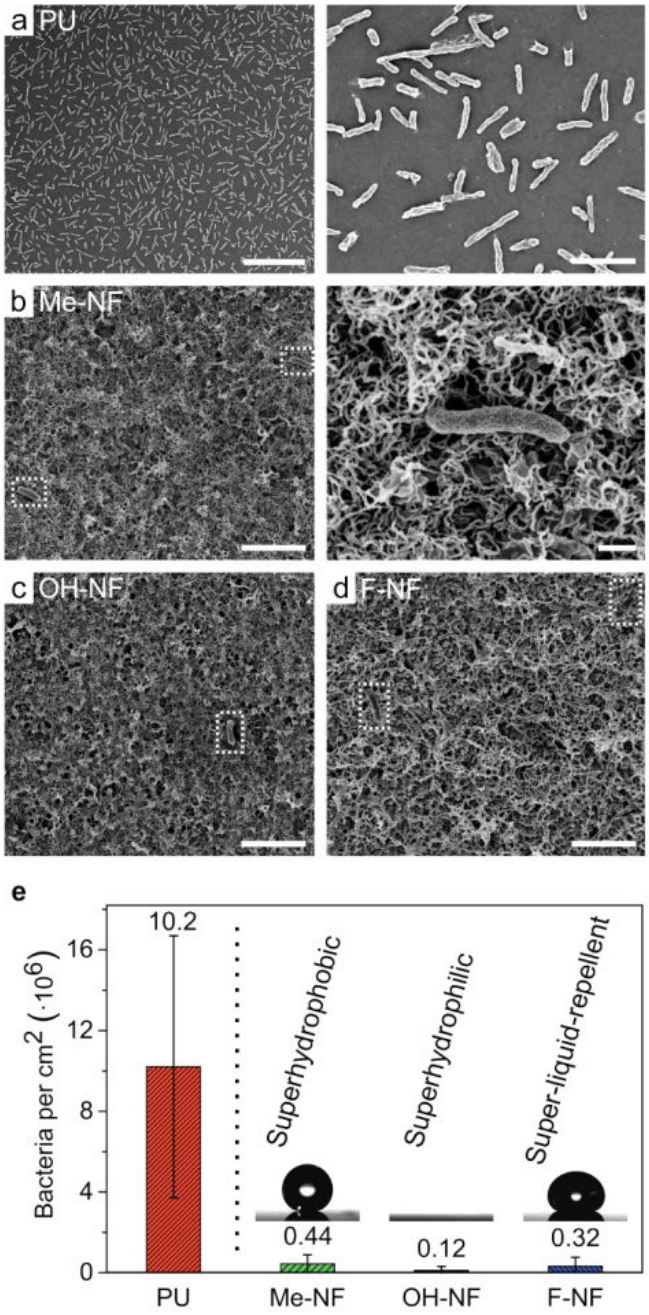

Figure 45. Antibacterial properties of a bare PU tube, a nanofilament-coated PU tube, a superhydrophilic nanofilament-coated PU tube, and a fluorinated nanofilament-coated PU tube after an incubation time of 168 h in an *E. coli* solution. **a**) Bare PU tube showing high *E. coli* coverage. Scale bars: 20 µm (left); 4 µm (right). **b**) Nanofilament-coated PU tube showing highly reduced bacterial coverage (left). High magnification of a single *E. coli* bacterium attached to nanofilaments (right). Scale bars: 4 µm (left); 500 nm (right). **c**) Superhydrophilic nanofilament-coated PU tube. Scale bar: 4 µm. **d**) Fluorinated-nanofilament-coated PU tube. Scale bar: 4 µm. **e**) Average number of bacteria per area adhered to the surface for the different tubes after 168 h of incubation.

Thus, the presented coating is capable of effectively reducing bacterial adhesion and biofilm formation in the superhydrophobic as well as in the fully wetted state, the so-termed

Wenzel state. We attribute this excellent anti-biofouling property to the characteristic spacing of the irregular three-dimensional layer of nanofilaments, which falls just below the size of *E. coli* (**Figure 45**b). Therefore, the stiff bacteria cannot enter the pores. Furthermore, the small diameter of the nanofilaments and their irregular three-dimensional arrangement reduces the anchoring area. This distinctive combination of length scales and morphology makes tubes coated with nanofilaments a highly promising candidate for medical applications, for example, as a catheter.

5.3 CONCLUSION

In conclusion, pumping Fenton's solution through thin polymeric tubes offers a versatile and simple method to activate their inner surfaces. The activated surfaces can subsequently be coated with a layer of nanofilaments. Due to the ability to pump both the Fenton solution and the coating solution, the wetting properties of meter-long and at the same time thin tubes (here: 2 m with 1 mm diameter) or other bicontinuous surfaces can be tuned from superhydrophilic to super-liquid-repellent. The Fenton activation may also be used to apply other liquid-repelling or antibacterial coatings, for example, liquid-like PDMS[68] coatings. Pumping offers the possibility that the activation and the coating step can easily be parallelized. Hundreds of parallel arranged tubes can be treated simultaneously. Coated medical catheters prove to be promising candidates for reducing bacterial growth. Remarkably, even in the superhydrophilic state, the attachment of bacteria is highly reduced. Thus, the irregular 3D topography of nanofilaments greatly reduces the anchoring area for bacteria. Besides the excellent antibacterial properties, the coating can also withstand high flow velocities, bending, and does not delaminate. The wide applicability of the nanofilament coating on tubes of various diameters and materials makes this method useful for a broad range of applications. It opens new avenues to fabricate biocide-free coatings of medical devices since the reduced bacterial adhesion and proliferation reduce the infection risk of patients.

5.4 EXPERIMENTAL SECTION

5.4.1 MATERIALS

If not stated otherwise, experiments were carried out at room temperature. The following chemicals were used: trichloromethylsilane (TCMS, 99%, Sigma-Aldrich), tetraethoxysilane (TEOS, 98%, Sigma-Aldrich), 1*H*,1*H*,2*H*,2*H*-perfluorodecyltrichlorosilane (PFDTS,

96%, Alfa Aesar), SU-8 3010 photoresist (MicroChem), mr-Dev 600 developer (micro resist technology), *n*-hexane (99.99%, Fisher Chemical), toluene (99.5%, VWR), ethanol (99.8%, Sigma-Aldrich), hexadecane (99%, Sigma-Aldrich), diiodomethane (99%, Sigma-Aldrich), iodobenzene (Sigma-Aldrich, 98%), sulfuric acid (99.99%, Sigma-Aldrich), iron sulfate heptahydrate (>99%, Sigma-Aldrich), hydrogen peroxide (35 wt%, VWR), phosphate-buffered saline (PBS, Gibco), glutaraldehyde (25 wt%, Sigma-Aldrich). The culture medium, LB (Lysogeny broth) medium, supplemented with Ampicillin (Cat. fas-am-b), was purchased from InvivoGen. Reagents were used as received. Cola and apple juice spritzer (60% apple juice concentrate) was obtained from the local supermarket. Whole blood was taken at the Department of Transfusion Medicine of the University Medical Center of the JGU Mainz from healthy donors. The study was approved by the local ethics committee and is in accordance with the Declaration of Helsinki. Sodium citrate was added to prevent clotting, and plasma was separated by centrifugation. The plasma was pooled, and aliquots were stored at -80 °C. A protein concentration of 65–70 g L^{-1} was determined by protein assay Pierce 660 nm. Urine was provided by F. Geyer. Purified and deionized water was obtained from a Sartorius Arium 661 VF water purification system and used for all experiments. Polypropylene (PP, inner diameter (ID): 1.6 mm, outer diameter (OD): 3.2 mm), high-density polyethylene (HDPE, ID: 2.0 mm, OD: 4.0 mm), and low-density polyethylene (LDPE, ID: 0.95 mm, OD: 2.0 mm) were obtained from RCT Reichelt Chemietechnik. Polyurethane (PU, ID: 1.3 mm, OD: 2.0 mm) and hybrid polyurethane/$BaSO_4$ (PU/$BaSO_4$, ID: 1.4 mm, OD: 2.1 mm) tubes were obtained from B. Braun. Ceramic tubes (Al_2O_3, ID: 1.5 mm, OD: 2.0 mm; ZrO_2, ID: 3.0 mm, OD: 6.0 mm) were obtained from Friatec AG. Diameters are based on manufacturer specifications (except ID of LDPE). Brass (ID: 2.9 mm, OD: 5.0 mm) and copper (Cu, ID: 2.9 mm, OD: 4.0 mm) tubes were obtained from a local hardware store. Glass slides of 24 × 60 mm^2 were obtained from Menzel-Gläser. Purified Milli-Q water from Sartorius Arium Pro VF was used for all experiments.

5.4.2 NANOFILAMENT-COATED GLASS SLIDES

Silicone nanofilaments on glass slides were synthesized by modifying previously reported methods.[112, 115] The fabrication contained the following steps:[116, 118, 233] Typically, glass slides were plasma-cleaned and activated in an oxygen plasma chamber (Diener Electronic Femto, 120 W, 5 min, 6 cm^3 min^{-1} oxygen flow rate). TCMS was mixed with toluene having a water content of 180 ± 10 ppm (400 µL TCMS per 100 mL toluene). The

water content was evaluated using a Karl Fischer coulometer (Mettler Toledo C20 Compact KF coulometer). The solution was stirred for 60 s. Afterward, the activated glass slides were immersed in the solution, and the reaction chamber was sealed. After 6 h, the TCMS-coated glass slides were rinsed with *n*-hexane and dried under a nitrogen stream. Further details about nanofilament synthesis can be found elsewhere.[112, 115, 127]

5.4.3 NANOFILAMENT-COATING OF THE HDPE, PP, LDPE, AND CERAMIC (Al_2O_3 AND ZrO_2) TUBES USING PLASMA ACTIVATION

Short HDPE, PP, LDPE, Al_2O_3 and ZrO_2 tubes were plasma-cleaned and activated in an oxygen plasma chamber using different exposure times ranging from 36 s to 2 min and different powers ranging from 30 W to 120 W (Diener Electronic Femto, 6 cm^3 min^{-1} oxygen flow rate). TCMS was mixed with toluene having a water content of 135 ± 10 ppm (400 µL TCMS per 100 mL toluene). The water content was evaluated using a Karl Fischer coulometer (Mettler Toledo C20 Compact KF coulometer). The solution was stirred for 60 s. Afterward, the tubes were immersed in the solution, and the reaction chamber was sealed. After 3 h (20 h for ceramic tubes), the TCMS-coated tubes were rinsed with *n*-hexane and dried under a nitrogen stream.

5.4.4 NANOFILAMENT-COATING OF THE BRASS AND COPPER (CU) TUBES

The brass and copper (Cu) tubes were cleaned by immersion in a 5 wt% sulfuric acid solution for 30 min. Afterward, the tubes were thoroughly rinsed with deionized water and activated in an oxygen plasma (Diener Electronic Femto, 120 W, 2 min, 6 cm^3 min^{-1} oxygen flow rate). TCMS was mixed with toluene having a water content of 225 ± 5 ppm (400 µL TCMS per 100 mL toluene). The water content was evaluated using a Karl Fischer coulometer (Mettler Toledo C20 Compact KF coulometer). The solution was stirred for 60 s. Afterward, the tubes were immersed in the solution, and the reaction chamber was sealed. After 3 h, the TCMS-coated tubes were rinsed with *n*-hexane and dried under a nitrogen stream.

5.4.5 NANOFILAMENT-COATING OF THE PU AND PU/$BaSO_4$ TUBES

The PU and PU/$BaSO_4$ tubes were cleaned by flushing with an ethanol/deionized water mixture (50:50 to 40:60) for 5–10 min. The flushing also leads to the adsorption of a thin water layer, which facilitates nanofilament growth. TCMS was mixed with *n*-hexane having a water content of 85 ± 5 ppm (200 µL TCMS per 100 mL *n*-hexane). The water content

was evaluated using a Karl Fischer coulometer (Mettler Toledo C20 Compact KF coulometer). The solution was stirred for 60 s. After flushing the tubes, they were immediately immersed in the solution, and the reaction chamber was sealed. Alternatively, the solution was injected or pumped through the tube. After 20 h, the TCMS-coated tubes were rinsed with *n*-hexane and dried under a nitrogen stream.

5.4.6 One-step fluorinated nanofilament-coating on HDPE tube

The one-step synthesis of fluorinated nanofilaments is based on a method by Zhang *et al.*[123] The HDPE tube was plasma-cleaned and activated in an oxygen plasma chamber (Diener Electronic Femto, 6 cm^3 min^{-1} oxygen flow rate, 150 W, 42 s). TEOS (100 µL) and PFDTS (16 µL) were mixed with toluene (80 mL) having a water content of 100 ± 5 ppm. The water content was evaluated using a Karl Fischer coulometer (Mettler Toledo C20 Compact KF coulometer). The solution was stirred for 60 s. Afterward, the tubes were immersed in the solution, and the reaction chamber was sealed. After 20 h, the coated tubes were rinsed with *n*-hexane and dried under a nitrogen stream.

5.4.7 Nanofilament-coating of tubes using Fenton reaction activation

Iron(II) sulfate heptahydrate (0.25 g, 0.90 mmol) was dissolved in 40 mL of deionized water in a reaction vessel having an in- and outlet. The pH of the solution was adjusted to pH = 2.8 using a pH meter by adding sulfuric acid. The mixture was cooled for at least 30 min in an ice bath. The polymeric tube (LDPE) to be activated was connected to the outlet of the reaction vessel using a Tygon connection tube. The end of the polymeric tube was connected to a peristaltic pump (Ismatic Reglo Digital MS-2/12) and finally to the inlet of the reaction vessel using Tygon connection tubes. Hydrogen peroxide solution (1.8 mL, 35 wt%, 21 mmol) was slowly added to the acidic aqueous ferrous sulfate solution under vigorous stirring, and the mixture was stirred for 10 min. Afterward, the pump was started using a flow rate of 8 mL min^{-1}. The Fenton[251] solution was pumped through the tube for the desired activation time. Typically, the activation time ranged between 20 min and 3 h. Every 15 min, the tube was emptied by reversing the pumping direction to eliminate gas bubbles, which may form on the inner surface due to the slight oxygen evolution during the Fenton reaction. After the desired activation time was reached, the tube was rinsed by flushing deionized water through the tube. Subsequently, the tube was dried by flushing dry nitrogen and further drying in vacuo. After drying, TCMS was mixed with toluene having a water content of 150 ± 5 ppm (400 µL TCMS per 100 mL toluene) in a reaction

vessel having an in- and outlet. The water content was evaluated using a Karl Fischer coulometer (Mettler Toledo C20 Compact KF coulometer). Similar to above, the Fenton-activated tube was connected to the reaction vessel and the pump. Here, Fluran F-5500-A tubes were used to connect the individual parts. After stirring the reaction mixture for 60 s, the reaction vessel was closed, the mixture was pumped into the activated tube, and the pump was stopped for 30 min. Subsequently, the pump was started again for 5 min with a flow rate of 0.1 mL min^{-1} and stopped again for 45 min. After that, the pumping process was continued for 20 h using a flow rate of 0.1 mL min^{-1}. Subsequently, the TCMS-coated tubes were rinsed with *n*-hexane and dried under a nitrogen stream.

5.4.8 PLASMA ACTIVATION OF NANOFILAMENT-COATED SURFACES AND TUBES

To activate nanofilament-coated surfaces and short tubes, they were exposed to an oxygen plasma (Diener Electronic Femto, 120 W, 2 min, 7 cm^3 min^{-1} oxygen flow rate).

5.4.9 FENTON ACTIVATION OF NANOFILAMENT-COATED SURFACES AND TUBES

To activate nanofilament-coated surfaces and tubes using Fenton reaction, iron(II) sulfate heptahydrate (2.5 g, 9.0 mmol) was dissolved in 10 mL of deionized water in a reaction vessel. The pH of the solution was adjusted to ≈3 by adding 10 µL of 10 wt% sulfuric acid. The nanofilament-coated substrate was immersed in ethanol, or ethanol was pumped through a nanofilament-coated tube to remove the air cushion (Cassie state) of the nanofilaments. Afterward, the substrate or tube was rinsed with deionized water to remove residual ethanol. The wet substrate was immersed in the acidic ferrous sulfate solution, and hydrogen peroxide solution (18 mL, 35 wt%, 0.21 mol) was slowly added (*caution: strong reaction and gas formation occurs!*) to the solution under vigorous stirring. After 10 and 20 min, additional H_2O_2 (each 18 mL, 35 wt%) was added. In the case of a tube, the solution mentioned above was pumped through the tube using a flow rate of 8 mL min^{-1}. After 50 min, the substrate or tube was rinsed with 10 wt% sulfuric acid and copious amounts of deionized water.

5.4.10 FLUORINATION OF ACTIVATED NANOFILAMENT-COATED TUBES OR SURFACES

PFDTS was mixed with *n*-hexane (50 µL PFDTS per 100 mL *n*-hexane). The activated nanofilament-coated tubes or surfaces were immersed in the solution, and the reaction chamber was sealed. Alternatively, the solution was pumped through the tube. After 20 min the fluorinated tubes or surfaces were rinsed with *n*-hexane and dried under a nitrogen stream.

5.4.11 Superhydrophobic SU-8 micropillars

SU-8 micropillar arrays were prepared on glass slides by photolithography as previously reported.[62, 77] The rectangular pillars were designed 10 µm high with 5 × 5 µm² top areas. The pillar–pillar distance between the centers of two adjacent pillars in a row was 20 µm. Details are described in Experimental Section 2.3.4. The SU-8 micropillars were activated in an oxygen plasma chamber (Diener Electronic Femto, 30 W, 2 min, 6 cm^3 min^{-1} oxygen flow rate). Subsequently, PFDTS was mixed with *n*-hexane (50 µL PFDTS per 100 mL *n*-hexane). The activated SU-8 micropillar-coated glass slides were immersed in the solution, and the reaction chamber was sealed. After 20 min the fluorinated pillars were rinsed with *n*-hexane and dried under a nitrogen stream.

5.4.12 Contact angle measurements and drop observation

Receding contact angles were measured using a DataPhysics OCA35 contact angle goniometer. Initially, 6 µL drops were deposited onto the substrate. Afterward, 20 µL of the liquid was added to and removed from the drop. The measurement was repeated at three different spots per substrate. The error of the receding contact angle measurements was estimated to be ±4°.

Roll-off angles were measured using the DataPhysics OCA35 contact angle goniometer. Therefore, 6 µL drops were deposited on the substrates, and the measuring plate was tilted until the drops rolled off. The roll-off angle was determined in at least 6 different spots per substrate, and mean roll-off angles and corresponding standard deviations were calculated.

The drop adhesion on the coated tubes was observed using the same DataPhysics OCA35 contact angle goniometer. Here, a syringe with a fluorinated tip was used. A 0.5–3 µL drop was generated at the tip and brought into contact with the coated tube. Afterward, the syringe was moved up and down to observe the adhesion of the drop to the tube.

5.4.13 Scanning electron microscopy

Scanning electron microscopy (SEM) images were taken with a Zeiss LEO 1530 Gemini SEM at gun voltages of 3 kV using the in-lens detector. To avoid charging, samples were sputtered with Pt before measurement using a BalTec MED 020 modular high vacuum coating system (with an argon pressure of 2×10^{-5} bar and a current of 30 mA, 7 nm Pt).

5.4.14 X-RAY PHOTOELECTRON SPECTROSCOPY

X-ray photoelectron spectra (XPS) were acquired using a Kratos Axis Ultra system. The X-ray source was monochromatic Al-K_α (source energy: 1486.69 eV). The take-off angle was 0°. The vacuum in the main chamber was below $4 \cdot 10^{-10}$ mbar. The hybrid detector mode was used. Survey spectra were recorded with a pass energy of 160 eV. Charge neutralization was applied (current: 2.1 A, balance: 2.8 V, bias: 1.3 V). The survey scans were obtained with 2 scans. The software CasaXPS (Casa Software Ltd) was used for data elaboration. The binding energies of the XPS spectra were calibrated with the help of the aliphatic C1s peak at 285.0 eV. To measure XPS spectra inside of the tubes, the investigated tubes were cut in half horizontally and glued on carbon tape.

5.4.15 CALCULATION OF THE SHEAR RATE:

The flow of a Newtonian liquid through a long cylindrical tube (**Figure 46**) of radius r_c is given by the Hagen-Poiseuille equation.

$$\frac{dV}{dt} = \frac{\pi \Delta P r_c^4}{8 \eta L} \tag{35}$$

Where $\frac{dV}{dt}$ is the volume of liquid flowing through the tube per unit of time, ΔP pressure drop along the tube of length L and η is the viscosity of the liquid. The velocity at a distance r from the center is given by:

$$v(r) = \frac{r_c^2 - r^2}{4\eta} \frac{\Delta P}{L} = \frac{r_c^2 - r^2}{4\eta} \frac{dV}{dt} \frac{8\eta}{\pi r_c^4} = \left(1 - \frac{r^2}{r_c^2}\right) \frac{dV}{dt} \frac{2}{\pi r_c^2} \tag{36}$$

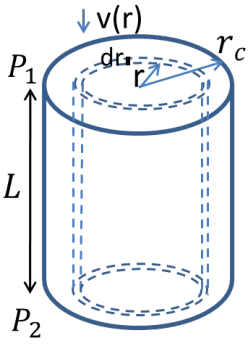

Figure 46. Sketch of the tube.

The volume flow also follows from the continuity equation:

$$\frac{dV}{dt} = 2\pi \int_0^{r_c} r v(r)\, dr$$

$$= 2\pi v_0 \int_0^{r_c} r \left(1 - \frac{r^2}{r_c^2}\right) dr = 2\pi v_0 \left[\frac{r^2}{2} - \frac{r^4}{4r_c^2}\right]_0^{r_c} = 2\pi v_0 \left(\frac{r_c^2}{2} - \frac{r_c^4}{4r_c^2}\right) = \frac{\pi}{2} v_0 r_c^2 \tag{37}$$

with $v_0 = v(r = 0) = \frac{dV}{dt} \frac{2}{\pi r_c^2}$

At $r = r_c$ the shear rate is:

$$\dot{\gamma} = \frac{dv(r = r_c)}{dr} = -\frac{2r_c}{r_c^2} \frac{2}{\pi r_c^2} \frac{dV}{dt} = -\frac{4}{\pi r_c^3} \frac{dV}{dt} \tag{38}$$

For the applied volume flow of $\frac{dV}{dt}$ = 11 mL min^{-1} = 1.8 × 10^{-7} m^3 s^{-1} and a tube radius of r_c = 0.475 mm, the shear rate is:

$$|\dot{\gamma}| = \frac{4}{\pi r_c^3}\frac{dV}{dt} = 2 \times 10^3 \text{ s}^{-1} \tag{39}$$

5.4.16 BACTERIA E. COLI ADHESION TESTING AND IMAGING

The tubes cut in half horizontally were fixed onto a sterile chambered glass with double-sided tape. Each chamber was covered with LB (Lysogeny broth)+Amp medium (1 mL, containing 100 μg mL^{-1} of Ampicillin as well as Arabinose added to a final concentration of 0.1%, in the following referred to as LB+Amp medium) containing *E. coli* expressing eGFP (10^8 cells mL^{-1} controlled through OD_{600}, Stellar™ Competent, HST08, Clontech) and left for incubation at 37 °C for 7 days. The bacterial solution was refreshed daily to avoid nutrient depletion of the bacteria. The bacteria solution for the experiment was prepared by mixing 1 mL of the mother solution containing *E. coli* expressing eGFP with 4 mL of LB+Amp medium, followed by 2 h of incubation at 37 °C at 350 rpm. The optical density of the bacteria-solution was adjusted by dilution with LB+Amp medium. To prepare the samples for SEM investigations, after the 7-day incubation period, the culture medium was carefully removed, and the samples were washed with phosphate-buffered saline (PBS, 1 mL, 3 times). The phosphate-buffered saline was free of $MgCl_2$ and $CaCl_2$. Adhered bacteria were then fixated by adding a 2.5% (V/V) glutaraldehyde solution in PBS for 30 min at room temperature. The fixative was removed afterward, and the remaining material was washed off by thorough rinsing with buffer solution (PBS, 1 mL, 2 times). Subsequently, the adhered bacteria were dehydrated by successive ethanol soaking (i.e., soaking in water-ethanol mixtures, 25, 50, 60, 70, 80, 90, and 100% (V/V), 15 min each, and last step twice). Then the samples were placed in a vacuum dryer overnight at room temperature. Sterilized consumables were used throughout. To avoid charging, the dried surfaces were sputter-coated with an nm-thick layer of Pt (BalTec MED 020 Modular High Vacuum Coating System, Argon at 2 × 10^{-2} mbar. 7 nm Pt and 30 mA).

5.4.17 DETECTION AND CALCULATION OF AVERAGE BACTERIA NUMBER ON BARE AND COATED PU TUBES

Based on SEM images, the area covered by bacteria on the PU tubes was evaluated using the Analyze Particles plugin of ImageJ. Background subtraction was applied before thresholding to correct for an inhomogeneous background. The threshold was chosen using the default method of ImageJ, being a modified IsoData algorithm. Statistics were derived from the evaluation of 14 to 24 images per sample (3 samples in total). The number of bacteria per image (and thus per area) was calculated by dividing the coverage area of the bacteria by the average area of a single bacterium. Afterward, the average number of bacteria per area of each sample was calculated. Finally, the average number of bacteria per area and corresponding standard deviation based on the samples was calculated. **Figure 47** shows an example of this analysis, recognized bacteria areas are highlighted in cyan.

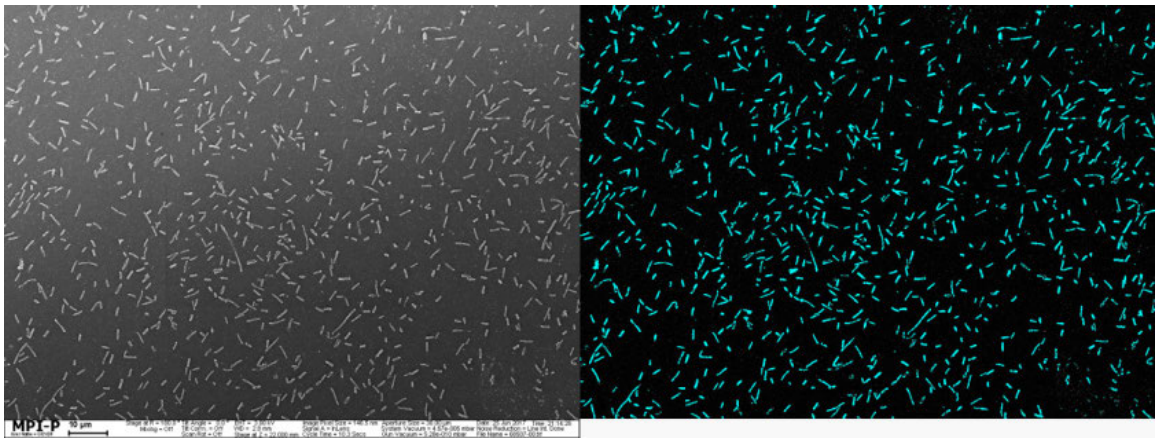

Figure 47. SEM image of original data (left) and the recognized bacteria (right, cyan) on a bare PU tube.

Due to the high surface roughness of the nanofilament-coated PU tubes, the bacteria could not reliably be detected using the above-mentioned procedure; therefore, bacteria per image (and thus area) were counted manually. Statistics were derived using at least 20 images per sample (2 samples for each nanofilament-coated PU tube). Afterward, the average number of bacteria per area, and the corresponding standard deviation over all samples was calculated.

5.5 AUTHOR CONTRIBUTIONS

F. Geyer fabricated the coated tubes, carried out the experiments unless stated otherwise below, and wrote the manuscript. M. D'Acunzi and M. Müller assisted with the coating of

the tubes. C.-Y. Yang, P. Baumli, N. Encinas, and V. Mailänder carried out the bacteria incubation experiments. A. Kaltbeitzel contributed to the data analysis of the bacteria experiments. P. Baumli conducted the XPS measurements. F. Geyer, D. Vollmer, and H.-J. Butt contributed to experimental planning, data analysis, and manuscript preparation. All authors reviewed and approved the manuscript.

5.6 ACKNOWLEDGMENTS

This work was supported by the ERC Advanced Grant 340391 – SUPRO (H.-J.B.), the German Research Foundation (DFG) with the Collaborative Research Center 1194 (H.-J.B., F.G.), the European Union's Horizon 2020 research and innovation program LubISS No. 722497 (D.V., P.B.), the DAAD-MoST sandwich scholarship (C-Y.Y.) and the Marie Skłodowska-Curie fellowship 660523-NoBios-ESR (N.E.). [redacted] are acknowledged for technical support.

6 POLYHEDRAL LIQUID MARBLES

Florian Geyer,[1] Yuta Asaumi,[2] Doris Vollmer,[1] Hans-Jürgen Butt,[1] Yoshinobu Nakamura,[3] and Syuji Fujii[3]

[1]Max Planck Institute for Polymer Research, Ackermannweg 10, 55128 Mainz, Germany
[2]Graduate School of Engineering, Osaka Institute of Technology, 5-16-1, Omiya, Asahi-ku, Osaka 535-8585, Japan
[3]Department of Applied Chemistry, Faculty of Engineering. Osaka Institute of Technology, 5-16-1, Omiya, Asahi-ku, Osaka 535-8585, Japan

Abstract: A new type of armored droplet, a so-called polyhedral liquid marble, is introduced in this work. These armored liquid marbles consist of liquid droplets stabilized by hydrophobic hexagonal plates made of poly(ethylene terephthalate), which adsorb to the liquid-air interface. Depending on the specific combination of plate size and droplet diameter, the plates self-assemble into highly ordered hexagonally-arranged domains. Even tetrahedral-, pentahedral-, and cube-shaped liquid marbles composed of only 4 to 6 plates are demonstrated. During evaporation of the internal liquid, due to the high adsorption energy of the plates at the liquid-air interface, the overall surface area stayed constant, resulting in strongly deformed polyhedral liquid marbles. In line with this, highly asymmetric polyhedral liquid marbles and letters are obtained due to the strong interfacial jamming exerted by the rigid hexagonal plates. This is particularly pronounced for larger plate sizes leading to liquid marbles with unusually sharp edges (for example, rectangular edges). The polyhedral liquid marbles exhibit various stimuli-responsive behaviors being exposed to water, ammonia, or tetrahydrofuran vapors. Air-driven polyhedral liquid marbles floating on water can reach velocities of several centimeters per second.

Keywords: liquid marbles, interfacial jamming, wetting, stimuli-responsive

This chapter is reprinted with permission from F. Geyer *et al., Adv. Funct. Mater.* **2019**, 1808826.

Important Supporting Figures can be found in Appendix 10.2.

6.1 INTRODUCTION

Studying the adsorption of solid particles at air-water and oil-water interfaces is of broad interest.[181] Recently, various novel concepts and materials such as colloidosomes,[196, 257] armored bubbles,[182, 302] dry water,[179] and liquid marbles (LMs) were introduced.[184, 186-188, 191, 197] LMs are liquid droplets coated with particles, which are adsorbed at the liquid-gas interface. These armored droplets are non-wetting, soft, and elastic since the particles protect the inner liquid from wetting the substrate underneath.[303] LMs in air are different from emulsions and foams as they require particles for stabilization and cannot be stabilized by molecular surfactants. LMs have been utilized in various potential applications, such as transport of liquids,[200] miniature reactors,[194, 199] microcapsules,[192] micro bioreactors for blood analysis,[198] sensors,[190] accelerometers,[203] and pressure-sensitive adhesives.[193]

LMs can be prepared using solid particles with various chemical compositions, including organic, inorganic, and composite particles. Most of the literature is concerned with (near) spherical particles and their aggregates. However, studies on LMs stabilized with non-spherical particles or stabilizers are rare. Thus, it is crucial to reveal and understand the relationship between solid particle shape and LM structure formation to utilize the LMs. Herein, we introduce a new type of LM, a so-called polyhedral LM. The polyhedral LMs are stabilized using hydrophobic hexagonal plates monodisperse in shape and size. The questions addressed in this study are: *(1)* Can hexagonal plates stabilize LMs? Which ratio between plate and droplet size can be achieved? *(2)* How do the plates self-assemble at a curved air-water interface, especially when the curvature and plate size are comparable? *(3)* What are the properties and functionalities of the polyhedral LMs?

6.2 RESULTS AND DISCUSSION

Poly(ethylene terephthalate) (PET) hexagonal plates (**Figure 48**a) with monomodal distributions in both size (Major axis: $A = 2s = 0.27 \pm 0.04$ mm (15% rel. error), 0.34 ± 0.01 mm (3% rel. error), 1.14 ± 0.04 mm (4% rel. error) and 2.48 ± 0.04 mm (2% rel. error); side length $s = 0.14$ mm, 0.17 mm, 0.57 mm and 1.24 mm, respectively) and thickness ($d = 40$–55 μm for all the samples) were used in this study (Figure S1 in Appendix 9.2 for optical and scanning electron microscopic (SEM) images). The original PET plates were hydrophilic and wetted by water, being unable to stabilize LMs. The plates were hydrophobized by modification with 1*H*,1*H*,2*H*,2*H*-perfluorodecyltrichlorosilane in *n*-hexane. Energy

dispersive X-ray (EDX) spectroscopy confirmed the surface coating of the PET plates by the silane (Figure S2). The static contact angle of a 10 µL water droplet measured on a fluorinated PET sheet was 110° ± 5° (critical surface tension was estimated to be approximately 5 ± 3 mN m^{-1} by Zisman plot; the value is quite low and likely influenced by the roughness of the substrate; Figure S3 in Appendix 10.2) indicating a hydrophobic fluorinated surface.

Water droplets (60 µL) were deposited onto the dried hydrophobic plates using a micropipette. During gentle rolling of the water droplets on the beds, the liquid was spontaneously encapsulated by the plates, and LMs were formed (**Figure 48**b). The coating of the water droplets by the plates rendered them both hydrophobic and non-wetting. The plates adsorbed at the air-water interface of the droplet form a certain contact angle θ with respect to the side wall of the plates (**Figure 48**c,d), which is mainly determined by the hydrophobic surface modification of the plates. Imaging of the lower side of a polyhedral LM using laser scanning confocal microscopy (LSCM) revealed that the contact line is pinned at the inner edge of the plates, roughly in parallel with the plate's long surface and perpendicular to its normal direction ($\theta \approx 90°$). The air-water interface and thus the droplet (**Figure 48**d, bottom; shown in blue) was trapped at the inner side of the plates. In accordance with that, the distance h between the outer side of the plates (**Figure 48**d, bottom, reflection on the outer side of the plate shown in yellow) and the air-water interface was ≈40 µm, which corresponds to the thickness of the plates. This resembles the situation of a water droplet on a superhydrophobic surface consisting of fluorinated micropillars.[61-62] Hence, the hexagonal plates act as a mobile micropillar layer. The LMs remained stable even after transfer from the plate beds onto solid substrates, such as PET or hydrophilic glass slides.

Optical microscopy images show the microstructure of the LMs prepared using 0.27 mm, 0.34 mm, 1.14 mm, and 2.48 mm-sized plates, placed on a hydrophilic glass slide (**Figure 48**e, left to right). Polyhedral LMs were formed in all cases. Plates spontaneously arranged in a hexagonal two-dimensional crystal-like structure, which is readily apparent on the LM surfaces of the 0.34 mm and 1.14 mm-sized plate systems (**Figure 48**f). If the droplet diameter (here: $D \approx 6$ mm) is considerably larger than the plate size, the droplet curvature is small compared to the plate size, and the plates can fully attach to the droplet, forming highly ordered two-dimensional domains on the surface of the droplet. LMs prepared with the 0.34 mm-sized plates showed the highest order. The plates spontaneously

self-assembled to form well-ordered arrays on the droplet's surface just by rolling, even though the LMs were formed from randomly oriented plate beds.

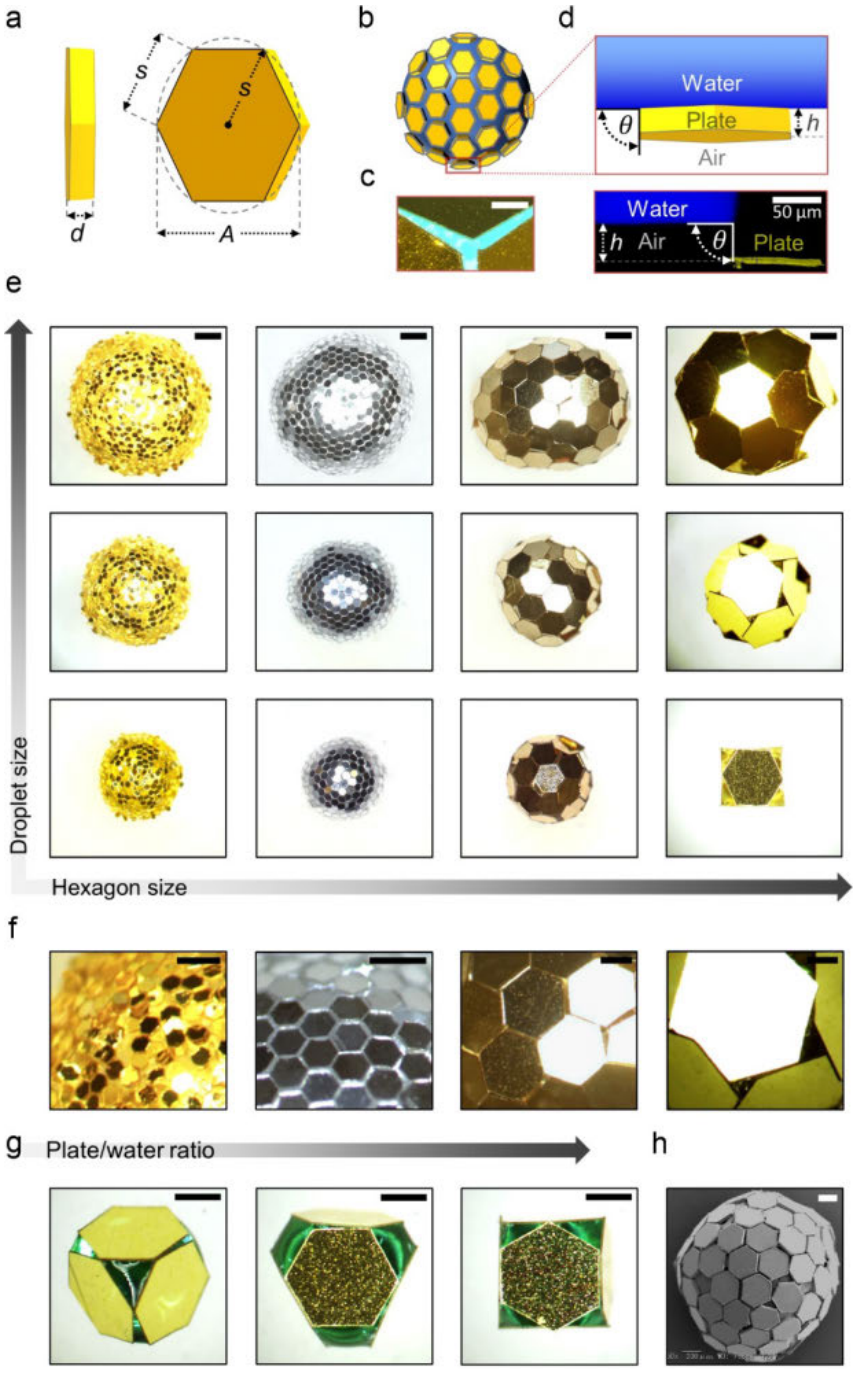

Figure 48. **a**) Schematic of the hexagonal fluorinated PET plates used to stabilize polyhedral liquid marbles (LMs) with thickness *d*, main axis *A*, and side length *s*. **b**) Schematic of a polyhedral LM. **c**) Optical microscopic image of plates (yellowish; with *A* = 2.48 mm) adsorbed on a 60 µL water droplet (with Brilliant Blue dye, 20 mg L^{-1}). Scale bar: 0.5 mm. **d**) The fluorinated plates adsorb to the air-water interface forming a contact angle *θ*. Laser scanning confocal microscopy (LSCM) image from underneath a polyhedral LM (15 µL water containing ATTO488, fluorescence shown in blue, reflections in yellow) shows that $\theta \approx 90°$. The distance *h* between the outer side of the plate and the air-water interface is ≈40 µm. **e**) Optical microscopy images of polyhedral LMs prepared with different plate sizes (*A* = 0.27 mm, 0.34 mm, 1.14 mm, and 2.48 mm; left to right) and different droplet volumes (60 µL, 30 µL, and 15 µL; top to bottom). Scale bar: 1 mm. **f**) Magnified microscopic images revealing the microstructure of the polyhedral LMs with different plate sizes (*A* = 0.27 mm, 0.34 mm, 1.14 mm, and 2.48 mm; left to right). Scale bars: 0.5 mm. **g**) By tuning the plate to water ratio (15 µL droplets with brilliant blue dye) using the largest 2.48 mm-sized plates (a total of 4 to 6 plates from left to right), different polyhedral morphologies were obtained. Scale bar: 1 mm. **h**) SEM image of a dried cyanoacrylate-treated 3 µL polyhedral LM using 0.34 mm-sized plates. Scale bar: 200 µm.

Parts of the plates stuck out of the LM's surface into the air phase in the case of the largest 2.48 mm-sized plate system, where the droplet diameter ($D \approx 6$ mm) was comparable to the plate size. The plates were tangent to the LM surface. A significantly lower degree of order was observed for the smallest 0.27 mm-sized plate system correlating to its higher polydispersity[304] and its smaller size.[305]

The diameters of the LMs were varied in a range between approximately 6 mm and 2.5 mm simply by changing the volume of the inner water droplet (60 µL–15 µL) (**Figure 48**e; top to bottom). For the 0.27 mm and 0.34 mm-sized plate systems, the decrease of droplet volume yielded more spherical LMs. Since the plate sizes were much smaller than the radii of the droplets, the plates could fully attach to the droplets' surfaces. The 1.14 mm-sized plates started to stick out of the LM surfaces into the air phase for droplet volumes ≤30 µL. The droplet curvature increased, and the stiff plates could only partially attach to the droplet surface. Using the 2.48 mm-sized plates, polyhedral LMs with a near-spherical shape formed for 30 µL droplets. Notably, when reducing the droplet volume to 15 µL ($D \approx 2.5$ mm), LMs with various polyhedral shapes, including tetrahedron, pentahedron, and cube, were obtained by tuning the plate to water ratio (**Figure 48**g). Depending on the number of plates adsorbed on the water droplet, the polyhedral LM spontaneously assumed the different shapes. Water droplets could be stabilized using as few as 4 to 6 plates. Due to the shape and rigidity of the hexagonal plates, the droplet could not be fully covered by the plates, leading to LMs with open faces. This is especially apparent for the polyhedral LM with 5 plates (**Figure 48**g; middle). Here, the hexagonal plate on the top and bottom of the LM kept the axial plates apart, whereas the capillary forces kept them in place, yielding a very uniquely shaped LM.

Large LMs using 0.34 mm and 2.48 mm-sized plates containing 120, 480, and 960 µL water drops were fabricated. Their shapes changed from oblong to puddle with an increase of drop volume (Figure S4 in Appendix 10.2). Crystalline two-dimensional array structures developed in large areas. Despite the difference in the nature of the materials and length scales, the patterns formed on the LM surfaces are similar to the honeycomb structure built by honey bees in their nests. For the large plates, the size of the crystalline domains continually increased as the droplet/plate size ratio became larger. On the other hand, using the smaller 0.34 mm-sized plates, crystalline domain sizes hardly changed for drop volumes of 480 µL and 960 µL. Up to 50 plates per two-dimensional crystal were observed, corresponding to domain sizes of approximately 3–4 mm.

The liquid-air interface of a 3 µL polyhedral LMs was solidified by exposing it to ethyl 2-cyanoacrylate vapor, the main component of superglues. Ethyl 2-cyanoacrylate readily absorbs and polymerizes at air-water interfaces,[306] solidifying the water interface between and underneath the plates. After superglue treatment, the polyhedral LM preserved its spherical, polyhedral morphology and did not collapse during/after the drying process, indicating that the surface of the LM was rigid (**Figure 48**h). The hexagonally-packed plate arrays were mostly preserved.

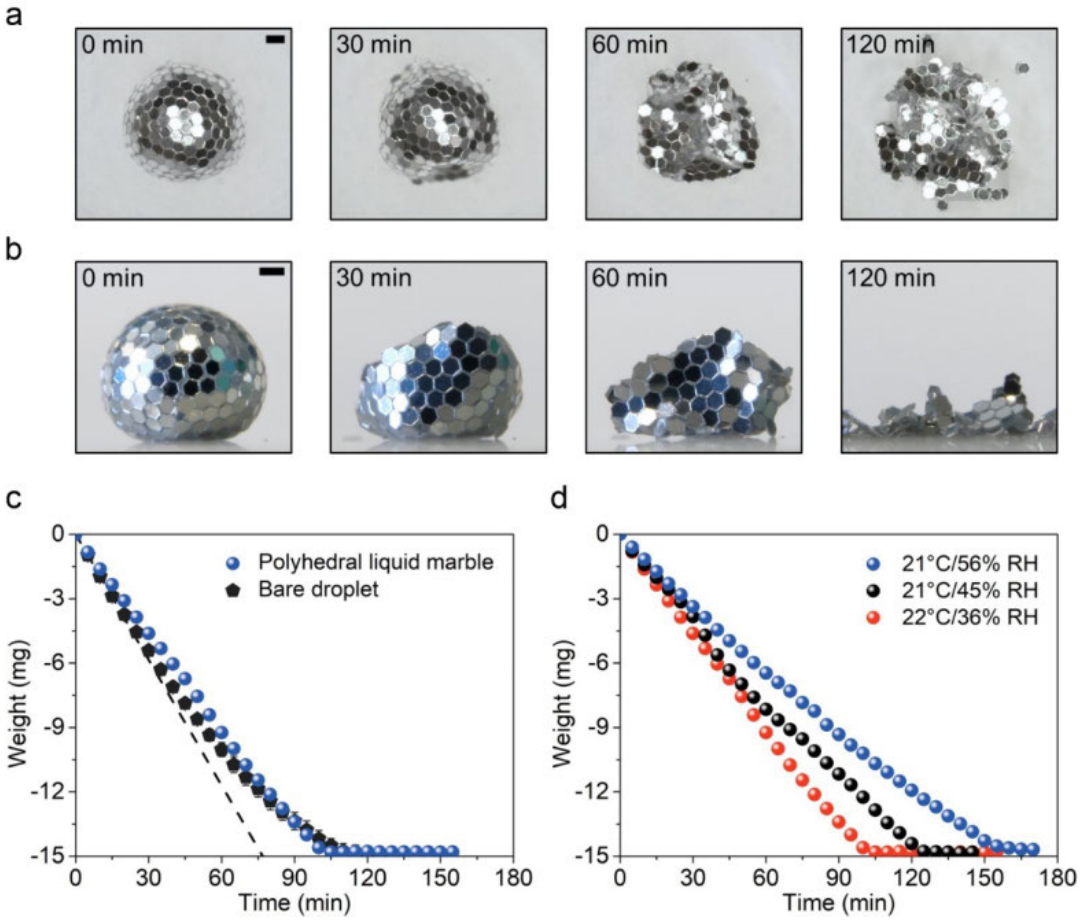

Figure 49. a,**b**) Microscopic images from the top (a) and side view (b) showing morphological changes of polyhedral LMs (15 µL; 0.34 mm-sized plates) during evaporation. Scale bars: 0.5 mm. **c**) Comparison of the evaporation of a polyhedral LM (15 µL; 0.34 mm-sized plates) at 36 ± 5% relative humidity (RH) versus a 15 µL water droplet on a superhydrophobic substrate (average of three repeats at an avg. RH of 37 ± 5%) at 21–22 °C. **d**) Weight loss during evaporation of polyhedral LMs (15 µL; 0.34 mm-sized plates) at different humidities (56 ± 5% RH, 45 ± 5% RH, and 36 ± 5% RH).

Detailed SEM images show that only a monolayer of the hexagonal plates was adsorbed at the air-water interface and confirm $\theta \approx 90°$ obtained by the LSCM images (Figure S6 in Appendix 10.2).

When drying the polyhedral LMs, the morphology changed. As an example, drying of polyhedral LMs of 15 µL volume armored with 0.34 mm-sized plates is shown in **Figure 49**a,b (Figure S7 for examples of the 0.27 mm and 1.14 mm-sized plate systems). Slow evaporation of the inner water of the LM induced buckling on the LM's surface. This can be explained by the surface jamming effect of the plates at the air-water interface due to the high adsorption energy ΔG at the interface. The adsorption energy (ΔG)[184, 307] is defined as the difference in free energy between a system where one face of a plate is in contact with water as compared to a system where the plate is fully in contact with air plus a free air-water interface. Thus, ΔG can be estimated using Eq. 40 (see Experimental Section 6.4.14 for details).

$$\Delta G = \frac{3\sqrt{3}}{2} s^2 (\gamma_{AS} + \gamma_{AW} - \gamma_{WS}) \quad (40)$$

where $\gamma_{AS} = 5$ mN m^{-1}, $\gamma_{WS} = 30$ mN m^{-1}, and $\gamma_{AW} = 73$ mN m^{-1} are the air-plate, water-plate, and air-water interfacial energies, respectively (γ_{WS} was determined using Young's equation with a water contact angle of 110°). Using Eq. 40, the ΔG values of the plates adsorbed at air-water interfaces were calculated to be 2×10^{-9} J, 4×10^{-9} J, 4×10^{-8} J, and 2×10^{-7} J for 0.27 mm, 0.34 mm, 1.14 mm, and 2.48 mm-sized plates, respectively. These values are more than three orders of magnitude higher than those of micrometer-sized spherical particles adsorbed at air-water and oil-water interfaces.[183]

The plates did not detach or flip off during evaporation, because of the high adsorption energy. The total surface area of the LM stayed almost constant, and the loss of volume was compensated by deformation. For comparison, a bare water droplet placed on a superhydrophobic substrate decreased its volume via evaporation while remaining nearly spherical (Figure S8). In contrast to the LM, the air-water interfacial area decreased along with the decrease of droplet volume.

The water evaporation of the LMs and bare water droplets (**Figure 49**c,d) was evaluated gravimetrically at 21–22 °C and three humidities varying between 35% and 55% relative humidity (RH). Surprisingly, the mass and thus volume decreased almost linearly with time for the LMs. The water evaporation rate of a polyhedral LM of 15 µL volume was ≈0.14 mg min^{-1}, and the water was completely evaporated after ≈105 min at 36 ± 5% RH. At 45 ± 5% and 56 ± 5% RH, the evaporation of the inner liquid slowed down, and evaporation times increased to ≈125 min and ≈155 min, respectively. The evaporation of bare water droplets of the same volume followed the $V^{2/3}$ law,[308] implying that evaporation is determined by the shrinking spherical shape of the droplet (Figure S9). At 21–22 °C and

avg. RH of 37 ± 5%, the droplet was evaporated after ≈110 min. Thus, even though the polyhedral LM was armored with hexagonal plates, the evaporation of the inner liquid was slightly faster than the evaporation of a bare droplet since the LM retained its surface areas whereas the bare droplet decreased its surface area.[309] The final stage of drying is interesting: the LMs broke down due to gravity and left cohesionless residues of plates after complete drying. Just before complete evaporation, the plates stuck to each other due to lateral capillary forces mediated by residual water.

Spherocylindrical polyhedral LMs (**Figure 50**a) with aspect ratios larger than 10 can be created by either (1) merging polyhedral LMs, by (2) withdrawing liquid from the marble, or by (3) placing excess plates on prepared LMs and deforming those by external forces. To obtain a cylindrical shape, the LMs were then rolled back and forth along one axis. Being able to create cylindrical LMs is strikingly different from bare droplets, where the surface area is minimized in order to minimize the interfacial energy. The LMs behaved in an inelastic manner, and the long cylindrical shapes did not undergo a Rayleigh-Plateau capillary instability. The inelastic characteristics arise from the steric jamming of plates at the air-water interface. Jamming of colloidal particles at interfaces has already been employed to kinetically trap fluid morphologies, including non-spherical armored bubbles and droplets[310-312] as well as bicontinuous interfacially jammed emulsion gels (bijels).[313] The shapes of the jammed LMs can be plastically rearranged to various stable configurations if subject to inhomogeneous external stresses (**Figure 50**b,c). The high aspect ratio cylindrical LM could be rearranged to write the letter “L” (**Figure 50**a to **Figure 50**b) by applying an external force using a spatula. Additionally, a dumbbell-like shape could be obtained (**Figure 50**c). We found that the large plates exhibit an even stronger interfacial jamming. Deposition and rolling of water droplets on the plates already yielded highly deformable polyhedral LMs. Thus, the liquid letter “A” was easily formed using the 2.48 mm-sized plates (**Figure 50**d). This principle was expanded to transparent $A = 2.35 \pm 0.03$ mm-sized plates (Figure S10). By merging a few LMs, the initials of polyhedral liquid marble “PHLM” were written (**Figure 50**e, Movie S1 shows the strong interfacial jamming behavior and formation of letters within a few seconds). It should be noted that these LMs can feature extremely sharp edges having an angle of 90° (see inset in **Figure 50**e).

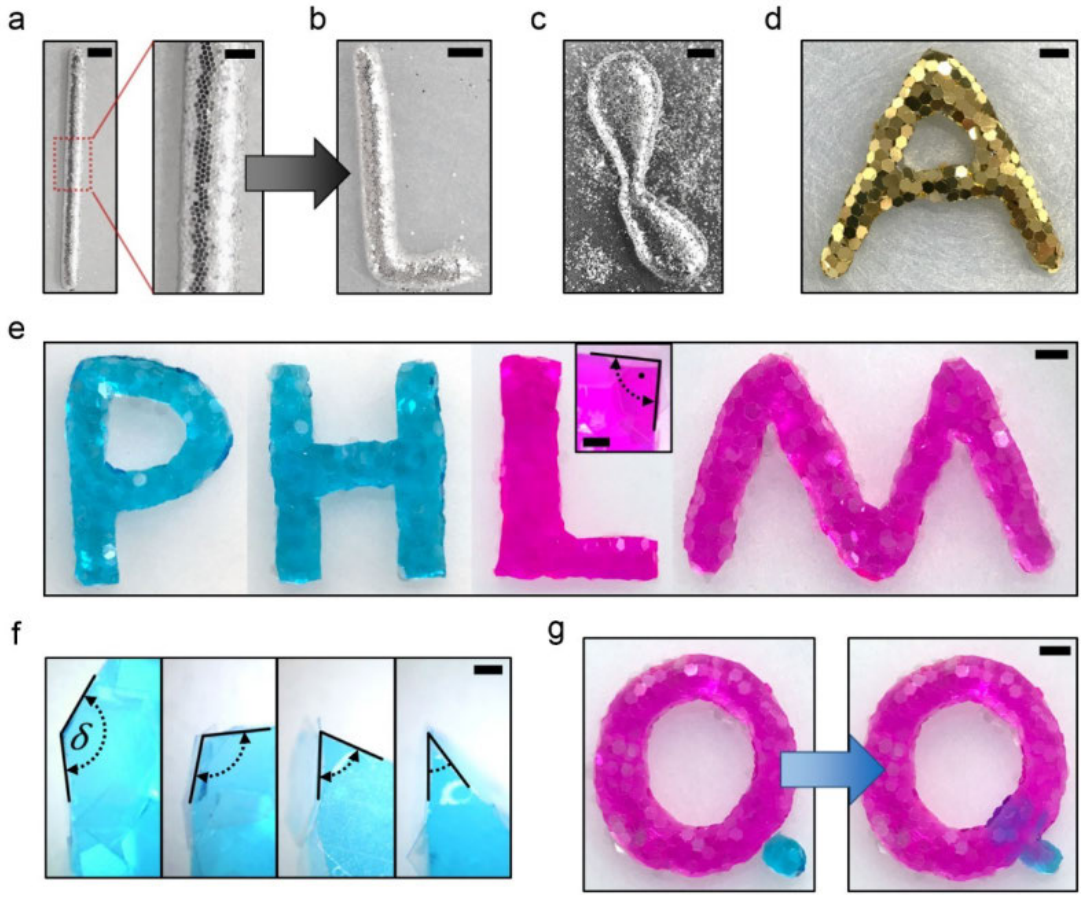

Figure 50. **a**) Spherocylindrical jammed polyhedral marble with an aspect ratio of 12 prepared with 0.34 mm-sized plates and containing water. Scale bars: 5 mm (left), 2 mm (right). **b**) Polyhedral letter "L" by deforming the high aspect ratio LM. Scale bar: 5 mm. **c**) Dumbbell-like shaped polyhedral LM with convex and concave areas. Scale bar: 5 mm. **d**) Polyhedral letter "A" showing strong interfacial jamming and shape control, formed with 2.48 mm-sized plates. Scale bar: 5 mm. **e**) Initials of the term polyhedral liquid marble: PHLM, formed using transparent 2.35 mm-sized plates and dyed water. The edges of the letters can be very sharp (see inset of letter "L"). Scale bar: 5 mm, 0.5 mm (inset). **f**) The edge angle δ of the polyhedral LMs can be tuned between >120° and <45°. Scale bar: 0.5 mm. **g**) Merging of two polyhedral LMs having a blue and a pink dye to form the letter "Q." The mixing of the two dyes can be observed inside of the resulting LM. Scale bar: 5 mm.

We tuned the edge angle δ of a polyhedral LM between >120° and <45° (**Figure 50**f). Such well-defined edges were previously not available with common LMs prepared using spherical particles or particle aggregates. By merging two LMs containing different dyes (pink and blue dye), the letter "Q" was formed (**Figure 50**g). The mixing of the dyes inside of the resultant LM could be observed through the transparent PET plates, indicating that the liquid phases became continuous.

To show that the jammed interface is not a thermodynamically stable state, we exposed a cylindrical polyhedral LM containing hygroscopic saturated LiCl solution to water vapor (Figure S11a in Appendix 10.2). The cylindrical shape gradually changed to a spherical shape during water uptake from the vapor phase (due to an increase of droplet volume

and surface area), indicating relaxation of the jammed interface. The polyhedral LM grown via water absorption was now placed under dry atmosphere in the presence of silica gel (Figure S11b in Appendix 10.2). The LM size decreased, keeping its spherical shape and eventually started buckling. After 50 h, the LM was dried. This dried polyhedral LM was now exposed to humid atmosphere again, leading to the growth of the LM. It resumed to its previous spherical shape (Figure S11c in Appendix 10.2), yet the LM could not return to its non-equilibrium jammed cylindrical shape. This further demonstrates that the jamming can be released by an external stimulus.

Polyhedral LMs are simultaneously responsive to different stimuli (**Figure 51**a,b). A transparent polyhedral LM (prepared with $A = 1.13 \pm 0.04$ mm-sized transparent PET plates) containing 30 µL water with the pH-responsive dye phenolphthalein was first exposed to ammonia vapor (**Figure 51**c). The absorption of ammonia increases the pH from neutral to slightly basic, resulting in a color change of the liquid inside of the LM at pH = 8.2. Close observation of the LM (Figure S12 in Appendix 10.2) shows that the ammonia vapor penetrated through the gaps between the PET plates and slowly diffused and distributed over the whole liquid marble. After complete color change, the LM was exposed to tetrahydrofuran (THF) vapor. Within the first 30 s of exposure, the volume of the LM increased slightly. Then, suddenly after 33 s, the polyhedral LM collapsed. Due to the uptake of THF, the surface tension of the liquid phase inside of the LM decreased. At a certain point, the liquid started wetting the plates, most likely inducing a Cassie-to-Wenzel-like[62] transition. The liquid started contacting and spreading on the glass slide underneath. A photograph, captured from underneath a broken LM (Figure S13 in Appendix 10.2) prepared with non-transparent plates and exposed to THF, shows that the liquid spread toward a certain direction (here: toward the left). Surprisingly, although polyhedral LMs exhibit only one monolayer of plates, they can be transferred and float on a planar water surface (**Figure 51**d). After transfer, the liquid-air interfaces of the water inside and underneath the LM are separated by just a monolayer of plates (Figure S14 in Appendix 10.2). The polyhedral LM remained stable on the water surface and could float for more than 1 h. The distance between the two interfaces h should be close to the plate thickness $d \approx 40$ µm. Nonetheless, this tiny air gap is enough to separate the two water interfaces and let the polyhedral LM float.

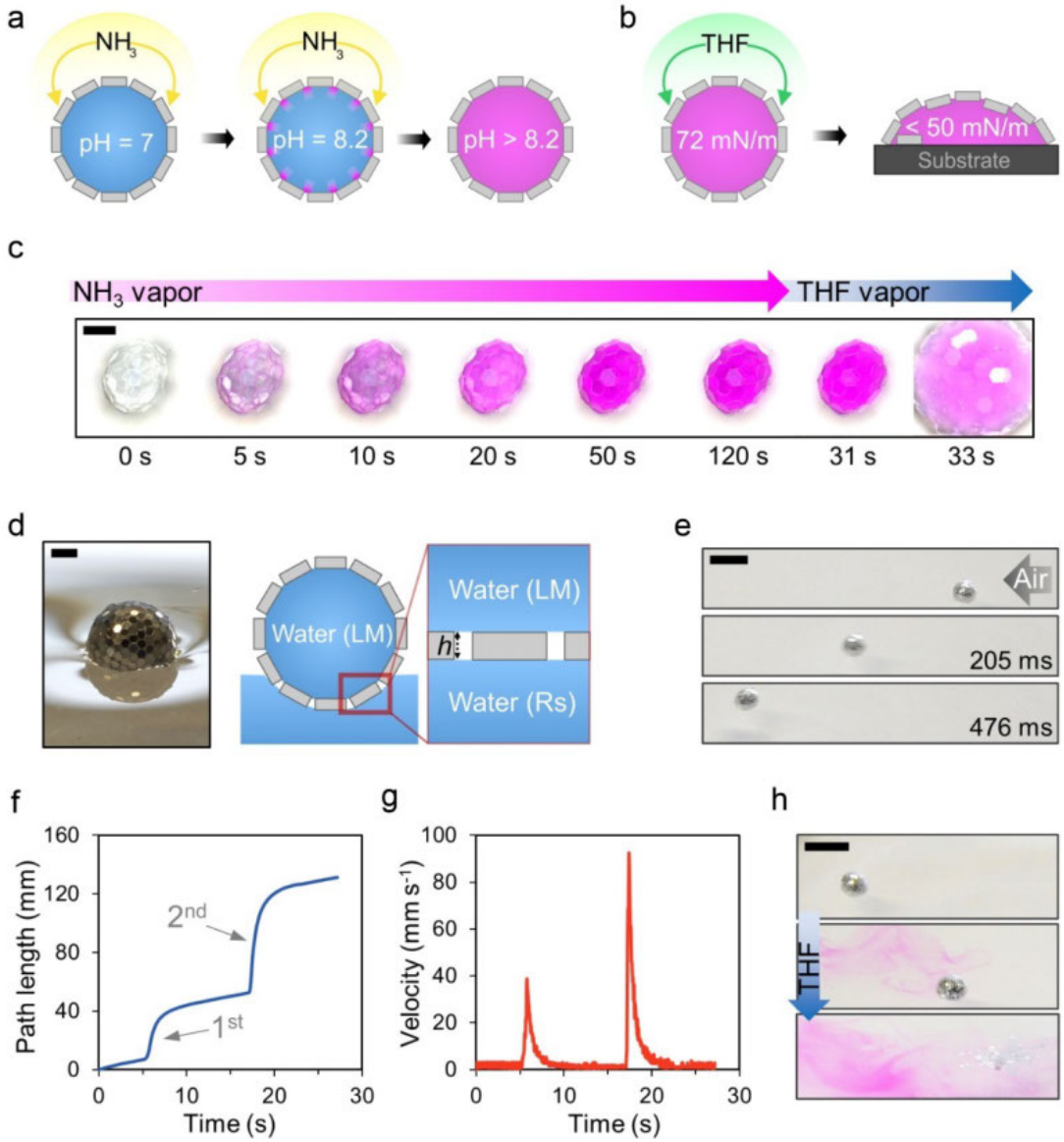

Figure 51. a,**b**) Schematic of a stimuli-responsive polyhedral LM. Due to the absorption of (a) NH_3 vapor and the resulting pH changes, the LM (containing phenolphthalein) changes its color from colorless and transparent to pink. The absorption of (b) tetrahydrofuran (THF) leads to a decrease of surface tension of the inner liquid and thus a Cassie-to-Wenzel-like transition between the hexagonal plates. **c**) Stimuli-responsive polyhedral LM (30 µL, 1.13 mm-sized transparent plates) exposed to NH_3 vapor for 120 s and subsequently to THF vapor. Scale bar: 2 mm. **d**) A polyhedral LM (15 µL; 0.34 mm-sized plates) floating on a planar water surface. The two air-water interfaces are separated by just a monolayer of plates, which corresponds to a distance of $h \approx d \approx 40$ µm. Scale bar: 1 mm. **e**) Locomotion of a 15 µL polyhedral LM on a water surface driven by air blows. Scale bar: 5 mm. **f**,**g**) Path and corresponding velocity analysis of air-driven polyhedral LM locomotion on water for 2 blows. **h**) Stimuli-induced disruption of a 15 µL polyhedral LM by the addition of THF to the water surface. The LM contained a 3 wt% NaOH solution, and the water reservoir contained phenolphthalein dye. Scale bar: 1 mm.

Fast locomotion of the LM on water can be induced by air blowing (**Figure 51**e). Depending on the strength of the blow, the LMs traveled several centimeters and reached peak velocities of almost 10 cm s^{-1}. This results in accelerations of up to 60 cm s^{-2} and forces of up to 10 µN (**Figure 51**f,g). A floating LM was disrupted by addition of THF to the water

surface (**Figure 51**h, Movie S2 shows the locomotion of a polyhedral LM induced by air blowing and disruption via THF). The LM contained 15 µL of a highly basic 3 wt% NaOH solution. After disruption, the LM changed the pH and color of the underlying water reservoir, which contained phenolphthalein. Thus, the LMs may be used as pH and surface tension sensitive sensors.

6.3 CONCLUSION

In conclusion, LMs stabilized by hydrophobic hexagonal PET plates are introduced. The arrangement of the plates depends on the ratio of the plate diameter *A* and the droplet diameter *D*. For small droplets, where *D* and *A* are of the same order of magnitude, the self-assembly of the hexagonal plates on the surface of the LMs results in the first examples of uniquely shaped polyhedral LMs, including cubic, tetrahedral and pentahedral structures. A similar yet different phenomenon is known from the so-called capillary origami where a highly elastic sheet wraps a droplet.[314] In contrast, the PET plates are rigid and not bend by the capillary forces. For large droplets ($D \gg A$), the surfaces of the LMs are composed of two-dimensional polycrystalline arrays of plates. The high adsorption energy of the plates at the air-water interface of the LMs prevents the plates from detaching, e.g., during evaporation, and leads to interfacial jamming. Highly jammed non-equilibrium shaped LMs, such as cylindrical droplets and letter-shaped marbles, can be formed. Those LMs exhibit tunable and extraordinarily sharp edges. The polyhedral LMs are stable enough to move on planar water surfaces and can be used as sensors as they are responsive to different stimuli. The use of the hexagonal plates enables unprecedented shape control, and the methodology for generation of these crystalline structures on curved surfaces is simple, scalable, and based on sustainable materials.

6.4 EXPERIMENTAL SECTION

6.4.1 MATERIALS

Experiments were carried out at room temperature. The following chemicals were used: 1*H*,1*H*,2*H*,2*H*-perfluorodecyltrichlorosilane (PFDTS, 96%, TCI), *n*-hexane (96%, Wako), ethanol (95%, Sigma-Aldrich), tetrahydrofuran (SAJ first grade, Sigma-Aldrich), ammonia solution (28 wt%, Sigma-Aldrich), lithium chloride (99.0%, Wako), sodium hydroxide (≥97%, Sigma-Aldrich), ethyl 2-cyanoacrylate (Aron Alpha Extra Sokkotayoto, Toagosei

Co., Ltd.), Brilliant Blue (San-Ei Gen F.F.I., Inc.), Food Red No. 106 (San-Ei Gen F.F.I., Inc.), phenolphthalein (extra pure, Kanto Chemical Co., Inc.), ATTO488 (ATTO-TEC). Purified and deionized water from Advantec MFS RFD240NA (GA25A-0715) and from Sartorius Arium Pro VF was used for all experiments. Hydrophilic PET plates ($A = 0.34 \pm 0.01$ mm) were purchased from Matsumura Kogei Co., Ltd. The other hydrophilic PET plates ($A = 0.27 \pm 0.04$ mm, 1.14 ± 0.04 mm, and 2.48 ± 0.04 mm) were purchased from Matsuno Industry Co., Ltd. Transparent hydrophilic PET plates ($A = 1.13 \pm 0.04$ mm and 2.35 ± 0.03 mm) were obtained from Nakajima Metal Leaf, Powder Co. Ltd. Reagents were used as received.

6.4.2 HYDROPHOBIZATION OF THE PLATES

The pristine plates (5–10 g) were washed repeatedly with ethanol (200–400 mL) until the supernatant remained clear (3–7 repeats). The washed plates were dried in vacuum overnight. Afterward, the dried plates were modified with PFDTS. Therefore, 3–10 g of the plates was suspended in a solution of 45 µL PFDTS in 45 mL *n*-hexane, and the mixture was shaken for approximately 30 s. During the reaction time of 30 min, the sedimented suspension was shaken every 5 min to ensure a homogeneous coating of the plates. Subsequently, the modified plates were rinsed at least twice with *n*-hexane.

6.4.3 PREPARATION OF POLYHEDRAL LIQUID MARBLES

The polyhedral liquid marbles (LMs) were prepared by simply rolling water droplets over a plate bed on a glass substrate or rough poly(chlorotrifluoroethylene) (PCTFE) dish. In the case of the tetrahedral-, pentahedral-, and cube-shaped LMs, 15 µL droplets were rolled over individual 2.48 mm plates placed on a surface-roughened PCTFE Petri dish. This allowed the droplet to pick up individual plates. Afterward, the prepared LMs may be transferred to other substrates like glass slides using a (plastic) spoon.

6.4.4 PREPARATION OF JAMMED POLYHEDRAL LIQUID MARBLES

To obtain jammed polyhedral LMs with non-equilibrium shapes, LMs prepared according to the previous paragraph (on roughened PCTFE Petri dish) were either merged, or water was withdrawn from the LM (half of the initial volume). Alternatively, an LM was prepared, and excess amounts of plates are placed on top of the LM. Now the LM could be deformed using a spoon, for instance, retaining the deformed shape. To prepare complex structures, the techniques mentioned above are combined to obtain the final result. LMs prepared with the large 2.48 mm and 2.35 mm-sized plates showed such strong interfacial

that they could be easily deformed even without the steps mentioned above (see Movie S1). Photographs were taken using an optical microscope and digital cameras. The colored LMs were dyed using Brilliant Blue (20 mg L^{-1}) and Food Red No. 106 (appears pink, 20 mg L^{-1}).

6.4.5 POLYMERIZATION OF ETHYL 2-CYANOACRYLATE ON THE AIR-WATER INTERFACE OF POLYHEDRAL LMS

A polyhedral LM (3 µL, 0.34 mm-sized plates) was placed on a pedestal in a reaction chamber with a vessel containing ethyl 2-cyanoacrylate. The ethyl 2-cyanoacrylate was then heated at 50 °C to saturate the gas phase with its vapor. Now, the ethyl 2-cyanoacrylate absorbed and polymerized at the air-water interface, solidifying the interface.[306] After a reaction time of 30 min, the polymerization was finished. Subsequently, the LM was dried up and imaged using the scanning electron microscope (SEM).

6.4.6 HYGROSCOPIC POLYHEDRAL LIQUID MARBLES

A polyhedral LM containing ≈100 µL of a saturated aqueous LiCl solution was prepared using 0.34 mm-sized plates and placed on a PCTFE Petri dish. A small watch glass (5 cm diameter) containing 500 µL water was placed near the LM, and the PCTFE dish was closed by placing another glass Petri dish onto it. For further sealing, Parafilm was applied. Afterward, the water uptake was observed using an optical microscope for 4 h. After that, the water reservoir was replaced by silica gel, and the drying process was observed for 50 h. Finally, the silica gel was replaced by a water reservoir again, and the water uptake was observed for 4 h.

6.4.7 STIMULI-RESPONSIVE POLYHEDRAL LIQUID MARBLES

A polyhedral LM (30 µL aqueous phenolphthalein solution, 1.1 mm-sized transparent plates) was placed on a large glass slide. The phenolphthalein solution was prepared by mixing 10 mL water with 10 µL 5 wt% ethanolic phenolphthalein solution. A small watch glass (5 cm diameter) containing 200 µL ammonia solution (28 wt%) was placed next to the LM, and both were covered by a glass Petri dish. The color change of the LM was observed using the optical microscope. After the color change was completed, the watch glass containing ammonia solution was removed and replaced by a watch glass containing 400 µL tetrahydrofuran (THF). Absorption of THF and breakage of the LM was observed using the optical microscope.

6.4.8 STIMULI-RESPONSIVE POLYHEDRAL LIQUID MARBLES ON WATER

A polyhedral LM (15 µL aqueous 3 wt% sodium hydroxide solution, 0.34 mm-sized plates) was transferred to a water surface (50 mL water containing 45 µL 5 wt% ethanolic phenolphthalein solution, in a glass Petri dish with a diameter of 10 cm). The LM was moved on the water surface by using an air blower. Afterward, a total of 330 µL THF was added to the water surface in 5 steps. Digital video cameras (Sony Handycam HDR-CX270 V with 30× optical zoom lens and Sony Alpha 7 II with Sony SEL2470Z Zeiss objective) were used to record photographs and movies. The velocity, acceleration, and applied force of and on the LMs were analyzed using the Keyence VW-9000 MotionAnalyzer software. The position of the center of mass $r(t)$ of the LMs was determined in each frame. The displacement $\Delta r(t)$ and the velocity $v(t) = \frac{\Delta r(t)}{\Delta t}$, with Δt being the video rate (30^{-1} s), were obtained from the time course of $r(t)$. The acceleration $a(t) = \frac{\Delta v(t)}{\Delta t}$, and the force $F(t) = ma(t)$, with m being the mass of the LM, were obtained from the changes of velocity $\Delta v(t)$. Thus, we could evaluate the velocity, acceleration, and force of the polyhedral LMs on the water surface, as previously reported.[315-316]

6.4.9 PREPARATION OF THE SUPERHYDROPHOBIC SURFACES

Candle soot-based superhydrophobic (and superoleophobic) surfaces were prepared according to ref.[41] The surfaces typically show static contact angles of >160° and 155° ± 5° as well as roll-off angles of 1° ± 1° and 5° ± 2° for 6 µL water and hexadecane droplets, respectively. The receding contact angle of water droplets was >160° as well. The PCTFE Petri dishes were roughened using sandpaper (grit size P200–P600).[317] Afterward, 15 µL droplets showed an almost spherical shape and could easily roll on the roughened Petri dish when tilted by 10–20°.

6.4.10 OPTICAL MICROSCOPY

Polyhedral LMs were observed using an optical microscope with an attached CCD camera (3.0 Megapixels USB Camera GR300BCM2, Shodensha Co., Japan). If not stated otherwise, the LMs were prepared and placed on a hydrophilic glass slide or a PCTFE dish and observed under the microscope under various magnifications. The scale bars were obtained by using a micrometer scale ruler. Brightness, contrast, and color temperature were adjusted to match between the individual images. For some images, background subtraction using ImageJ was applied.

6.4.11 LASER SCANNING CONFOCAL MICROSCOPY

Laser scanning confocal microscopy (LSCM) images were taken using an inverted confocal microscope (Leica TCS SP8 SMD, HC PL APO 40×/1.10 CORR CS2 water objective) using Leica LAS X software. A polyhedral LM (15 µL water containing ATTO488 dye, 0.34 mm-sized plates) was placed onto a glass slide (≈150 µm thickness), and the lower side of the LM was imaged using the LSCM. The fluorescence of ATTO488 in water is shown in blue, and the reflection of light (at the lower side of the plate) is shown in yellow **(Figure 48**d**)**. Reflection and fluorescence signals were recorded simultaneously. It should be noted that the water phase behind the hexagonal plate is not visible because the used plate was non-transparent. Only a strong reflection at the lower side of the plate is visible.

6.4.12 SCANNING ELECTRON MICROSCOPY

Scanning electron microscopy (SEM) images were taken with a VE-8800 instrument (Keyence, Japan) at gun voltages of 12 kV. To avoid charging, the samples were sputter-coated with gold using an Au coater (SC-701 Quick Coater, Elionix, Japan).

6.4.13 ADSORPTION ENERGY OF A PLATE

The adsorption energy (ΔG)[184, 307] is the free energy required for a plate to desorb from the air-water interface into the air phase and is defined as the difference in free energy between a system E_{Air}, where the plate is entirely in contact with air plus a free air-water interface, as compared to a system $E_{\mathrm{Interface}}$, where one face of a plate is in contact with water, and the other faces of the plate are in contact with air ($E_{\mathrm{Air}} - E_{\mathrm{Interface}}$). The energies E_{Air} and $E_{\mathrm{Interface}}$ for hexagonal plates are given by Eqs. 41 and 42, respectively.

$$E_{\mathrm{Air}} = \left(3\sqrt{3}s^2 + 6sd\right)\gamma_{\mathrm{AS}} + \frac{3\sqrt{3}}{2}s^2\gamma_{\mathrm{AW}} \tag{41}$$

$$E_{\mathrm{Interface}} = \left(\frac{3\sqrt{3}}{2}s^2 + 6sd\right)\gamma_{\mathrm{AS}} + \frac{3\sqrt{3}}{2}s^2\gamma_{\mathrm{WS}} \tag{42}$$

where s is the side length of the hexagonal plate; d is the thickness of the plate; and γ_{AS}, γ_{WS}, and γ_{AW} are the air-plate, water-plate, and air-water interfacial energies, respectively. Using Eqs. 41 and 42, ΔG is given by Eq. 43.

$$\Delta G = \frac{3\sqrt{3}}{2}s^2(\gamma_{\mathrm{AS}} + \gamma_{\mathrm{AW}} - \gamma_{\mathrm{WS}}) \tag{43}$$

Here, it was assumed that only one large plane of the plate is in contact with water, and side planes remained in contact with air. This simple approximation neglects the fact that the droplet has a spherical shape while the plate-water interface is planar.

6.5 AUTHOR CONTRIBUTIONS

F. Geyer fabricated the polyhedral liquid marbles and carried out the experiments. Y. Asaumi assisted with the preparation of the liquid marbles and took the SEM images. Y. Asaumi conducted the locomotion analysis of the air-driven liquid marbles on water. S. Fujii and F. Geyer wrote the manuscript. S. Fujii suggested the project; S. Fujii and F. Geyer planned the experiments. All authors reviewed, edited, and approved the manuscript.

6.6 ACKNOWLEDGMENTS

We thank [redacted] for technical support. [redacted] is thanked for the dyes (Brilliant Blue and Food Red No. 106). This work was supported by Grant-in-Aid for Scientific Research (B) (JSPS KAKENHI Grant Number JP16H04207; S.F.), Scientific Research on Innovative Areas “Engineering Neo-Biomimetics (No. 4402)” (JSPS KAKENHI Grant Numbers JP15H01602 and JP25120511; S.F.), “New Polymeric Materials Based on Element-Blocks (No. 2401)” (JSPS KAKENHI Grant Numbers JP15H00767 and JP25102542; S.F.), “Molecular Soft Interface Science (No. 2005)” (JSPS KAKENHI Grant Number 23106720; S.F.), ERC Advanced Grant No. 340391 “SUPRO” (H.-J.B., F.G.), the German Research Foundation (DFG) with the Collaborative Research Center 1194 (H.-J.B., F.G.), and the European Union’s Horizon 2020 research and innovation program LubISS No. 722497 (D.V.).

7 IMPACT AND OUTLOOK

This thesis contributes to the fabrication, application, and understanding of superhydrophobic and super-liquid-repellent surfaces as well as the basic understanding of drop movement on such surfaces. To fabricate super-liquid-repellent surfaces, silicone nanofilament coatings were employed. These coatings can be applied to a broad range of different surfaces, including flexible and stiff, organic and inorganic substrates.

By applying nanofilament coatings to such substrates, various kinds of applications can be realized, ranging from self-cleaning surfaces, antibacterial surfaces to gas exchange membranes. Self-cleaning surfaces are important for various environments, e.g., for walls, windows, or as cover for solar cells. A key parameter to maintain the integrity of superhydrophobic surfaces and their self-cleaning properties is to prevent clogging of the pores. Therefore, the pores need to be smaller than the contaminant size. Even nanoparticles with a diameter of 600 nm can be cleaned off a nanoporous nanofilament surface. However, not only the particle size is important but also the polarity. While hydrophobic particles only cause minor harm to such surfaces, small hydrophilic particles dispersed in a liquid are detrimental. A pore size of a few hundred nanometers (<500 nm) is suitable to keep off most possible contaminations. In industrial environments with higher nanoparticle concentrations, the pore size may be reduced accordingly. The self-cleaning properties of the coating are also reflected in the low lateral adhesion and friction forces of drops on the coating. As soon as self-cleaning fails, the adhesion increases. The DAFI method used to quantify the lateral adhesion and friction forces is a highly promising tool to characterize surfaces and self-cleaning and can be applied to various substrates. Furthermore, the method may be used to investigate the influence of other contamination types, such as biological contaminations.

Superomniphobic membranes based on nanofilament-coated fabrics can be utilized as gas contactor membranes. Even highly concentrated amine solutions can be repelled, yielding enhanced CO_2 exchange performances compared to conventional membranes. Wetting of the membrane is prevented. In times when humanity is threatened by global warming, and CO_2 emissions reach new record highs, research on such topics is highly relevant and may contribute to the search for efficient methods for carbon capture and storage. The superomniphobic membranes are not restricted to CO_2 capture and may also be useful for the separation and capture of other gases, such as H_2S and SO_2,[318-319] or related applications like membrane distillation.[320] Recently, new liquids for CO_2 capture,

such as ionic liquids showing higher loading capacities, were introduced.[321-323] Here, a superomniphobic membrane is essential since conventional membranes cannot repel such low surface tension liquids. Factors like impalement pressure and long-term stability of the Cassie state need to be carefully investigated and related to structural features of such membranes.

Finally, the results may be transferred to porous hollow fiber membranes to maximize the packing density and thus the exchange efficiency per volume. Here, nanofilament coatings are a suitable candidate to coat such fibers and tubes. Meter-long and narrow tubes can be coated with nanofilaments after activation, e.g., by Fenton reaction. The coating can be applied to a wide range of materials. The coatings also show antibacterial properties and may be suitable for medical devices like catheters to reduce infections of patients due to restrained biofilm formation. A major benefit of these coatings is that they maintain these properties independent of the wetting state, i.e., even in a fully wetted superhydrophilic state. These properties are also important for other applications where the surfaces are in contact with aqueous solutions, such as water pipelines or membrane distillation, to prevent fouling of such systems.[324]

Liquid marbles and self-cleaning of superhydrophobic surfaces are closely related. Liquid marbles can be formed during the pickup of contamination particles. During self-cleaning, the particles accumulate at the liquid-air interface at the bottom of the drop and are finally picked up at the receding contact line. The particle layer at the liquid-air interface forms a mobile superhydrophobic layer itself in the case of hydrophobic particles. This principle was utilized to prepare uniquely shaped liquid marbles with polyhedral shapes like a cube. A droplet on a plate bed basically sits on a loose superhydrophobic layer and picks up the particles from this bed in a self-cleaning manner. Despite the random orientation of the hexagonal plates on such a bed, highly ordered two-dimensional layers were formed on the polyhedral liquid marbles. Such liquid marbles have the potential to manipulate and transport small amounts of liquids or to be used as sensors since various gases can be exchanged through the gaps between the plates. They also present a novel model system to investigate crystallization on curved liquid surfaces.

8 REFERENCES

[1] P. G. de Gennes, *Rev. Mod. Phys.* **1985**, *57*, 827.

[2] S. Herminghaus, *Europhys. Lett.* **2000**, *52*, 165.

[3] D. Quéré *Annu. Rev. Mater. Res.* **2008**, *38*, 71.

[4] D. Bonn, J. Eggers, J. Indekeu, J. Meunier, E. Rolley, *Rev. Mod. Phys.* **2009**, *81*, 739.

[5] H.-J. Butt, K. Graf, M. Kappl, *Physics and Chemistry of Interfaces*, Wiley-VCH, Weinheim, Germany **2003**.

[6] G. Lagubeau, M. Le Merrer, C. Clanet, D. Quere, *Nat. Phys.* **2011**, *7*, 395.

[7] D. W. Pilat, P. Papadopoulos, D. Schäffel, D. Vollmer, R. Berger, H. J. Butt, *Langmuir* **2012**, *28*, 16812.

[8] D. 't Mannetje, A. Banpurkar, H. Koppelman, M. H. G. Duits, D. van den Ende, F. Mugele, *Langmuir* **2013**, *29*, 9944.

[9] R. Tadmor, P. Bahadur, A. Leh, H. E. N'guessan, R. Jaini, L. Dang, *Phys. Rev. Lett.* **2009**, *103*, 266101.

[10] M. J. Kreder, J. Alvarenga, P. Kim, J. Aizenberg, *Nat. Rev. Mater.* **2016**, *1*, 15003.

[11] I. Shestopalov, J. D. Tice, R. F. Ismagilov, *Lab Chip* **2004**, *4*, 316.

[12] Y. Zheng, H. Bai, Z. Huang, X. Tian, F.-Q. Nie, Y. Zhao, J. Zhai, L. Jiang, *Nature* **2010**, *463*, 640.

[13] K.-C. Park, S. S. Chhatre, S. Srinivasan, R. E. Cohen, G. H. McKinley, *Langmuir* **2013**, *29*, 13269.

[14] P. Cheng, X. Quan, S. Gong, X. Liu, L. Yang, in *Advances in Heat Transfer*, Vol. 46 (Eds: Y. I. C. J. P. A. Ephraim M. Sparrow, G. John M), Elsevier **2014**, p. 187.

[15] K. Rykaczewski, A. T. Paxson, M. Staymates, M. L. Walker, X. Sun, S. Anand, S. Srinivasan, G. H. McKinley, J. Chinn, J. H. J. Scott, K. K. Varanasi, *Sci. Rep.* **2014**, *4*.

[16] A. T. Paxson, J. L. Yagüe, K. K. Gleason, K. K. Varanasi, *Adv. Mater.* **2014**, *26*, 418.

[17] C. Yang, U. Kaipa, Q. Z. Mather, X. Wang, V. Nesterov, A. F. Venero, M. A. Omary, *J. Am. Chem. Soc.* **2011**, *133*, 18094.

[18] J. G. Nguyen, S. M. Cohen, *J. Am. Chem. Soc.* **2011**, *132*, 4560.

[19] K. P. Rao, M. Higuchi, K. Sumida, S. Furukawa, J. Duan, S. Kitagawa, *Angew. Chem. Int. Ed* **2014**, *126*, 8364.

[20] K. Jayaramulu, K. K. R. Datta, C. Rösler, M. Petr, M. Otyepka, R. Zboril, R. A. Fischer, *Angew. Chem. Int. Ed.* **2016**, *55*, 1178.

[21] S. Roy, V. M. Suresh, T. K. Maji, *Chem. Sci.* **2016**, *7*, 2251.

[22] Y. Zheng, X. Gao, L. Jiang, *Soft Matter* **2007**, *3*, 178.

[23] Z. Guo, W. Liu, B.-L. Su, *J. Colloid Interface Sci.* **2011**, *353*, 335.

[24] T. Young, *Phil. Trans. R. Soc. Lond.* **1805**, *95*, 65.

[25] K.-Y. Law, *J. Phys. Chem. Lett.* **2014**, *5*, 686.

[26] R. N. Wenzel, *Ind. Eng. Chem.* **1936**, *28*, 988.

[27] A. B. D. Cassie, S. Baxter, *Trans. Faraday Soc.* **1944**, *40*, 546.

[28] A. Lafuma, D. Quéré, *Nat. Mater.* **2003**, *2*, 457.

[29] M. Callies, D. Quéré, *Soft Matter* **2005**, *1*, 55.

[30] L. Feng, S. H. Li, Y. S. Li, H. J. Li, L. J. Zhang, J. Zhai, Y. L. Song, B. Q. Liu, L. Jiang, D. B. Zhu, *Adv. Mater.* **2002**, *14*, 1857.

[31] B. Bhushan, Y. C. Jung, *Prog. Mater. Sci.* **2011**, *56*, 1.

[32] Y. Y. Yan, N. Gao, W. Barthlott, *Adv. Colloid Interface Sci.* **2011**, *169*, 80.

[33] R. H. Dettre, J. Johnson, Rulon E., in *Contact Angle, Wettability, and Adhesion*, DOI: 10.1021/ba-1964-0043.ch008 (Ed: F. M. Fowkes), American Chemical Society, Washington, D.C. **1964**, Ch. 8, p. 136.

[34] W. Barthlott, C. Neinhuis, *Planta* **1997**, *202*, 1.

[35] X. Gao, L. Jiang, *Nature* **2004**, *432*, 36.

[36] H. J. Ensikat, P. Ditsche-Kuru, C. Neinhuis, W. Barthlott, *Beilstein J. Nanotechnol.* **2011**, *2*, 152.

[37] L. Mammen, K. Bley, P. Papadopoulos, F. Schellenberger, N. Encinas, H.-J. Butt, C. K. Weiss, D. Vollmer, *Soft Matter* **2014**, *11*, 506.

[38] M. D'Acunzi, L. Mammen, M. Singh, X. Deng, M. Roth, G. K. Auernhammer, H.-J. Butt, D. Vollmer, *Faraday Discuss.* **2010**, *146*, 35.

[39] A. Marmur, *Langmuir* **2004**, *20*, 3517.

[40] H. Teisala, M. Tuominen, M. Aromaa, J. M. Mäkelä, M. Stepien, J. J. Saarinen, M. Toivakka, J. Kuusipalo, *Surf. Coat. Technol.* **2010**, *205*, 436.

[41] X. Deng, L. Mammen, H.-J. Butt, D. Vollmer, *Science* **2012**, *335*, 67.

[42] E. Martines, K. Seunarine, H. Morgan, N. Gadegaard, C. D. W. Wilkinson, M. O. Riehle, *Nano Lett.* **2005**, *5*, 2097.

[43] D. Öner, T. J. McCarthy, *Langmuir* **2000**, *16*, 7777.

[44] B. Qian, Z. Shen, *Langmuir* **2005**, *21*, 9007.

[45] S. Minko, M. Müller, M. Motornov, M. Nitschke, K. Grundke, M. Stamm, *J. Am. Chem. Soc.* **2003**, *125*, 3896.

[46] X. Wang, B. Ding, J. Yu, M. Wang, *Nano Today* **2011**, *6*, 510.

[47] K. S. Birdi, CRC Press, Boca Raton **2015**.

[48] K. S. Birdi, *Handbook of Surface and Colloid Chemistry*, CRC Press, Boca Raton **2015**.

[49] P. L. du Noüy, *J. Gen. Physiol.* **1925**, *7*, 625.

[50] L. Wilhelmy, *Pogg. Ann.* **1863**, *119*, 177.

[51] W. A. Zisman, in *Contact Angle, Wettability, and Adhesion* (Ed: F. M. Fowkes), American Chemical Society, Washington, D.C. **1964**, Ch. 1, p. 1.

[52] F. M. Fowkes, *Ind. Eng. Chem.* **1964**, *56*, 40.

[53] D. K. Owens, R. C. Wendt, *J. Appl. Polym. Sci.* **1969**, *13*, 1741.

[54] W. Rabel, *Farbe und Lacke* **1971**, *77*, 997.

[55] D. H. Kaelble, *J. Adhesion* **1970**, *2*, 66.

[56] N. L. Jarvis, W. A. Zisman, *Surface Chemistry of Fluorochemicals*, U.S. Naval Research Laboratory, Washington, D.C. **1965**.

[57] J. J. Gilman, *J. Appl. Phys.* **1960**, *31*, 2208.

[58] T. Nishino, M. Meguro, K. Nakamae, M. Matsushita, Y. Ueda, *Langmuir* **1999**, *15*, 4321.

[59] T. Huhtamäki, X. Tian, J. T. Korhonen, R. H. A. Ras, *Nat. Protoc.* **2018**, *13*, 1521.

[60] X. Zhang, F. Shi, J. Niu, Y. Jiang, Z. Wang, *J. Mater. Chem.* **2008**, *18*, 621.

[61] F. Schellenberger, N. Encinas, D. Vollmer, H.-J. Butt, *Phys. Rev. Lett.* **2016**, *116*, 096101.

[62] P. Papadopoulos, L. Mammen, X. Deng, D. Vollmer, H.-J. Butt, *Proc. Natl. Acad. Sci. USA* **2013**, *110*, 3254.

[63] L. Gao, T. J. McCarthy, *Langmuir* **2006**, *22*, 6234.

[64] H.-J. Butt, R. Berger, W. Steffen, D. Vollmer, S. A. L. Weber, *Langmuir* **2018**, *34*, 11292.

[65] R. H. A. Ras, X. Tian, I. S. Bayer, in *Handbook of Nanocellulose and Cellulose Nanocomposites*, Vol. 1 (Eds: H. Kargarzadeh, I. Ahmad, S. Thomas, A. Dufresne), Wiley-VCH, Weinheim, Germany **2017**, Ch. 22.

[66] C. J. Long, J. F. Schumacher, A. B. Brennan, *Langmuir* **2009**, *25*, 12982.

[67] L. Gao, T. J. McCarthy, *J. Am. Chem. Soc.* **2006**, *128*, 9052.

[68] L. Wang, T. J. McCarthy, *Angew. Chem. Int. Ed.* **2016**, *55*, 244.

[69] M. Miwa, A. Nakajima, A. Fujishima, K. Hashimoto, T. Watanabe, *Langmuir* **2000**, *16*, 5754.

[70] F. Schellenberger, J. Xie, N. Encinas, A. Hardy, M. Klapper, P. Papadopoulos, H.-J. Butt, D. Vollmer, *Soft Matter* **2015**, *11*, 7617.

[71] T.-S. Wong, S. H. Kang, S. K. Y. Tang, E. J. Smythe, B. D. Hatton, A. Grinthal, J. Aizenberg, *Nature* **2011**, *477*, 443.

[72] Y. I. Frenkel, *J. Exp. Theor. Phys.* **1948**, *18*, 658.

[73] K. Kawasaki, *J. Colloid Sci.* **1960**, *15*, 402.

[74] R. A. Brown, F. M. Orr Jr., L. E. Scriven, *J. Colloid Interface Sci.* **1980**, *73*, 76.

[75] C. W. Extrand, A. N. Gent, *J. Colloid Interface Sci.* **1990**, *138*, 431.

[76] C. W. Extrand, Y. Kumagai, *J. Colloid Interface Sci.* **1995**, *170*, 515.

[77] N. Gao, F. Geyer, D. W. Pilat, S. Wooh, D. Vollmer, H.-J. Butt, R. Berger, *Nat. Phys.* **2018**, *14*, 191.

[78] L. Feng, Z. Zhang, Z. Mai, Y. Ma, B. Liu, L. Jiang, D. Zhu, *Angew. Chem. Int. Ed.* **2004**, *43*, 2012.

[79] J. Zhang, S. Seeger, *Adv. Funct. Mater.* **2011**, *21*, 4699.

[80] Z. Chu, Y. Feng, S. Seeger, *Angew. Chem. Int. Ed.* **2015**, *54*, 2328.

[81] K. Tsujii, T. Yamamoto, T. Onda, S. Shibuichi, *Angew. Chem., Int. Ed.* **1997**, *36*, 1011.

[82] A. Tuteja, W. Choi, M. Ma, J. M. Mabry, S. A. Mazzella, G. C. Rutledge, G. H. McKinley, R. E. Cohen, *Science* **2007**, *318*, 1618.

[83] A. K. Kota, G. Kwon, A. Tuteja, *NPG Asia Mater.* **2014**, *6*, e109.

[84] M. Paven, P. Papadopoulos, S. Schöttler, X. Deng, V. Mailänder, D. Vollmer, H.-J. Butt, *Nat. Commun.* **2013**, *4*, 2512.

[85] S. Movafaghi, V. Leszczak, W. Wang, J. A. Sorkin, L. P. Dasi, K. C. Popat, A. K. Kota, *Adv. Healthcare Mater.* **2017**, *6*, 1600717.

[86] A. Tuteja, W. Choi, J. M. Mabry, G. H. McKinley, R. E. Cohen, *Proc. Natl. Acad. Sci. USA* **2008**, *105*, 18200.

[87] H.-J. Butt, C. Semprebon, P. Papadopoulos, D. Vollmer, M. Brinkmann, M. Ciccotti, *Soft Matter* **2013**, *9*, 418.

[88] Z. Chu, S. Seeger, *Chem. Soc. Rev.* **2014**, *43*, 2784.

[89] S. Peng, X. Yang, D. Tian, W. Deng, *ACS Appl. Mater. Interfaces* **2014**, *6*, 15188.

[90] D. Wang, X. Wang, X. Liu, F. Zhou, *J. Phys. Chem. C* **2010**, *114*, 9938.

[91] W. Wu, X. Wang, D. Wang, M. Chen, F. Zhou, W. Liu, Q. Xue, *Chem. Commun.* **2009**, DOI: 10.1039/B818633B1043.

[92] L. Li, V. Breedveld, D. W. Hess, *ACS Appl. Mater. Interfaces* **2013**, *5*, 5381.

[93] A. Ahuja, J. A. Taylor, V. Lifton, A. A. Sidorenko, T. R. Salamon, E. J. Lobaton, P. Kolodner, T. N. Krupenkin, *Langmuir* **2008**, *24*, 9.

[94] H. Teisala, F. Geyer, J. Haapanen, P. Juuti, J. M. Mäkelä, D. Vollmer, H. J. Butt, *Adv. Mater.* **2018**, *30*, 1706529.

[95] K. Golovin, D. H. Lee, J. M. Mabry, A. Tuteja, *Angew. Chem. Int. Ed.* **2013**, *52*, 13007.

[96] S. Pan, R. Guo, M. Björnmalm, J. J. Richardson, L. Li, C. Peng, N. Bertleff-Zieschang, W. Xu, J. Jiang, F. Caruso, *Nat. Mater.* **2018**, *17*, 1040.

[97] H. Zhou, H. Wang, H. Niu, A. Gestos, T. Lin, *Adv. Funct. Mater.* **2013**, *23*, 1664.

[98] W. Choi, A. Tuteja, S. Chhatre, J. M. Mabry, R. E. Cohen, G. H. McKinley, *Adv. Mater.* **2009**, *21*, 2190.

[99] C.-T. Hsieh, F.-L. Wu, W.-Y. Chen, *J. Phys. Chem. C,* **2009**, *113*, 13683.

[100] S. Pan, A. K. Kota, J. M. Mabry, A. Tuteja, *J. Am. Chem. Soc.* **2013**, *135*, 578.

[101] T. Darmanin, F. Guittard, S. Amigoni, E. T. de Givenchy, X. Noblin, R. Kofman, F. Celestini, *Soft Matter* **2010**, *7*, 1053.

[102] N. J. Shirtcliffe, G. McHale, M. I. Newton, Y. Zhang, *ACS Appl. Mater. Interfaces* **2009**, *1*, 1316.

[103] Z. Yu, X. Liu, G. Kuang, *Chinese J. Chem. Eng.* **2015**, *23*, 763.

[104] C. Xiang, L. Sun, Y. Wang, G. Wang, X. Zhao, S. Zhang, *J. Phys. Chem. C* **2017**, *121*, 15448.

[105] C. Q. Lai, J. C. W. Shen, W. C. W. Cheng, C. H. Yap, *RSC Adv.* **2016**, *6*, 62451.

[106] Y. W. Kim, J. M. Lee, I. Lee, S. H. Lee, J. S. Ko, *J. Precis. Eng. Manuf.* **2013**, *14*, 299.

[107] B. H. Kwon, H. H. Kim, H. J. Jeon, M. C. Kim, I. Lee, S. Chun, J. S. Go, *Exp. Fluids* **2014**, *55*, 1722.

[108] J. M. Nokes, R. Liedert, M. Y. Kim, A. Siddiqui, M. Chu, E. K. Lee, M. Khine, *Adv. Healthcare Mater.* **2016**, *5*, 593.

[109] D. Kim, W. Hwang, *J. Micromech. Microeng.* **2010**, *20*, 027002.

[110] S. Hoshian, E. Kankuri, R. H. A. Ras, S. Franssila, V. Jokinen, *Sci. Rep.* **2017**, *7*, 16019.

[111] N. R. Geraldi, L. E. Dodd, B. B. Xu, G. G. Wells, D. Wood, M. I. Newton, G. McHale, *Surf. Topogr.: Metrol. Prop.* **2017**, *5*, 034001.

[112] G. R. J. Artus, S. Jung, J. Zimmermann, H.-P. Gautschi, K. Marquardt, S. Seeger, *Adv. Mater.* **2006**, *18*, 2758.

[113] J. Zimmermann, F. A. Reifler, G. Fortunato, L. C. Gerhardt, S. Seeger, *Adv. Funct. Mater.* **2008**, *18*, 3662.

[114] J. Zhang, L. Li, B. Li, S. Seeger, J. Zhang, L. Li, B. Li, S. Seeger, *RSC Adv.* **2014**, *4*, 33424.

[115] J. Zhang, S. Seeger, *Angew. Chem. Int. Ed.* **2011**, *50*, 6652.

[116] F. Geyer, C. Schönecker, H.-J. Butt, D. Vollmer, *Adv. Mater.* **2017**, *29*, 1603524.

[117] J. Zhang, L. Li, B. Li, S. Seeger, *RSC Adv.* **2014**, *4*, 33424.

[118] F. Geyer, M. D'Acunzi, C. Y. Yang, M. Müller, P. Baumli, A. Kaltbeitzel, V. Mailänder, N. Encinas, D. Vollmer, H. J. Butt, *Adv. Mater.* **2019**, *31*, 1801324.

[119] D.-a. E. Rollings, J. G. C. Veinot, *Langmuir* **2008**, *24*, 13653.

[120] D.-a. E. Rollings, S. Tsoi, J. C. Sit, J. G. C. Veinot, *Langmuir* **2007**, *23*, 5275.

[121] M. Jin, J. Wang, Y. Hao, M. Liao, Y. Zhao, *Polym. Chem.* **2011**, *2*, 1658.

[122] J. X. H. Wong, H. Asanuma, H.-Z. Yu, *Thin Solid Films* **2012**, *522*, 159.

[123] J. Zhang, A. Wang, S. Seeger, *Polym. Chem.* **2014**, *5*, 1132.

[124] L. Gao, T. J. McCarthy, *Langmuir* **2008**, *24*, 362.

[125] J. Zimmermann, G. R. J. Artus, S. Seeger, *Appl. Surf. Sci.* **2007**, *253*, 5972.

[126] J. Zimmermann, F. A. Reifler, U. Schrade, G. R. J. Artus, S. Seeger, *Colloid Surface A* **2007**, *302*, 234.

[127] G. R. J. Artus, S. Seeger, *Adv. Colloid Interface Sci.* **2014**, *209*, 144.

[128] G. R. J. Artus, S. Olveira, D. Patra, S. Seeger, *Macromol. Rapid Commun.* **2017**, *38*, 1600558.

[129] S. Olveira, A. Stojanovic, S. Seeger, *J. Nanopart. Res.* **2018**, *20*, 307.

[130] G. R. J. Artus, S. Seeger, *Advances in Colloid and Interface Science* **2014**, *209*, 144.

[131] J. T. Korhonen, T. Huhtamäki, T. Verho, R. H. A. Ras, *Surf. Innov.* **2014**, *2*, 116.

[132] J. Zimmermann, M. Rabe, G. R. J. Artus, S. Seeger, *Soft Matter* **2008**, *4*, 450.

[133] G. R. J. Artus, J. Zimmermann, F. A. Reifler, S. A. Brewer, S. Seeger, *Appl. Surf. Sci.* **2012**, *258*, 3835.

[134] X. Deng, M. Paven, P. Papadopoulos, M. Ye, S. Wu, T. Schuster, M. Klapper, D. Vollmer, H.-J. Butt, *Angew. Chem. Int. Ed.* **2013**, *52*, 11286.

[135] A. M. S. Costa, M. Alatorre-Meda, N. M. Oliveira, J. F. Mano, *Langmuir* **2014**, *30*, 4535.

[136] S. Wooh, H. Huesmann, M. N. Tahir, M. Paven, K. Wichmann, D. Vollmer, W. Tremel, P. Papadopoulos, H.-J. Butt, *Adv. Mater.* **2015**, *27*, 7338.

[137] T. Sekido, S. Wooh, R. Fuchs, M. Kappl, Y. Nakamura, H.-J. Butt, S. Fujii, *Langmuir* **2017**, *33*, 1995.

[138] J. T. Pham, M. Paven, S. Wooh, T. Kajiya, H.-J. Butt, D. Vollmer, *Nat. Commun.* **2017**, *8*, 905.

[139] B. Deng, R. Cai, Y. Yu, H. Q. Jiang, C. L. Wang, J. A. Li, L. F. Li, M. Yu, J. Y. Li, L. D. Xie, Q. Huang, C. H. Fan, *Adv. Mater.* **2010**, *22*, 5473.

[140] Y. Shang, Y. Si, A. Raza, L. Yang, X. Mao, B. Ding, J. Yu, *Nanoscale* **2012**, *4*, 7847.

[141] Y. Si, Q. Fu, X. Wang, J. Zhu, J. Yu, G. Sun, B. Ding, *ACS Nano* **2015**, *9*, 3791.

[142] X. Zhou, Z. Zhang, X. Xu, F. Guo, X. Zhu, X. Men, B. Ge, *ACS Appl. Mater. Interfaces* **2013**, *5*, 7208.

[143] L. Cao, A. K. Jones, V. K. Sikka, J. Wu, D. Gao, *Langmuir* **2009**, *25*, 12444.

[144] S. A. Kulinich, M. Farzaneh, *Appl. Surf. Sci.* **2009**, *255*, 8153.

[145] R. Fürstner, W. Barthlott, C. Neinhuis, P. Walzel, *Langmuir* **2005**, *21*, 956.

[146] B. Bhushan, Y. C. Jung, K. Koch, *Langmuir* **2009**, *25*, 3240.

[147] R. J. Daniello, N. E. Waterhouse, J. P. Rothstein, *Phys. Fluids* **2009**, *21*, 085103.

[148] B. J. Privett, J. Youn, S. A. Hong, J. Lee, J. Han, J. H. Shin, M. H. Schoenfisch, *Langmuir* **2011**, *27*, 9597.

[149] Y. Liao, R. Wang, A. G. Fane, *J. Membrane Sci.* **2013**, *440*, 77.

[150] A. Razmjou, E. Arifin, G. Dong, J. Mansouri, V. Chen, *J. Membr. Sci.* **2012**, *415*, 850.

[151] U. Pöschl, *Angew. Chem. Int. Ed.* **2005**, *44*, 7520.

[152] X.-M. Li, D. Reinhoudt, M. Crego-Calama, *Chem. Soc. Rev.* **2007**, *36*, 1350.

[153] B. Bhushan, Y. C. Jung, K. Koch, *Langmuir* **2009**, *25*, 3240.

[154] Y.-B. Park, H. Im, M. Im, Y.-K. Choi, *J. Mater. Chem.* **2011**, *21*, 633.

[155] K. M. Wisdom, J. A. Watson, X. Qu, F. Liu, G. S. Watson, C.-H. Chen, *Proc. Natl. Acad. Sci. USA* **2013**, *110*, 7992.

[156] M. Jönsson-Niedziólka, F. Lapierre, Y. Coffinier, S. J. Parry, F. Zoueshtiagh, T. Foat, V. Thomy, R. Boukherroub, *Lab Chip* **2011**, *11*, 490.

[157] S. Wooh, H. Huesmann, M. N. Tahir, M. Paven, K. Wichmann, D. Vollmer, W. Tremel, P. Papadopoulos, H. Butt, *Adv. Mater.* **2015**, *27*, 7338.

[158] Q. Zhu, Q. Pan, F. Liu, *J. Phys. Chem. C* **2011**, *115*, 17464.

[159] R. B. Pernites, C. M. Santos, M. Maldonado, R. R. Ponnapati, D. F. Rodrigues, R. C. Advincula, *Chem. Mater.* **2012**, *24*, 870.

[160] C.-Y. Loo, P. M. Young, W.-H. Lee, R. Cavaliere, C. B. Whitchurch, R. Rohanizadeh, *Acta Biomater.* **2012**, *8*, 1881.

[161] X. X. Zhang, L. Wang, E. Levanen, *RSV Adv.* **2013**, *3*, 12003.

[162] X.-Q. Dou, D. Zhang, C. Feng, L. Jiang, *ACS Nano* **2015**, *9*, 10664.

[163] G. B. Hwang, K. Page, A. Patir, S. P. Nair, E. Allan, I. P. Parkin, *ACS Nano* **2018**, *12*, 6050.

[164] M. Meier, V. Dubois, S. Seeger, *Appl. Surf. Sci.* **2018**, *459*, 505.

[165] J. W. Costerton, P. S. Stewart, E. P. Greenberg, *Science* **1999**, *284*, 1318.

[166] L. D. Renner, D. B. Weibel, *MRS Bull.* **2011**, *36*, 347.

[167] P. S. Stewart, J. W. Costerton, *Lancet* **2001**, *358*, 135.

[168] V. K. Truong, R. Lapovok, Y. S. Estrin, S. Rundell, J. Y. Wang, C. J. Fluke, R. J. Crawford, E. R. Ivanova, *Biomaterials* **2010**, *31*, 3674.

[169] S. J. Cho, H. Nam, H. Ryu, G. Lim, *Adv. Funct. Mater.* **2013**, *23*, 5577.

[170] T. C. Merkel, H. Lin, X. Wei, R. Baker, *J. Membr. Sci.* **2010**, *359*, 126.

[171] P. H. M. Feron, A. E. Jansen, R. Klaassen, *Energy Convers. Manage.* **1992**, *33*, 421.

[172] A. Gabelman, S.-T. Hwang, *J. Membr. Sci.* **1999**, *159*, 61.

[173] A. Mansourizadeh, A. F. Ismail, *J. Hazard. Mater.* **2009**, *171*, 38.

[174] P. Luis, T. Van Gerven, B. Van der Bruggen, *Prog. Energy Combust. Sci.* **2012**, *38*, 419.

[175] M. T. Ravanchi, T. Kaghazchi, A. Kargari, *Desalination* **2009**, *235*, 199.

[176] R. Wang, H. Y. Zhang, P. H. M. Feron, D. T. Liang, *Sep. Purif. Technol.* **2005**, *46*, 33.

[177] G. T. Rochelle, *Science* **2009**, *325*, 1652.

[178] R. S. Haszeldine, *Science* **2009**, *325*, 1647.

[179] B. P. Binks, R. Murakami, *Nat. Mater.* **2006**, *5*, 865.

[180] S. U. Pickering, *J. Chem. Soc., Trans.* **1907**, *91*, 2001.

[181] B. P. Binks, T. S. Horozov, *Colloidal Particles at Liquid Interfaces*, Cambridge University Press, Cambridge **2006**.

[182] S. Fujii, Y. Nakamura, *Langmuir* **2017**, *33*, 7365.

[183] S. Fujii, Y. Yokoyama, S. Nakayama, M. Ito, S. Yusa, Y. Nakamura, *Langmuir* **2017**, *34*, 933.

[184] G. McHale, M. I. Newton, *Soft Matter* **2011**, *7*, 5473.

[185] P. Aussillous, D. Quéré, *Nature* **2001**, *411*, 924.

[186] P. Aussillous, D. Quéré, *Proc. R. Soc. A* **2006**, *462*, 973.

[187] G. McHale, M. I. Newton, *Soft Matter* **2015**, *11*, 2530.

[188] E. Bormashenko, *Langmuir* **2017**, *33*, 663.

[189] N. Pike, D. Richard, W. Foster, L. Mahadevan, *Proc. Biol. Sci.* **2002**, *269*, 1211.

[190] D. Dupin, S. P. Armes, S. Fujii, *J. Am. Chem. Soc.* **2009**, *131*, 5386.

[191] P. M. Ireland, C. A. Thomas, B. T. Lobel, G. B. Webber, S. Fujii, E. J. Wanless, *Front. Chem.* **2018**, *6*, 280.

[192] D. Matsukuma, H. Watanabe, M. Minn, A. Fujimoto, T. Shinohara, H. Jinnai, A. Takahara, *RSC Adv.* **2013**, *3*, 7862.

[193] S. Fujii, S. Sawada, S. Nakayama, M. Kappl, K. Ueno, K. Shitajima, H.-J. Butt, Y. Nakamura, *Mater. Horiz.* **2016**, *3*, 42.

[194] Y. Sheng, G. Sun, J. Wu, G. Ma, T. Ngai, *Angew. Chem. Int. Ed.* **2015**, *54*, 7012.

[195] A. T. Tyowua, J. M. Mooney, B. P. Binks, *Colloids Surf. A* **2019**, *560*, 288.

[196] A. D. Dinsmore, M. F. Hsu, M. G. Nikolaides, M. Marquez, A. R. Bausch, D. A. Weitz, *Science* **2002**, *298*, 1006.

[197] S. Fujii, S.-i. Yusa, Y. Nakamura, *Adv. Funct. Mater.* **2016**, *26*, 7206.

[198] T. Arbatan, L. Li, J. Tian, W. Shen, *Adv. Healthcare Mater.* **2012**, *1*, 80.

[199] Y. Xue, H. Wang, Y. Zhao, L. Dai, L. Feng, X. Wang, T. Lin, *Adv. Mater.* **2010**, *22*, 4814.

[200] E. Bormashenko, R. Pogreb, Y. Bormashenko, A. Musin, T. Stein, *Langmuir* **2008**, *24*, 12119.

[201] N. M. Oliveira, R. L. Reis, J. F. Mano, *Adv. Healthcare Mater.* **2017**, *6*, 1700192.

[202] N. M. Oliveira, C. R. Correia, R. L. Reis, J. F. Mano, *Adv. Healthcare Mater.* **2015**, *4*, 264.

[203] H. Zeng, Y. Zhao, *Appl. Phys. Lett.* **2010**, *96*, 114104.

[204] J. F. Archard, *J. Appl. Phys.* **1953**, *24*, 981.

[205] B. T. Persson, in *Encyclopedia of Lubricants and Lubrication*, DOI: 10.1007/978-3-642-22647-2_80 (Ed: T. Mang), Springer Berlin Heidelberg **2014**, Ch. 80, p. 791.

[206] H.-J. Butt, M. Kappl, *Friction*, Wiley-VCH, Weinheim, Germany **2010**.

[207] P. Calvert, *Chem. Mater.* **2001**, *13*, 3299.

[208] F. P. Bowden, D. Tabor, *The Friction and Lubrication of Solids*, Clarendon Press, **2001**.

[209] B. Bhushan, J. N. Israelachvili, U. Landman, *Nature* **1995**, *374*, 607.

[210] C. Semprebon, M. Brinkmann, *Soft Matter* **2014**, *10*, 3325.

[211] C. W. Extrand, A. N. Gent, *J. Colloid Interface Sci.* **1990**, *138*, 431.

[212] R. A. Brown, F. M. Orr Jr, L. E. Scriven, *J. Colloid Interface Sci.* **1980**, *73*, 76.

[213] C. W. Extrand, Y. Kumagai, *J. Colloid Interface Sci.* **1995**, *170*, 515.

[214] Y. I. Frenkel, *J. Exp. Theor. Phys.* **1948**, *18*, 658.

[215] K. Kawasaki, *J. Colloid Sci.* **1960**, *15*, 402.

[216] A. ElSherbini, A. Jacobi, *J. Colloid Interface Sci.* **2006**, *299*, 841.

[217] V. Dussan, *J. Fluid Mech.* **1987**, *174*, 381.

[218] E. Wolfram, R. Faust, in *Wetting, Spreading, and Adhesion* (Ed: J. F. Padday), Academic Press, New York **1978**, p. 213.

[219] C. Antonini, F. J. Carmona, E. Pierce, M. Marengo, A. Amirfazli, *Langmuir* **2009**, *25*, 6143.

[220] V. Berejnov, R. E. Thorne, *Phys. Rev. E* **2007**, *75*, 066308.

[221] J. V. I. Timonen, M. Latikka, O. Ikkala, R. H. A. Ras, *Nat. Commun.* **2013**, *4*.

[222] P. Olin, S. B. Lindström, T. Pettersson, L. Wågberg, *Langmuir* **2013**, *29*, 9079.

[223] E. Pierce, F. J. Carmona, A. Amirfazli, *Colloid Surf. A-Physicochem. Eng. Asp.* **2008**, *323*, 73.

[224] M. Sakai, J.-H. Song, N. Yoshida, S. Suzuki, Y. Kameshima, A. Nakajima, *Langmuir* **2006**, *22*, 4906.

[225] P. R. Griffiths, *Master of Science in Mechanical Engineering* University of South Florida, **2013**.

[226] J. H. Snoeijer, B. Andreotti, *Annu. Rev. Fluid Mech.* **2013**, *45*, 269.

[227] H. Perrin, R. Lhermerout, K. Davitt, E. Rolley, B. Andreotti, *Phys. Rev. Lett.* **2016**, *116*, 184502.

[228] K. Huang, I. Szlufarska, *Phys. Rev. E* **2014**, *89*, 032119.

[229] D. Daniel, J. V. I. Timonen, R. Li, S. J. Velling, J. Aizenberg, *Nat. Phys.* **2017**, *advance online publication*.

[230] H.-J. Butt, N. Gao, P. Papadopoulos, W. Steffen, M. Kappl, R. Berger, *Langmuir* **2017**, *33*, 107.

[231] J. N. Israelachvili, *Intermolecular and Surface Forces*, Elsevier Science, **2011**.

[232] H.-J. Butt, M. Kappl, *Surface and Interfacial Forces*, Wiley, **2010**.

[233] C. Shi, X. Cui, X. Zhang, P. Tchoukov, Q. Liu, N. Encinas, M. Paven, F. Geyer, D. Vollmer, Z. Xu, H.-J. Butt, H. Zeng, *Langmuir* **2015**, *31*, 7317.

[234] J. W. Krumpfer, T. J. McCarthy, *Farad. Discuss.* **2010**, *146*, 103.

[235] S. Wooh, J. H. Koh, S. Lee, H. Yoon, K. Char, *Adv. Funct. Mater.* **2014**, *24*, 5550.

[236] H. Suda, S. Yamada, *Langmuir* **2003**, *19*, 529.

[237] K. L. Johnson, K. L. Johnson, *Contact Mechanics*, Cambridge University Press, **1987**.

[238] T. Darmanin, F. Guittard, *J. Mater. Chem. A* **2014**, *2*, 16319.

[239] L. Mishchenko, B. Hatton, V. Bahadur, J. A. Taylor, T. Krupenkin, J. Aizenberg, *ACS Nano* **2010**, *4*, 7699.

[240] R. P. Garrod, L. G. Harris, W. C. E. Schofield, J. McGettrick, L. J. Ward, a. D. O. H. Teare, J. P. S. Badyal*, *Langmuir* **2006**, *23*, 689.

[241] K.-C. Park, S. S. Chhatre, S. Srinivasan, R. E. Cohen, G. H. McKinley, *Langmuir* **2013**, *29*, 13269.

[242] P. Saxena, L. M. Hildemann, *J. Atmos. Chem.* **1996**, *24*, 57.

[243] A. P. Sullivan, R. J. Weber, A. L. Clements, J. R. Turner, M. S. Bae, J. J. Schauer, *Geophys. Res. Lett.* **2004**, *31*, L13105.

[244] R. D. Deegan, O. Bakajin, T. F. Dupont, G. Huber, S. R. Nagel, T. A. Witten, *Nature* **1997**, *389*, 827.

[245] O. Pitois, X. Chateau, *Langmuir* **2002**, *18*, 9751.

[246] Y. Tang, S. Cheng, *Phys. Rev. E* **2018**, *98*, 032802.

[247] K. L. Johnson, K. Kendall, A. D. Roberts, *Proc. R. Soc. Lond. A* **1971**, *324*, 301.

[248] J. B. Boreyko, C.-H. Chen, *Phys. Rev. Lett.* **2009**, *103*, 184501.

[249] M. D'Acunzi, *PhD thesis* Johannes Gutenberg-University, Mainz, Mainz, **2010**.

[250] N. A. M. Verhaegh, A. van Blaaderen, **1994**, *10*, 1427.

[251] H. J. H. Fenton, *J. Chem. Soc., Trans.* **1894**, *65*, 899.

[252] J. J. Pignatello, E. Oliveros, A. MacKay, *Crit. Rev. Environ. Sci. Technol.* **2006**, *36*, 1.

[253] L. Zhang, M. D'Acunzi, M. Kappl, G. K. Auernhammer, D. Vollmer, C. M. van Kats, A. van Blaaderen, *Langmuir* **2009**, *25*, 2711.

[254] W. Schaertl, H. Sillescu, *J. Colloid Interface Sci.* **1993**, *155*, 313.

[255] C. Huh, S. G. Mason, *Can. J. Chem.* **1976**, *54*, 969.

[256] E. Bayramli, C. Huh, S. G. Mason, *Can. J. Chem.* **1978**, *56*, 818.

[257] O. D. Velev, K. Furusawa, K. Nagayama, *Langmuir* **1996**, *12*, 2374.

[258] S. E. Anachkov, I. Lesov, M. Zanini, P. A. Kralchevsky, N. D. Denkov, L. Isa, *Soft Matter* **2016**, *12*, 7632.

[259] H. H. Kausch, D. G. Fesko, N. W. Tschoegl, *J. Colloid Interface Sci.* **1971**, *37*, 603.

[260] P. M. Cox, R. A. Betts, C. D. Jones, S. A. Spall, I. J. Totterdell, *Nature* **2000**, *408*, 184.

[261] C. L. Quéré, R. Moriarty, R. M. Andrew, G. P. Peters, P. Ciais, P. Friedlingstein, S. D. Jones, S. Sitch, P. Tans, A. Arneth, T. A. Boden, L. Bopp, Y. Bozec, J. G. Canadell, L. P. Chini, F. Chevallier, C. E. Cosca, I. Harris, M. Hoppema, R. A. Houghton, J. I. House, A. K. Jain, T. Johannessen, E. Kato, R. F. Keeling, V. Kitidis, K. Klein Goldewijk, C. Koven, C. S. Landa, P. Landschützer, A. Lenton, I. D. Lima, G. Marland, J. T. Mathis, N. Metzl, Y. Nojiri, A. Olsen, T. Ono, S. Peng, W. Peters, B. Pfeil, B. Poulter, M. R. Raupach, P. Regnier, C. Rödenbeck, S. Saito, J. E. Salisbury, U. Schuster, J. Schwinger, R. Séférian, J. Segschneider, T. Steinhoff, B. D. Stocker, A. J. Sutton, T. Takahashi, B. Tilbrook, G. R. v. d. Werf, N. Viovy, Y.-P. Wang, R. Wanninkhof, A. Wiltshire, N. Zeng, *Earth Syst. Sci. Data* **2015**, *7*, 47.

[262] D. M. D'Alessandro, B. Smit, J. R. Long, *Angew. Chem. Int. Ed.* **2010**, *49*, 6058.

[263] S. J. Datta, C. Khumnoon, Z. H. Lee, W. K. Moon, S. Docao, T. H. Nguyen, I. C. Hwang, D. Moon, P. Oleynikov, O. Terasaki, K. B. Yoon, *Science* **2015**, *350*, 302.

[264] H. W. Kim, H. W. Yoon, S. M. Yoon, B. M. Yoo, B. K. Ahn, Y. H. Cho, H. J. Shin, H. Yang, U. Paik, S. Kwon, J. Y. Choi, H. B. Park, *Science* **2013**, *342*, 91.

[265] S. A. Freeman, R. Dugas, D. H. Van Wagener, T. Nguyen, G. T. Rochelle, *Int. J. Greenh. Gas Con.* **2010**, *4*, 119.

[266] P. Luis, B. Van der Bruggen, T. Van Gerven, *J. Chem. Technol. Biotechnol.* **2011**, *86*, 769.

[267] S.-W. Rho, K.-P. Yoo, J. S. Lee, S. C. Nam, J. E. Son, B.-M. Min, *J. Chem. Eng. Data* **1997**, *42*, 1161.

[268] A. Criscuoli, E. Drioli, *Ind. Eng. Chem. Res.* **2007**, *46*, 2268.

[269] A. Stankiewicz, *Chem. Eng. Process.* **2003**, *42*, 137.

[270] T. Van Gerven, A. Stankiewicz, *Ind. Eng. Chem. Res.* **2009**, *48*, 2465.

[271] E. Drioli, A. I. Stankiewicz, F. Macedonio, *J. Membr. Sci.* **2011**, *380*, 1.

[272] Y. Lv, X. Yu, J. Jia, S.-T. Tu, J. Yan, E. Dahlquist, *Appl. Energy* **2012**, *90*, 167.

[273] Y.-F. Lin, Q. Ye, S.-H. Hsu, T.-W. Chung, *Chem. Eng. J.* **2016**, *284*, 888.

[274] X. Yu, L. An, J. Yang, S.-T. Tu, J. Yan, *J. Membr. Sci.* **2015**, *496*, 1.

[275] T. Liu, C.-J. Kim, *Science* **2014**, *346*, 1096.

[276] H. A. Al-Ghawas, D. P. Hagewiesche, G. Ruiz-Ibanez, O. C. Sandall, *J. Chem. Eng. Data* **1989**, *34*, 385.

[277] G. Richner, *Energy Procedia* **2013**, *37*, 423.

[278] C. W. Extrand, *Langmuir* **2002**, *18*, 7991.

[279] L. Gao, T. J. McCarthy, *Langmuir* **2007**, *23*, 3762.

[280] W. Choi, A. Tuteja, J. M. Mabry, R. E. Cohen, G. H. McKinley, *J. Colloid Interface Sci.* **2009**, *339*, 208.

[281] P. S. H. Forsberg, C. Priest, M. Brinkmann, R. Sedev, J. Ralston, *Langmuir* **2010**, *26*, 860.

[282] B. M. Mognetti, J. M. Yeomans, *Langmuir* **2010**, *26*, 18162

[283] C. W. Extrand, *Langmuir* **2016**, *32*, 8608.

[284] P. Papadopoulos, X. Deng, L. Mammen, D.-M. Drotlef, G. Battagliarin, C. Li, K. Muellen, K. Landfester, A. del Campo, H.-J. Butt, D. Vollmer, *Langmuir* **2012**, *28*, 8392.

[285] E. P. Barrett, L. G. Joyner, P. P. Halenda, *J. Am. Chem. Soc.* **1951**, *73*, 373.

[286] S. Brunauer, P. H. Emmett, E. Teller, *J. Am. Chem. Soc.* **1938**, *60*, 309.

[287] F. Y. Jou, A. E. Mather, F. D. Otto, *Ind. Eng. Chem. Process. Des. Dev.* **1982**, *21*, 539.

[288] D. Menne, F. Pitsch, J. E. Wong, A. Pich, M. Wessling, *Angew. Chem. Int. Ed.* **2014**, *53*, 5706.

[289] H. A. Stone, A. D. Stroock, A. Ajdari, *Annu. Rev. Fluid Mech.* **2004**, *36*, 381.

[290] E. H. Kass, L. J. Schneiderman, *N. Engl. J. Med.* **1957**, *256*, 556.

[291] X. J. Feng, L. Jiang, **2006**, *18*, 3063.

[292] D. C. Leslie, A. Waterhouse, J. B. Berthet, T. M. Valentin, A. L. Watters, A. Jain, P. Kim, B. D. Hatton, A. Nedder, K. Donovan, E. H. Super, C. Howell, C. P. Johnson, T. L. Vu, D. E. Bolgen, S. Rifai, A. R. Hansen, M. Aizenberg, M. Super, J. Aizenberg, D. E. Ingber, *Nat. Biotechnol,* **2014**, *32*, 1134.

[293] T. Verho, C. Bower, P. Andrew, S. Franssila, O. Ikkala, R. H. A. Ras, *Adv. Mater.* **2011**, *23*, 673.

[294] X. Yao, Y. Song, L. Jiang, *Adv. Mater.* **2011**, *23*, 719.

[295] C. W. Extrand, *Langmuir* **2004**, *20*, 5013.

[296] D. Quéré, *Rep. Prog. Phys.* **2005**, *68*, 2495.

[297] S. Herminghaus, *EPL* **2007**, *79*, 59901.

[298] A. T. Paxson, K. K. Varanasi, *Nat. Commun.* **2013**, *4*, 1492.

[299] H. Teisala, M. Tuominen, M. Aromaa, M. Stepien, J. M. Mäkelä, J. J. Saarinen, M. Toivakka, J. Kuusipalo, *Langmuir* **2012**, *28*, 3138.

[300] M. R. Sanchis, V. Blanes, M. Blanes, D. Garcia, R. Balart, *Eur. Polym. J.* **2006**, *42*, 1558.

[301] X. Tian, T. Verho, R. H. A. Ras, *Science* **2016**, *352*, 142.

[302] A. B. Subramaniam, M. Abkarian, H. A. Stone, *Nat. Mater.* **2005**, *4*, 553.

[303] K. Kido, P. M. Ireland, T. Sekido, E. J. Wanless, G. B. Webber, Y. Nakamura, S. Fujii, *Langmuir* **2018**, *34*, 4970.

[304] S. Wong, V. Kitaev, G. A. Ozin, *J. Am. Chem. Soc.* **2003**, *125*, 15589.

[305] H. W. Deckman, J. H. Dunsmuir, S. Garoff, J. A. McHenry, D. G. Peiffer, *J. Vac. Sci. Technol. B* **1998**, *6*, 333.

[306] N. Vogel, J. Ally, K. Bley, M. Kappl, K. Landfester, C. K. Weiss, *Nanoscale* **2014**, *6*, 6879.

[307] Y. Nonomura, S. Komura, K. Tsujii, *Langmuir* **2004**, *20*, 11821.

[308] R. G. Picknett, R. Bexon, *J. Colloid Interface Sci.* **1977**, *61*, 336.

[309] B. Laborie, F. Lachaussée, E. Lorenceau, F. Rouyer, *Soft Matter* **2013**, *9*, 4822.

[310] A. B. Subramaniam, M. Abkarian, L. Mahadevan, H. A. Stone, *Nature* **2005**, *438*, 930.

[311] M. Cui, T. Emrick, T. P. Russell, *Science* **2013**, *342*, 460.

[312] X. Li, H. Shi, Y. Wang, R. Wang, S. Huang, J. Huang, X. Geng, D. Zang, *Adv. Mater. Interfaces* **2018**, *5*, 1701139.

[313] K. Stratford, R. Adhikari, I. Pagonabarraga, J. C. Desplat, M. E. Cates, *Science* **2005**, *309*, 2198.

[314] C. Py, P. Reverdy, L. Doppler, J. Bico, B. Roman, C. N. Baroud, *Phys. Rev. Lett.* **2007**, *98*, 156103.

[315] H. Kawashima, H. Mayama, Y. Nakamura, S. Fujii, *Polym. Chem.* **2017**, *8*, 2609.

[316] H. Kawashima, M. Paven, H. Mayama, H.-J. Butt, Y. Nakamura, S. Fujii, *ACS Appl. Mater. Interfaces* **2017**, *9*, 33351.

[317] M. A. Nilsson, R. J. Daniello, J. P. Rothstein, *J. Phys. D: Appl. Phys.* **2010**, *43*, 045301.

[318] C. Wang, G. Cui, X. Luo, Y. Xu, H. Li, S. Dai, *J. Am. Chem. Soc.* **2011**, *133*, 11916.

[319] M. S. Shah, M. Tsapatsis, J. I. Siepmann, *Chem. Rev.* **2017**, *117*, 9755.

[320] S. Lin, S. Nejati, C. Boo, Y. Hu, C. O. Osuji, M. Elimelech, *Environ. Sci. Technol. Lett.* **2014**, *1*, 443.

[321] E. D. Bates, R. D. Mayton, I. Ntai, J. H. Davis, *J. Am. Chem. Soc.* **2002**, *124*, 926.

[322] C. Wang, X. Luo, H. Luo, D. e. Jiang, H. Li, S. Dai, *Angew. Chem. Int. Ed.* **2011**, *50*, 4918.

[323] M. Ramdin, T. W. de Loos, T. J. H. Vlugt, *Ind. Eng. Chem. Res.* **2012**, *51*, 8149.

[324] L. D. Tijing, Y. C. Woo, J.-S. Choi, S. Lee, S.-H. Kim, H. K. Shon, *J. Membr. Sci.* **2015**, *475*, 215.

9 ACKNOWLEDGMENTS

[redacted]

10 APPENDIX

The following section contains important Supporting Information for Chapters 3 and 6. For Chapters 2, 4, and 5, the Supporting Information is available online; the hyperlinks are provided at the beginning of each chapter. For consistency, the numbering of the figures is kept consistent with the submitted manuscripts.

10.1 SUPPORTING INFORMATION FOR CHAPTER 3

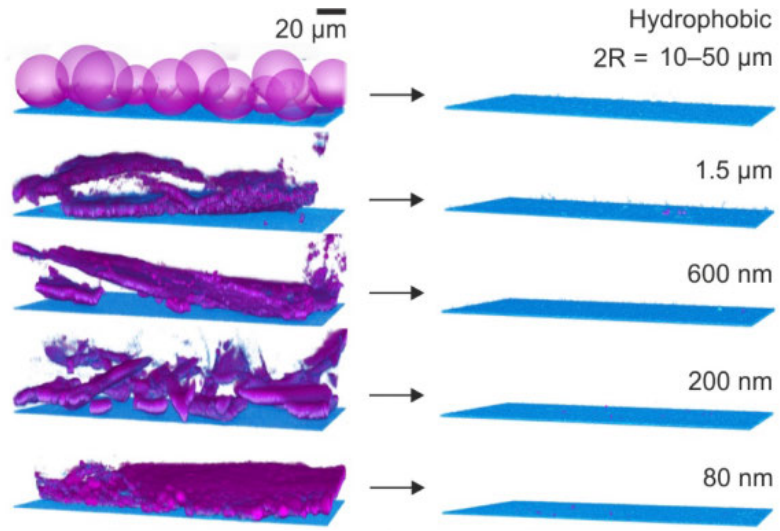

Figure S2. Representative laser scanning confocal (LSCM) images of the nanoporous surfaces (blue) contaminated with hydrophobic particle powder (purple) ranging between 80 nm and 50 µm before (left) and after self-cleaning (right). Some particle aggregates were not directly or easily cleaned, as the drops rolled over these hydrophobic aggregates but could eventually be removed.

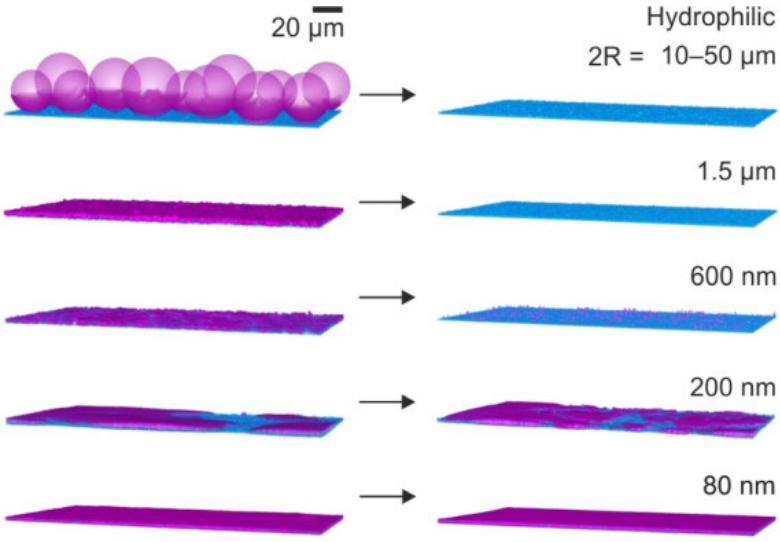

Figure S4. Representative LSCM of the nanoporous surfaces (blue) contaminated with hydrophilic particles from ethanol dispersion (purple) ranging between 80 nm and 50 µm before (left) and after self-cleaning (right).

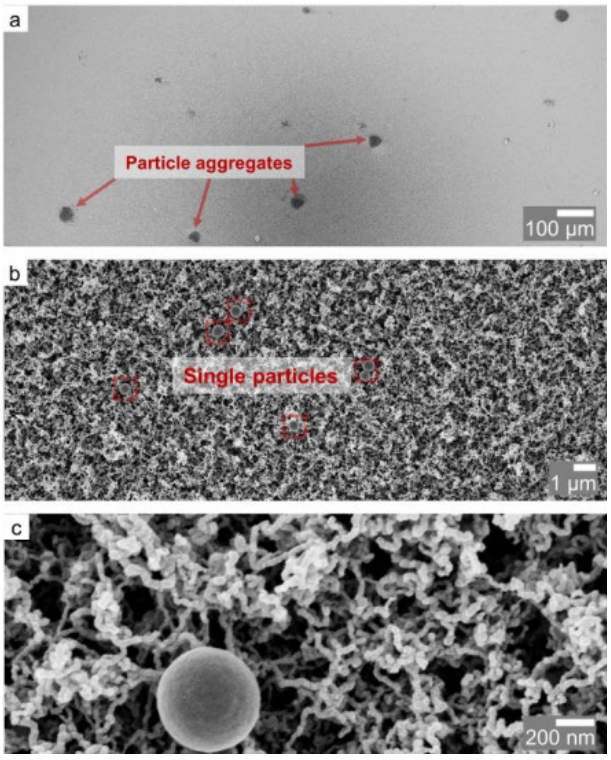

Figure S5. a–c) Representative SEM images in different magnifications of the nanostructured surfaces after contamination with 600 nm hydrophilic particles dispersed in ethanol and subsequent self-cleaning. Few particle aggregates could not be easily removed by sliding water drops.

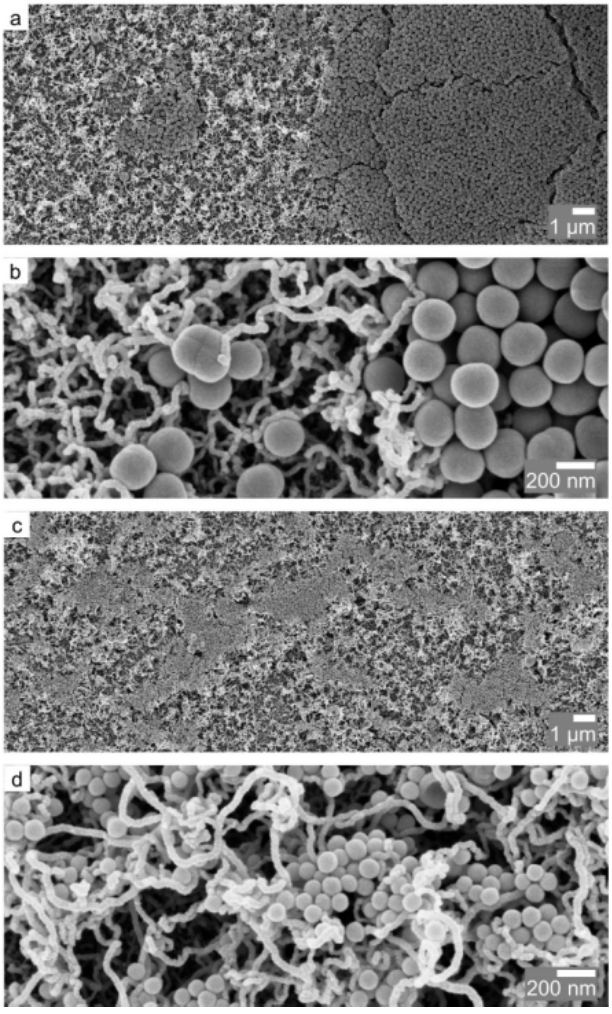

Figure S7. a–d) Representative SEM images in different magnifications of the nanoporous surfaces after contamination with 200 nm (a,b) and 80 nm (c,d) hydrophilic particles dispersed in ethanol and subsequent rinsing.

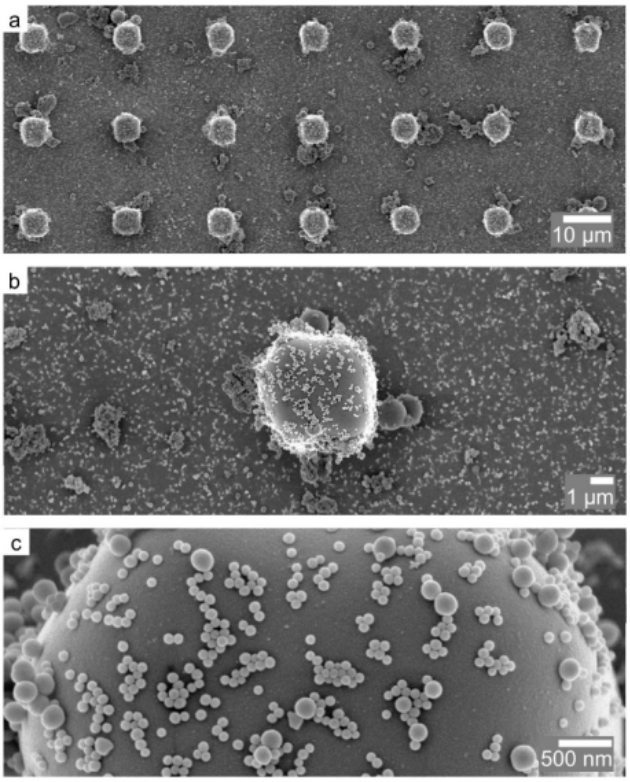

Figure S11. a–**c**) SEM images of the superhydrophobic microstructured SU-8 pillar surface that was consecutively contaminated with powders of the hydrophobic particles (50 µm to 80 nm). After self-cleaning, 600 nm particles and especially 200 nm as well as 80 nm particles remained on the surface, providing an additional roughness resulting in lower roll-off angles.

Figure S12. Photographs of the superomniphobic fabrics on the car after 257 days of outdoor exposure. **a**) Superomniphobic fabrics fixed on the front window. **b**) Fabric fixed on the left mirror. **c**) Fabric fixed at the rear side windows. **d**) Fabrics fixed at the back window. All superomniphobic fabrics remained white without any obvious stains.

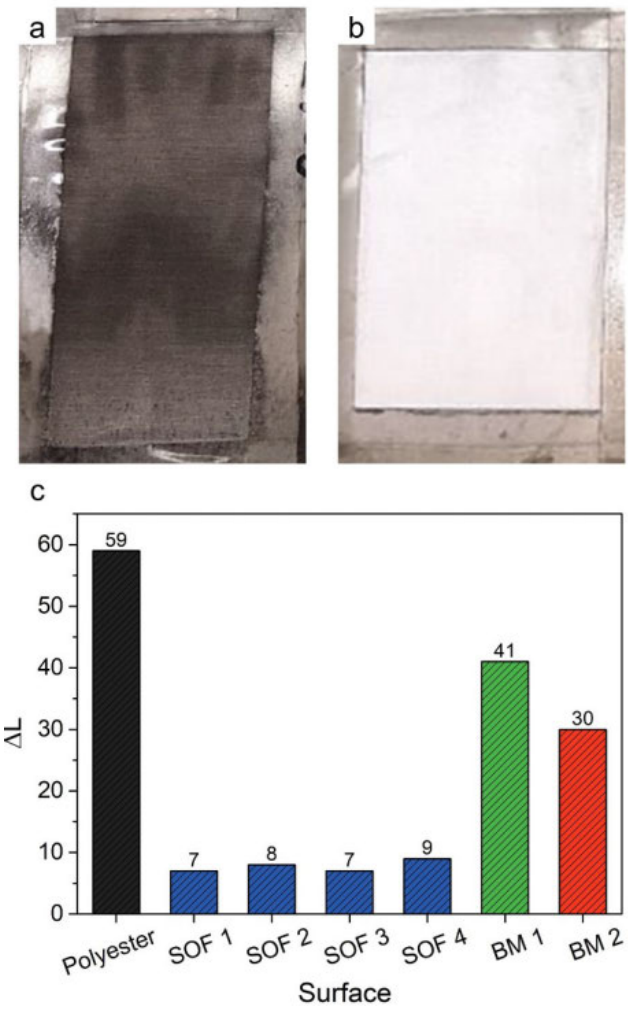

Figure S14. a,**b**) Photographs of a bare (a) and superomniphobic fabric (b) after the industrial standardized contamination test using a dirt dishwasher, conducted by Evonik Resource Efficiency GmbH. The bare fabric turned black due to the pickup of contamination, whereas the superomniphobic remained white. **c**) Industrial standardized contamination tests for easy-to-clean surfaces using a dirt dishwasher, conducted by Evonik Resource Efficiency GmbH. The tested surfaces included a bare polyester fabric, superomniphobic fabrics (SOF), and two benchmark surfaces (BM).

Table S1. Temperatures (T), rainfall, and humidities (RH) during the outdoor exposure of the superomniphobic fabrics. Temperatures and rain total were collected from www.wetterkontor.com. The humidities from www.timeanddate.de. The experiment started beginning of October 2016.

Period [days]	Min. T [°C]	Max. T [°C]	Avg. min. T [°C]	Avg. max. T [°C]	Avg. T [°C]	Rain total [L m^{-2}]	Avg. min. RH [%]	Avg. max. RH [%]
0–4	5.1	13.6	6.7	12.4	9.1	0.8	54	76
22–56	-5.4	15.3	3.0	8.4	5.7	40.6	69	93
92–133	-9.6	10.6	-1.9	3.3	0.6	32.5	66	90
189–249	-0.9	32.0	9.0	18.9	13.9	94.6	46	87
308–426	-2.8	29.1	8.3	15.5	11.8	194.7	65	96

10.2 SUPPORTING INFORMATION FOR CHAPTER 6

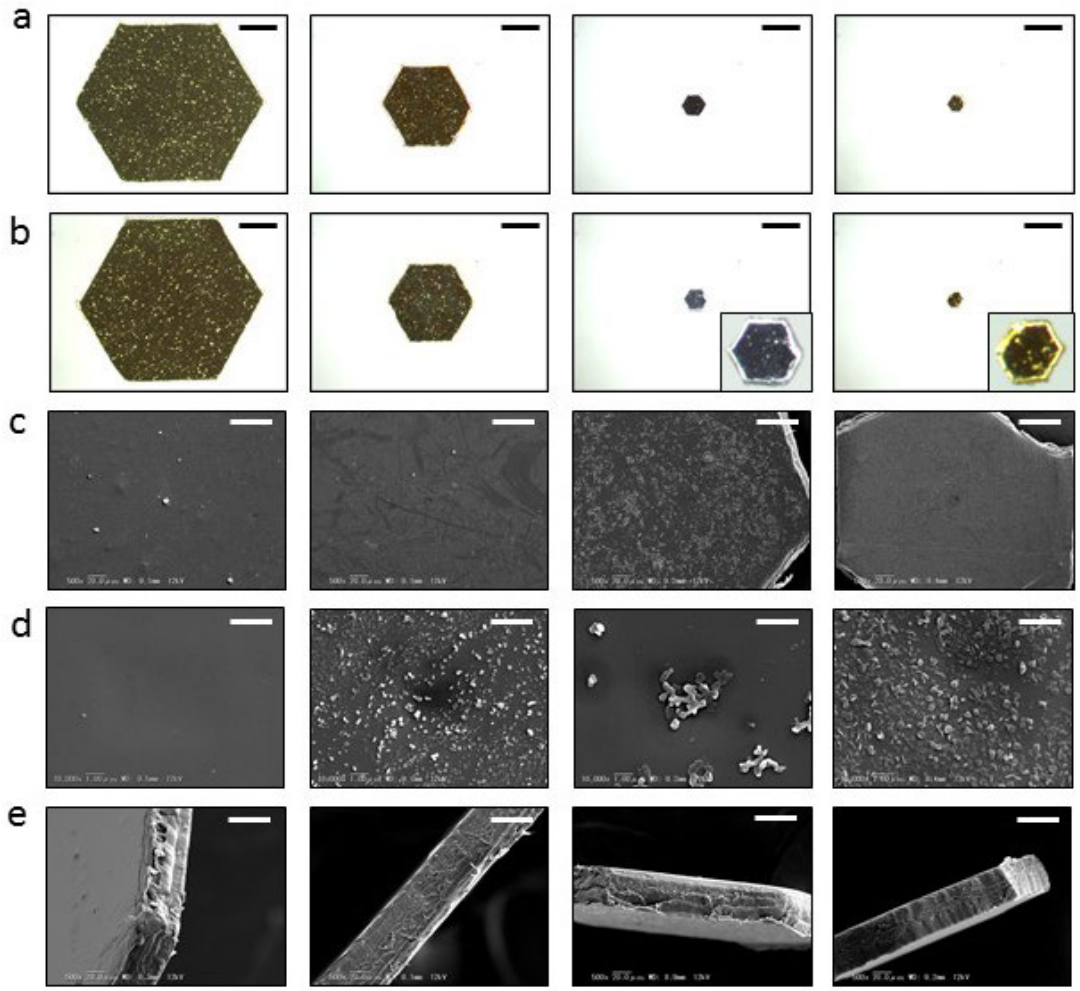

Figure S1. Optical microscopic and scanning electron microscopic (SEM) images of the hexagonal plates. **a**,**b**) Optical microscopic images of the plates before (a) and after (b) fluorination treatment with 1*H*,1*H*,2*H*,2*H*-perfluorodecyltrichlorosilane. Scale bar: 0.5 mm. **c**,**d**) Scanning electron microscopic (SEM) images of the fluorinated plates at different magnifications. Scale bars: 40 μm (c), 2 μm (d). **e**) Side-view SEM images of the fluorinated plates. Scale bar: 40 μm.

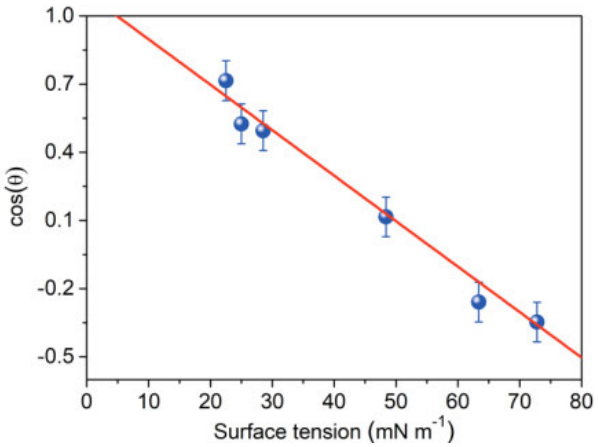

Figure S3. Zisman plot to evaluate the critical surface energy of the fluorinated PET plates (here: conducted on a fluorinated PET substrate). The measurement should be influenced by the surface roughness of the PET substrate.

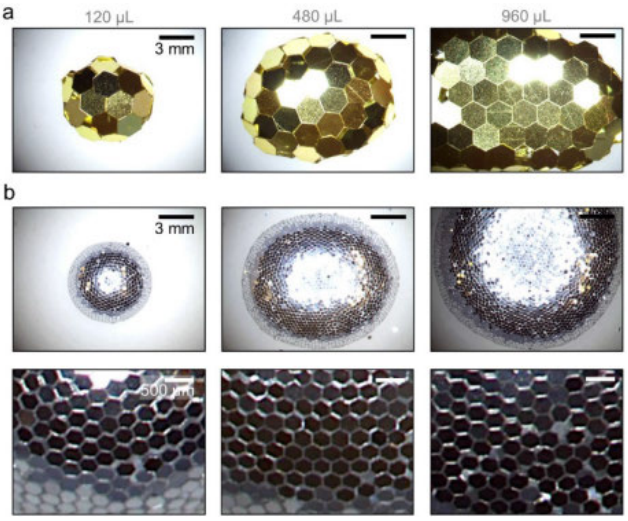

Figure S4. Optical microscopic images of large polyhedral LMs. **a**) Polyhedral LMs prepared with 2.48 mm-sized plates and 120 µL, 480 µL, and 960 µL water droplets. **b**) Polyhedral LMs prepared with 0.34 mm-sized plates and 120 µL, 480 µL, and 960 µL water droplets (top). Higher magnification images are also shown (bottom).

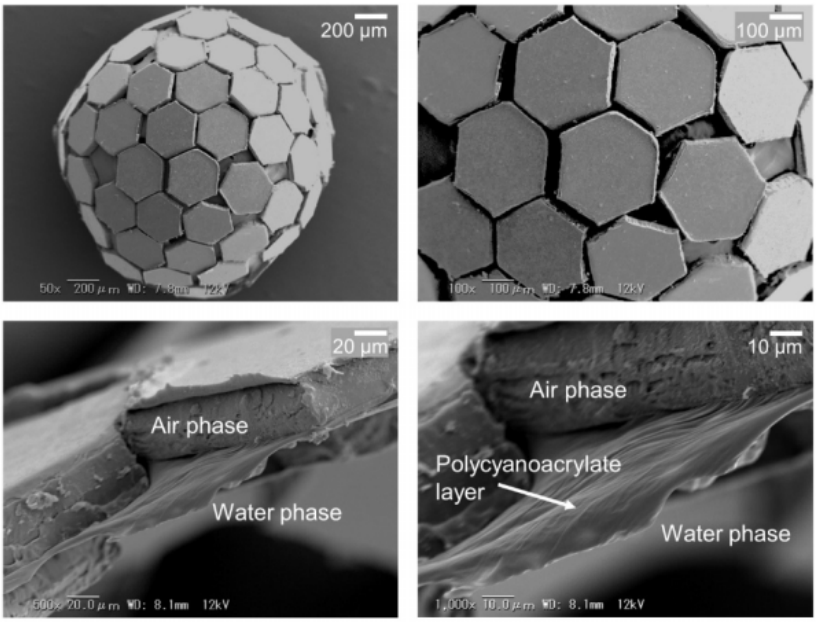

Figure S6. SEM images of a dried polyhedral PM prepared with 0.34 mm-sized plates and a 3 µL water droplet after superglue (cyanoacrylate) treatment at different magnifications. The cyanoacrylate polymerizes and solidifies the air-water interface. The positions of the polycyanoacrylate layer as well as the air and water phase, before drying of the LM, are indicated.

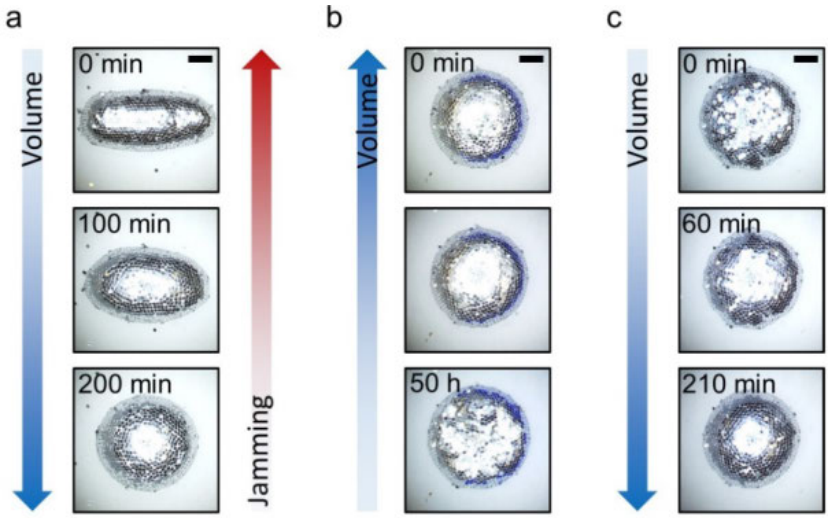

Figure S11. Interfacial jamming of polyhedral LMs. **a**) A spherocylindrical LM containing ≈100 µL of a hygroscopic aqueous saturated LiCl solution (0.34 mm-sized plates) exposed to water vapor. The volume of the LM increased over time, leading to a decrease in interfacial jamming. The LM resumed to a near-spherical shape. **b)** The same LM in the presence of silica gel, which absorbed water from the atmosphere. The volume of the LM decreased slowly, and the LM dried, yet the LM could not return to a cylindrical shape. **c**) After the removal of silica gel and exposure to water vapor, the LM resumed to the near-spherical shape again due to water uptake. Scale bars: 2 mm.

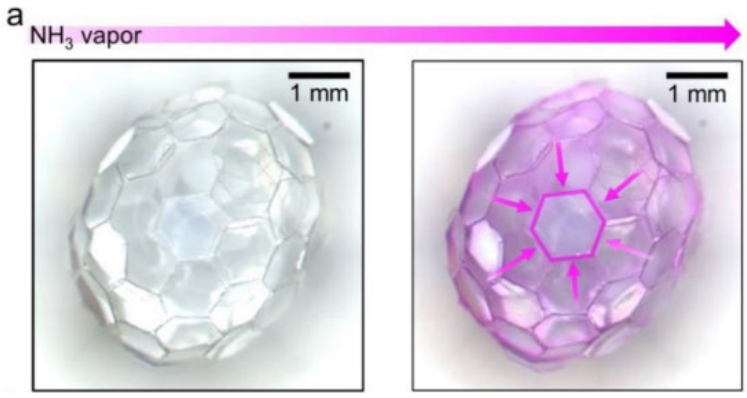

Figure S12. NH_3-induced color change of polyhedral LMs. **a**) The ammonia gas penetrated through the gaps between the plates of a 30 µL polyhedral LM prepared using 1.13 mm-sized transparent plates. Therefore, a slight color gradient is visible between the edges and the middle of each plate in the aqueous solution underneath.

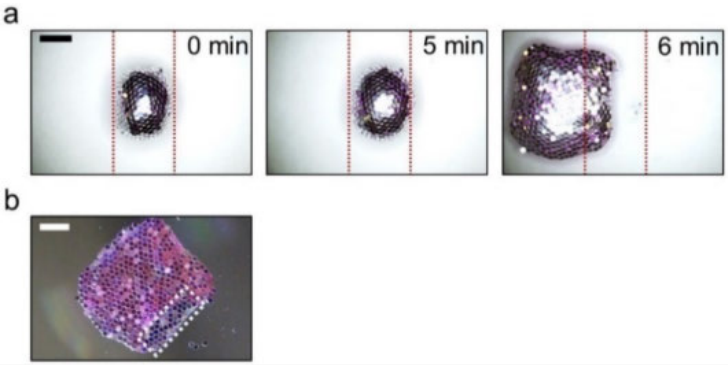

Figure S13. THF-induced breakage of a polyhedral LM. **a**) Stimuli-responsive 30 µL polyhedral LM (0.34 mm-sized plates) containing dyed water broke after 5–6 min exposure to THF vapor. **b**) Backside view of broken liquid marble. The liquid marble broke on the bottom right edge (marked with white dots), and the liquid spread over the glass slide afterward. Scale bars: 2 mm.

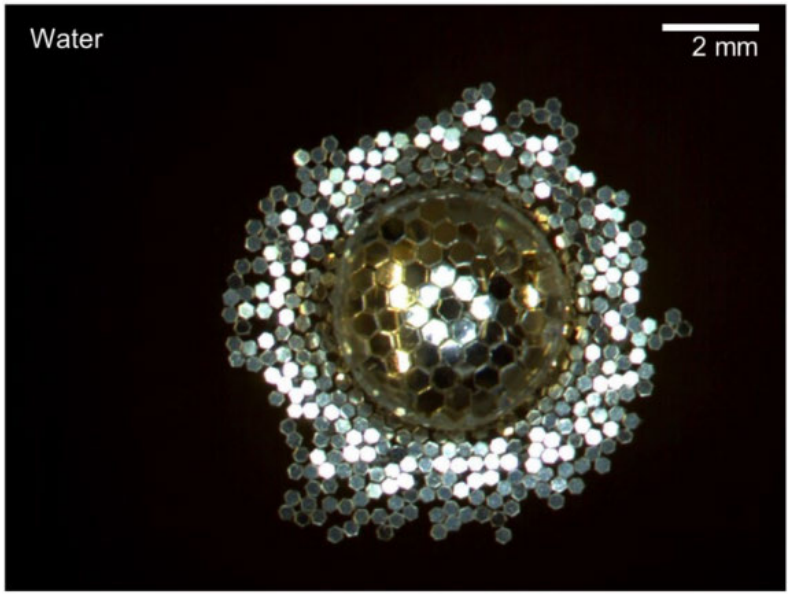

Figure S14. Broken polyhedral LM (containing ≈60 µL aqueous saturated LiCl solution) floating on a water surface. The magnifying effect of the water droplet on top of the plates allows close observation of the plates separating the two air-water interfaces.

11 CURRICULUM VITAE

[redacted]

[redacted]

12 LIST OF PUBLICATIONS AND CONTRIBUTIONS

12.1 PUBLICATIONS

1. C. Shi, X. Cui, X. Zhang, P. Tchoukov, Q. Liu, N. Encinas, M. Paven, F. Geyer *et al.*, Interaction between air bubbles and super-hydrophobic surfaces in aqueous solutions, *Langmuir* **2015**, *31*, 7317.
2. F. Geyer, C. Schönecker, H.-J. Butt, D. Vollmer, Enhancing CO_2 Capture Using Robust Superomniphobic Membranes, *Adv. Mater.* **2017**, *29*, 1603524.
3. K. Jayaramulu, F. Geyer, M. Petr, R. Zboril, D. Vollmer, R. A. Fischer, Shape Controlled Hierarchical Porous Hydrophobic/Oleophilic Metal-Organic Nanofibrous Gel Composites for Oil Adsorption, *Adv. Mater.* **2017**, *29*, 1605307.
4. N. Gao, F. Geyer, D. W. Pilat, S. Wooh, D. Vollmer, H.-J. Butt, R. Berger, How drops start sliding over solid surfaces, *Nat. Phys.* **2018**, *14*, 191.
5. H. Teisala, F. Geyer, J. Haapanen, P. Juuti, J. M. Mäkelä, D. Vollmer, H.-J. Butt, Ultra-fast processing of hierarchical nanotexture for a transparent superamphiphobic coating with extremely low roll-off angle and high impalement pressure, *Adv. Mater.* **2018**, *30*, 1706529.
6. F. Geyer, M. D'Acunzi, C.-Y. Yang, M. Müller, P. Baumli, N. Encinas, D. Vollmer, H.-J. Butt, How to Coat the Inside of Narrow and Long Tubes with a Super-Liquid-Repellent Layer – A Promising Candidate for Antibacterial Catheters, *Adv. Mater.* **2019**, *31*, 1801324.
7. F. Geyer, P. M. Seiler, D. Vollmer, R. Berger, Wie sich Tropfen bewegen, *Phys. Unserer Zeit* **2019**, *50*, 90.
8. P. Baumli, H. Teisala, H. Bauer, D. Garciá-González, V. Damle, F. Geyer *et al.*, Flow-induced long-term stable slippery surfaces, *Adv. Sci.* **2019**, 1900019.
9. F. Geyer, Y. Asaumi, D. Vollmer, H.-J. Butt, Y. Nakamura, S. Fujii, Polyhedral Liquid Marbles, *Adv. Funct. Mater.* **2019**, 1808826.
10. F. Geyer, M. D'Acunzi, A. Sharifi-Aghili, A. Saal, N. Gao, A. Kaltbeitzel, D. Vollmer, H.-J. Butt, When and how self-cleaning of superhydrophobic surfaces works, **2019**, submitted.

11. C.-Y. Yang, N. Encinas, F. Geyer, A. Kaltbeitzel, P. Baumli, J. Reinholz, V. Mailänder, D. Vollmer, H.-J. Butt, Sub-micrometer sized roughness suppresses bacteria adhesion, **2019**, submitted.

12.2 PATENT APPLICATIONS

1. H.-J. Butt, D. Vollmer, F. Geyer, C.-Y. Yang, N. Encinas, M. D'Acunzi, *EP17207768.7* patent application, **2018**.

12.3 PRESENTATIONS (SELECTED)

[redacted]

[redacted]